LASER POWDER BED FUSION OF NICKEL-BASED SUPERALLOYS

LASER POWDER BED FUSION OF NICKEL BASED-SUPERALLOYS

By

Mohamed Balbaa, B.Sc., M.Sc.

A Thesis

Submitted to the School of Graduate Studies in Partial Fulfillment of the Requirements

for the Degree Doctor of Philosophy

McMaster University

DOCTOR OF PHILOSOPHY (2022) McMaster University

(Mechanical Engineering) Hamilton, Ontario

TITLE: Laser Powder Bed Fusion of Nickel Based Superalloys

AUTHOR: Mohamed Balbaa

B.Sc. in Mechanical Engineering (Alexandria University)

M.Sc. in Mechanical Engineering (Alexandria University)

SUPERVISORS: Dr. M. A. Elbestawi

NUMBER OF PAGES: xxxii, 325

"You can tell if a man is clever by his answers.

You can tell if a man is wise by his questions."

- Naguib Mahfouz (1911-2006)

Preface

This thesis is an integrated article thesis aiming to study the laser powder bed fusion (LPBF) process of nickel-based superalloys, IN625 and IN718. The thesis is compiled of five journal articles presented in chapters 2-6, and whose contributions are listed below:

Chapter 2: A version of this chapter is published as a research article “Balbaa, M. A., M. A. Elbestawi, and J. McIsaac."An experimental investigation of surface integrity in selective laser melting of Inconel 625." The International Journal of Advanced Manufacturing Technology 104.9 (2019): 3511-3529. Mohamed Balbaa performed the experimental work, data collection, and analysis and wrote the first draft. Dr. Mohamed A. Elbestawi revised and edited the manuscript. Jeffery McIsaac provided the manufacturing facility.

Chapter 3: A version of this chapter is published as a research article “Balbaa, M., Mekhiel, S., Elbestawi, M., & McIsaac, J. (2020). On selective laser melting of Inconel 718: Densification, surface roughness, and residual stresses. *Materials & Design*, *193*, 108818.” Mohamed Balbaa performed the experimental work, data collection, and analysis and wrote the first draft. Dr. Sameh Mekheil helped perform the experimental work and data collection, revised and edited the manuscript Dr. Mohamed A. Elbestawi revised and edited the manuscript. Jeffery McIsaac provided the manufacturing facility.

Chapter 4: A version of this chapter is published as a research article ‘Balbaa, Mohamed, and Mohamed Elbestawi. "Multi-Scale Modeling of Residual Stresses

Evolution in Laser Powder Bed Fusion of Inconel 625." *Journal of Manufacturing and Materials Processing* 6.1 (2022): 2." Mohamed Balbaa performed the experimental work, numerical modeling, data collection, analysis, and wrote the manuscript. Dr. Mohamed A. Elbestawi revised and edited the manuscript.

Chapter 5: A version of this chapter is submitted to the journal of materials processing technology "Influence of Shot Peening on the Fatigue Performance of Laser Powder Bed Fusion Fabricated IN625 and IN718 Superalloys". Mohamed Balbaa performed the experimental work, data collection, analysis, and writing the manuscript, Ali Ghasemi performed the experimental work, data collection, analysis, and co-wrote the manuscript, Dr. Eskandar Fereiduni performed the experimental work, data collection, analysis, and co-wrote the manuscript, Dr. Kassim Al-Rubaie performed data analysis, and co-wrote the manuscript, Dr. Mohamed A. Elbestawi revised and edited the manuscript.

Chapter 6: A version of this chapter is published as a research article in the international journal of advanced manufacturing technology, "Balbaa, Mohamed, et al. "A novel post-processing approach towards improving hole accuracy and surface integrity in laser powder bed fusion of IN625." *The International Journal of Advanced Manufacturing Technology* (2022): 1-10.". Mohamed Balbaa performed the experimental work, data collection and analysis, and writing the first draft Dr. Ramy Hussein performed the experimental work, data collection, and analysis, and wrote the first draft, Dr. Lloyd Hackel performed the experimental

work, and revised the manuscript Dr. Mohamed A. Elbestawi revised and edited the manuscript.

Mohamed Balbaa
January 2022

Abstract

This thesis aims to investigate the manufacturability of nickel-based superalloys, IN625 and IN718, using the laser powder bed fusion (LPBF) process. The study provides a better understanding of the process-structure-property of nickel-based superalloys, their fatigue life, and subsequent post-processing.

First, the process-structure-property was investigated by selecting a wide range of process parameters to print coupons for IN625 and IN718. Next, a subset of process parameters was defined that would produce high relative density (>99%), low surface roughness (~2 μm), and a low tensile RS.

Second, a multi-scale finite element model was constructed to predict the temperature gradients, cooling rates, and their effect on RS. At constant energy density, RS is affected by scan speed, laser power, and hatch spacing, respectively.

Third, the optimum set of parameters was used to manufacture and test as-built and shot-peened samples to investigate the fatigue life without costly heat treatment processes. It was found that shot peening resulted in a fatigue life comparable to wrought heat-treated unnotched specimen. Additionally, IN625 had a better fatigue life compared to IN718 due to higher dislocations density as well as the absence of γ′ and γ′′ in IN718 due to the rapid cooling in LPBF.

Finally, the effect of post-processing on dimensional accuracy and surface integrity was investigated. A new approach using low-frequency vibration-assisted drilling (VAD) proved feasible by enhancing the as-built hole accuracy while inducing compressive in-depth RS compared to laser peening, which only affects the RS.

These favorable findings contributed to the scientific knowledge of LPBF of nickel-based superalloys by determining the process parameters optimum window and reducing the post-processes to obtain a high fatigue life, a better dimensional accuracy, and improved surface integrity.

Acknowledgments

First and foremost, I would like to express my deepest gratitude to my supervisor, Dr. Elbestawi, for his continuous guidance, patience, and motivation throughout this long journey. I am always humbled by his modesty and sincere advice in my academic and professional choices. Dr. Elbestawi taught me how to always look at the big picture before tackling problems one at a time. I will always be honored to be one of his students and to have him as my mentor.

I want to thank my esteemed supervisory committee: Dr. Zurob and Dr. Ng, for their insightful discussions, different points of view, and guidance. Special thanks to Ramy, Dalia, Mostafa, and Sameh for the ongoing discussions, coffee breaks, support, and friendship over the past few years.

I want to thank my friends and colleagues in the AMG group at McMaster University: my buddies Ali Ghasemi and Eskandar, Abdelhafiz, Ali Safdel, Morteza, Hossein, Hatem, and Mahmoud. Thank you for all the good times, talks, and laughs.

All my heart felt love and appreciation for my family. I am eternally indebted to my parents for their love and support throughout my life. My sisters, for all the love and memories that we share together. Most importantly, my wife Farida, thank you for your love and for keeping up with me throughout this journey. Finally, my son Yaseen, I love you and hope to make you proud.

Contents

Page

List of Figures

List of Tables

List of Abbreviations

AB	As-built
AM	Additive Manufacturing
BC	Boundary Condition
CFD	Computational Fluid Dynamics
CR	Cooling Rate
EDS	Energy-dispersive X-ray Spectroscopy
FE	Finite Element
HIP	Hot Isostatic Pressing
LF-VAD	Low-frequency Vibration-assisted Drilling
LPBF	Laser Powder Bed Fusion
LP	Laser Peening
OPD	Optical Penetration Depth
PSD	Particle Size Distribution
RS	Residual Stress
SEM	Scanning Electron Microscope
SLM	Selective Laser Melting
SP	Shot Peening
TGM	Temperature Gradient Mechanism
XRD	X-ray Diffraction

List of Nomenclature

A	Initial yield strength [MPa]
A_c	Absorption coefficient
A_H	Porous area fraction of powder surface
B	Strain hardening coefficient [MPa]
C	Strain rate coefficient
C_s	Specific heat capacity [J/kg.K]
C_{pl}	Quescient liquid thermal conductivity [J/kg.K]
D_p	Average diameter of powder particles [m]
d	Optical penetration depth [mm]
E	Modulus of Elasticity [GPa]
h	Hatch spacing [mm]
h_o	Overall heat transfer coefficient due to forced convection [W/m^{2}K]
k	Thermal conductivity [W/m.K]
k_g	Gas thermal conductivity [W/m.K]
k_{pb}	Powder bed thermal conductivity [W/m.K]
k_s	Thermal conductivity of the bulk material [W/m.K]
k_r	Equivalent conductivity to thermal radiation between powder particles [W/m.K]
k_{eff}	Effective thermal conductivity [W/m.K]
L	Characteristic length [m]
L_f	Latent heat of fusion [kJ/kg.K]
L_V	Latent heat of vaporization [kJ/kg.K]

Ma	Marangoni number
m	Thermal softening exponent
Nu	Nusselt number
n	Strain hardening exponent
P	Laser power [W]
Pr	Prandtl number
$\dot{q}$	Energy generated per unit volume [W/m^3]
Re	Reynolds number
r	Laser spot radius [mm]
T	Temperature [K]
T_b	Boiling temperature [K]
T_f	The film temperature [K]
T_L	Liquidus temperature [K]
T_s	Solidus temperature [K]
Tm	Melting temperature [K]
Tr	Reference temperature [K]
T_∞	Ambient temperature [K]
t	Time [s]
U_∞	Inert gas velocity [m/s]
v	Laser scan speed [mm/s]
α	Thermal expansion coefficient [K^{-1}]
ε	Equivalent plastic strain
$\dot{\varepsilon}$	Equivalent plastic strain rate [s^{-1}]

$\dot{\varepsilon_o}$	Reference plastic strain rate [s^{-1}]
ε_s	Emissivity of bulk material
γ_g	Kinematic viscosity [m^2/s]
μ	Dynamics viscosity [Pa.s]
φ	Powder bed porosity ratio
ρ	Density of the powder bed [kg/m^3]
σ	Von mises flow stress
σ_s	Stefan-Boltzmann constant [$W/m^2.K^4$]

Chapter 1

Introduction

1.1. Background

Additive manufacturing (AM) started as a rapid prototyping technique with stereolithography (SLA) invention during the 1980s. Continuous research and development of AM of polymers led to new technologies leading to selective laser sintering. However, AM of metals was quite elusive until the early 2000's with the advancement in high power laser that laser powder deposition (LPD) and laser powder bed fusion (LPBF) processes were invented [1].

The American society for testing and materials (ASTM) defined AM as "a process of joining materials to make objects from 3D model data, usually layer upon layer, as opposed to subtractive manufacturing methodologies" [2]. This is the crucial difference between AM and subtractive manufacturing, where the latter process starts with a bulk material then removes over 90% of it to reach the final part. Therefore, AM becomes highly advantageous because it produces near-zero material waste. In addition, AM can create custom complex designs that are otherwise impossible to manufacture using subtractive manufacturing with faster

lead times. However, for AM to outweigh subtractive manufacturing cost-wise, it must be utilized to produce a low number of highly complex parts such as lattice structures, dies, and molds with conformal cooling channels, topology optimized heat exchangers, and turbine blades with conformal cooling channels to name a few. Therefore, these new designs make AM suitable for different industries such as the biomedical, tooling, automotive, and aerospace sectors [3, 4].

LPBF has been extensively researched and used over the past decade due to its capability to produce parts with high complexity, fine features, and relatively high accuracy [5]. The LPBF process is schematically shown in Figure 1-1, where a thin layer of metal powder is uniformly spread over a bed using a recoater, either a blade or a roller. The laser beam selectively melts the powder based on the CAD file to form the first layer. Once the layer is exposed, the bed drops by one layer thickness, and the recoater spreads another layer, and the process is repeated until the whole part is printed. In order to prevent oxidation of the molten material during printing, the entire process is carried out in an enclosed chamber filled with inert gas, either nitrogen or argon.

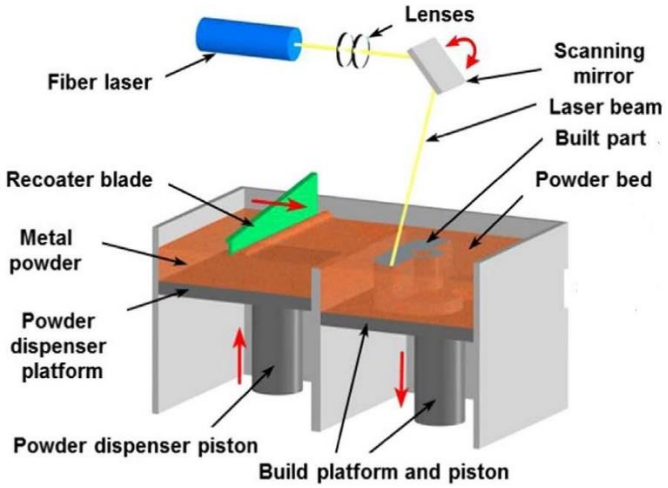

Figure 1-1 Schematic of the LPBF process [6]

LPBF can successfully process several alloys, including stainless steel [7, 8], tools steels [9], aluminum alloys [10, 11], titanium alloys [12, 13], and nickel-based superalloys [6, 14-18], to name a few. Nickel-based superalloys are of particular interest due to their superior mechanical properties such as high tensile strength and high fatigue life even at high-temperature applications and their corrosion resistance [14, 19], making them ideal candidates for the aerospace, marine, and nuclear industries. IN718 has a γ face-centered cubic (γ-FCC) matrix which acquires its strength from the formation of γ”-body-centered tetragonal (γ”-BCT) precipitates, due to the addition of niobium and aluminum, that resists the motion of dislocations [20]. The precipitates are stable up to a temperature of 600 ˚C, above which the alloy starts to lose its strength. This high temperature makes IN718 a suitable candidate for use in high-temperature applications. IN625 obtains its strength through the solid-solution strengthening of the γ matrix with elements such as Mo and Cr. Moreover, for both alloys, the addition of chromium, molybdenum,

and aluminum improves corrosion resistance to withstand the harsh environment in the intended applications, as well as a solid-solution strengthener [21].

Despite the favorable mechanical properties and characteristics of nickel-based superalloys, they are characterized as hard-to-cut materials, which is due to their tendency to work harden, low thermal conductivity, which causes a high-temperature gradient at the tool-workpiece interface, and the formation of carbides, all of which lead to a higher tool wear rate. Therefore, nickel-based superalloys are considered ideal candidates for LPBF as it facilitates their manufacturability with minimal machining required while expanding the design envelope to produce highly complex geometries that were not possible using subtractive manufacturing [22, 23].

1.2. Motivation

The AM market is estimated at 12.7 billion US dollars as of 2020, with the metal AM market roughly estimated to account for 20% of the market. LPBF is currently the dominant metal printing process because it can produce complex parts with high accuracy and fine features. Additionally, it was reported that post-processing such as machining, stress relief, hot isostatic pressing (HIP)…etc. account for 27.9% of an AM part production cost [24]. On the other hand, the suitability and superiority of nickel-based superalloys in highly demanding applications have been established, with IN625 and IN718 accounting for 20% and 55% of the nickel-based superalloys used currently in a different application. Therefore, all three

aspects mentioned above, market growth of AM, need for cost reduction, and broad demand for IN625 and IN718, drive the need to investigate the whole manufacturing workflow end-to-end. Therefore, the investigation would start with LPBF of IN625 and IN718 to produce dense parts with good surface integrity to explore the possibility of reducing the number of post-processes to obtain parts with better mechanical properties.

Research Objectives

The main objective of the current thesis is to identify the best LPBF process parameters to produce parts with good mechanical properties and the effect of post-processing on the possible enhancement of the mechanical properties. This objective can be divided into the following sub-objectives:

1. Exploring the process-structure-property (PSP) for LPBF of IN625 and IN718
2. Develop process maps for relative density, surface roughness, and surface residual stresses (RS) for both alloys
3. Development of a multi-scale numerical model to predict the temperature gradients, thermal history, and cooling rate, and their subsequent effect on RS generation
4. Selection of an optimum process parameters window followed by tensile testing and fatigue testing of as-built and shot-peened samples

5. Investigating the effect of post-printing conventional machining processes such as drilling and unconventional machining such as low-frequency vibration-assisted drilling (VAD) on dimensional accuracy and surface integrity.
6. Exploring the feasibility of reducing the number of post-processes needed to obtain AM parts with desirable mechanical properties and surface integrity using drilling, VAD, and peening.

Thesis Outline

Overall, the main results of this thesis have been written in five journal articles, three of which are already published, one is accepted, and the other article is submitted to a peer-review journal. The thesis is divided into the following chapters:

Chapter 1 introduces the background of AM, the motivation behind the research topic, and the objectives of the current thesis.

Chapter 2 is the first published journal article addressing the first two objectives by investigating the effects of a wide range of process parameters on the density, surface roughness, and surface RS in the LPBF of IN625.

Chapter 3 presents the second published journal article, which covers the PSP of LPBF IN718. The study investigates the meltpool dimensions of single tracks to help narrow the window of process parameters to be used for printing coupons. Process maps were developed for the relative density, surface roughness, and surface RS.

Chapter 4 is the third published journal article that presents the multi-scale finite element (FE) model to address the third objective. Single tracks, multi-tracks, and multi-layers models were set up to predict meltpool dimensions, temperature history, temperature gradients, and the induced RS. In addition, the effect of the individual process parameters on RS was investigated, and the impact of applying the same energy density on the generated RS.

Chapter 5 is a submitted journal article that investigates the fatigue life of IN625 and IN718 to fulfill objectives four and six. The optimum process parameters were selected to produce high density, low surface roughness, and low tensile RS. In addition, the fatigue life of as-built and shot-peened samples was investigated to explore the feasibility of obtaining a fatigue life similar to or superior to wrought alloy without the need for heat treatments.

Chapter 6 is an accepted journal article investigating the feasibility of using conventional drilling or VAD as a post-process to improve as-built part dimensions while improving the surface integrity, specifically by inducing in-depth compressive RS. The proposed methods are compared to laser peening, which only enhances the RS without improving the dimensional accuracy; thus, using drilling would reduce the number of post processing steps and costs required and address the fifth and sixth objectives.

Chapter 7 summarizes the thesis's main conclusions, contributions, and suggestions for future work.

References

[1] I. Gibson, D. Rosen, and B. Stucker, *Additive manufacturing technologies: 3D printing, rapid prototyping, and direct digital manufacturing*: Springer, 2014.

[2] ISO/ASTM52900-15, "Standard Terminology for Additive Manufacturing – General Principles – Terminology," ed. ASTM International, West Conshohocken, PA, 2015, www.astm.org.

[3] S. Mellor, L. Hao, and D. Zhang, "Additive manufacturing: A framework for implementation," *International Journal of Production Economics*, vol. 149, pp. 194-201, 2014.

[4] S. Ford and M. Despeisse, "Additive manufacturing and sustainability: an exploratory study of the advantages and challenges," *Journal of Cleaner Production*, vol. 137, pp. 1573-1587, 2016.

[5] W. E. Frazier, "Metal additive manufacturing: a review," *Journal of Materials Engineering and Performance*, vol. 23, pp. 1917-1928, 2014.

[6] L. E. Criales, Y. M. Arısoy, B. Lane, S. Moylan, A. Donmez, and T. Özel, "Laser powder bed fusion of nickel alloy 625: Experimental investigations of effects of process parameters on melt pool size and shape with spatter analysis," *International Journal of Machine Tools and Manufacture*, 2017.

[7] E. Liverani, S. Toschi, L. Ceschini, and A. Fortunato, "Effect of selective laser melting (SLM) process parameters on microstructure and mechanical properties of 316L austenitic stainless steel," *Journal of Materials Processing Technology*, vol. 249, pp. 255-263, 2017.

[8] M. Yakout, M. Elbestawi, and S. C. Veldhuis, "Density and mechanical properties in selective laser melting of Invar 36 and stainless steel 316L," *Journal of Materials Processing Technology*, vol. 266, pp. 397-420, 2019.

[9] M. Narvan, K. S. Al-Rubaie, and M. Elbestawi, "Process-structure-property relationships of AISI H13 tool steel processed with selective laser melting," *Materials*, vol. 12, p. 2284, 2019.

[10] N. T. Aboulkhair, I. Maskery, C. Tuck, I. Ashcroft, and N. M. Everitt, "The microstructure and mechanical properties of selectively laser melted AlSi10Mg: The effect of a conventional T6-like heat treatment," *Materials Science and Engineering: A*, vol. 667, pp. 139-146, 2016.

[11] M. Balbaa, A. Ghasemi, E. Fereiduni, M. Elbestawi, S. Jadhav, and J.-P. Kruth, "Role of Powder Particle Size on Laser Powder Bed Fusion Processability of AlSi10Mg Alloy," *Additive Manufacturing*, p. 101630, 2020.

[12] N. Levkulich, S. Semiatin, J. Gockel, J. Middendorf, A. DeWald, and N. Klingbeil, "The effect of process parameters on residual stress evolution and distortion in the laser powder bed fusion of Ti-6Al-4V," *Additive Manufacturing,* vol. 28, pp. 475-484, 2019.

[13] N. Soro, N. Saintier, J. Merzeau, M. Veidt, and M. S. Dargusch, "Quasi-static and fatigue properties of graded Ti–6Al–4V lattices produced by Laser Powder Bed Fusion (LPBF)," *Additive Manufacturing,* vol. 37, p. 101653, 2021.

[14] Z. Tian, C. Zhang, D. Wang, W. Liu, X. Fang, D. Wellmann, *et al.*, "A review on laser powder bed fusion of inconel 625 nickel-based alloy," *Applied Sciences,* vol. 10, p. 81, 2020.

[15] M. Komarasamy, S. Shukla, S. Williams, K. Kandasamy, S. Kelly, and R. S. Mishra, "Microstructure, fatigue, and impact toughness properties of additively manufactured nickel alloy 718," *Additive Manufacturing,* vol. 28, pp. 661-675, 2019.

[16] P. R. Gradl, D. C. Tinker, J. Ivester, S. W. Skinner, T. Teasley, and J. L. Bili, "Geometric feature reproducibility for laser powder bed fusion (L-PBF) additive manufacturing with Inconel 718," *Additive Manufacturing,* vol. 47, p. 102305, 2021.

[17] M. Balbaa and M. Elbestawi, "Multi-Scale Modeling of Residual Stresses Evolution in Laser Powder Bed Fusion of Inconel 625," *Journal of Manufacturing and Materials Processing,* vol. 6, p. 2, 2022.

[18] M. Balbaa, S. Mekhiel, M. Elbestawi, and J. McIsaac, "On selective laser melting of Inconel 718: Densification, surface roughness, and residual stresses," *Materials & Design,* p. 108818, 2020.

[19] D. F. Paulonis and J. J. Schirra, "Alloy 718 at Pratt & Whitney-Historical perspective and future challenges," *Superalloys,* vol. 718, pp. 13-23, 2001.

[20] N. A. Kistler, "Characterization of inconel 718 fabricated through powder bed fusion additive manufacturing," Bachelor's Thesis, The Pennsylvania State University, University Park, PA, USA, 2015.

[21] L. N. Carter, "Selective laser melting of nickel superalloys for high temperature applications," University of Birmingham, 2013.

[22] D. Dudzinski, A. Devillez, A. Moufki, D. Larrouquere, V. Zerrouki, and J. Vigneau, "A review of developments towards dry and high speed machining of Inconel 718 alloy," *International Journal of Machine Tools and Manufacture,* vol. 44, pp. 439-456, 2004.

[23] E. Ezugwu, Z. Wang, and A. Machado, "The machinability of nickel-based alloys: a review," *Journal of Materials Processing Technology,* vol. 86, pp. 1-16, 1999.

[24] T. Wohlers, *Wohlers report 2021*: Wohlers Associates, Inc, 2021.

Chapter 2

An experimental investigation of surface integrity in selective laser melting of Inconel 625

Complete Citation:

Balbaa, M. A., M. A. Elbestawi, and J. McIsaac. "An experimental investigation of surface integrity in selective laser melting of Inconel 625." *The International Journal of Advanced Manufacturing Technology* 104.9 (2019): 3511-3529.

Copyright:

Relative Contributions:

M. A. Balbaa: Performed experiments, analysis, and data interpretation; wrote the first draft of the manuscript

M. A. Elbestawi: Revised and edited the manuscript

J. McIsaac: Provided the manufacturing facility

Abstract:

Inconel 625 is a Ni-based superalloy widely used in nuclear and aerospace applications because of its high strength and corrosion resistance. The current paper investigates selective laser melting of Inconel 625 using a wide range of process parameters; four laser powers, five scan speeds and three hatch spacings. Cube coupons are produced and their end properties are measured, specifically, relative density, surface roughness, microhardness and surface residual stresses. Process maps are constructed to correlate processing parameters to the part surface integrity, and the possible underlying causes are highlighted. Experimental results show that highly dense parts can be produced using selective laser melting and low average surface roughness can be obtained in both the scan and hatch directions. Hatch spacing is the most prominent factor to attain relative densities above 99% while high laser powers are key to lower the average surface roughness. Microhardness and microstructure examination are done for a subset of the process parameters and found to not significantly change with laser power. Surface residual stresses are measured on the top surface in the scan and hatch directions and process maps are developed. There is no particular parameter that solely affects surface residual stresses, despite several cases where the increase in laser power reduced the surface residual stresses. 90% of measurements showed surface tensile residual stresses except for a few cases that resulted in surface compressive residual stress.

Keywords:

Selective Laser Melting; Inconel 625; Density; Surface roughness; Residual stresses.

Acronyms:

AM	Additive Manufacturing
EDS	Energy-dispersive X-ray Spectroscopy
FE	Finite Element
HIP	Hot Isostatic Pressing
PSD	Particle Size Distribution
RS	Residual Stress
SEM	Scanning Electron Microscope
SLM	Selective Laser Melting

Notations:

E_d	Volumetric energy density [J/mm^3]
E	Modulus of elasticity [MPa]
P	Laser power [W]
T	Temperature [ºK]
h	Hatch spacing [mm]
t	Layer thickness [mm]
v	Scan speed [mm/s]
α	Coefficient of thermal expansion [ºK^{-1}]
ρ	Density [kg/m^3]
σ_{th}	Thermal stresses [MPa]
τ_s	Molten droplet solidification time [s]

2.1. Introduction

Additive manufacturing (AM) is a relatively new technology that fabricates a part by sequentially fusing material layer by layer. In contrast to subtractive manufacturing, AM adds material incrementally, either in powder or wire form, to areas where it is needed; leading to high-cost savings [1, 2]. Metal AM gained momentum in the industry including; aerospace, automotive and biomedical sectors, over the past two decades due to its ability to produce new complex designs and a high level of customization. Although currently, metal AM can only process reliably about two dozen alloys, it has been successfully used in processing aerospace alloys such as; Ti-6Al-4V, Ni-based superalloys and stainless steels [2, 3].

The SLM process can be simplified as a block diagram, Figure 2-1, where it has two main inputs; namely metallic powder and process parameters. The output is a built part with certain mechanical properties that require characterization, such as; density, surface roughness, RS, microhardness, to determine the quality of that part.

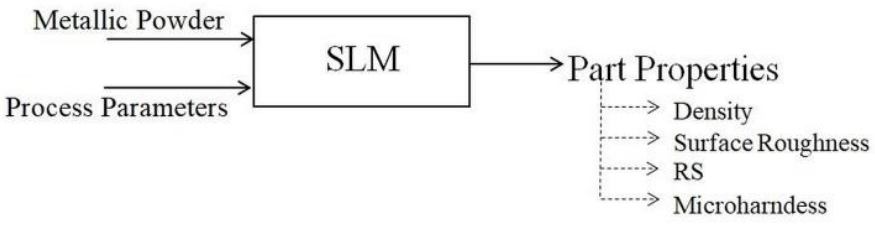

Figure 2-1Block diagram of the SLM process

There is a wide range of process parameters to be considered (see Figure 2-2), but the most widely used ones are; laser power, scan speed, hatch spacing, and layer

thickness. Building a part starts with the exposure of the pre-spread layer of powder using a certain laser power value and translating along a straight line at a constant speed. However, a series of adjacent scan lines is needed for full exposure of the built part. The distance between two adjacent scan lines is termed hatch spacing. In addition, there are other factors which include; scan strategy, stripe width, part orientation, laser diameter, contouring, and layer rotation [4, 5].

2.1.1. SLM of Inconel 625

Inconel 625 is a solid-solution hardened Ni-based superalloy well known for its high-temperature strength, corrosion and fatigue resistance. These high mechanical properties make it favorable for use in aerospace, marine and nuclear applications [6, 7]. However, they are considered as hard-to-cut alloys in subtractive manufacturing due to their high-temperature strength, work hardening causing high tool wear and welding to cutting tool [8].

SLM represented an alternate solution to processing these superalloys, thus making it the focus of a number of recent studies to understand the behavior during manufacturing and the expected outcome. Criales et al. [9-11] studied the effects of process parameters on density, melt pool dimensions, grain size, and orientation. A statistical correlation was established to correlate process parameters to the aforementioned part properties. It was found that maximum density was obtained at high laser power (195 W) and medium scan speed (>800 mm/s). High energy density resulted in larger grain size while grain alignment in the build direction was achieved at medium to high scan speed. In addition, a sensitivity analysis of process

parameters and material properties was performed using a finite element (FE) model of SLM [12]. It was evident that laser power, scan speed, and laser reflectivity had a dominant effect on the melt pool size and peak temperature. The effect of layer thickness on density was examined [13, 14], and it was observed that a 20 µm layer resulted in higher density compared to a 40 µm layer thickness. Carter et al. [15] expanded the study of density to include five Ni-based superalloys to find a minimum threshold for the energy density of 85 J/mm^3 above which parts were considered fully dense.

Process maps are a method to represent output properties in term of input variables [16]. Such maps were developed based on simulations for melt pool dimensions at varying laser powers and scan speeds[17]. The microstructure of SLM parts was the second most studied property, and there is a general finding that SLM results in a mix of cellular structures, and columnar grains oriented mainly in build the direction [6, 11, 18].

These columns are primarily fcc-NiCr and shown to be coincident with bct-Ni_3Nb precipitates using X-ray diffraction (XRD) for phase analysis [18]. Carbides were absent in as-built specimen, however; heat treatment resulted in the formation of MC type carbides containing Mo and Nb which were confirmed by XRD [19, 20]. Surface roughness is another property that was measured in a few studies. It was found that lowering the surface roughness of the top surface required a low scan speed and a higher melt pool overlap while the opposite is true for side surface roughness[21]. The use of contour and hatch process parameters was studied along

with the inclination angle of the part to the build plate [5]. It was observed that surface roughness decreased with increasing scan speed or increasing laser power. Increasing the part inclination angle changed the trend by lowering surface roughness until a laser power of 140 W then it increases again. However, for both inclination angles, the surface roughness on the down skin surface was higher than that on the upper skin.

Tensile properties of as printed and heat treated samples were evaluated by Srinivasan et al. [22] at a fixed set of process parameters. As printed coupons showed higher yield and ultimate tensile strength but lower ductility compared to heat treated and wrought material. These findings match the results found in other studies [23, 24]. As built and post-processed tensile coupons were tested at room temperature and high temperature [25, 26]. The use of hot isostatic pressing (HIP) resulted in the highest ductility at high temperature while as-built coupons showed a brittle behavior. Build orientation is also an important factor to consider, where tensile coupons grown with the load axis parallel to build direction (Z) showed a slightly lower tensile strength and higher ductility compared to those built horizontally [24-26]. An opposite trend was found for fatigue life under completely reversed loading. As-built coupons had a lower fatigue life compared to HIPed, and wrought material outperformed both of them [23, 27]. Shot peening helped improve fatigue life for as-built coupons, while HIPed and shot peened samples had the longest fatigue life compared to as-built and wrought materials. Fatigue life of as-built and polished specimens was examined, and it was found that polished samples

have a slightly better fatigue life due to the removal of any embedded powder particles in the part surface which may act as a crack initiator[5]. Fracture surfaces showed that the dominant mechanism for crack initiation was the local plasticity in the material matrix hence explaining the relatively close fatigue life of as-built and polished specimens. Residual stresses (RS) in SLM of Inconel 625 were narrowly investigated in the literature. RS in the hoop and axial direction were measured for cylinders built with different diameters and heights [28]. It was found that both hoop and axial stresses start as tension at the outer surface and became compressive at the inner surface of the hollow cylinders.

Prior investigations of SLM of Inconel 625 focused mainly on a limited process window with a maximum power of 195 W and corresponding outcomes including; density, melt pool geometry, microstructure and tensile strength. There are very limited studies on surface roughness, fatigue, and residual stresses. In general, several research issues need to be addressed to fully define the process-structure-property relationships for Inconel 625. These include:

- Process maps with a wide range of laser powers, scan speeds, and hatch spacing
- Development of these process maps for density and surface roughness
- Effect of process parameters on microhardness
- Surface residual stresses
- Evolution of in-depth residual stresses

In this paper, the results of a comprehensive experimental investigation focused on surface integrity for Inconel 625 are presented.

2.2. Experimental Work

2.2.1. Metallic Powder

SLM requires a fine, ideally spherical, powder to ensure good quality for built parts. A gas atomized Inconel 625 powder was supplied by Sandvik Osprey with a chemical composition listed in Table 2-1. The powder had a size distribution of 15 µm – 45 µm.

Table 2-1 Chemical Composition of Inconel 625 powder (wt%)

Ni	Cr	Mo	Nb		Fe	Si
Bal.	20-23	8-10	3.15-4.15		<5	<0.5
Mn	Al	C	Co	S	Ti	P
<0.5	<0.4	<0.1	<1	<0.015	<0.4	<0.015

It should be noted that the parts built for the current study used a one-time recycled powder. Characterization of the powder was done to ensure that there were no differences between the fresh and recycled powders. Three characterization tests were performed, first was powder size distribution using Laser diffraction [29]. Second, powder morphology was analyzed using a scanning electron microscope (SEM). Finally, a qualitative analysis of chemical composition was performed using energy dispersive X-ray spectroscopy (EDS) [29, 30].

2.2.2. Machine and Process Parameters

The samples used in the current study were built using an EOS M280 machine equipped with a 400 W Ytterbium fiber laser having a laser spot size of 100 µm set in focused mode. The build chamber was flooded with nitrogen to keep the oxygen level to a minimum while the build plate was preheated to 80 ºC. The samples were designed as cube coupons of side length 10 mm and were built directly to the build plate without any supports. The coupons were built fully with core parameters without any contouring. In order to reduce the chance of recoater blade jamming, the coupons were oriented at 45 degrees.

A wide range of process parameters was studied (Table 2-2), which included; 4 laser powers, 5 scanning speeds and 3 hatch spacing to give a total of 60 different combinations for process parameters. Energy density is a combination of laser power, scan speed, hatch spacing, and layer thickness, Eqn.1, which covered the range from 41.67 J/mm^3 up to 168.75 J/mm^3, under the applied process window. The layer thickness was kept constant at 40 microns and the laser scan rotated 90º each consecutive layer as shown in Figure 2-2. A stripe scan strategy was applied with a stripe width of 10 mm and each layer was exposed once.

$$E_d = \frac{P}{v \times h \times t} \quad (J/mm^3) \tag{1}$$

Table 2-2 Process parameters for Inconel 625

Power, P (W)	Scan speed, v (mm/s)	Hatch spacing, h (mm)	Layer thickness, t (mm)
140,170,220,270	500,550,600,650,700	0.08,0.1,0.12	0.04

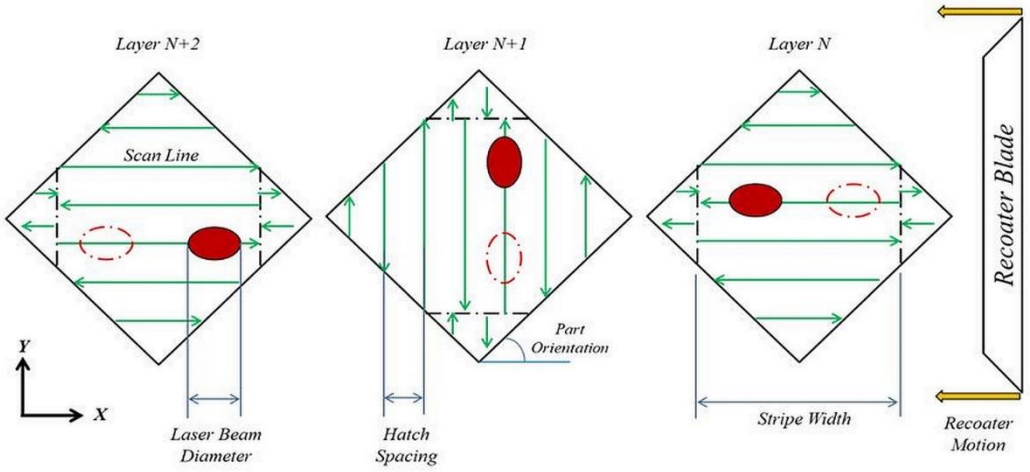

Figure 2-2 Schematic diagram of SLM process parameters

2.2.3. Part Properties

Density measurement

The densities of built coupons were measured using the Archimedes method which is considered an inexpensive, accurate, non-destructive method of measurement compared to optical microscopy or X-ray CT [31]. Each coupon is weighed in air (m_a) then immersed in a liquid and weighed again (m_{fl}) using a scale with a resolution of ± 0.01 g. The density is calculated using, Eqn. 2, where ρ_p is the part density and $\rho_{fl}$is the fluid density. The fluid used was acetone as it results in a better accuracy and repeatability compared to water [31]. The density of acetone,

adjusted for temperature, is 784 kg/m^3 and the density equation was corrected to include the buoyancy effect of air having a temperature corrected density (ρ_{air}) of 1.19 kg/m^3. In the current study, density measurements are represented in the form of relative density (%), where the measured density is divided by the bulk density of Inconel 625 of 8440 kg/m^3.

$$\rho_p = (\rho_{fl} - \rho_{air}).\frac{m_a}{m_a - m_{fl}} + \rho_{air} \ \ (kg/m^3) \tag{2}$$

Surface Roughness

Surface roughness was measured for the top surface of the cube coupons (XY plane). The arithmetic mean deviation R_a is measured and two values are reported. The first is the average of 5 measurements taken parallel to the scan lines (scan direction) and the other is the average of another 5 measurements perpendicular to the scan lines (hatch direction). A Mitutoyo SJ-410 stylus profilometer was used, and measurement was done over a set distance of 4.8 mm divided into 5 equal sections [32]

Microhardness

Microhardness was measured using a Vickers hardness test, where a diamond indenter with a vertex angle of 136º was used. A load of 100 gf was applied for 10 s and the two diagonals of the indentation, Figure 2-3, were measured using an optical microscope, and Vickers hardness is calculated using Eqn.3. Microhardness was measured at 3 different heights; 2.5 mm, 4.5 mm and 6.5 mm from the bottom

surface of the cube and the hardness at each height is the average of 5 measurements.

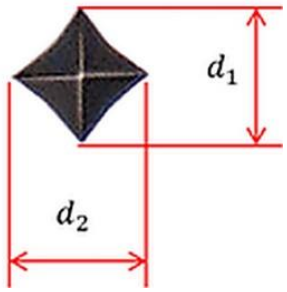

Figure 2-3 Vickers indentation with main diagonals

$$H_V = 1.854\frac{F}{d^2} \quad (3)$$

Where:

F: Applied load (kgf)

$d = \frac{d_1+d_2}{2}$ (mm)

Residual stresses

XRD is a non-destructive reliable method to measure RS [33]. A CoKα radiation source was used having a wavelength of 1.79206 Å with a 1 mm collimator and the 2Theta angle was 111.4º corresponding to a lattice plane of index 3 1 1. A total of 20 frames were taken comprising of 5 Phi angles (0º, 72º, 144º, 216º & 288º) and 4 Psi angles (10º, 25º, 40º & 55º). In order to capture more data from differently oriented diffraction planes, an oscillation angle of 2 degrees was applied to the Psi angles. Measurements were taken on the top surface, and the instrument was set so that its X-axis is in the scan direction and its Y-axis is in the hatch direction

2.3. Results

2.3.1. Powder Characterization

Powders were sieved before every build using an 80 µm sieve then the PSD for both sieved powders, was measured. It was found that the PSDs were almost identical, Figure 2-4, and follow a Gaussian distribution.

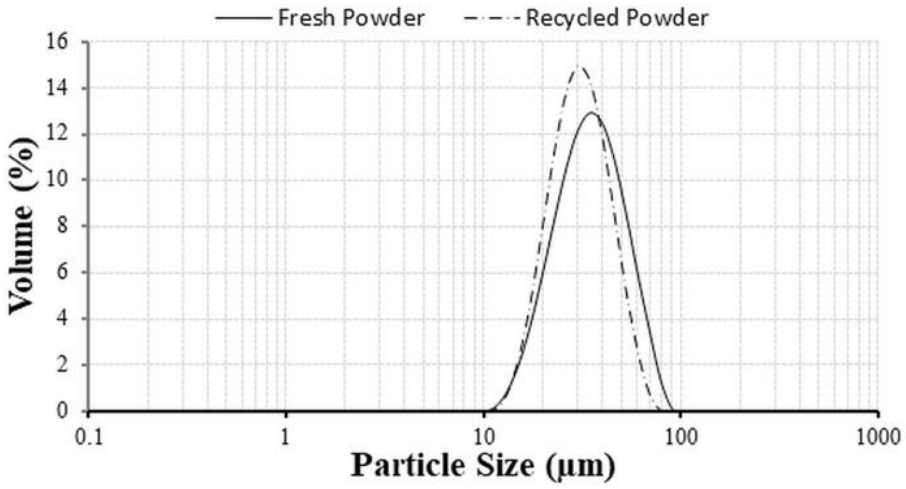

Figure 2-4 PSD of fresh vs recycled powder

The slight difference in mean particle size, Table 2-3, could be traced back to the sieving and consequent removal of any agglomerates that might have formed after the use of the powder for the first time. In addition, examination of powder morphology using SEM, Figure 2-5, showed mostly spherical powder particles with some fine satellite particles.

Table 2-3 Powder particles size (µm)

Percent	D(10)	D(50)	D(90)
Fresh	18.805	32.251	53.472
Recycled	18.087	28.558	44.746

The chemical composition of both powders was compared using EDS [29, 30]. EDS was used as a qualitative method, and showed that both fresh and recycled powders match closely in chemical compositions (Table 2-4).

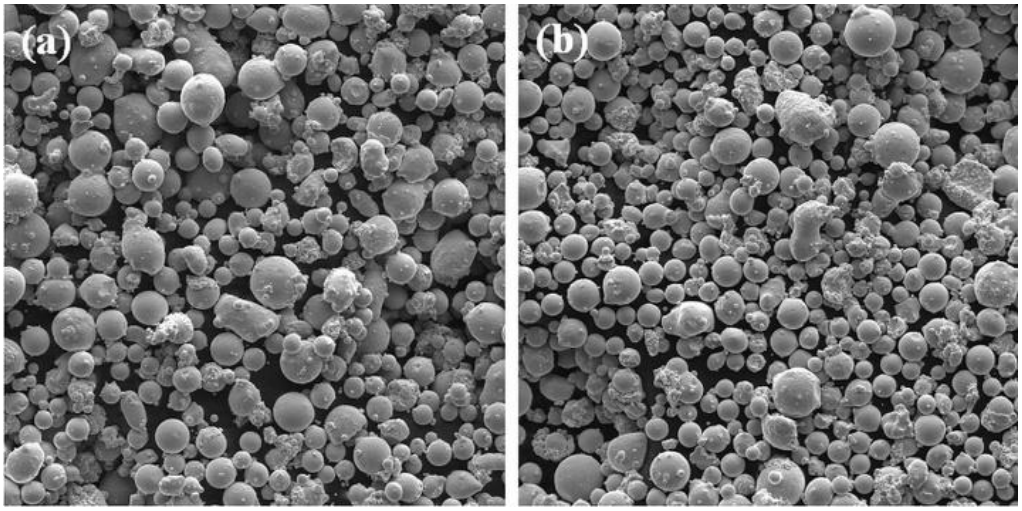

Figure 2-5 SEM images at 500X of (a) Fresh powder (b) Recycled once powder

Table 2-4 Chemical composition using EDS (wt%)

Element	Al	Si	Ti	Cr	Mn	Fe	Co	Ni	Nb	Mo
Fresh	0.37	0.27	0.1	21.56	0.18	1.89	0	61.29	3.85	10.5
Recycled	0.4	0.29	0.08	21.71	0.23	1.94	0.05	61.52	3.48	10.29

2.3.2. Density

The relative density was measured for the all 60 parameters combinations where each coupon was measured 3 times and the average relative density was calculated. Measurement error was calculated and found to be 0.33% on average. First the effect of hatch spacing on relative density, Figure 2-6, was examined at different scan speeds and constant laser power. It was found that hatch spacing had a relatively more prominent effect on density compared to scan speed. Increasing hatch spacing to 0.1 mm lead to an increase in relative density, however; further increase in hatch spacing caused a reduction in relative density for all laser power except 140 W. The variation in relative density is small especially after factoring in the uncertainty of measurements. The increase in relative density with the increase in hatch spacing can be attributed to the larger overlap between melt tracks. Since part of the previously solidified track melts and due to surface tension, it attaches itself to the new melt pool, thus possibly leaving behind pores [34]. In addition, the higher energy density at constant laser power and scan speed can result in evaporation of the molten powder and entrapment of gas or vapor pockets which show up as small spherical pores. Therefore, increasing hatch spacing reduced the effects of these two factors and improved the resulting relative density. On the other hand, a further increase in hatch spacing can lead to a lack of overlap between adjacent melt tracks and thus the formation of voids [34, 35]. Future work is considered to investigate the formation of voids and keyhole defects at the part core.

Three process maps, Figure 2-7, are constructed corresponding to different hatch spacing. Each process map shows the relative density at different power-scan speed (P-V) combinations. The maps are divided into 3 main zones; Zone I represents relative densities above 99% which can be considered fully dense, Zone II is for the relative density range of 98% to 99% and Zone III includes relative densities below 98%.

It can be seen that Zone I is only achieved at a hatch spacing of 0.1 mm with all laser power values above 140 W. Using a hatch spacing of 0.08 mm results in Zone II (>98%). It also leads to the lowest relative density at high laser powers which can be attributed to evaporation of powder and pore formation at high energies. Finally, the variation of laser power or speed does not appear to have a significant effect on relative density when operating at a hatch spacing of 0.12 mm; however, the reported relative densities are quite high being above 98%.

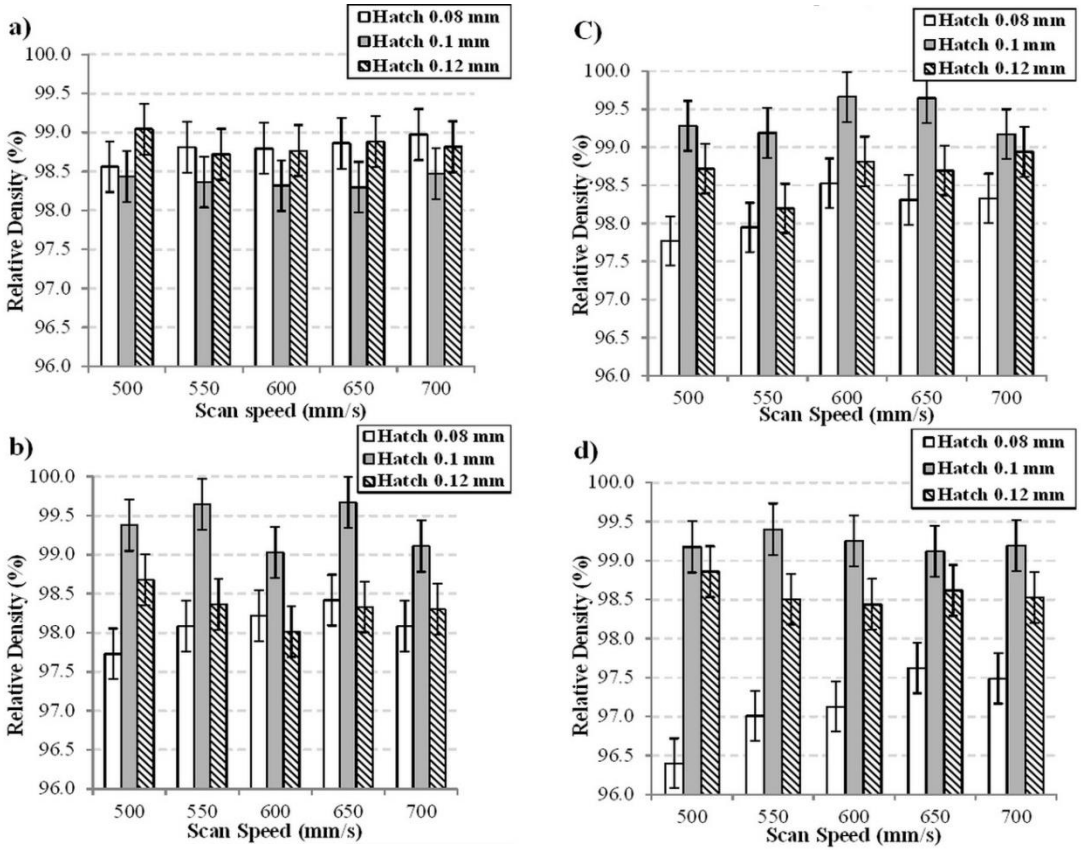

Figure 2-6 Relative density variation with hatch spacing at a) 140 W b) 170 W c) 220 W d) 270 W

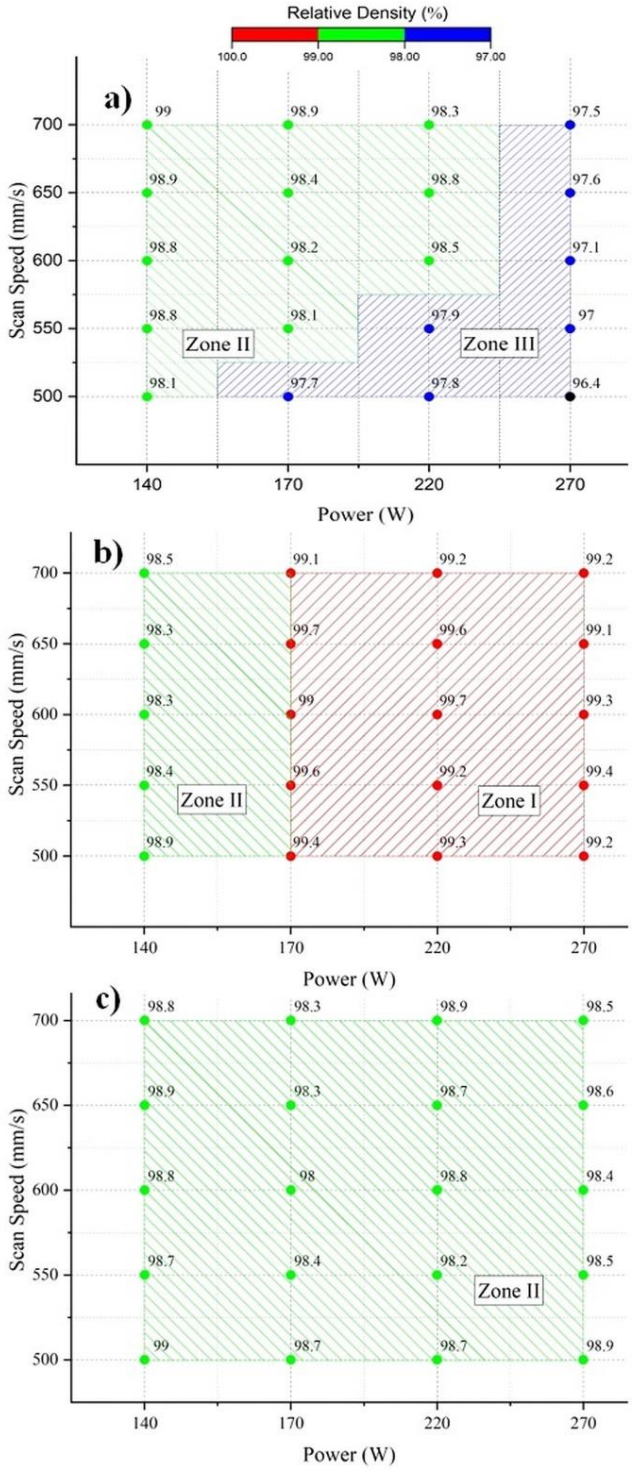

Figure 2-7 Relative density P-V process maps at hatch spacing a) 0.08 mm b) 0.1 mm c) 0.12 mm

2.3.3. Surface Roughness

The average roughness (Ra) was measured on the top plane in a direction parallel to the scan lines, Figure 2-8, and in hatch direction, Figure 2-9. It was found that increasing laser power from 140 W to 270 W reduced the average roughness consequently across all hatch spacing and scan speeds which is in agreement with the literature [36, 37]. However, the increase in scan speed and hatch spacing did not have a consistent prominent effect on the average roughness of the top surface. The decrease of average roughness was due to the increase in input heat which in return yielded a wider melt pool [36] causing a better overlap between adjacent scan tracks as shown in Figure 2-10. This result can be explained more in terms of solidification, whereas a simplification of the time required for a molten droplet of metal to solidify [36, 38] can be calculated using Eqn.4

$$\tau_s = \frac{s^2 k}{3 a k_{sub}} \left[\ln\left(\frac{T_o - T_{sub}}{T_l - T_{sub}}\right) + \left(1 + \frac{k_{sub}}{2k}\right) \frac{L}{C(T_l - T_{sub})}\right] \quad (4)$$

Where s is the initial size of the droplet, a is the diffusivity, k_{sub} is the thermal conductivity of the substrate or underlying solidified material, T_o is the initial temperature of the droplet, T_l is the liquidus temperature of the material, L is the latent heat of fusion and C is the material specific heat capacity.

Based on Eqn. 4, as the laser power increases, more powder is melted hence the melt pool is wider i.e. the molten droplet size (s) increases. Also, the initial temperature increase adds to the time required for cooling and solidification of the melt pool. The increased solidification time allows the molten metal to spread and

cover the surrounding powder and previous melt pool track. However, for this spreading to occur, from a fluid mechanics perspective, the wettability of the molten metal must increase, which happens in the case of the reduction of surface tension.

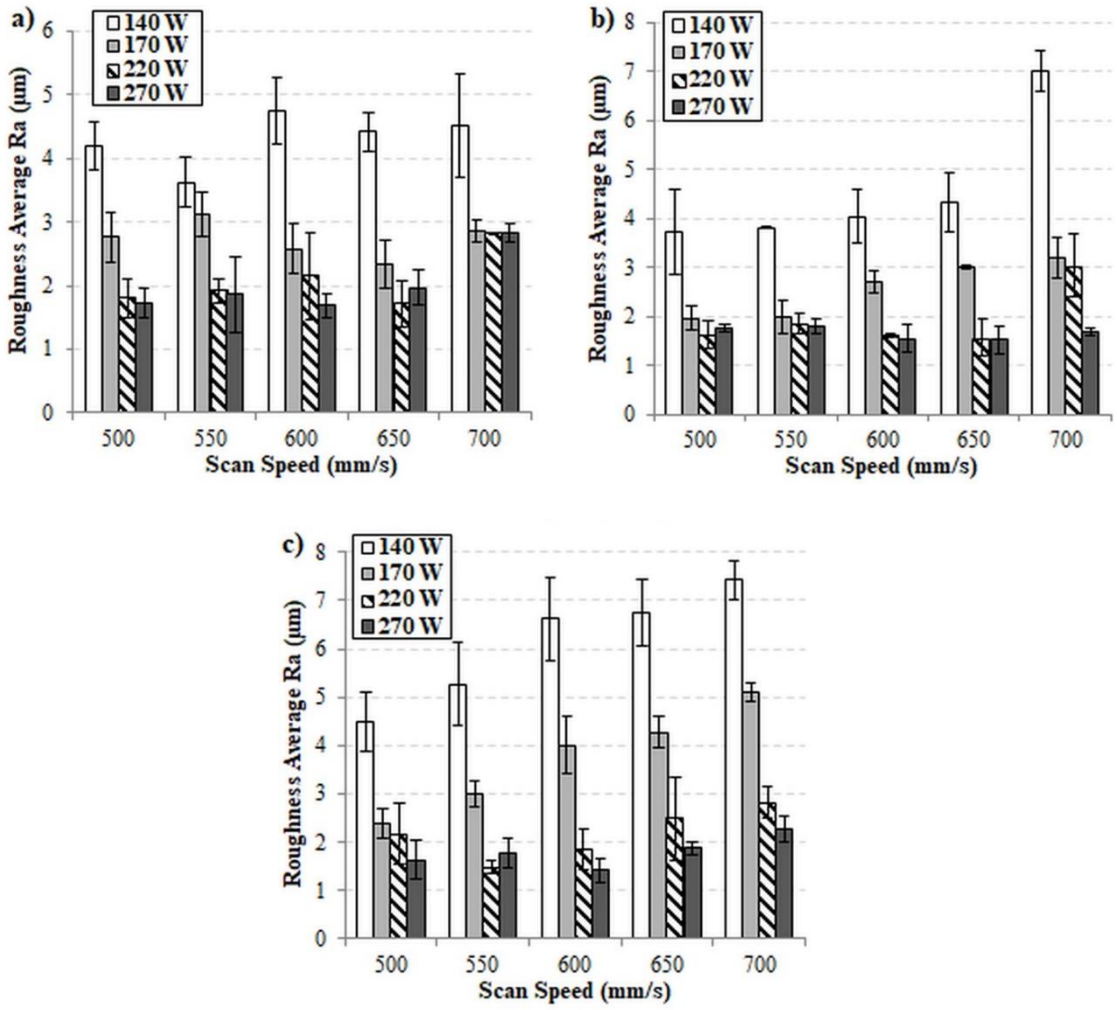

Figure 2-8 Average roughness along scan direction at hatch a) 0.08 mm b) 0.1 mm c) 0.12 mm

There are no measurements of the surface tension for Inconel 625 in the literature. However, measurements were done for a Nickel based alloy (Fe-Ni-Cr-S) [39, 40]. The measurements showed that the temperature coefficient of surface tension is inversely proportional to temperature, which means that as the temperature of the melt pool increases the surface tension drops thus relieving the cohesive forces in the melt pool and favoring the adhesive forces or wettability of the melt pool. For this reason, fewer satellite powder particles are found on the surface as shown in Figure 2-10 and the possibility of balling occurring is lower, which is in agreement with the results found in the literature [36, 41, 42]

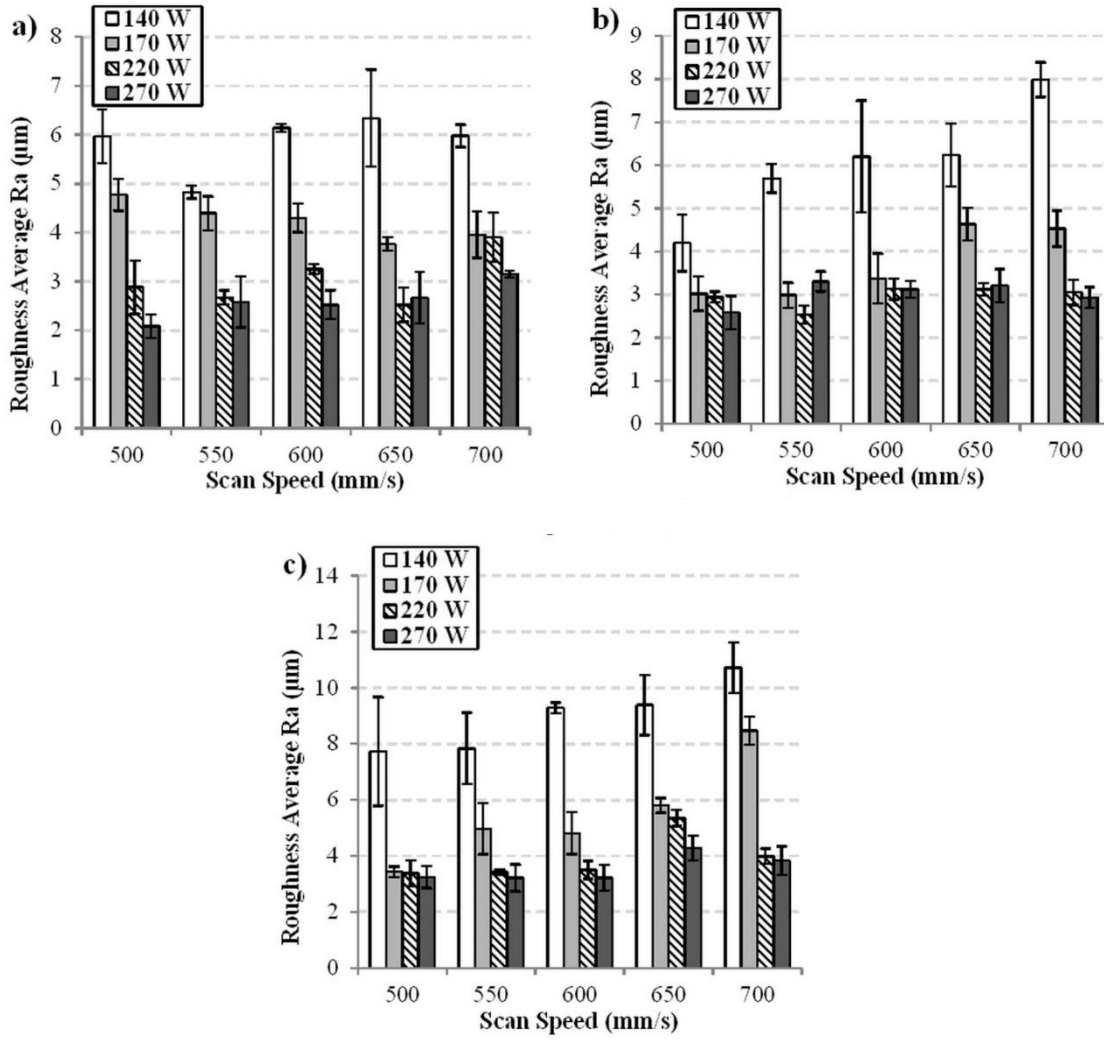

Figure 2-9 Average roughness in hatch direction at hatch a) 0.08 mm b) 0.1 mm

c) 0.12 mm

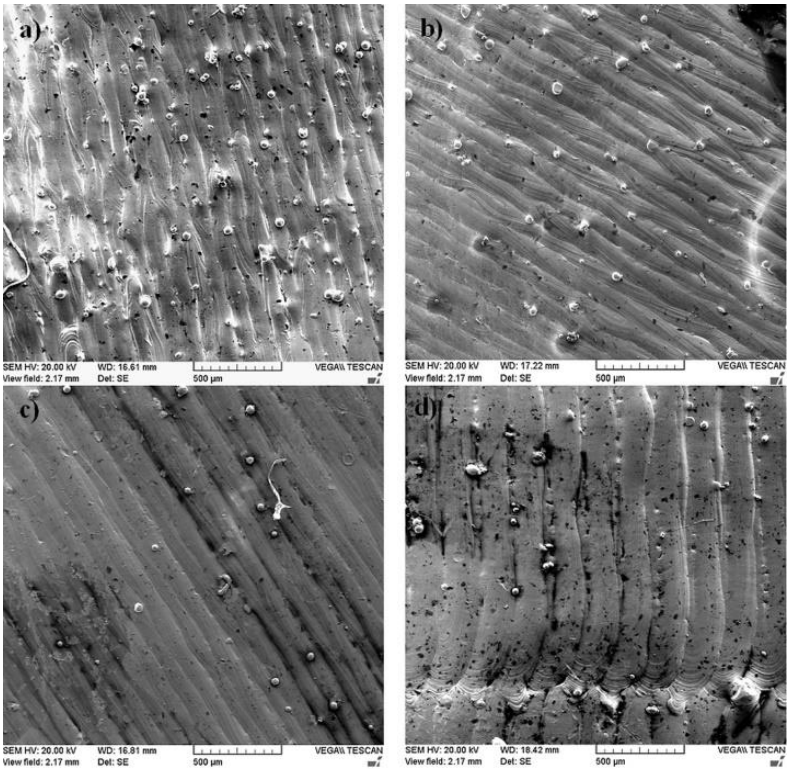

Figure 2-10 SEM of surface morphology at 600 mm/s, 0.1 mm and laser power

a) 140 W b) 170 W c) 220 W d) 270 W

Process maps were constructed for average roughness in both scan and hatch directions, Figure 2-11. Average roughness values were based on roughness grade numbers [43] where N7 ranges from 1.6 µm to 3.2 µm, N8 ranges from 3.2 µm to 6.3 µm and N9 ranges from 6.3 µm to 12.5 µm. Generally, it can be seen that SLM of Inconel 625 results in a fairly smooth surface with roughness grades N7 or N8 for the laser power range of 170 W to 270 W with all scan speeds and hatch spacing. Ideally, a hatch spacing of 0.1 mm gives the widest window of operation to obtain an N7 roughness in both scan and hatch directions.

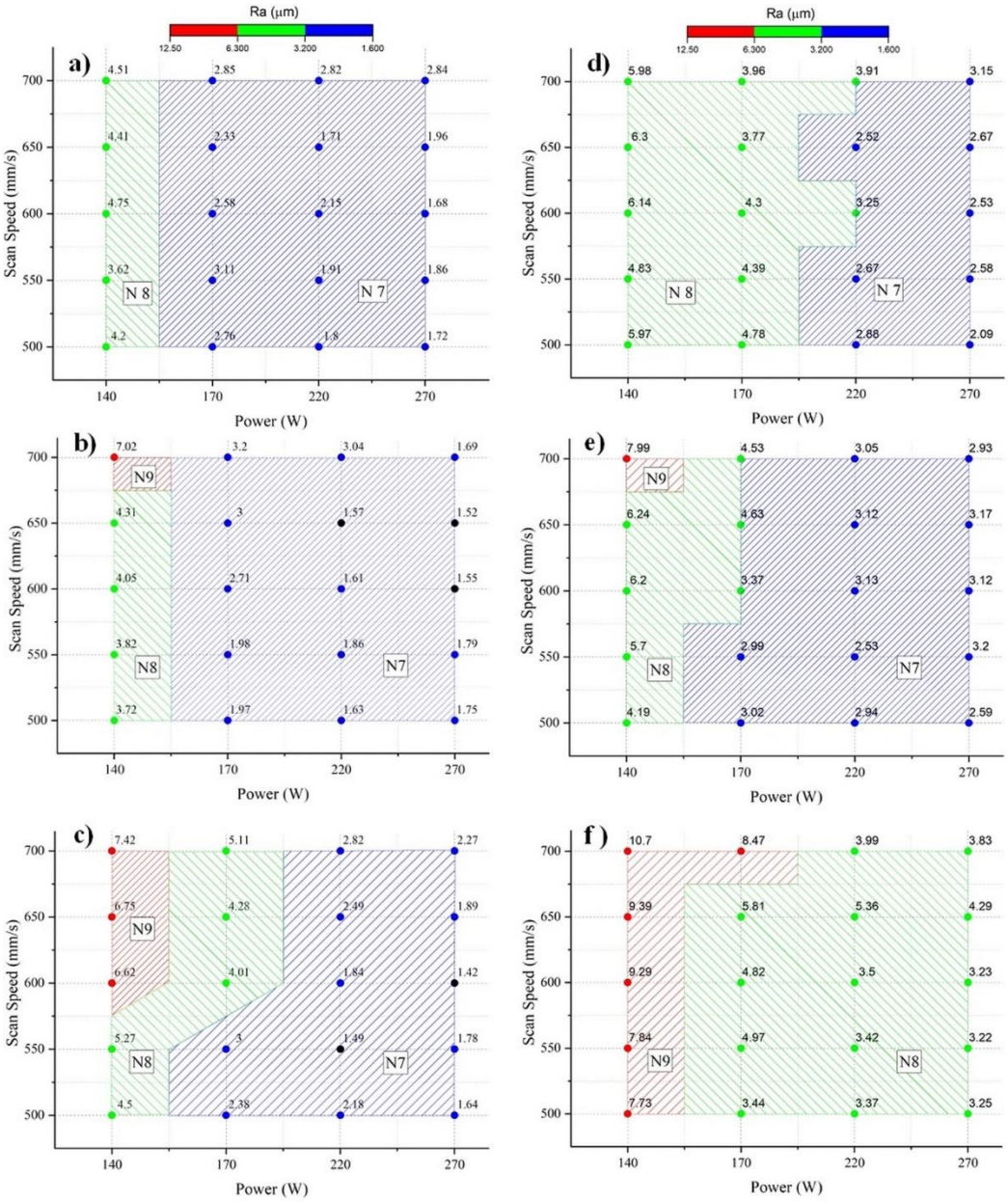

Figure 2-11 Average roughness P-V process maps in scan direction a) 0.08 mm b) 0.1 mm c) 0.12 mm and in hatch direction at d) 0.08 mm e) 0.1 mm f) 0.12 mm

2.3.4. Microhardness

Comparison of average microhardness measured in the Z direction at a constant laser power of 170 W, Figure 2-12, shows that increasing hatch spacing to 0.1 mm led to the highest hardness for all 3 scan speeds. Further increase of hatch spacing lowers the hardness of the parts.

Examining the effect of laser power at 2 different scan speeds and hatch spacing, shown in Figure 2-13, it is observed that at a speed of 600 mm/s, increasing power from 170 W to 270 W reduces microhardness regardless of hatch spacing. An opposite trend is found at a scan speed of 700 mm/s. However, by factoring in the standard deviation, no difference in microhardness would be noted which was also confirmed by examining the microstructure under an optical microscope. For example, at a scan speed of 600 mm/s and hatch spacing of 0.12 mm, a higher microhardness at 170 W could indicate a finer microstructure, however; there was no noticeable difference in the microstructure fine grain size as shown in Figure 2-14 with the only visible difference being the growth directions of the grains.

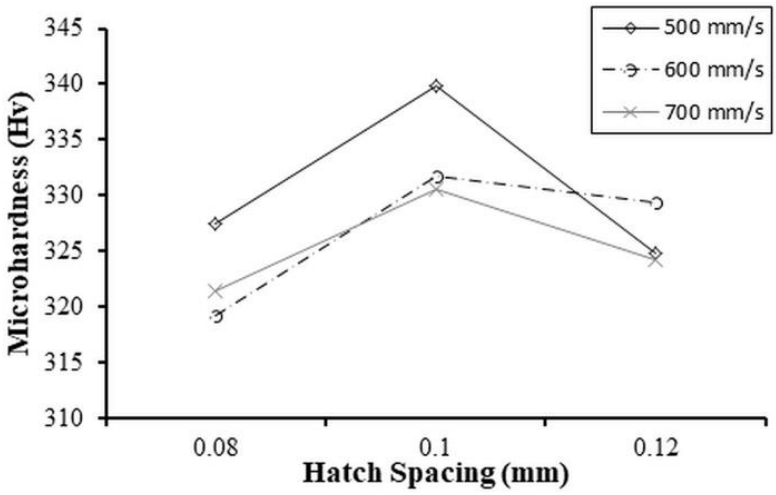

Figure 2-12 Average microhardness in the Z direction at 170 W with different scan speeds and hatch spacings

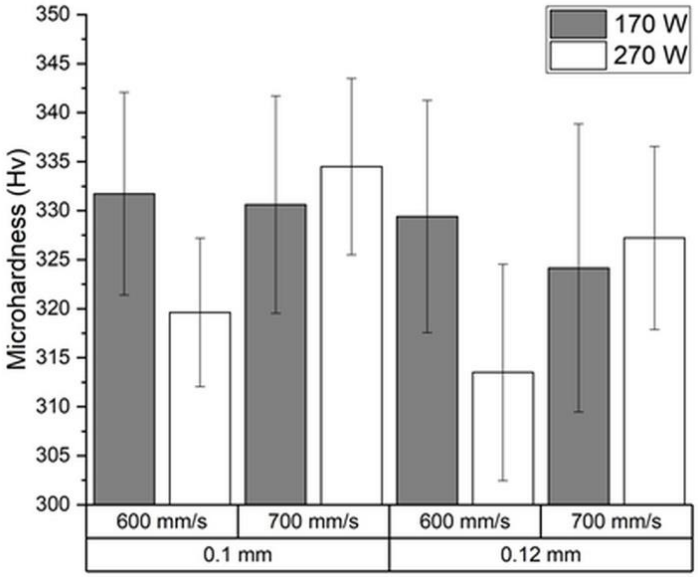

Figure 2-13 Effect of laser power on microhardness at different speeds and hatch spacing

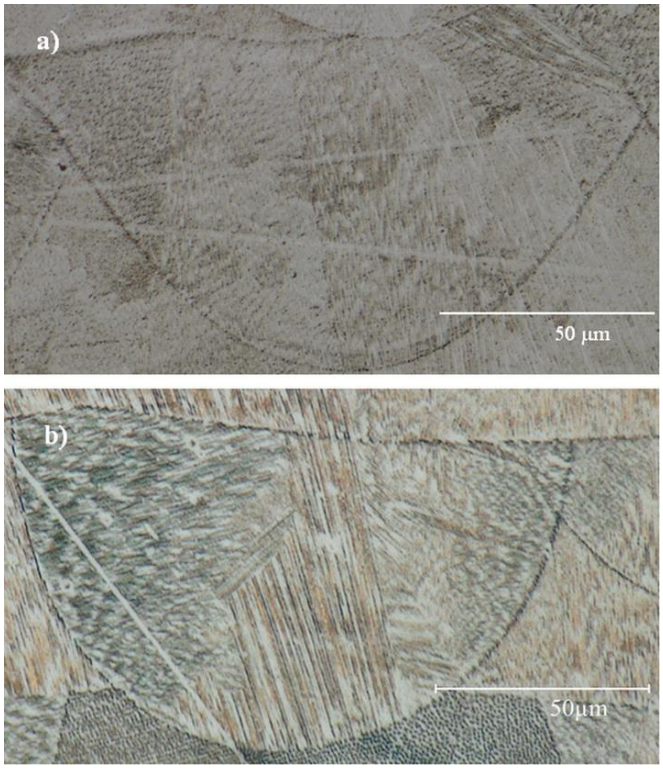

Figure 2-14 Microstructure of Inconel 625 for scan speed 600 mm/s and hatch spacing of 0.12 mm at a) 170 W b) 270W

The variation of Microhardness along the build direction shown in Figure 2-15 was also measured and it is shown that in most cases the hardness is highest near the top surface. However, there are cases at hatch spacing of 0.1 mm that contradict the aforementioned trend but the difference in microhardness is not significant.

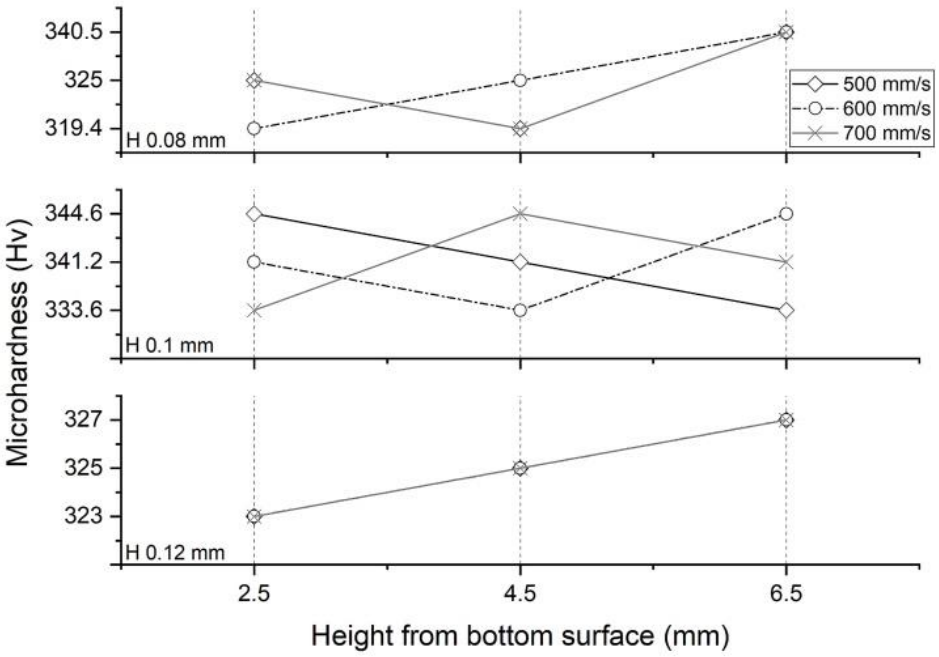

Figure 2-15 Variation of microhardness along the height at 170 W, different speeds and hatches

2.3.5. Surface Residual Stresses

Location of RS Measurement

XRD measurement of RS on the top surface started by pointing the collimator at a fixed point. For a chosen set of parameters, this approach yielded surface RS, in the scan direction, of -110 ± 65 MPa but analysis showed that only a few data were collected due to the relatively large grains of the specimen.

The common solution was to oscillate the specimen ±2 mm in both X and Y directions. The new solution gave surface RS of 220.8 ± 17.3 MPa. However, there was the uncertainty that RS varies across the surface due to the difference in scan lines lengths as you move from the center of the coupons to the outer edges.

Therefore, an alternative approach was proposed to measure at a fixed point while oscillating the Psi angle by 2 degrees which gave an RS measurement of 465.7 ± 27.7 MPa. In addition, a sensitivity analysis was done to examine the variation of RS across the top surface. Five measuring points were taken, starting at the center and followed by two points 1 mm apart in the X direction and another two points 2 mm apart in the Y direction as shown in Figure 2-16. For consistency, the measurement point was chosen on the diagonal of the cube coupons, roughly 6 mm from the right corner.

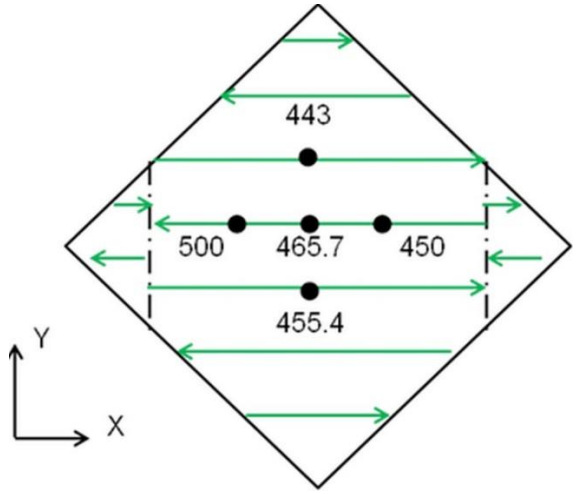

Figure 2-16 Variation of RS (MPa) across the top surface

Residual Stress Measurements

RS were measured in both scan and hatch directions at the center of the top surface of the coupons. Results show that RS is mostly tensile, in both scan and hatch directions, except for a few cases which exhibited compressive surface RS, as shown in Figure 2-17. SLM is prone to the generation of tensile RS due to the high-temperature gradient between the top layers and the underlying material and

substrate in what is termed as temperature gradient mechanism (TGM) [44, 45]. The high temperature is generated due to laser irradiation, causing the top pre-melting layer to expand against the constriction of the underlying material. In reaction, the top layers are compressed and with the drop of yield strength at high temperatures; a compressive plastic strain is developed. Once the temperature exceeds the liquidus temperature, the material in the top layer fully melts and the melt pool expands to ensure sufficient overlap with adjacent tracks and the layer below to achieve good consolidation. As the laser source moves away, the temperature starts to decrease and the melt pool solidifies, thus shrinking in volume. The shrinking melt pool starts to pull inwards on the surrounding solid material [44]. The shrinkage of the solidified melt pool coupled with the previously compressed layers during TGM induces tensile RS in the top layers [46].

Results in Figure 2-17 show that there is no specific monotonic trend relating surface RS to individual process parameters, however; many cases exhibit a drop in surface RS with an increase in laser power. This decrease can be attributed to the formation of a deep melt, thus reducing the temperature gradient between the top and bottom of the part and consequently reduce surface RS[27]. However, there are other factors that could also determine the final surface RS, such as the generation of a large enough melt pool area that would generate a high shrinkage pull on the surrounding solid material, hence increasing the surface tensile RS. This means that there is a threshold for the melt pool size above which the reduction of surface RS, with increasing the input energy, is inverted as observed in the literature [27].

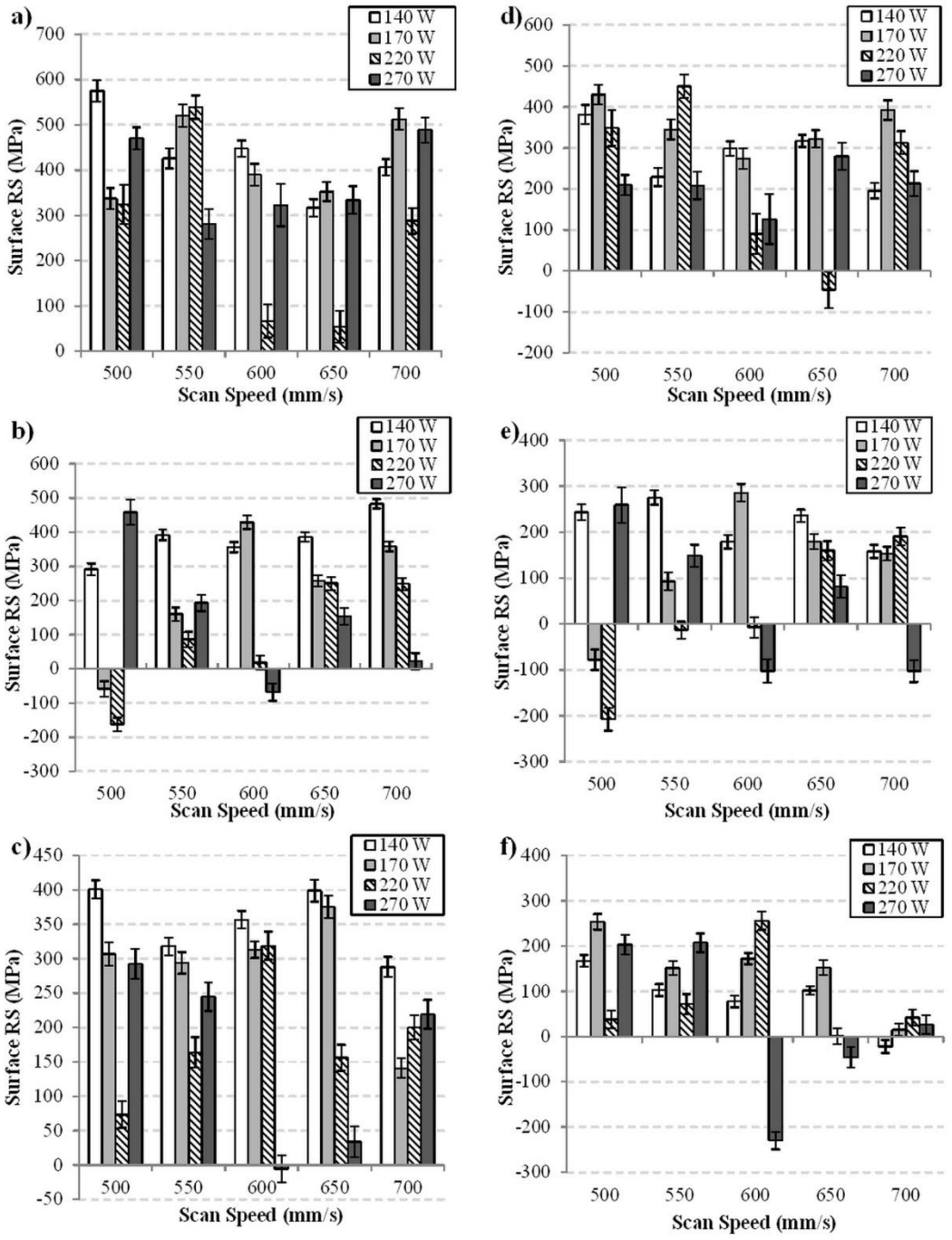

Figure 2-17 Surface residual stress variation with laser power in scan direction at a) 0.08 mm b) 0.1 mm c) 0.12 mm and hatch direction at d)0.08 mm e) 0.1 mm f) 0.12 mm

In addition, increasing laser power generates a higher temperature which in return causes the thermal conductivity and the coefficient of thermal expansion to increase [47]. These two properties have opposite effects on RS that can be explained by using Eqn.5 as a simple method to calculate RS analytically, where RS depends on the coefficient of thermal expansion (α) and the temperature gradient (ΔT).

As the thermal conductivity increases heat is conducted further down the part thus reducing the high-temperature gradient (ΔT) between the part and the substrate and finally reducing the RS. Conversely, increasing the coefficient of thermal expansion directly increases the surface RS.

$$\sigma_{th} = \alpha \, E \, \Delta T \tag{5}$$

Also, for the cases that contradict the aforementioned trend, their resulting behavior can be potentially attributed to the difference in scan track length. It was shown in the literature [46, 48] that a shorter scan track will result in lower surface RS compared to longer scan tracks. Therefore, the length of the scan track has an opposing effect, on surface RS, to the increase in laser power. To illustrate, observation of RS at a scan speed of 550 mm/s and hatch spacing of 0.1mm, shows a decrease in RS as laser power increases, but then it increases at the highest power. Due to the distribution of the built coupons all over the build plate, their top surface was sectioned with different sizes. Examination of the top surface under an optical microscope as seen in Figure 2-18 shows that the scan track length decreases until

a power of 220 W but increases at the highest power thus contributing to the increase in surface RS.

Figure 2-18 Variation of scan track length on the top surface for a scan speed of 550 mm/s and hatch spacing of 0.1 mm at a laser power of a) 140 W b)170 W c) 220 W d) 270 W

Additionally, a number of coupons exhibited surface RS exceeding the yield strength of 400 MPa for Inconel 625; therefore, the top surface deformed and bulged at some areas, particularly near the edges, relieving some of the RS as indicated by the arrows in Figure 2-19. It is also observed that surface RS in scan

direction are higher in tension compared to the hatch direction, which is in agreement with the results found in the literature [39, 46, 47].

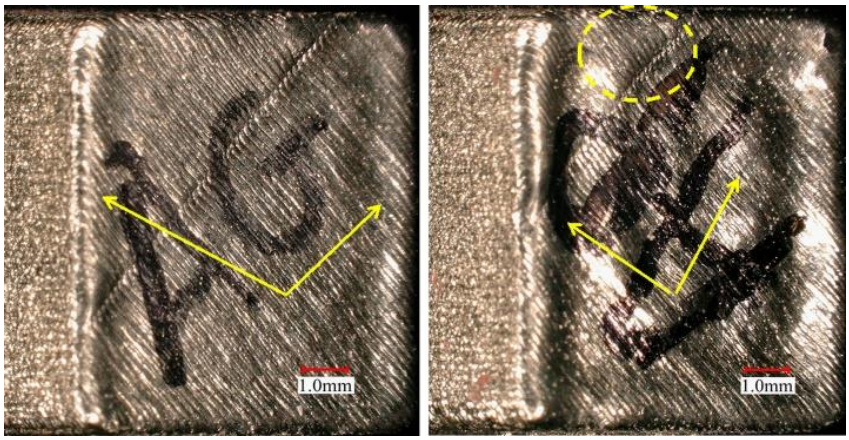

Figure 2-19 Deformation of the top surface due to high residual stresses

Process maps for surface RS, measured in the scan direction and hatch direction, are plotted in Figure 2-20. The maps are divided into three main areas relative to the material yield strength of 400 MPa. Firstly, surface tensile RS higher than the yield strength. Secondly, there are areas corresponding to surface tensile RS below the yield strength. Finally, process parameters that induced surface compressive RS. Compressive surface RS were reported in literature [44] with varying the part height, however, since this is not the case in the current study. Surface compressive RS could be attributed to the strain hardening of the part surface due to plastic deformation, shown in Figure 2-19, which would induce compressive RS [49]. It is observed that most process parameters combinations resulted in surface tensile RS below yield strength while RS higher than yield strength are prominently exhibited at the lowest hatch spacing. However, a hatch spacing of 0.1 mm and 0.12 mm

resulted in a wider window of process parameters that induce surface RS below yield strength. In addition, the average surface RS in scan direction calculated from all process parameters, at each hatch spacing, shows that the average surface RS is around 220 MPa for 0.1 mm and 0.12 mm while the average is much higher for 0.08 mm at 370 MPa. Also, as the ratio between the surface RS in scan and hatch directions was calculated as a measure of the built part anisotropy. It was found that a hatch of 0.12 mm resulted in the highest anisotropy followed by a hatch of 0.08 mm and finally 0.1 mm.

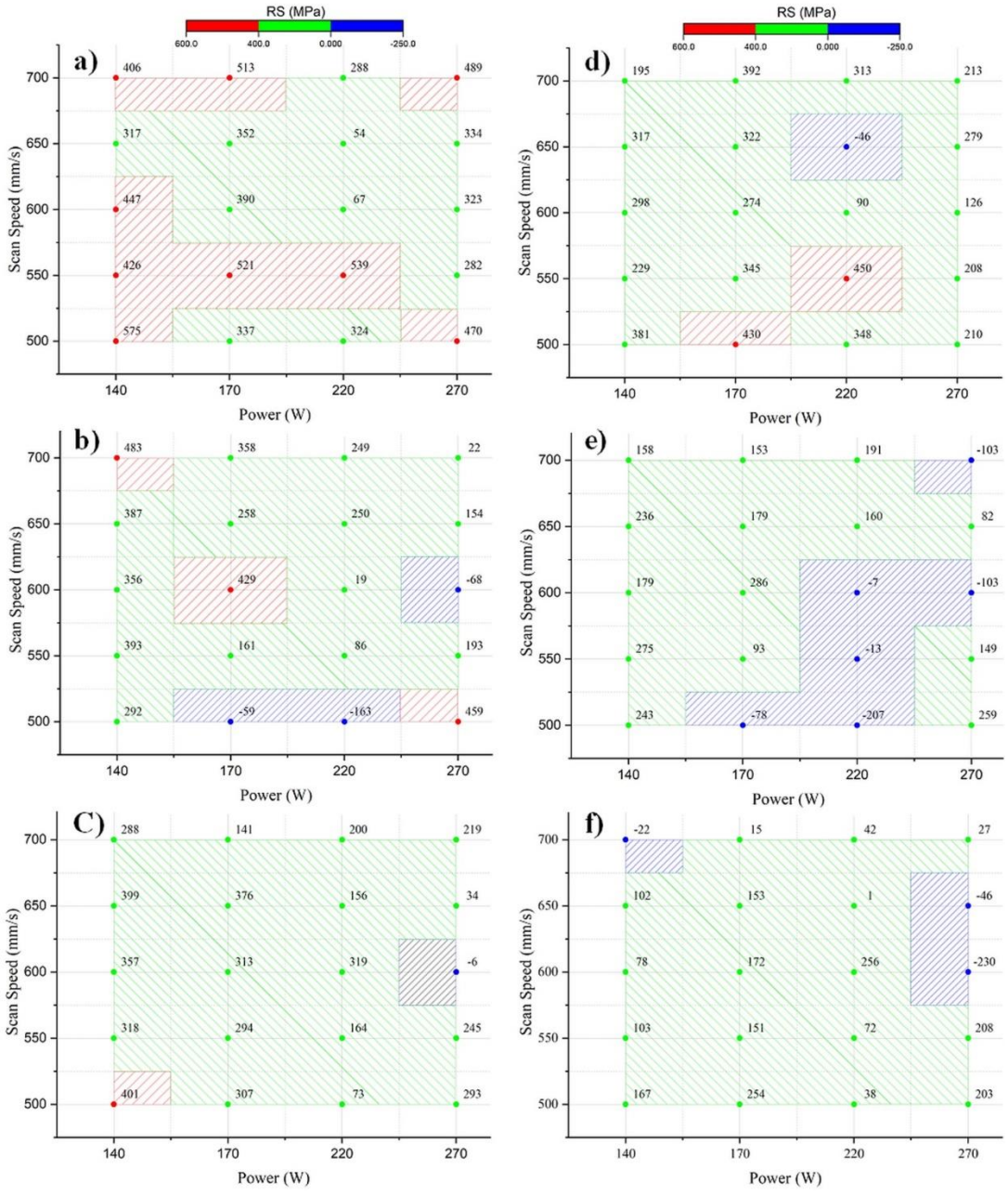

Figure 2-20 Surface residual stress P-V process maps in scan direction

a) 0.08 mm b) 0.1 mm c) 0.12 mm and in hatch direction at d) 0.08 mm

e) 0.1 mm f) 0.12 mm

Therefore, a hatch of 0.1 mm offers the best option in the selection of parameters to process Inconel 625. Based on the results and above- mentioned factors affecting RS, it is clear that further studies are needed to determine the dominant factors, especially the thermal history of the part, and any interaction between them that would affect the surface RS. Furthermore, surface RS is not indicative of in-depth RS which raises the need for an investigation of in-depth RS.

Energy density is often used as a lump sum quantity to correlate the effect of process parameters to the measured part property [9, 15, 34, 50]. However, skepticism was raised regarding its viability as an input parameter to predict end part properties [51]. Based on that finding, four groups of coupons each having a different energy density values were built. The energy densities were 58.33 J/mm3, 70.83 J/mm3, 91.67 J/mm3, 112.5 J/mm3 corresponding to laser powers of 140 W, 170 W, 220 W, and 270 W, respectively.

Each energy density group had two coupons built with the first set of coupons having a scan speed of 600 mm/s and hatch spacing of 0.1 mm. The second set of coupons had a scan speed of 500 mm/s and hatch spacing of 0.12 mm. By measuring and comparing the surface RS, for each group, in the scan and hatch directions, it was found that using the same energy density would result in different surface RS for both measurement directions as shown in Figure 2-21. The difference is more prominent at energy densities; 70.83 J/mm^3 and 112.5 J/mm^3. Despite these results, a further investigation is needed to examine a wide range of

individual process parameters within the same energy density group and their correlation to the end part properties.

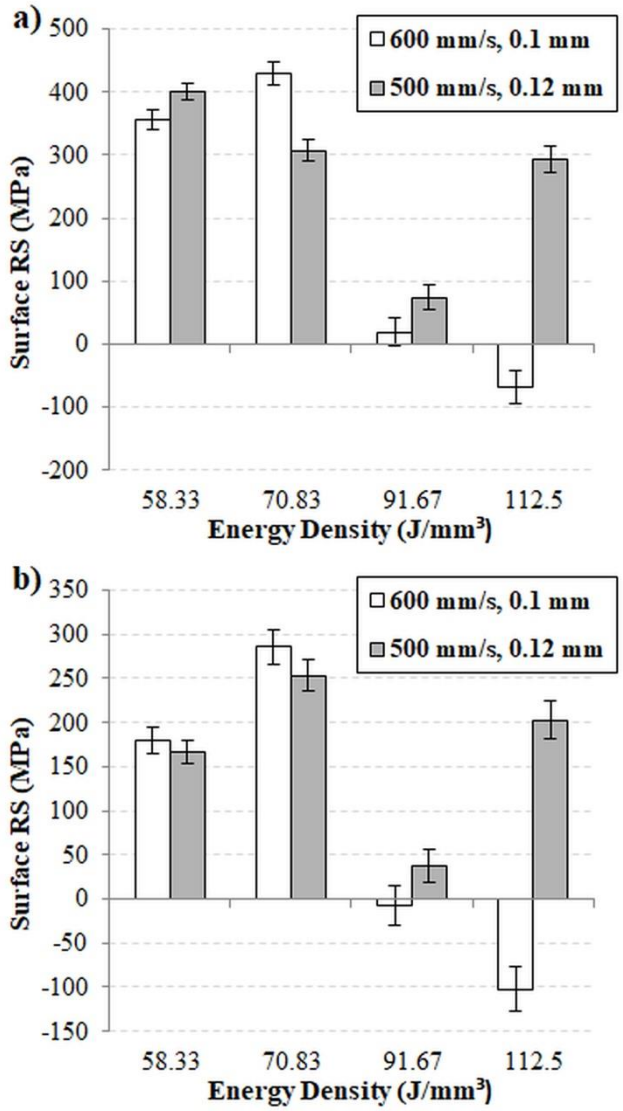

Figure 2-21 Surface RS at constant energy densities in

a) scan direction b) hatch direction

2.4. Conclusion and future work

The current work aimed at investigating the effect of a wide range of process parameters on surface integrity of Inconel 625 parts produced using selective laser melting. Relative density, surface roughness and surface residual stresses on the top plane were measured, and process maps were developed.

The developed process maps provide an encompassing overview of the process-structure-property relations, thus serving as a general guide to prediction of the surface integrity in selective laser melting of Inconel 625.

Based on the results, the following conclusions were drawn:

- Selective laser melting produced parts with a relative density above 97% for all process parameters.
- A hatch spacing of 0.1 mm produced the highest relative density (>99%) for all laser powers tested except a power of 140 W.
- Surface roughness measured in both scan and hatch directions decreased with increasing laser power. However, surface roughness was higher in the hatch direction compared to the scan direction
- At the highest laser power, the lowest surface roughness produced ranged between 1.5 μm to 3 μm.
- Measurement of top surface residual stress is location dependent.
- There is no specific trend for the effect of process parameters on surface residual stresses. However, selective laser melting produced mostly surface

tensile residual stresses with the exception of a few surface compressive residual stresses.

- A hatch spacing of 0.1 mm resulted in mostly surface tensile residual stresses below the material yield strength, and the least anisotropy for the parts produced.
- Despite the use of the same energy density, surface residual stress magnitude will differ depending on the individual process parameters.
- Although microhardness measured in build (z) direction varied with increasing laser power, the variation was insignificant taking into consideration the standard deviation and microstructure.

Selective laser melting is a multiphysics complex process which requires further investigations through multi-physics multi-scale modeling and online monitoring of melt pool to gain an insight into the thermal history and gradient that would affect melt pool dynamics and end part properties, particularly residual stresses.

References

[1] L. E. Murr, E. Martinez, K. N. Amato, S. M. Gaytan, J. Hernandez, D. A. Ramirez, *et al.*, "Fabrication of metal and alloy components by additive manufacturing: examples of 3D materials science," *Journal of Materials Research and technology,* vol. 1, pp. 42-54, 2012.

[2] D. Gu, W. Meiners, K. Wissenbach, and R. Poprawe, "Laser additive manufacturing of metallic components: materials, processes and mechanisms," *International materials reviews,* vol. 57, pp. 133-164, 2012.

[3] W. E. Frazier, "Metal additive manufacturing: a review," *Journal of Materials Engineering and Performance,* vol. 23, pp. 1917-1928, 2014.

[4] Z. Lu, J. Cao, H. Jing, T. Liu, F. Lu, D. Wang, *et al.*, "Review of main manufacturing processes of complex hollow turbine blades: This paper critically reviews conventional and advanced technologies used for manufacturing hollow turbine blades," *Virtual and Physical Prototyping*, vol. 8, pp. 87-95, 2013.

[5] S. Bontha, "The effect of process variables on microstructure in laser-deposited materials," 2006.

[6] G. Marchese, X. Garmendia Colera, F. Calignano, M. Lorusso, S. Biamino, P. Minetola, *et al.*, "Characterization and Comparison of Inconel 625 Processed by Selective Laser Melting and Laser Metal Deposition," *Advanced Engineering Materials*, vol. 19, 2017.

[7] J. Strößner, M. Terock, and U. Glatzel, "Mechanical and microstructural investigation of nickel-based superalloy IN718 manufactured by selective laser melting (SLM)," *Advanced Engineering Materials*, vol. 17, pp. 1099-1105, 2015.

[8] E. Ezugwu, Z. Wang, and A. Machado, "The machinability of nickel-based alloys: a review," *Journal of Materials Processing Technology*, vol. 86, pp. 1-16, 1999.

[9] L. E. Criales, Y. M. Arısoy, B. Lane, S. Moylan, A. Donmez, and T. Özel, "Laser powder bed fusion of nickel alloy 625: Experimental investigations of effects of process parameters on melt pool size and shape with spatter analysis," *International Journal of Machine Tools and Manufacture*, 2017.

[10] L. E. Criales, Y. M. Arısoy, B. Lane, S. Moylan, A. Donmez, and T. Özel, "Predictive modeling and optimization of multi-track processing for laser powder bed fusion of nickel alloy 625," *Additive Manufacturing*, vol. 13, pp. 14-36, 2017.

[11] Y. M. Arısoy, L. E. Criales, T. Özel, B. Lane, S. Moylan, and A. Donmez, "Influence of scan strategy and process parameters on microstructure and its optimization in additively manufactured nickel alloy 625 via laser powder bed fusion," *The International Journal of Advanced Manufacturing Technology*, vol. 90, pp. 1393-1417, 2017.

[12] L. E. Criales, Y. M. Arısoy, and T. Özel, "Sensitivity analysis of material and process parameters in finite element modeling of selective laser melting of Inconel 625," *The International Journal of Advanced Manufacturing Technology*, vol. 86, pp. 2653-2666, 2016.

[13] M. A. Anam, D. Pal, and B. Stucker, "Modeling and experimental validation of nickel-based super alloy (Inconel 625) made using selective laser melting," in *Solid Freeform Fabrication (SFF) Symposium, University of Texas at Austin, Austin, TX, Aug*, 2013, pp. 12-14.

[14] M. A. Anam, J. Dilip, D. Pal, and B. Stucker, "Effect of scan pattern on the microstructural evolution of Inconel 625 during selective laser melting," in *Proceedings of 25th Annual International Solid Freeform Fabrication Symposium*, 2014.

[15] L. N. Carter, X. Wang, N. Read, R. Khan, M. Aristizabal, K. Essa, *et al.*, "Process optimisation of selective laser melting using energy density model for nickel based superalloys," *Materials Science and Technology*, vol. 32, pp. 657-661, 2016.

[16] Y. Liu, Y. Yang, and D. Wang, "A study on the residual stress during selective laser melting (SLM) of metallic powder," *The International Journal of Advanced Manufacturing Technology*, vol. 87, pp. 647-656, 2016.

[17] C. Montgomery, J. Beuth, L. Sheridan, and N. Klingbeil, "Process mapping of Inconel 625 in laser powder bed additive manufacturing," in *Solid Freeform Fabrication Symposium*, 2015, pp. 1195-1204.

[18] K. Amato, J. Hernandez, L. Murr, E. Martinez, S. Gaytan, P. Shindo, *et al.*, "Comparison of microstructures and properties for a Ni-base superalloy (alloy 625) fabricated by electron beam melting," *Journal of Materials Science Research*, vol. 1, p. 3, 2012.

[19] Z. Gan, Y. Lian, S. E. Lin, K. K. Jones, W. K. Liu, and G. J. Wagner, "Benchmark study of thermal behavior, surface topography, and dendritic microstructure in selective laser melting of Inconel 625," *Integrating Materials and Manufacturing Innovation*, vol. 8, pp. 178-193, 2019.

[20] J. C. Heigel and B. M. Lane, "The effect of powder on cooling rate and melt pool length measurements using in situ thermographic techniques," in *Solid freeform fabrication symposium*, 2017.

[21] G. E. Totten, *Handbook of residual stress and deformation of steel*: ASM international, 2002.

[22] S. Raghavan, S. Chen-Nan, Z. Baicheng, S. W. Jack, P. Wang, N. M. L. Sharon, *et al.*, "Mechanical Properties and Microstructures of As Printed and Heat Treated Samples of Selective Laser Melted IN625 Alloy Powder," in *MATEC Web of Conferences*, 2015.

[23] M. Xia, D. Gu, G. Yu, D. Dai, H. Chen, and Q. Shi, "Influence of hatch spacing on heat and mass transfer, thermodynamics and laser processability during additive manufacturing of Inconel 718 alloy," *International Journal of Machine Tools and Manufacture*, vol. 109, pp. 147-157, 2016.

[24] R. Li, J. Liu, Y. Shi, L. Wang, and W. Jiang, "Balling behavior of stainless steel and nickel powder during selective laser melting process," *The International Journal of Advanced Manufacturing Technology*, vol. 59, pp. 1025-1035, 2012.

[25] Y. Ueda, H. Murakawa, and N. Ma, *Welding deformation and residual stress prevention*: Elsevier, 2012.

[26] S. Kou, "Welding metallurgy," *New Jersey, USA*, pp. 431-446, 2003.

[27] D. B. Witkin, T. V. Albright, and D. N. Patel, "Empirical approach to understanding the fatigue behavior of metals made using additive manufacturing," *Metallurgical and Materials Transactions A*, vol. 47, pp. 3823-3836, 2016.

[28] F. Hull, S. Hwang, J. Wells, and R. Jaffee, "Effect of composition on thermal expansion of alloys used in power generation," *Journal of materials engineering*, vol. 9, pp. 81-92, 1987.

[29] J. A. Slotwinski, E. Garboczi, P. E. Stutzman, C. F. Ferraris, S. S. Watson, and M. A. Peltz, "Characterization of metal powders used for additive manufacturing," *Journal of research of the National Institute of Standards and Technology*, vol. 119, pp. 460-494, 2014.

[30] A. T. Sutton, C. S. Kriewall, M. C. Leu, and J. W. Newkirk, "Powder characterisation techniques and effects of powder characteristics on part properties in powder-bed fusion processes," *Virtual and Physical Prototyping*, vol. 12, pp. 3-29, 2017.

[31] D. F. Paulonis and J. J. Schirra, "Alloy 718 at Pratt & Whitney-Historical perspective and future challenges," *Superalloys*, vol. 718, pp. 13-23, 2001.

[32] N. A. Kistler, "Characterization of inconel 718 fabricated through powder bed fusion additive manufacturing," Bachelor's Thesis, The Pennsylvania State University, University Park, PA, USA, 2015.

[33] D. Dudzinski, A. Devillez, A. Moufki, D. Larrouquere, V. Zerrouki, and J. Vigneau, "A review of developments towards dry and high speed machining of Inconel 718 alloy," *International Journal of Machine Tools and Manufacture*, vol. 44, pp. 439-456, 2004.

[34] J.-P. Choi, G.-H. Shin, S. Yang, D.-Y. Yang, J.-S. Lee, M. Brochu, *et al.*, "Densification and microstructural investigation of Inconel 718 parts fabricated by selective laser melting," *Powder Technology*, vol. 310, pp. 60-66, 2017.

[35] Z. Wang, K. Guan, M. Gao, X. Li, X. Chen, and X. Zeng, "The microstructure and mechanical properties of deposited-IN718 by selective laser melting," *Journal of Alloys and Compounds*, vol. 513, pp. 518-523, 2012.

[36] E. Chlebus, K. Gruber, B. Kuźnicka, J. Kurzac, and T. Kurzynowski, "Effect of heat treatment on the microstructure and mechanical properties of Inconel 718 processed by selective laser melting," *Materials Science and Engineering: A*, vol. 639, pp. 647-655, 2015.

[37] D. S. Watring, K. C. Carter, D. Crouse, B. Raeymaekers, and A. D. Spear, "Mechanisms driving high-cycle fatigue life of as-built Inconel 718 processed by laser powder bed fusion," *Materials Science and Engineering: A*, vol. 761, p. 137993, 2019.

[38] S. Ghosh, L. Ma, L. E. Levine, R. E. Ricker, M. R. Stoudt, J. C. Heigel, *et al.*, "Single-track melt-pool measurements and microstructures in inconel 625," *Jom*, vol. 70, pp. 1011-1016, 2018.

[39] M. Yakout, M. Elbestawi, and S. C. Veldhuis, "Density and mechanical properties in selective laser melting of Invar 36 and stainless steel 316L," *Journal of Materials Processing Technology*, vol. 266, pp. 397-420, 2019.

[40] Z. Chen, Z. Wei, P. Wei, S. Chen, B. Lu, J. Du, *et al.*, "Experimental research on selective laser melting AlSi10Mg alloys: Process, densification and performance," *Journal of Materials Engineering and Performance*, vol. 26, pp. 5897-5905, 2017.

[41] C. Pei, D. Shi, H. Yuan, and H. Li, "Assessment of mechanical properties and fatigue performance of a selective laser melted nickel-base superalloy Inconel 718," *Materials Science and Engineering: A*, vol. 759, pp. 278-287, 2019.

[42] J. R. Lawrence, *Advances in laser materials processing: technology, research and applications*: Woodhead Publishing, 2017.

[43] K. Moussaoui, W. Rubio, M. Mousseigne, T. Sultan, and F. Rezai, "Effects of Selective Laser Melting additive manufacturing parameters of Inconel 718 on porosity, microstructure and mechanical properties," *Materials Science and Engineering: A*, vol. 735, pp. 182-190, 2018.

[44] P. Mercelis and J.-P. Kruth, "Residual stresses in selective laser sintering and selective laser melting," *Rapid Prototyping Journal*, vol. 12, pp. 254-265, 2006.

[45] J.-P. Kruth, J. Deckers, E. Yasa, and R. Wauthlé, "Assessing and comparing influencing factors of residual stresses in selective laser melting using a novel analysis method," *Proceedings of the institution of mechanical engineers, Part B: Journal of Engineering Manufacture*, vol. 226, pp. 980-991, 2012.

[46] X. Wang, X. Gong, and K. Chou, "Review on powder-bed laser additive manufacturing of Inconel 718 parts," *Proceedings of the Institution of Mechanical Engineers, Part B: Journal of Engineering Manufacture*, vol. 231, pp. 1890-1903, 2017.

[47] D. B. Witkin, D. Patel, T. V. Albright, G. E. Bean, and T. McLouth, "Influence of surface conditions and specimen orientation on high cycle fatigue properties of Inconel 718 prepared by laser powder bed fusion," *International Journal of Fatigue*, vol. 132, p. 105392, 2020.

[48] I. Koutiri, E. Pessard, P. Peyre, O. Amlou, and T. De Terris, "Influence of SLM process parameters on the surface finish, porosity rate and fatigue behavior of as-built Inconel 625 parts," *Journal of Materials Processing Technology*, vol. 255, pp. 536-546, 2018.

[49] Y. Yang, M. Allen, T. London, and V. Oancea, "Residual strain predictions for a powder bed fusion Inconel 625 single cantilever part," *Integrating Materials and Manufacturing Innovation*, vol. 8, pp. 294-304, 2019.

[50] M. Komarasamy, S. Shukla, S. Williams, K. Kandasamy, S. Kelly, and R. S. Mishra, "Microstructure, fatigue, and impact toughness properties of additively manufactured nickel alloy 718," *Additive Manufacturing,* vol. 28, pp. 661-675, 2019.

[51] V. P. Sabelkin, G. R. Cobb, T. E. Shelton, M. N. Hartsfield, D. J. Newell, R. P. O'Hara, *et al.*, "Mitigation of anisotropic fatigue in nickel alloy 718 manufactured via selective laser melting," *Materials & Design,* vol. 182, p. 108095, 2019.

Chapter 3

On Selective Laser Melting of Inconel 718: Densification, Surface Roughness, and Residual Stresses

Complete Citation:

Balbaa, Mohamed, et al. "On selective laser melting of Inconel 718: Densification, surface roughness, and residual stresses." *Materials & Design* 193 (2020): 108818.

Relative Contributions:

M. A. Balbaa: Performed experiments, analysis, and data interpretation; wrote the first draft of the manuscript

S. Mekheil: Helped with experiments and data collection

M. A. Elbestawi: Revised and edited the manuscript

J. McIsaac: Provided the manufacturing facility

Abstract:

The current study investigates the effects of a wide range of process parameters on three part properties; density, surface roughness, and surface residual stresses simultaneously for selective laser melting of Inconel 718. In addition to the lack of investigations on surface roughness and residual stresses in selective laser melting of Inconel 718, process maps were developed for the selection of the best process parameters to achieve the desired values for the three parameters combined. Five laser powers, six scan speeds and three hatch spacings were chosen from the stable single tracks tests. Based on each property, a 99.5% density or a 2 μm surface roughness or the least surface tensile residual stress of 248 MPa were possible. However, no single process parameter combination was able to achieve good values for all three parameters. Prioritizing density and surface roughness, being crack initiators, over residual stresses for their effect on fatigue failure, it was found that 99.2% density and relatively low roughness of 3.5 μm are feasible at 320 W, 600 mm/s and 0.12 mm hatch spacing. Finally, opposite to the commonly observed columnar grain in Inconel 718, mixed grain structure was obtained at 600 mm/s and 1000 mm/s, indicating reduced anisotropy.

Keywords:

Inconel 718, Selective Laser Melting, Single Tracks, Density, Surface Roughness, Residual Stresses

3.1. Introduction

Aerospace parts are regularly subjected to high mechanical and thermal loads during their service life. Accordingly, certified parts are required to have high density, high surface integrity, i.e., low surface roughness and compressive residual stresses (RS), and high tensile and fatigue strengths. In addition, complex design geometries and lightweighting are required to achieve the desired aerodynamic flows and low fuel consumption [1]. The gas turbine blade is an excellent example of complex geometry with internal cooling channels manufactured to extract the highest possible energy while offering adequate cooling during service. However, these geometries and cooling channels are limited by conventional manufacturing constraints, which does not allow the freedom to explore a broader range of designs with possible superior functionality. Additionally, a turbine blade goes through several manufacturing processes such as investment casting, hot isostatic pressing (HIP), turning, milling, wire electric discharge machining (EDM)…etc [2].

Nickel-based superalloys emerged as an ideal candidate to meet these challenging demands. A frequently used Ni-based superalloy in gas turbines is Inconel 718 (IN718), which is well known for its high strength, high temperature, and corrosion resistance [3]. However, IN718 is considered difficult to machine due to its ability to work harden, and maintain their strength at high temperatures. Also, the presence of abrasive carbides increases the tool wear rate. IN718 has low thermal conductivity, causing a steep temperature gradient at the tool/chip interface leading to tool life deterioration [4, 5]. All these difficulties add to the number of constraints

facing conventional manufacturing of turbine blades, hence motivating the exploration of a more suitable technology to manufacture IN718 gas turbine blades.

Additive manufacturing (AM) and, in particular, laser powder bed fusion (L-PBF), which is also known as selective laser melting (SLM), offers a flexible solution to the difficulties mentioned above [6, 7]. SLM provides the design freedom needed to manufacture complex geometries without the need for special tooling, thus saving costs and time. Design for AM can help reduce the number of parts and assemblies required by integrating several parts into one, while having very little material waste, with powder recycling, thus making it possible to achieve a buy to fly ratio of almost 1:1[8]. The main goal in SLM is to produce high-quality parts with predictable mechanical properties such as; density, surface roughness, residual stresses (RS), tensile strength… etc. The main controllers in SLM are the process parameters, which include, for example, laser power, scan speed, hatch spacing, and scan strategy, which will consequently produce specific microstructure and part properties. The main research thrust is to identify and tune the effect of process parameters on the end part structure and resulting properties.

Table 3-1 Process parameters reported in the literature on SLM of IN718

Part property measured	Process Parameters				Ref.
	Laser power (W)	Scan speed (mm/s)	Hatch spacing (μm)	Misc.	
Density	75 - 300	800 - 2200	N/A	Layer thickness: 40 μm	[9]
	90	100-1600	80	Layer thickness: 25 μm	[10]
	150 - 450	1000-1800	50-90	As-built vs. Heat Treated	[11]
	180	600	150	Island scan strategy	[12]
Surface roughness	150 - 450	1000-1800	50-90	As-built vs. Heat Treated	[11]
	115-465	620-1770	100	Different Orientations	[13]
Tensile strength	180	600	150	Island scan strategy	[12]
	285	960	110	As-built vs. Heat Treated	[14]
	180	600	105	As-built vs. Heat Treated	[15]
Fatigue	115-465	620-1770	100	Different Orientations	[13]
	285	960	110	As-built vs. Heat Treated	[14]
	200	200	180	Layer thickness: 50 μm	[16]
Melt pool dimensions	75 - 300	800 - 2200	N/A	Layer thickness: 40 μm	[9]
	100-370	200-1400	N/A	Single tracks	[17]
	40-300	200-2500	N/A	Single tracks	[18]
Microstructure	90	100-1600	80 μm	Layer thickness: 25 μm	[10]

	150 - 450	1000-1800	50-90	As-built vs. Heat Treated	[11]
	180	600	150	Island scan strategy	[12]
	170	416	30% overlap	Layer thickness: 20 μm	[19]
	100	85.7	160	As-built vs Heat treated	[20]
Residual Stresses	180	600	150	Island scan strategy	[12]
Micro-hardness	90	100-1600	80 μm	Layer thickness: 25 μm	[10]
	170	416	30% overlap	Layer thickness: 20 μm	[19]

Although the literature covers different parts properties, it lacks a comprehensive systematic study on the effect of a wide range of process parameters on part density and especially surface integrity combined, including surface roughness and surface residual stresses. These three properties are highly crucial for the aerospace sector as they will affect the fatigue life of the manufactured parts. Therefore, the current study starts by examining the possibility of producing stable single tracks under different power and speed combinations to serve as the basis for manufacturing multi-track multi-layer coupons. The selected parameters, along with varying hatch spacings will be tested to investigate their effect on relative density, surface roughness, surface RS and microstructure, to develop process maps for the selection of the best process parameters.

3.2. Experiments and Part Characterization

3.2.1. Experimental Procedures

A gas atomized IN718 powder, characterized with a fine spherical morphology and a powder size distribution in the range of 15 µm to 45 µm, was used. The IN718 powder has the chemical composition, provided by the supplier, shown in Table 3-2

Table 3-2 Chemical composition of as-received Inconel 718 (weight %)

Ni	Cr	Fe	Nb + Ta	Mo	Ti	Al	Si	C	Co	O	Misc.
51.88	19.4	18.9	5.14	3.1	1.02	0.46	0.04	0.03	0.02	0.01	Bal.

The printing process using SLM, done on an EOS M280, is divided into two steps. The first step is the exposure of single tracks under different combinations of laser power and scan speed to observe their effect on the melt pools morphologies and dimensions. Six levels of laser powers and six scan speeds were chosen for a total of 48 different process parameters combinations, as shown in Table 3-3. All single tracks were built on top of a 4 mm high IN718 coupon, which will act as the substrate to avoid any diffusion of alloying elements such as the case with printing the tracks directly on the steel build plate. All substrate coupons were built with the same process parameters of 140 W, 650 mm/s, and 0.1 mm hatch spacing. The build was performed in a surrounding atmosphere of Nitrogen to keep the oxygen percent below 0.13% to minimize the possibility of oxidation. The laser beam nominal diameter was 100 µm.

Table 3-3 Process parameters for single tracks exposure

Parameter	Levels
Power (W)	120,170, 220, 270, 320, 370
Scan speed (mm/s)	400, 600, 800, 1000,1200
Layer thickness (μm)	40

The second step consisted of printing full coupons of side length 10 mm and a height of 12 mm, with an inter-coupons spacing of 5 mm shown in Figure 3-1, using process parameters selected based on the stable tracks determined from the first half of the study. The lowest laser power and two scan speeds were excluded from the test matrix based on the single line results, as will be presented later on in the results section. Consequently, the full coupons are manufactured using five laser powers, six scan speeds, and three hatch spacings, as detailed in Table 3-4. The scan speed levels of 500 mm/s, and 700 mm/s were added as intermediate steps to observe any change in the trends of the results.

Table 3-4 Process parameters for SLM of Inconel 718 full coupons

Parameter	Levels
Power (W)	170, 220, 270, 320, 370
Scan speed (mm/s)	500, 600, 700, 800, 1000,1200
Hatch spacing (mm)	0.08, 0.1, 0.12
Layer thickness (μm)	40

The coupons were built directly on to the build plate with no supports under the same environmental conditions as those applied for the single tracks coupons. The coupons were built with a bi-directional sweeping scan strategy with a rotation of 90° between each layer [21]. The coupons were arranged across the build plate in a manner such that the average energy density of any row or column would be almost constant to avoid the presence of areas with high energy concentration. Following the build, the coupons were separated from the base plate using wire EDM to induce minimum heat effect on the resulting residual stresses.

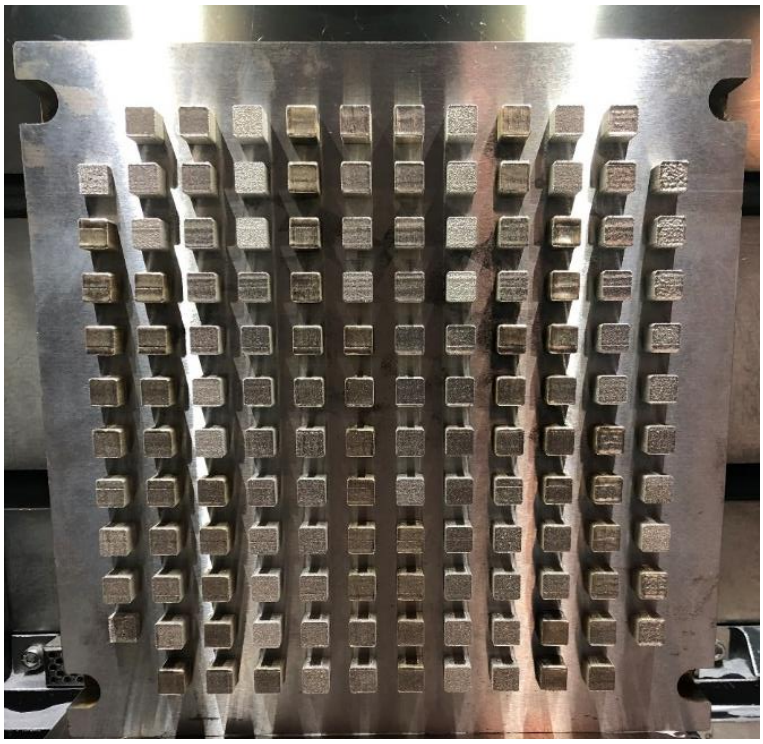

Figure 3-1 Inconel 718 cube coupons before separation from the build plate

3.2.2. Property Characterization

Single Track Measurement

The printed single tracks were first examined from the top view under a TESCAN VP scanning electron microscope (SEM) to determine the morphology of the scan tracks being either continuous or discontinuous. Consequently, the tracks are sectioned perpendicular to the scan direction and polished according to the metallographic steps shown in Table 3-5. The samples were etched using Kalling's reagent No. 2 to reveal the melt pool boundaries. The etched tracks were examined under a Nikon LV100 optical microscope to measure the melt pool dimensions and determine the melt pool type. Keyhole-type melt pools are characterized by severe depth, which could develop even more defects in the case of material vaporization during consolidation and formation of keyhole porosity. Melt pools were considered of keyhole type if the ratio of the melt pool depth to half its width is higher than 2.5 [22].

On the other hand, melt pools having a depth less than the layer thickness would lead to a lack of penetration into the solidified layer beneath and termed as under melted. Furthermore, the free surface of the under melted pools could start to curl up due to surface tension leading to balling. The width and depth of the melt pool were measured by setting the surface of the 4 mm substrate as the datum for measurements.

Table 3-5 Metallographic steps for IN718

Step/Surface	Time (min)	Load (N)	Speed (rpm)
SiC #500	1.5	25	300
SiC#1200	1.5	20	300
MD-Plan 9µm	4	20	150
MD-Dac 3 µm	3	20	150
MD-Nap 1 µm	3	20	150
MD-Chem OPS	2	10	150

Density Measurement

The non-destructive Archimedes method was used to measure the densities of the coupons to a high degree of accuracy [3, 23]. A Mettler analytical balance with a resolution of ± 0.1 mg was used to measure the mass of the coupons once in the air (m_a) and then while submerged in de-ionized water (m_{fl}), as shown in Figure 3-2. Both readings were measured up to 5 times, and the density was calculated according to Eqn.1 [24], where the effect air buoyancy is corrected for by including the air density ($\rho_{air} = 1.19\ kg/m^3$). The de-ionized water had a density of 997.76 kg/m^3 and the part density is reported relative (%) to the bulk density of Inconel 718 ($\rho_{bulk} = 8220\ kg/m^3$).

$$\rho_p = (\rho_{fl} - \rho_{air}).\frac{m_a}{m_a - m_{fl}} + \rho_{air}\ \ (kg/m^3) \quad (1)$$

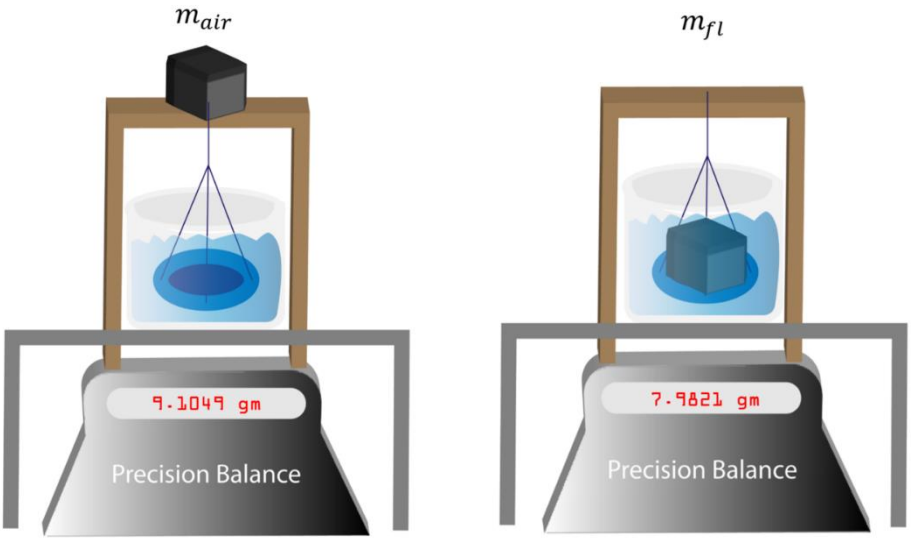

Figure 3-2 Archimedes density measurement setup with the mass in air (left) and fluid (right)

Surface Roughness

A Mitutoyo SJ-410 stylus profilometer was used to measure the surface roughness of the top surface of the coupons in terms of the arithmetic mean deviation R_a. The surface roughness measurements were implemented over five segments totaling a cut-off length of 4.8 mm [25]. The roughness profiles were measured five times in directions across the laser scan tracks on the top surface.

Residual Stress Measurement

X-ray diffraction (XRD) is an excellent candidate for non-destructive measurements of RS [4]. It depends on x-rays capability of measuring the inter-atomic lattice spacing, which deforms under any stresses, whether applied or residual stresses. These deformations are linear in the elastic zone, which in return make residual stresses elastic stresses by nature. Due to attenuation, the penetration

depth of x-ray in the diffraction method is minimal, about 5 μm for Inconel 718; therefore, it can be used only to measure surface RS, which are considered plane stresses [4].

A Bruker D8 instrument with a Co-Kα radiation source was used to measure the surface RS, installed with a 1 mm collimator. At first, several Bragg's angles (θ) were scanned, and a 2theta angle of 111.4° was selected as it gave the most definite diffraction peaks. The x-rays emitter was targeted at the center of the coupon top surface, as shown in Figure 3-3, with the x-direction of measurement aligned with the scan tracks on the top surface (in scan direction). The y-direction of measurement was oriented perpendicular to the scan tracks (in hatch direction). During measurement, the coupon is rotated through 5 Phi angles ($\varphi = 0^{o}$, 72^{o}, 144^{o}, 216^{o}, 288^{o}) around its axis, to capture more diffraction frames from one location. Besides, the coupon is tilted sideways to 4 Psi angles ($\psi = 10^{o}$, 25^{o}, 40^{o}, 55^{o}). Additionally, the coupon was oscillated within 2^{o} at each Psi angle to increase the amount of captured diffraction planes. Moreover, to account for anisotropy in the crystal, the anisotropy factor A_{RX} was set to 1.52 for Ni-based alloys [26].

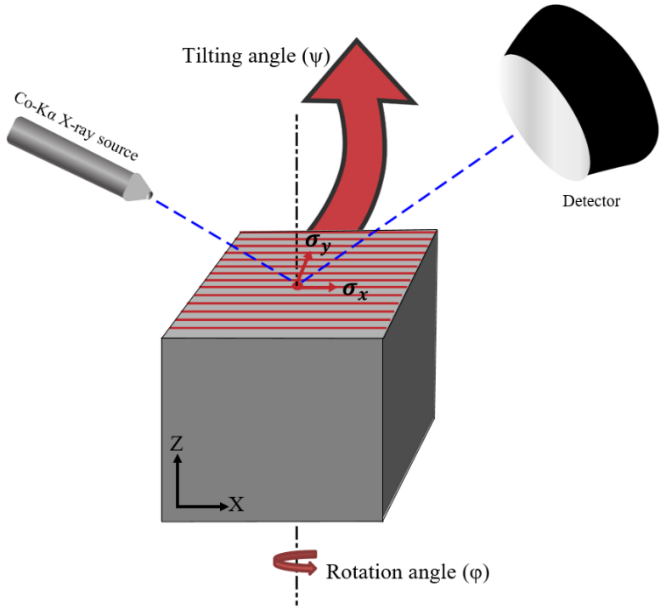

Figure 3-3 X-ray diffraction setup

Melt Pools Microstructure

A subset of the coupons was selected, partitioned, and prepared for metallographic examination. The melt pools were first examined under an optical microscope to observe the morphology of the melt pools in multi-track and multi-layer formation. Next, SEM microscopy was used to explore the formed microstructure within the melt pools. In addition, phase analysis was done on the powder and the coupon to investigate the available phases post rapid solidification. Moreover, the chemical composition of a sample set was accurately measured using inductively coupled plasma (ICP) to investigate the change in chemical composition from powder form due to the possible evaporation of alloying elements.

3.3. Results

3.3.1. Single Tracks

The deposited single tracks for different process parameters were first examined, as shown in Figure 3-4, under SEM. It is observed that a low linear energy density or a low power to speed ratio would yield a discontinuous melt pool and the formation of balling, such as the case for the lowest laser power (120 W). Balling was also observed at high scan speeds as evident by the images of the tracks at 1400 mm/s and some cases at 1200 mm/s up to a point where the increasing laser power would counterbalance the effect of the high speed and raise the linear energy density. Therefore, the lowest laser power (120 W) can be excluded along with the top scan speed (1400 mm/s). In addition, there are cases where the solidified track becomes irregular by having varying width along its length, as indicated by the yellow arrows in Figure 3-4. Although melt pool irregularities and balling occur at high scan speeds, they could not be the only basis for the elimination of process parameters set, due to the absence of the added effect of hatch spacing on the consolidation and densification of built coupons.

Further assessment of the quality of single tracks is required by examining their cross-sections under an optical microscope to rule out the possibility of severe keyhole formation or lack of fusion with the underlying substrate. Figure 3-5 shows the changes in melt pool sizes with the variation of process parameters. The melt pool boundaries are outlined with red dotted lines, which reveal the shrinkage in melt pool depth with the increase in scan speed regardless of the power applied. It

is also evident that at high speeds, the penetration depth of the melt pool is small compared to the effective layer thickness, Figure 3-7 (a), which might lead to weak bonding between subsequent layers and the formation of interlayer voids. Examination of the melt pool at the lowest scan speed shows their formation by the keyhole mode up to a power of 220 W, as shown in Figure 3-5.

Increasing the laser power above 220 W at low scan speeds caused severe keyhole, characteristic of its elongated melt pool depths. The severe keyhole melt pool, shown in Figure 3-6, reveals that the penetration of the melt pool is significantly deep that it increased from 8.4 times the theoretical layer thickness to nearly 13 times the layer thickness, thus leading to possible future defects. The melt pools depths and widths were measured and plotted for different process parameters in Figure 3-7. It is seen that the width and depth decrease with increasing the scan speed or decreasing the laser power. It is noted that at 270 W and 1400 mm/s, the melt pool width increases sharply, which could be due to the irregular melt track having different widths along its length where the cross-section could correspond to a thick track location, as in Figure 3-4. Moreover, laser power has a more significant effect on melt pool stability and depth compared to the scan speed.

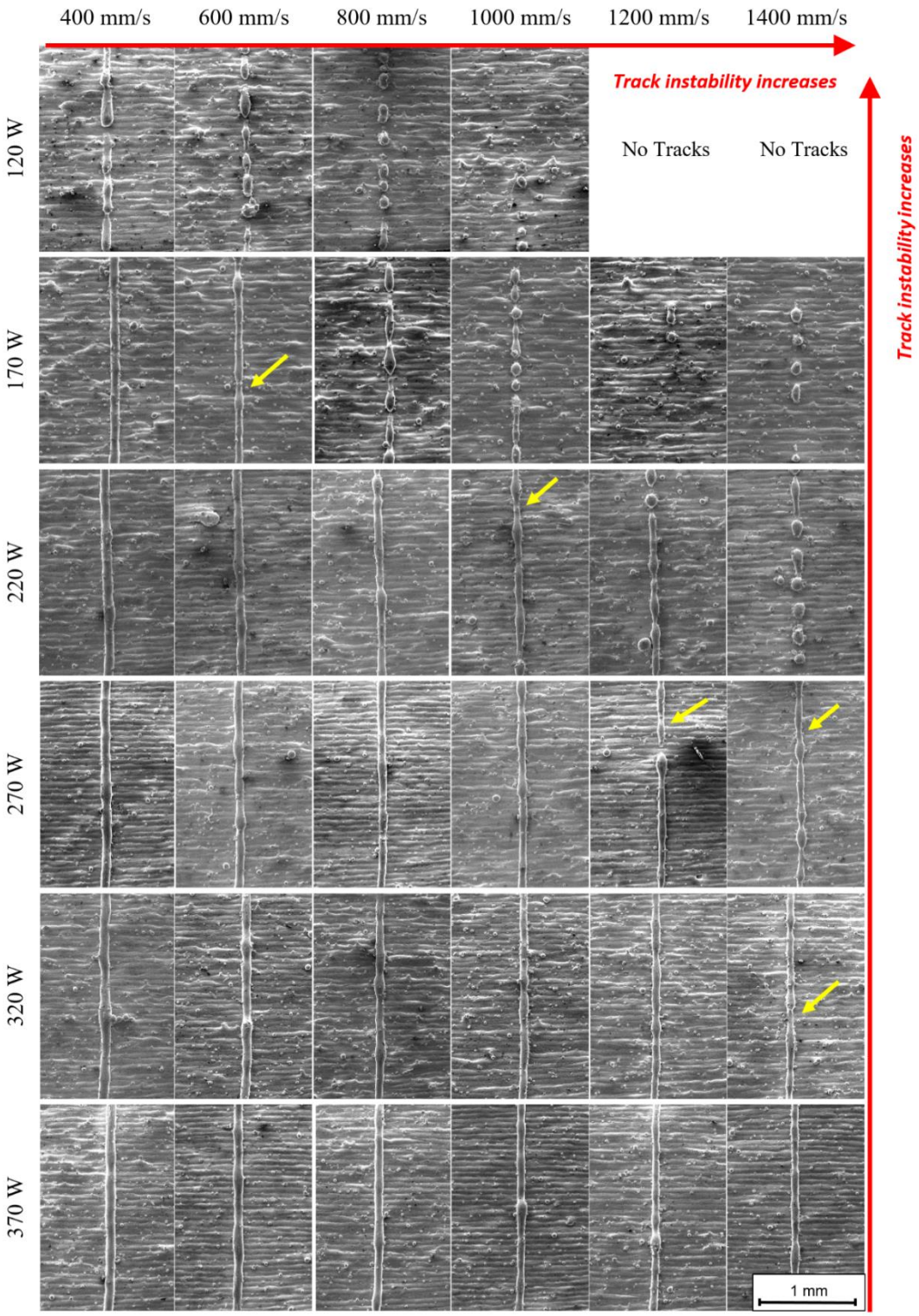

Figure 3-4 Top view of single tracks morphologies

Figure 3-5 Cross-sectional view of etched single tracks melt pools

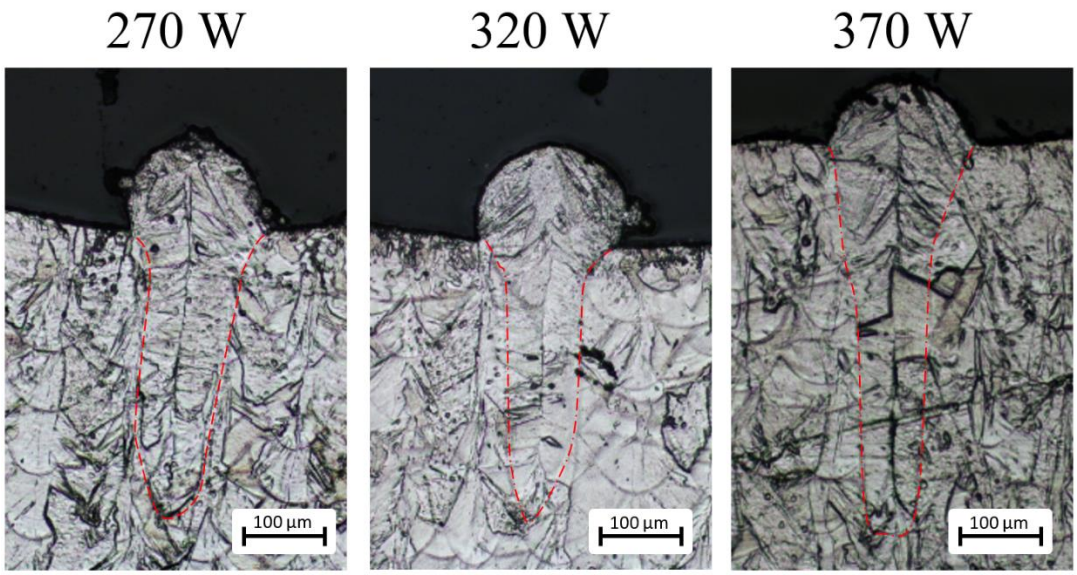

Figure 3-6 Keyhole effect at high laser powers

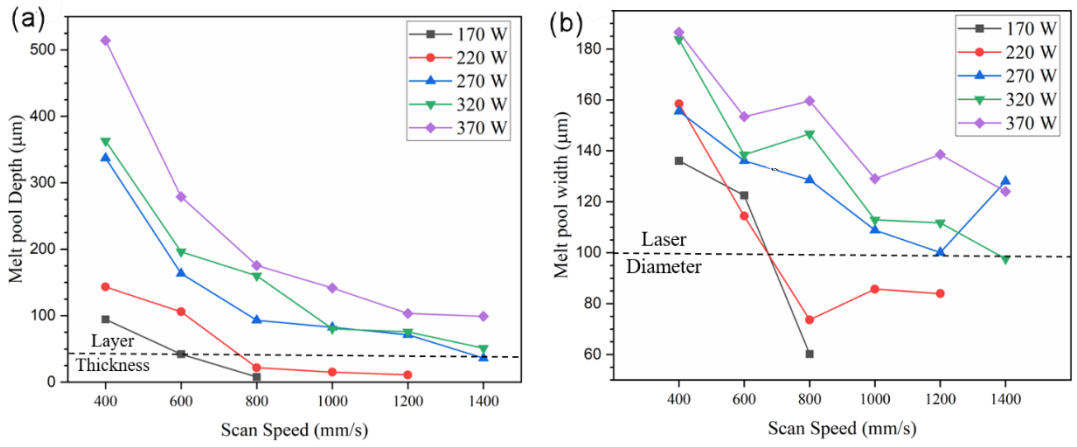

Figure 3-7 Melt pool dimensions a) Depth b) Width

Finally, the types of melt tracks can be summarized in the form of a process map relating the expected track morphology with the different laser power/ scan speed combinations, as illustrated in Figure 3-8. Based on this map, the 120 W power and 1400 mm/s speed was excluded when building the full coupons, as mentioned

earlier. Although balling appeared at different speeds for the remaining laser powers, they were used in the full coupons build to assess the possibility of hatch spacing counterbalancing these defects by remelting in the melt pools overlap zones.

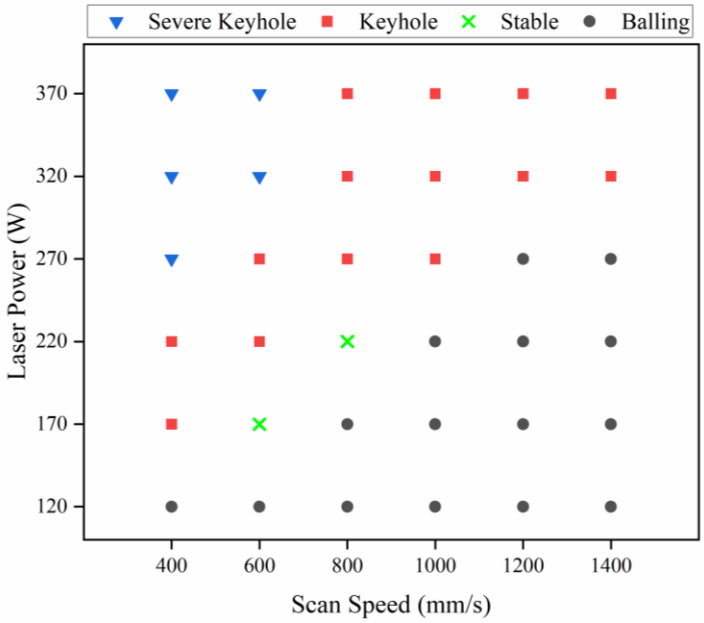

Figure 3-8 Process map for melt tracks types

3.3.2. Relative Density

Density of the coupons was measured using the Archimedes method, and subsequently, the relative density was calculated and plotted for different process parameters, as shown in Figure 3-9. It is shown that the relative density for most process parameters combinations is in the 98% to 99% range. Within this range, it is seen that as the speed increases, the relative density increases to its maximum value at 600 mm/s to 700 mm/s depending on the laser power used. The most

noticeable outliers are the lowest energy parameters combinations at 170 W and 1000 mm/s – 1200 mm/s for hatch spacing 0.1 mm and 0.12 mm. At these low input energies, the relative density dropped to 96% and 93%, respectively.

These observations are clearer by plotting the power-scan speed (PV) maps, Figure 3-10, for different hatch spacing. The map is color-based, where the green areas represent the desired parameter combinations that yield a relative density above 99%. Red zones represent the undesired parameters having relative densities below 98%. The highest relative density achieved is 99.56% at 270 W laser power, 700 mm/s scan speed, and 0.1 mm hatch spacing. It is also evident that the largest zone of the desired high densities occurs at a hatch spacing of 0.1 mm. Although the change in relative density is small across different process parameters, the relative density can be seen to increase with laser power up to a certain threshold then decreases. The threshold power is 220 W at 0.08 mm and increases to 270 W and 320 W for hatch spacing 0.1 mm and 0.12 mm, respectively.

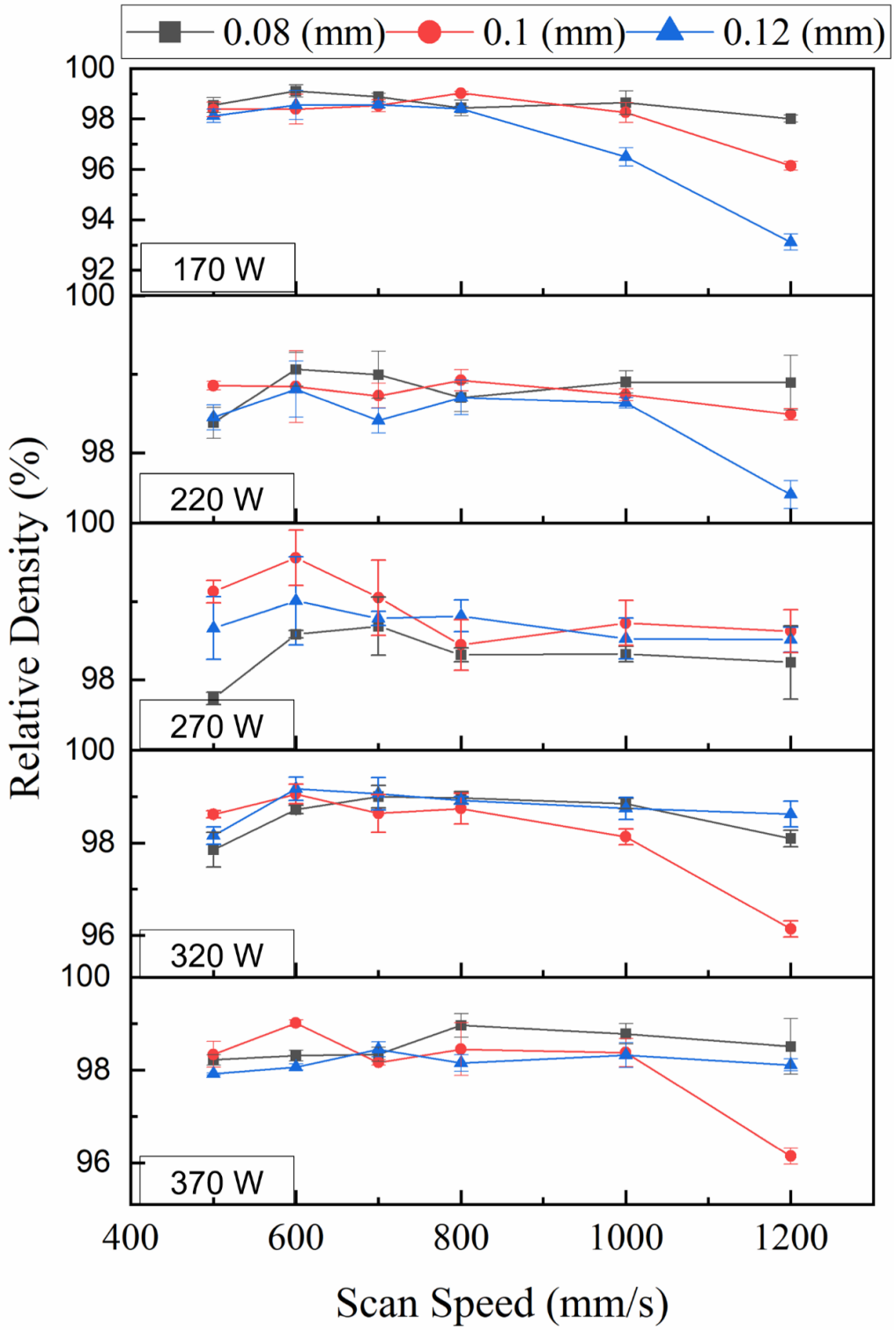

Figure 3-9 Relative density variation with process parameters

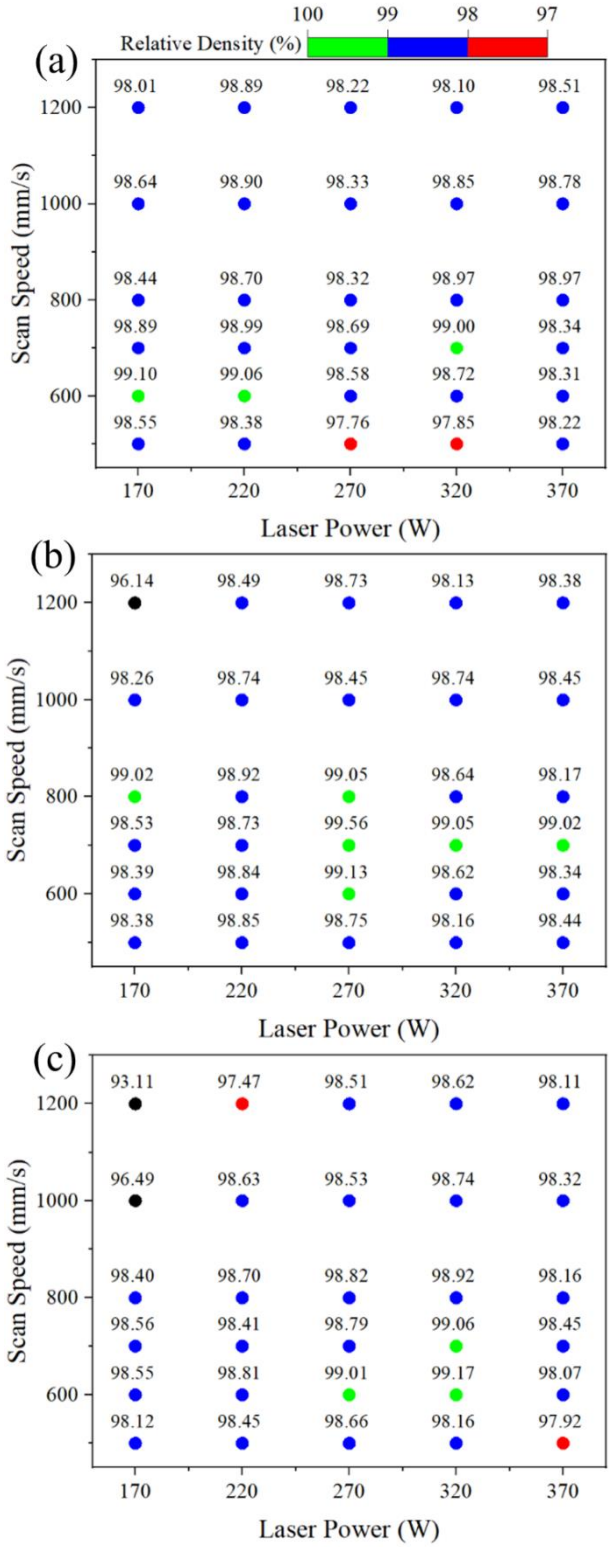
100
99
98
97
Relative Density (%)
(a)
98.01 98.89 98.22 98.10 98.51
98.64 98.90 98.33 98.85 98.78
98.44 98.70 98.32 98.97 98.97
98.89 98.99 98.69 99.00 98.34
99.10 99.06 98.58 98.72 98.31
98.55 98.38 97.76 97.85 98.22
1200
1000
800
600
Scan Speed (mm/s)
170 220 270 320 370
Laser Power (W)
(b)
96.14 98.49 98.73 98.13 98.38
98.26 98.74 98.45 98.74 98.45
99.02 98.92 99.05 98.64 98.17
98.53 98.73 99.56 99.05 99.02
98.39 98.84 99.13 98.62 98.34
98.38 98.85 98.75 98.16 98.44
1200
1000
800
600
Scan Speed (mm/s)
170 220 270 320 370
Laser Power (W)
(c)
93.11 97.47 98.51 98.62 98.11
96.49 98.63 98.53 98.74 98.32
98.40 98.70 98.82 98.92 98.16
98.56 98.41 98.79 99.06 98.45
98.55 98.81 99.01 99.17 98.07
98.12 98.45 98.66 98.16 97.92
1200
1000
800
600
Scan Speed (mm/s)
170 220 270 320 370
Laser Power (W)

Figure 3-10 Relative density PV map for hatch spacing a) 0.08 mm b) 0.1 mm c) 0.12 mm

3.3.3. Surface Roughness

The average surface roughness measured across the top surface is plotted in Figure 3-11 for different process parameters. It is seen that for all hatch spacing, the lowest power (170 W) produced the highest surface roughness, but it decreased as the laser power increased up to 370 W, which agrees with the literature [21]. However, it is noted that above a laser power of 220 W, the produced surface roughness is almost the same regardless of laser power, as seen in Figure 3-11. Contrarily, scan speed has a more prominent effect on surface roughness, where in general, increasing the scan speed leads to an increase in surface roughness. One exception is at a hatch spacing of 0.08 mm, as increasing the scan speed from 500 mm/s to 800 mm/s caused the average roughness to drop. Further increase in scan speed, increased the average roughness again, as shown in Figure 3-11, for powers 170 W and 220 W. The scan speed effect is highlighted more at speeds higher than 800 mm/s where the value of the surface roughness starts to increase steeply. Increasing the hatch spacing has a prevailing effect on surface roughness as the region for local minima for all power combined shifts towards a lower speed. It is observed in Figure 3-11 that at a 0.08 mm hatch spacing, the minimum roughness is at 800 mm/s, while at 0.1 mm, the minimum roughness is in the range of 600-700 mm/s and finally, 500 mm/s at 0.12 mm.

Surface roughness PV process maps, Figure 3-12, are constructed for different hatch spacing, which is color-coded based on the roughness grade numbers used in conventional machining [11]. The green color represents the desired region of process parameters selection, which has a roughness grade N7 that represents a roughness value between 1.6 µm to 3.2 µm. The largest desirable area is found at a hatch spacing of 0.08 mm with laser powers starting at 270 W and low to medium scan speed range, as shown in Figure 3-12. It is also observed that in general increasing laser power reduces the average roughness while increasing the scan speed increases the average roughness.

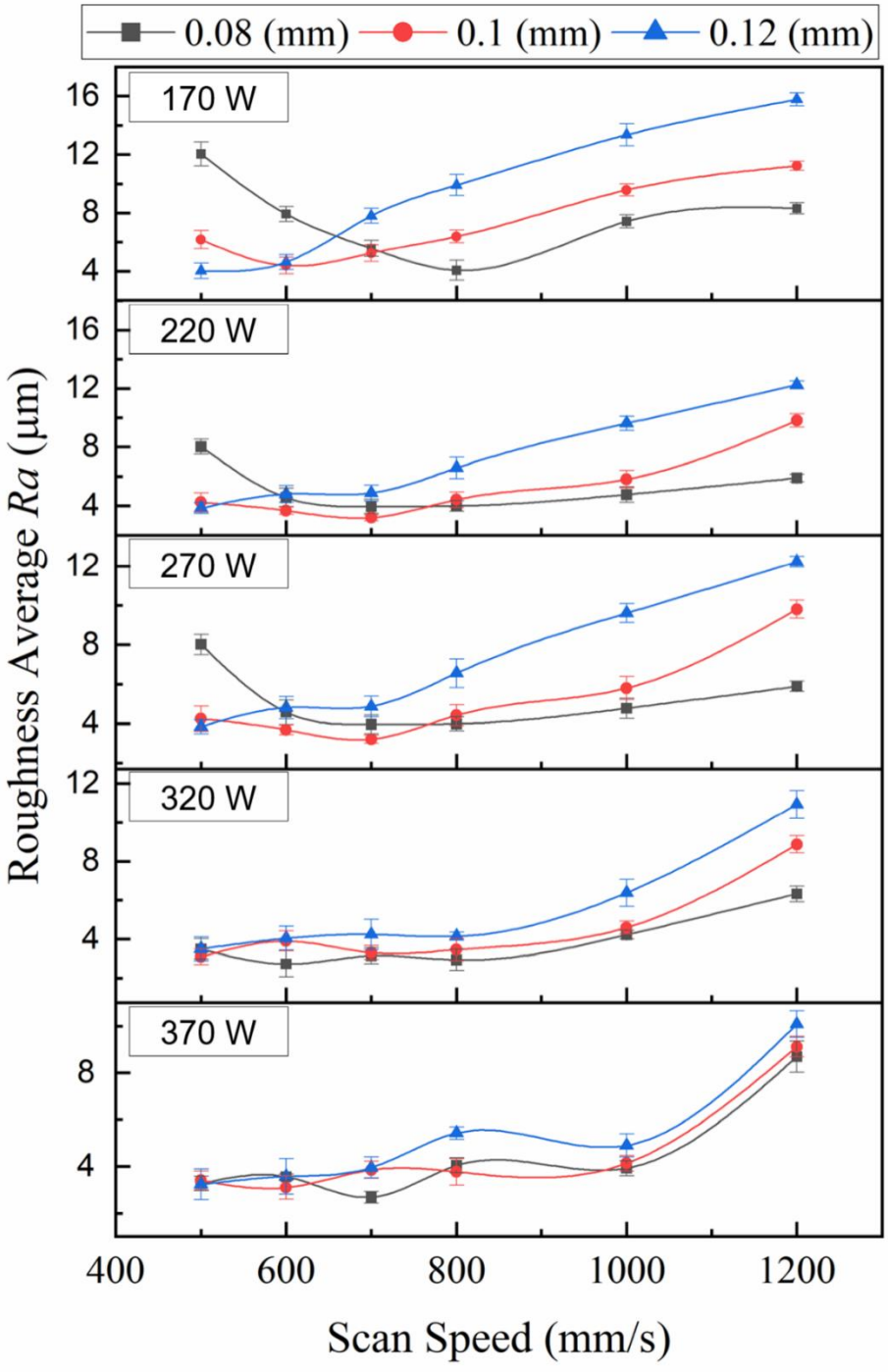

Figure 3-11 Average surface roughness variation with process parameters

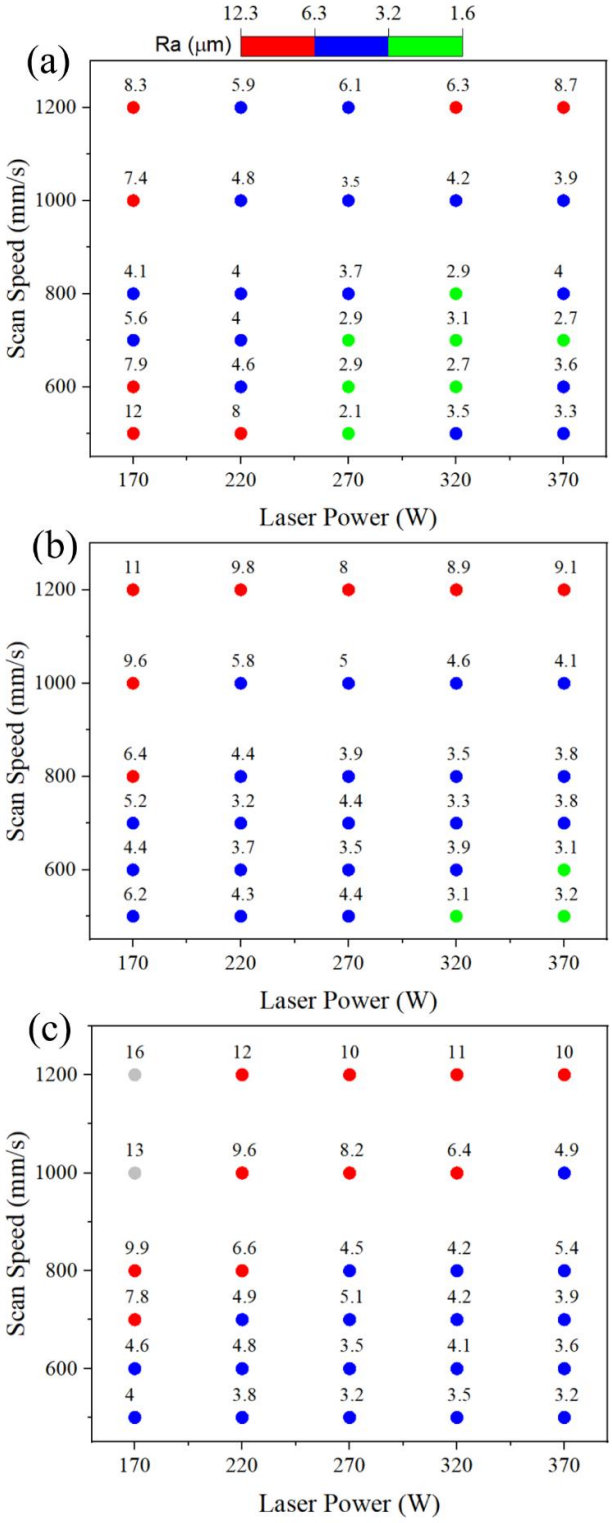
12.3
6.3
3.2
1.6
Ra (μm)
(a)
8.3 5.9 6.1 6.3 8.7
7.4 4.8 3.5 4.2 3.9
4.1 4 3.7 2.9 4
5.6 4 2.9 3.1 2.7
7.9 4.6 2.9 2.7 3.6
12 8 2.1 3.5 3.3
Scan Speed (mm/s)
1200
1000
800
600
170 220 270 320 370
Laser Power (W)
(b)
11 9.8 8 8.9 9.1
9.6 5.8 5 4.6 4.1
6.4 4.4 3.9 3.5 3.8
5.2 3.2 4.4 3.3 3.8
4.4 3.7 3.5 3.9 3.1
6.2 4.3 4.4 3.1 3.2
Scan Speed (mm/s)
1200
1000
800
600
170 220 270 320 370
Laser Power (W)
(c)
16 12 10 11 10
13 9.6 8.2 6.4 4.9
9.9 6.6 4.5 4.2 5.4
7.8 4.9 5.1 4.2 3.9
4.6 4.8 3.5 4.1 3.6
4 3.8 3.2 3.5 3.2
Scan Speed (mm/s)
1200
1000
800
600
170 220 270 320 370
Laser Power (W)

Figure 3-12 Surface roughness PV map for hatch spacing a) 0.08 mm b) 0.1 mm c) 0.12 mm

3.3.4. Residual Stresses

Surface RS was measured at the center of the top surface in the scan line directions for a subset of the process parameters, as seen in Figure 3-13. There is no monotonic trend for the relation between the surface RS and the increase in process parameters. For a hatch spacing of 0.08 mm, the surface RS mostly increases with a scan speed up to 800 mm/s and then decreases with a further increase in scan speed. However, for a hatch spacing of 0.1 mm at the lowest power (170 W), surface RS decreases with increasing the scan speed. Beyond 170 W, the surface RS exhibits the same trend as the 0.08 mm hatch; however, the trend is flipped for the highest two powers. A similar variety of surface RS trends is observed for a hatch spacing of 0.12 mm. Examining the relation between surface RS and laser power shows that in most cases, increasing the laser power leads to a decrease in surface RS.

In addition, PV maps for surface RS are plotted in Figure 3-14 for both scan and hatch direction at different hatch spacing. All surface RS are tensile, which is typical of the SLM process due to high-temperature change and rapid cooling rates. Red zones represent the highest surface RS, while the green zones are the relatively lowest surface RS. The non-monotonic trends are seen for both directions, which are in agreement with the literature [21]. It was observed that surface RS in the scan direction is higher than that in the hatch direction; moreover, principal stresses were in line with the scan and hatch directions except for a limited number of cases.

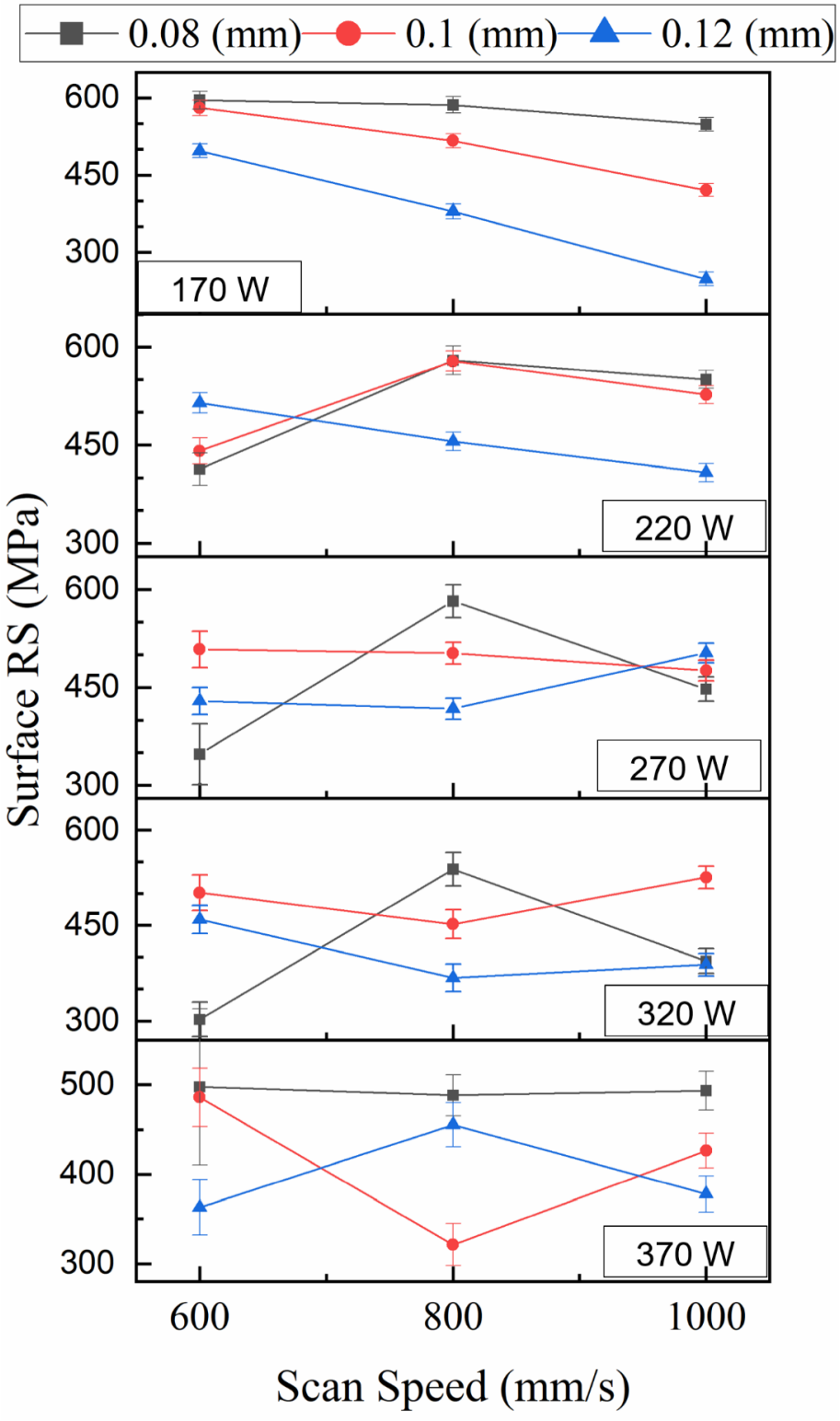

Figure 3-13 Surface RS in scan direction at different process parameters

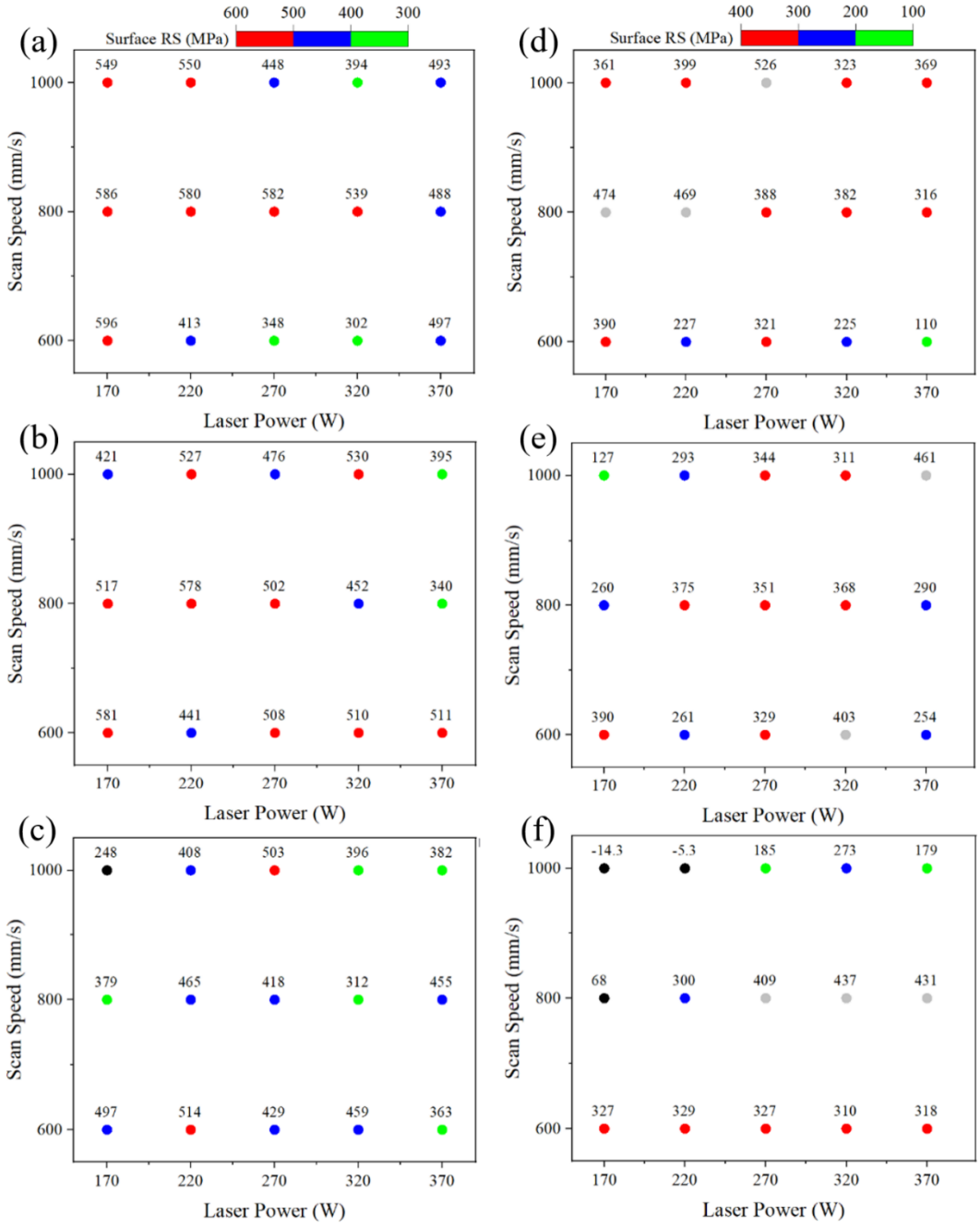

Figure 3-14 Surface RS PV maps for scan and hatch directions (a,d) 0.08 mm (b,e) 0.1 mm (c,f) 0.12 mm

3.3.5. Melt Pool Morphology and Microstructure

A subset of the printed coupons selected to examine the melt pool morphology and microstructure in a multi-track and multi-layer scenario. The etched samples were first examined under an OM to investigate the increase in melt pool size. Therefore the top layer was selected to see the full melt pool dimensions, which would otherwise be overlapped by the layer above, as shown in Figure 3-15. The single track melt pool dimensions, highlighted with the dotted red line, at 220 W and 1000 mm/s, for example, is compared to the melt pools at the same power and speed combination at 0.08 mm and 0.12 mm hatch spacing, respectively, Figure 3-15 (b) & (c). The single track showed a high tendency to ball due to the instability of the melt track and insufficient melt pool depth. The single melt pool had a depth of 15 µm and a width of 86 µm. In comparison, at a hatch spacing of 0.08 mm the average of seven melt pools was measured and showed an average depth of 153 µm ± 13 µm and an average width of 233.3 µm ± 11 µm. At a hatch of 0.12 mm, the average melt pool depth was 126 µm ± 17 µm and the average width was 195 µm ± 17 µm.

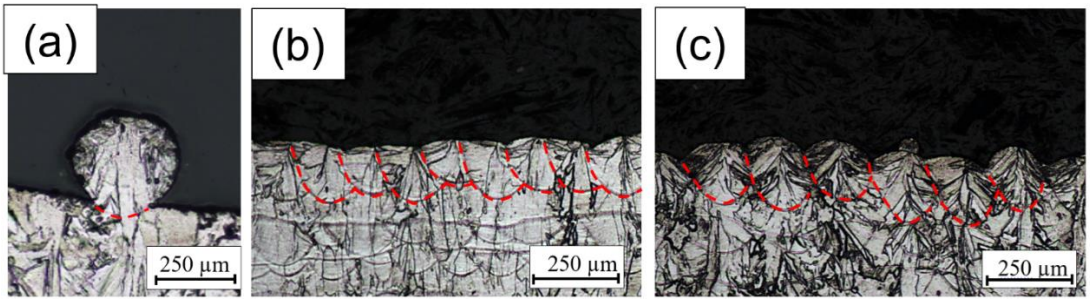

Figure 3-15 Melt pool dimensions at 220 W and 1000 mm/s a) single track b) hatch 0.08 mm c) hatch 0.12 mm

Further examination of the microstructure of several layers in the build direction, shown in Figure 3-16, reveals the formation of columnar grains, highlighted by red arrows, at a scan speed of 800 mm/s, which is in agreement with the literature [10]. These columns extend across several layers at the low hatch spacing of 0.08 mm and are aligned along the build direction (Z), Figure 3-16 (a) and (b); however, increasing the hatch spacing to 0.12 mm develops a mixed grain structure. For the latter grain structure, columnar areas are observed to have shorter columnar grains that are often limited to two layers and deviate away from the build direction. Comparison of the grain microstructure under different scan speeds, as shown in Figure 3-17, revealed the formation of equiaxed grains at the lowest speed of 600 mm/s. Increasing the scan speed to 800 mm/s, the grains become columnar at 0.08 mm hatch and mixed grains at 0.12 mm hatch, Figure 3-17 (b) & (e). At 1000 mm/s formation of mixed grains structure occurred at the lowest and highest hatch spacings, as shown in Figure 3-17 (c) & (f).

Detailed examination of the in-grain microstructure under SEM, revealed the formation of fine columnar dendritic grains inside the melt pool, as shown in Figure 3-18. These fine dendrites are aligned in the build direction for a hatch spacing of 0.08 mm, Figure 3-18 (a) and (b), but for a hatch spacing of 0.12 mm, they have grown towards the centerline of the meltpool, Figure 3-18 (c) and (d).

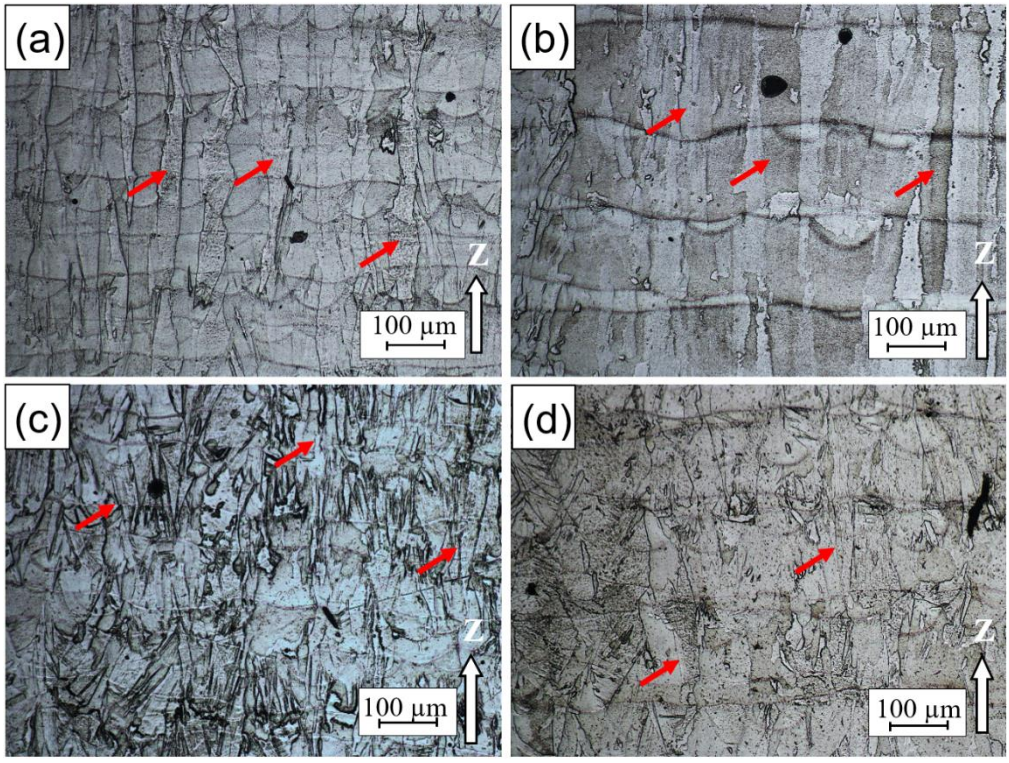

Figure 3-16 Grain structure with columnar grains under OM at 800 mm/s and a) 220 W, 0.08 mm b) 320 W, 0.08 mm c) 220 W, 0.12 mm d) 320 W, 0.12 mm

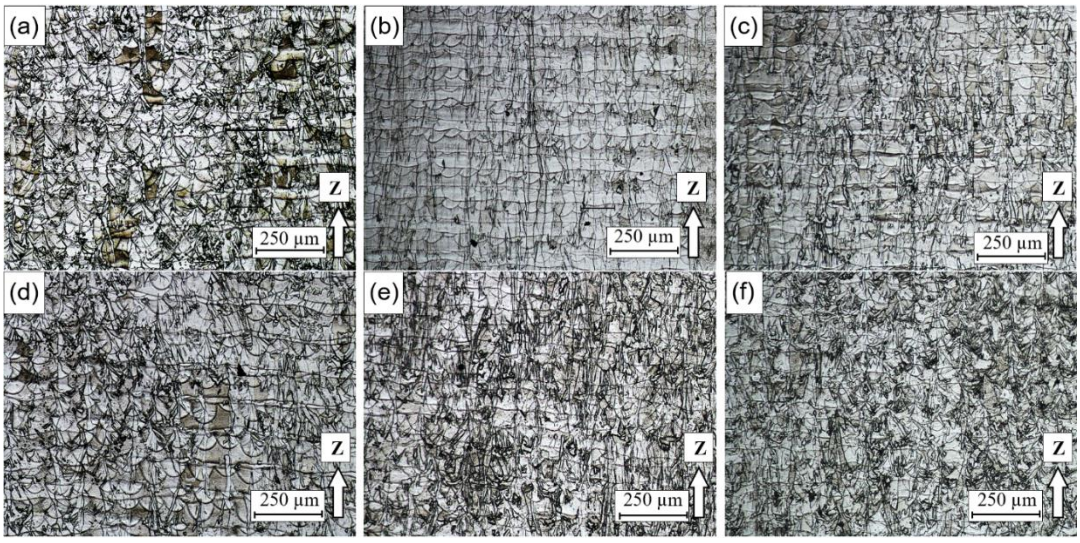

Figure 3-17 Grain structure at 220 W, (a-c) hatch spacing 0.08 mm (d-f) 0.12 mm for scan speeds 600 mm/s, 800 mm/s and 1000 mm/s

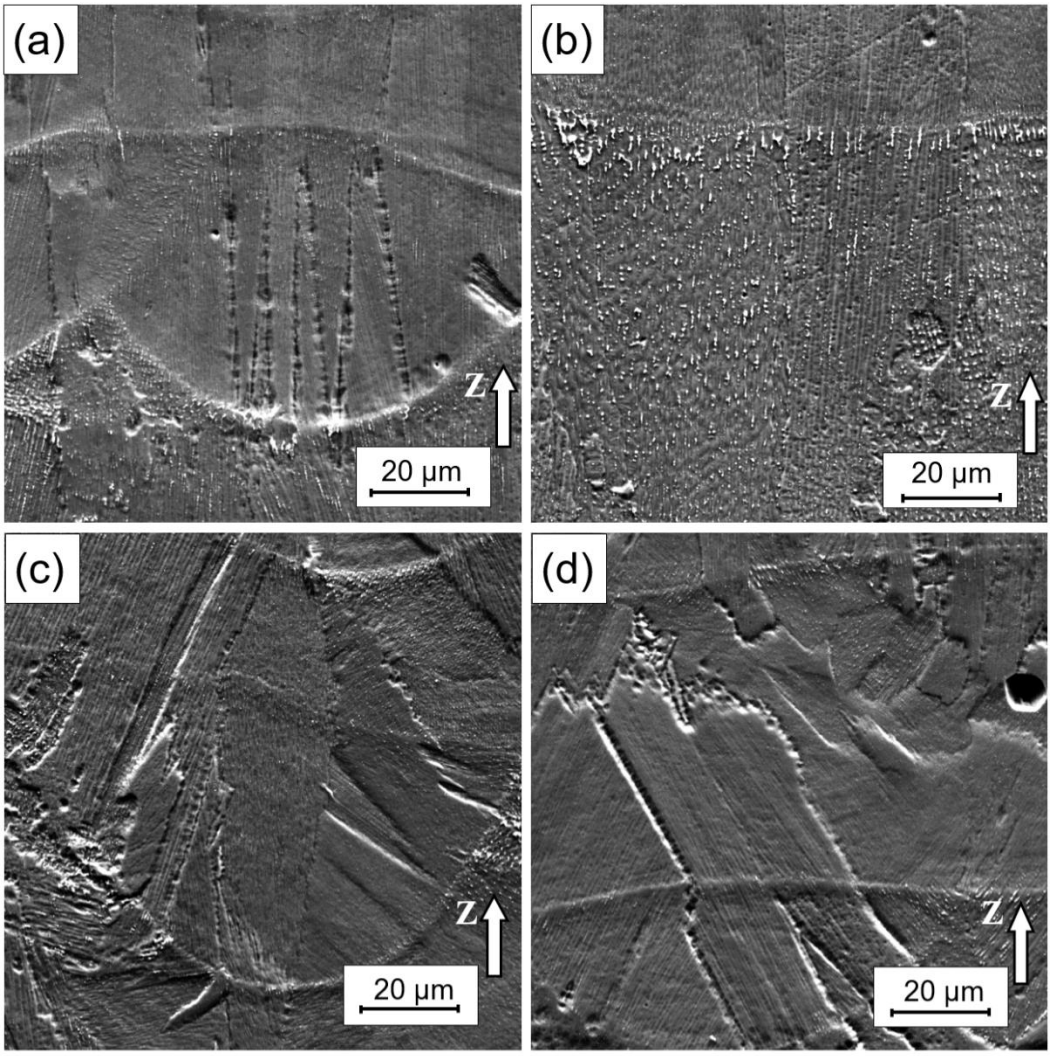

Figure 3-18 In-grain microstructure under SEM at 800 mm/s and a) 220 W, 0.08 mm b) 320 W, 0.08 mm c) 220 W, 0.12 mm d) 320 W, 0.12 mm

Phase analysis using XRD was done on a sample built with 220 W, 800 mm/s, and 0.12 mm detected five peaks, as shown in Figure 3-19, where only the γ phase was identified. The literature reported [27, 28] the detection of γ and γ" which was not able with the characterization used in the current study. Moreover, texture analysis was done on the same sample and plotting the pole figures, Figure 3-20, showed

strong texture in (200), which is along the laser scan line, as indicated by a black arrow. This texture is in agreement with the observed in-grain microstructure observed in Figure 3-18.

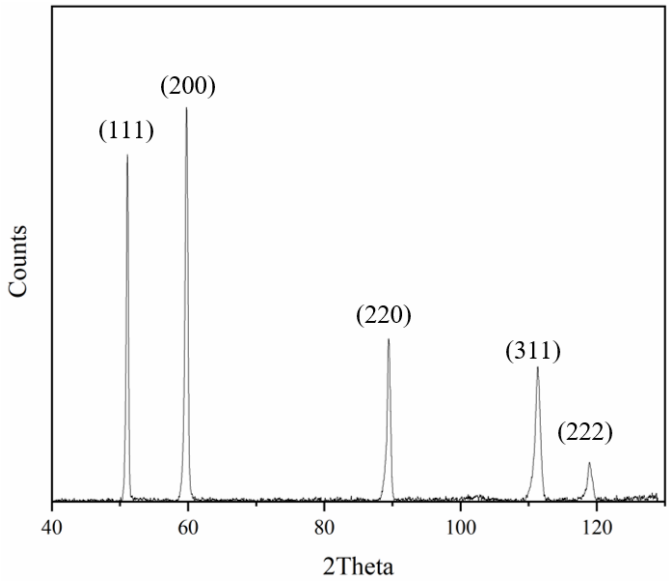

Figure 3-19 XRD phase analysis of IN718 sample at 220 W, 800 mm/s, and 0.12 mm

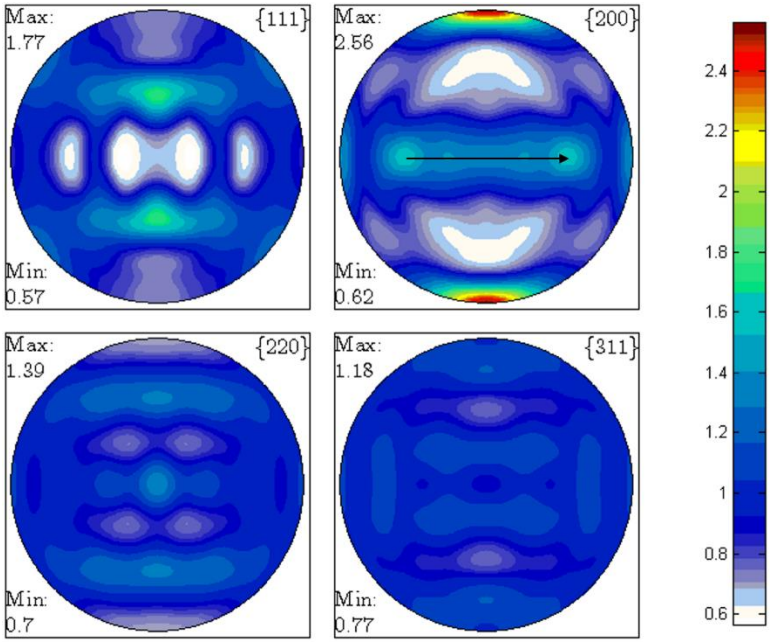

Figure 3-20 Pole figure of IN718 at 220 W, 800 mm/s and 0.12 mm

The change in chemical composition from powder form to cube coupons built at different laser power and scan speed at a hatch spacing of 0.12 mm was measured. The chemical composition measured using ICP was not capable of detecting the light elements such as oxygen and carbon. The results in Table 3-6 show varying changes in chemical compositions from powder form. Different powers and speed exhibited vaporization of nickel with different percentages. Vaporization also occurred in niobium and tantalum as well as titanium, thus raising the weight percentage of the remaining major elements such as iron and chromium.

Table 3-6 Chemical composition of different samples (weight %)

Power/ speed	Al	Co	Cr	Cu	Fe	Mn	Mo	Nb+ Ta	Si	Ti	Ni
Powder	0.46	0.02	19.4	0.03	18.89	0.02	3.1	5.14	0.04	1.02	51.88
220/600	0.46	0.04	21.15	0.04	20.02	0.03	3.19	5.09	0.02	0.97	48.99
220/800	0.46	0.05	20.84	0.04	19.87	0.03	3.16	5.05	0.02	0.97	49.51
220/1000	0.52	0.06	20.03	0.08	19.07	0.05	3.05	4.82	0.04	0.95	51.34
320/600	0.53	0.06	19.96	0.08	19.02	0.05	3.05	4.71	0.03	0.97	51.53
320/800	0.52	0.06	20.36	0.08	19.56	0.05	3.11	4.91	0.04	0.95	50.36
320/1000	0.52	0.06	20.29	0.08	19.41	0.05	3.12	4.82	0.04	0.98	50.64

3.4. Discussion

3.4.1. Formation of single tracks

The first step in determining the melt tracks integrity is the formation of regular, continuous tracks. However, specific process parameters combinations lead to the breakage of such tracks. In other instances, these broken-up segments curl up into balls as an indication of a phenomenon called balling [29, 30]. This behavior is assumed to be controlled by surface tension during solidification, particularly the Plateau-Rayleigh instability [30, 31]. To establish this assumption, the dimensionless Bond and Laplace numbers [32] can be calculated using Eqn. 2 and 3. The Bond number (*Bo*) is the ratio of gravity to surface tension, while the Laplace number (*La*) is the ratio of surface tension to viscosity.

$$Bo = \frac{\rho g L^2}{\sigma} \tag{2}$$

$$La = \frac{\sigma g L}{\eta^2} \tag{3}$$

Where ρ, g, σ, *L*, η represent density, gravitational acceleration, surface tension, melt pool length, and viscosity, respectively. Assuming an arbitrary melt pool length of 100 µm and thermo-physical properties obtained from [33], yields a Bond number of 3.8×10^{-4} and a Laplace number of 2.96×10^{4} which proves that surface forces dominate the melt pool behavior. The continuous molten bead is similar to a cylinder bounded at the bottom to the substrate, as shown in Figure 3-21 (a). The introduction of any axisymmetric periodically harmonic perturbation can drive the melt pool into instability [30, 31], as shown in Figure 3-21 (b). The perturbed melt pool is signified by area of high and low pressures, which develop pinched zones. The pinched zones could reach an extent were the melt pool breaks into smaller segments, and due to surface tension, the molten material curls into spheres. The stability criterion of the melt pool can be determined using Eqn. 4, where *D* is the melt pool diameter, and *L* is the perturbation wavelength (approximately the melt pool length).

$$\frac{\pi D}{L} = \sqrt{2}\sqrt{\frac{\phi(1+\cos 2\phi)-\sin 2\phi}{2\phi(2+\cos 2\phi)-3\sin 2\phi}} \tag{4}$$

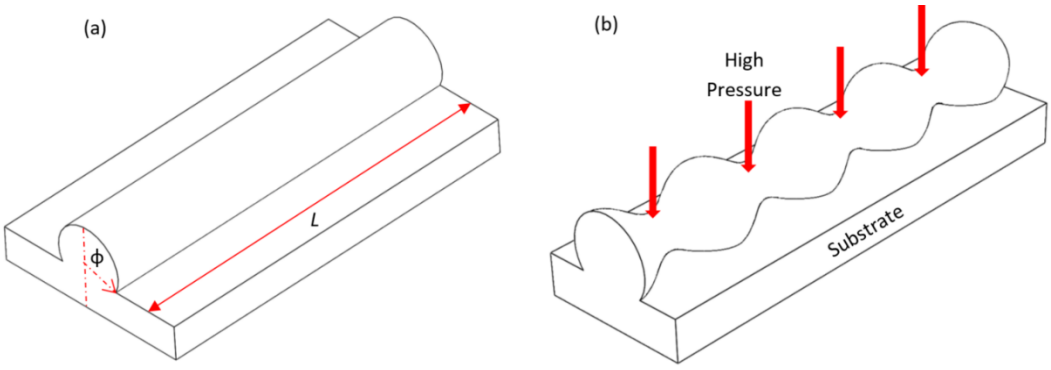

Figure 3-21 Morphology of single bead a) stable track b) Plateau-Rayleigh instability

During SLM, the laser beam having a diameter (d) irradiates the powder surface, and heat is conducted to down through the powder layer, raising its temperature above the melting temperature to form a melt pool. At the surface, the intensity of the laser beam has a Gaussian distribution, as shown in Figure 3-22, which is calculated based on Eqn.6. For a moving laser beam, the peak temperature can also be calculated using Eqn. 5, which will have the same Gaussian distribution as the laser intensity. Hence, assuming laser absorption is the same across the whole laser area, the depth of the powder layer reaching a peak temperature above the melting temperature will be a near reflection of the Gaussian profile, and thus the formation of a parabola shaped melt pool. The aspect ratio of the melt pool can be calculated as the ratio of the melt pool depth to half its width, as mentioned earlier. If the aspect ratio is less than 1, then the melt pool formation mode is called conduction mode [22, 34, 35], as shown in Figure 3-22 (a). Conduction mode melt pools were observed in only two cases, 170 W at 600 mm/s and 220 W at 800 mm/s, as seen

in Figure 3-5, despite having a shallow depth (under melt). Moving beyond an aspect ratio of 1 the melt pools switch to a keyhole mode, where the intensity of the laser beam at the center is high enough, causing deep penetration of the melt pool, as illustrated in Figure 3-22 (b). A large percentage of the melt pools measured in Figure 3-5 falls under the keyhole criterion [22, 32, 35, 36]. Further increase in the laser intensity with a combination of low scan speed and high laser power, the aspect ratio could exceed 2.5, which shifts the melt pool into severe keyhole [22], which could set the stage up for the formation of pores.

Keyhole porosity is dependent on the equilibrium between the two opposing pressure acting on the keyhole. Ablation pressure, which occurs due to the evaporation of the molten metal and its ejection in the form of a vapor, thus inducing a pressure to keep the keyhole open. Conversely, the capillary pressure due to surface tension, resulting from the temperature gradient across the melt pool surface, acts to close the keyhole [37]. For high laser powers, higher evaporation rate occurs as more heat is absorbed due to the Inverse Bremsstrahlung effect, which increases the diameter and depth of the formed vapor column. As the vapor column diameters increase the ablation pressure becomes greater than the capillary pressure, causing a stable open keyhole. However, as the vapor column increases beyond the laser beam diameter, the ablation pressure decreases and is overcome by the surface tension leading to the closure of the keyhole. In such case, the keyhole might not form porosities, as is the case of the results shown in Figure 3-6. However, such large depths could increase the chance of Rayleigh instabilities if

the length to diameter ratio of the vapor column is high. This will lead to closures along the keyhole axis due to surface tension and entrapment of escaping vapor causing a keyhole porosity [38], as shown in Figure 3-22 (c).

$$T = \frac{\sqrt{2}AIr_o}{k\sqrt{\pi}} \tan^{-1} \sqrt{\frac{2\alpha}{vr_o}} \tag{5}$$

$$I = \frac{P}{2\pi {r_o}^2} e^{(-r^2/2\,{r_o}^2)} \tag{6}$$

Where:

T: Temperature inside the melt pool (K)

α : Thermal diffusivity (m^2/s)

A: Laser absorptivity

v : Scan speed (m/s)

I : Laser intensity (W/m^2)

P : Laser power (W)

r_o: Beam radius (m)

r : radial position (m)

k : Material thermal conductivity (W/m.K)

It was observed from Figure 3-7, and mentioned earlier that the laser power has a more significant impact on the change in melt pool dimensions compared to the scan speed. This observation can be explained in light of Eqn. 5, as it shows that the increase in the melt pool temperature occurs due to the rise in power or decrease in speed. However, the change in temperature is proportional to only the square root of the scan speed.

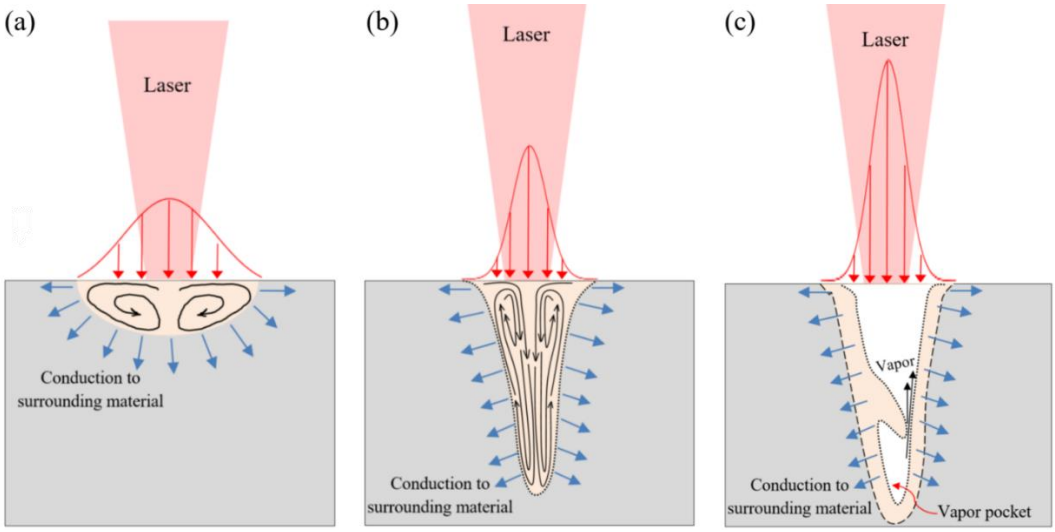

Figure 3-22 Melt pool formation mechanisms a) conduction mode b) keyhole mode c) keyhole with porosity

3.4.2. Relative Density and Pore Formation

Porosity in SLM can be due to three main reasons; firstly is the lack of fusion, where the formed melt pool is not large enough to ensure good overlap with the layer below or adjacent melt pools [9]. This type of pores is characterized by its relatively large non-circular shape with some sharp edges, as shown in Figure 3-23.

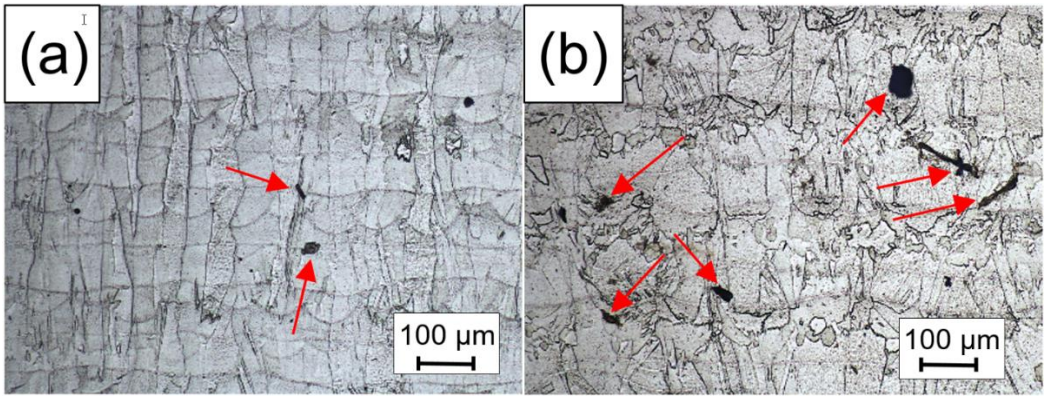

Figure 3-23 Lack of fusion at 800 mm/s for a) 220 W, 0.08 mm

b) 320 W, 0.12 mm

The lack of fusion pores appeared at 220 W and 320 W at 800 mm/s; however, the measurements of the single line, Figure 3-7, showed a melt pool depth of approximately 22 µm and 160 µm, respectively, which in the latter case should be larger than the layer thickness. Although lack of fusion is usually limited to low energy cases, for example, 170 W, 1200 mm/s, and 0.12 mm, where a shallow melt pool is formed, it occasionally forms at higher input energies. This case could be attributed to the fact that the actual layer thickness is larger than the theoretical layer thickness due to the powder bed density [23]. It was found that due to powder bed porosity, the solidified layer will shrink in height, thus increasing the gap between the new surface and the recoater blade. For an EOS machine, the expected powder bed density is 40%-60% of the full density. Therefore the actual layer thickness can be calculated using Eqn 7. Based on the assumption of a powder bed density of 50%, the actual layer thickness will be 80 µm instead of 40 µm, which will affect the absorption of the laser power and the energy need to ensure good bonding with underlying layers. Therefore, increasing the incident energy could eliminate such pores.

$$t_{actual} = \frac{\rho_{full}}{\rho_{bed}} t_{theoretical} \quad (7)$$

Where:

t_{actual}: Actual layer thickness (µm) $t_{theoretical}$: theoretical layer thickness (µm)

ρ_{bed} : Powder bed density (kg/ m^3) ρ_{full} : Bulk density of material (kg/ m^3)

Lack of fusion can also occur across melt pool tracks within the same layer due to powder denudation. The use of high laser power or low scan speed results in high input energy, which upon striking the surface of the powder, pushes the surrounding powder away from the melt track. Lack of powder causes a problem in multi-track scanning, as there will be not enough powder to melt and fill the gap between adjacent melt pools, thus creating a lack of fusion pore [39].

The second type of pores to form in SLM is gas entrapped pores, which are signified by their spherical shape [40], as shown in Figure 3-24. The pores could either be due to trapped nitrogen gas, used for protection from oxidation, or microscopic entrapped vapors previously present in the powder itself during production.

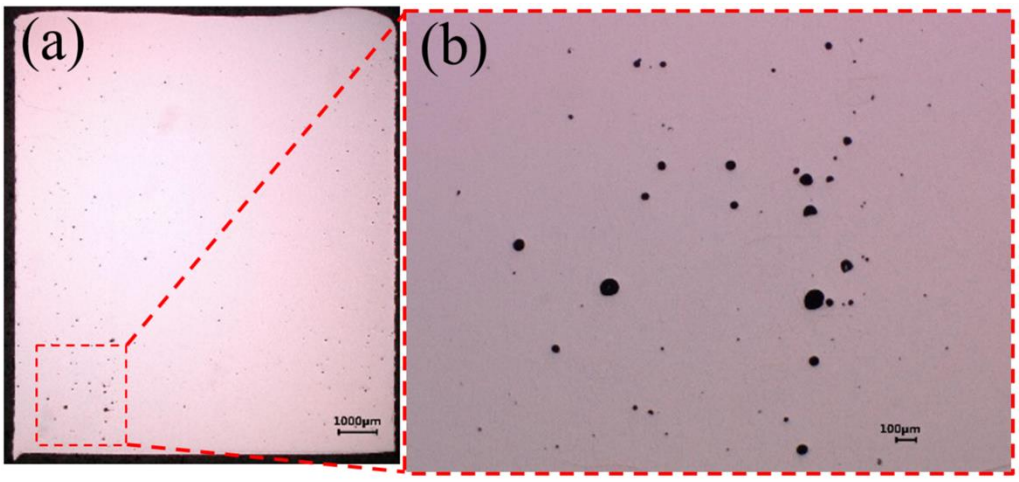

Figure 3-24 Entrapped gas pores at 320 W, 600 mm/s and 0.08 mm

The third type of defect that occurs in SLM is the keyhole porosity, which occurs at very high energies (high power, low scan speed). Keyhole melt pools are infamous for their elongated melt pool depths that could cause material vaporization at the bottom of the melt pool. Due to the recoil pressure, the melt pool collapses on itself and entrapping the metal vapor before escaping to the free surface, as discussed in section 4.1. Keyhole pores are near-circular and can be found near the bottom end of keyhole melt pools. However, keyhole pores were not observed in the studied process window for full coupons, which could be reverted to the observation that the formation and subsequent collapse of vapor pockets do not frequently occur [41].

The second type of pores is the most common for the tested process window. Still, its elimination could be harder than the other two types as it requires a balance between the three process parameters to produce suitable energy. This balance can be observed through the results in Figure 3-10, where the relative density increases with laser power to a peak value, then decreases again, and the same trend is observed for scan speed [42, 43]. At low power or high scan speed (low energy), lack of fusion is the dominant defect formation mechanism. Increasing the laser power or decreasing the scan speed improves the relative density, but the pore formation mechanism switches to the gas/vapor entrapment until reaching a point where enough molten material is produced with enough time to ensure good wettability, i.e., the molten metal fills in the pores left behind. Further increase in laser power or decrease in scan speed (higher energy) will disrupt this balance

causing the formation of gas pores again either due to entrapped gas or keyhole along with powder denudation. Although the use of input energy as a lump sum is convenient for an explanation, the produced relative densities did not correlate well with the energy density, proving that the desired balance point differs based on the individual process parameters, which is in agreement with the literature [44].

3.4.3. Surface Roughness Evolution

Surface roughness can develop due to several reasons, the most important of which is the periodic humps that represent the adjacent scan tracks on the top surface. The formation of these humps is controlled by the amount of input heat and solidification time available. High energy would melt the powder and form a large enough melt pool that would ensure melt flow and wetting of adjacent tracks, thus good overlap with previously formed tracks. Therefore, to have a high enough input heat, either low scan speed or high laser power or a combination of both is needed, as seen in Figure 3-25, and Figure 3-26. It can be observed in Figure 3-25 (a) that the solidified melt pool tracks are smoothed out to the degree that they do not have a clear definition. As the speed increases, i.e., input heat input decreases, the lines become more defined (higher roughness) as highlighted within the yellow perimeter. Finally, at the highest scan speed, the scan lines are quite evident and protruding higher from the surface, thus resulting in the highest surface roughness. The same result can be observed for increasing laser power, as in Figure 3-26. That is why, as shown in Figure 3-11, the lowest surface roughness is found in the low scan speed range. Moreover, for good wetting to happen, then the solidification

time needs to be long enough to ensure such wetting takes place, and good smoothing out of these humps occurs. Eqn 8 represents a prediction of the solidification time of a molten droplet of metal [20, 45].

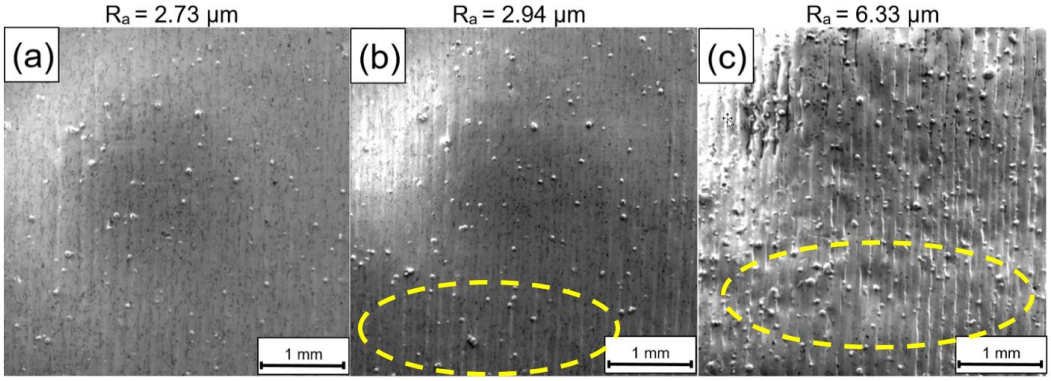

Figure 3-25 Top surface morphology at 320 W a) 600 mm/s b) 800 mm/s c) 1200 mm/s

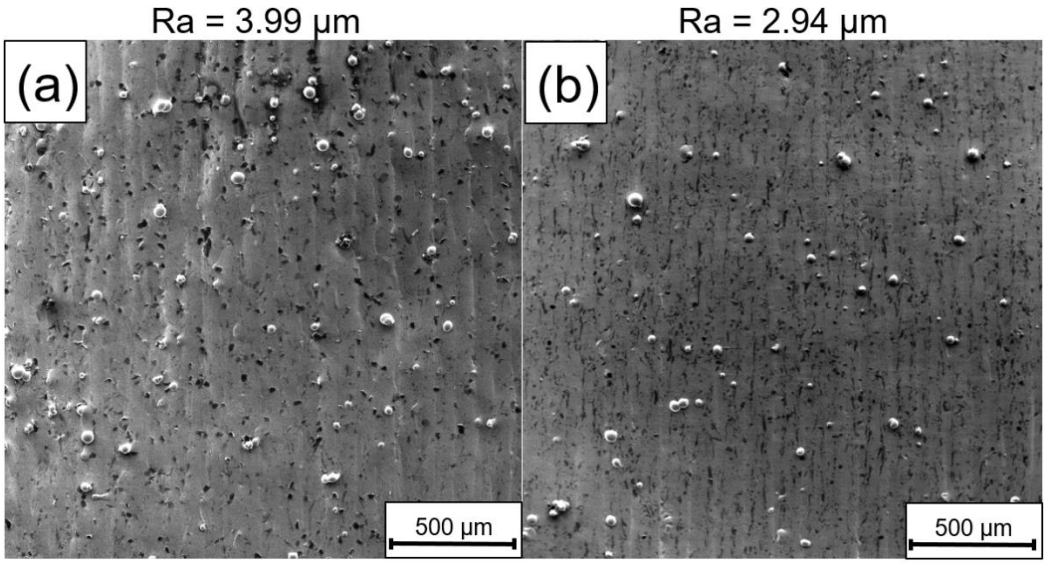

Figure 3-26 Top surface morphology at 800 mm/s a) 170 W b) 320 W

$$\tau_s = \frac{s^2 k}{3 a k_{sub}} \left[\ln\left(\frac{T_o - T_{sub}}{T_l - T_{sub}}\right) + \left(1 + \frac{k_{sub}}{2k}\right) \frac{L}{C(T_l - T_{sub})}\right] \quad (8)$$

Where:

s: initial droplet size (m)	a : Thermal diffusivity (m^2/s)
k : thermal conductivity (W/m.K)	C : specific heat capacity (J/kg.K)
T_o: initial temperature of a droplet (K)	T_l : Liquidus temperature (K)
k_{sub} : Substrate thermal conductivity (W/m.K)	T_{sub} : Substrate temperature (K)

Since the molten material starts to solidify at the same initial temperature (Liquidus temperature) to the solidus temperature and assuming the same thermal conductivity for coupons manufactured with different process parameters, it can be found that the solidification time depends mainly on the droplet size. Therefore, a low scan speed will produce a larger melt pool having a relatively long time to wet a large surrounding area.

Other factors that affect surface roughness include balling and melt tracks irregularities, which are characterized by the non-periodic bulging and humping along the top surface, as shown by yellow arrows in Figure 3-27. Balling was not observed in the full coupons compared to the single tracks as the introduction of the hatch spacing caused melt tracks to overlap, thus remelting the balled-up material into scattered bulges. There is also the added effect of satellite powders sintering to the top surface, as highlighted within the red circles in Figure 3-27, which adds to the surface roughness. These two factors are the reasons why at 170

W, the roughness was the highest at the lowest speed and highest speed, as seen in Figure 3-27.

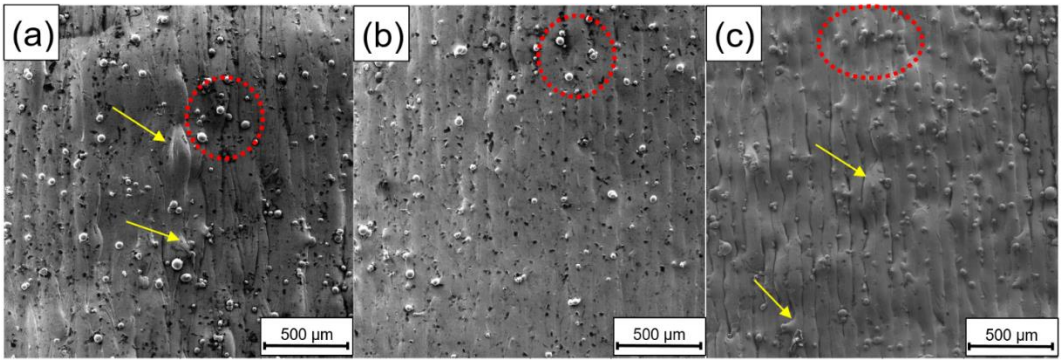

Figure 3-27 SEM of top surface defects at 170 W and a) 600 mm/s b) 800 mm/s c) 1200 mm/s

By comparing the surface roughness across hatch spacing, it is found that increasing the hatch spacing decreases the surface roughness, as shown in Figure 3-11. This observation is contradictory to the discussion mentioned earlier because as the hatch spacing increases, the input energy decreases, and the molten material will need to flow further to the sides to wet the adjacent tracks. The reason for the decrease in surface roughness, which is particularly significant at the lowest scan speed, is due to the morphology of the single tracks and the subsequent heat accumulation due to multi-tracks. For a single track, the amount of laser energy hitting the powder is relatively high at the lowest speed. The impact of laser with the powder surface will cause a powder denudation zone surrounding the scan track, i.e., a zone with no powder. Therefore, the use of a small hatch spacing will result in a large overlap area; however, there is a lack of material to fill the denudated

area in the overlap zone [39]. Added to that, the effect of heat accumulation from the previous track, which will increase the temperature higher in the overlap zone, causing material vaporization. Conversely, increasing the hatch spacing lowers the overlap area and its adverse effects.

3.4.4. Residual Stress Formation

Residual stresses are elastic stresses that remain within a part after the load is removed. RS risers are confined to three factors; plastic strain, thermal strain, and phase transformation. Since SLM is a pure heat transfer process with the absence of any mechanical loading that would cause plastic deformation, RS arises due to thermal strain and phase transformations. For IN718, no phase transformation was observed, as shown in section 3.5. Although there are three types of RS, the current study is interested in type I, macroscopic stresses, which can be measured using XRD [46, 47]. Since RS are elastic in nature, any stresses that exceed the yield strength will cause plastic deformation, and only the elastic portion will remain and detected by XRD. For the tested coupons, the top surface did not exhibit any plastic deformation or bulging except at the edges where stresses are the highest [48], as indicated by the red arrows in Figure 3-28.

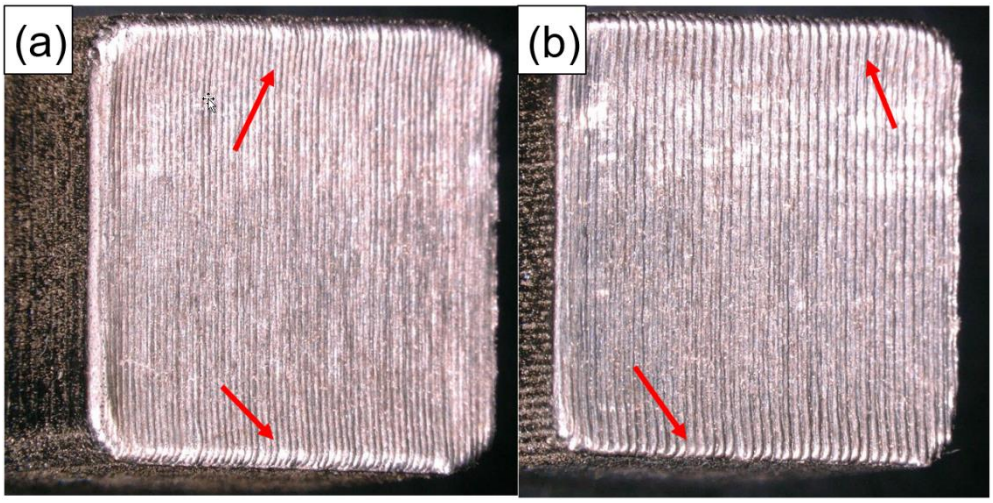

Figure 3-28 Deformation of top surface edges at 320 W, 800 mm/s for a) 0.08 mm b) 0.12 mm

RS formation due to thermal strain occurs due to the varying rates of expansion of the solidified material around the melt pool during heating and the subsequent shrinkage during cooling, which is governed by Eqn. 9 & 10. The thermal stresses generated are affected by the material thermal expansion coefficient CTE (α, $1/℃$) and the temperature gradient ($\Delta T, ℃$). Consequently, the mechanism for RS formation is termed the temperature gradient mechanism (TGM) [49, 50].

$$\varepsilon_{th} = \alpha \Delta T \tag{9}$$

$$\sigma_{th} = \alpha E \Delta T \tag{10}$$

If the exposed tracks are heated so that it expands within the elastic zone, then upon cooling, the part would exhibit zero-stress state. Hence, plastic strain occurs at some point during heating or cooling, causing the strains to be "locked-in" which would induce RS. To explain RS formation and the TGM, an example coupon, shown in

Figure 3-29a, is examined, where the middle of the top surface is being heated and subsequently cooled in a multi-track layer. Since XRD measures in-plane stress, the top surface only of the cube can be examined, Figure 3-29b. As the material is heated and cooled, it is constrained only by the solidified material and not the loose powder. Therefore, to simplify the part, it can be represented as two bars, as shown in Figure 3-29c, connected in parallel to a rigid wall at one end and movable support on the other end, representing the ductility of the connected solidified tracks [51]. The solidified tracks have a total cross-sectional area of A_S, while the exposed track has a cross sectional area of A_T. The temperature at yield point will be adequetly termed the yield temperature (T_y), therefore, since SLM increases the temperature of the material to the melting point, consequently plastic deformation will occur at some point in the solidified material.

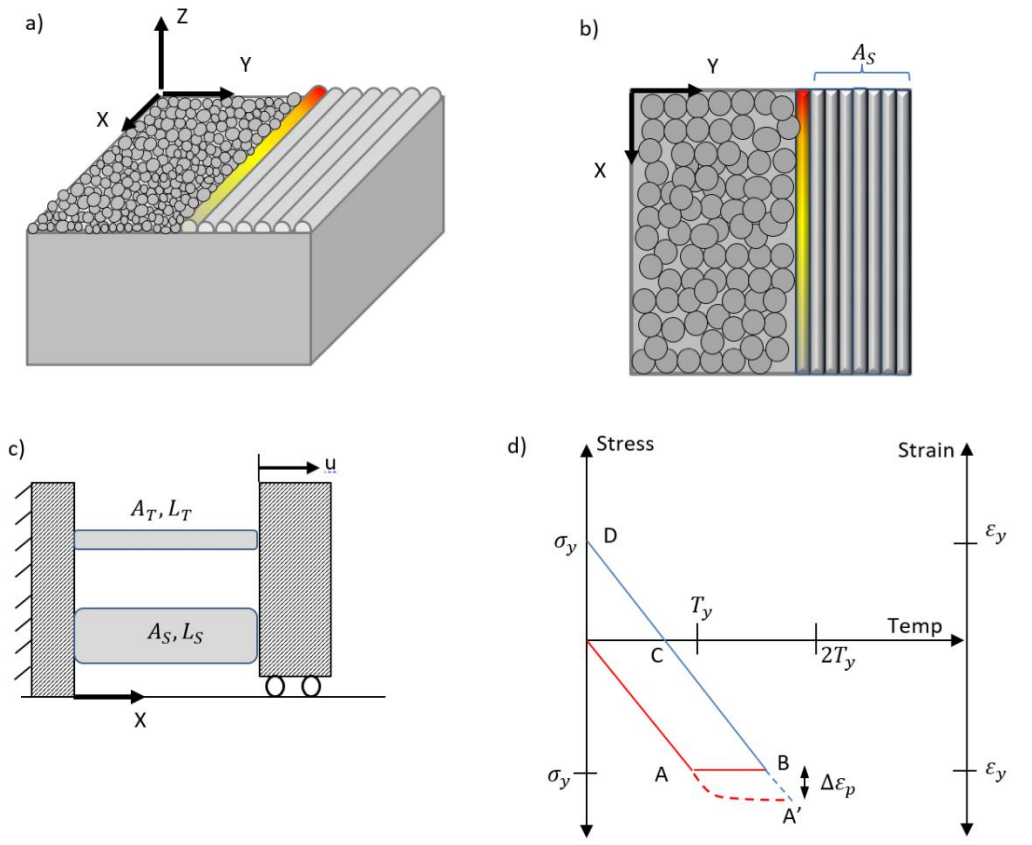

Figure 3-29 The residual stress formation mechanism a) 3D geometry b) Plane Stress approximation c) Bar model analogy d) Stress evolution with temperature

The analysis of the bar model is based on the plot in Figure 3-29d, which traces the evolution of stress with temperature. It can be visualized that during heating, the "track" bar (T) expand, pushing the movable support, similar to the stress exerted by the track on the adjacent solidified tracks. The "solidified" bar (S) resists the motion of the support by inducing compressive stress. During heating, the compressive stress increases with temperature until reaching the yield point, shown as point A on the red line in Figure 3-29d, where the material plastically deforms. Since the bar yields, there will be no further increase in stress, represented as point

B in Figure 3-29d, and the thermal strain is locked in as plastic strain. The incremental change in strain is given in Eqn.11 & 12, where the plastic strain is offset by the thermal strain resulting in a zero change in strain.

$$\Delta\varepsilon = \Delta\varepsilon_p + \Delta\varepsilon_{th} = 0 \tag{11}$$

$$\Delta\varepsilon_{p1} = -\Delta\varepsilon_{th} = -\alpha(T_{max} - T_y) \tag{12}$$

As the bar "T" cools down with its temperature dropping by T_y, during solidification of the track, the shrinkage strain is reduced by $(-\alpha T_y)$ reaching a point of zero stress, represented as point C in Figure 3-29d. The bar "T" cools down further, pulling on the moving support and bar "S" with a displacement Δu, where the bars deform elastically from point C onwards to point D in Figure 3-29d. The final total strains and stresses, presented in Eqn. 13 & 14, for bar "T" consist of elastic and thermal strain as it cools down to initial temperature.

$$\varepsilon = \frac{A_S}{A_T + A_S}\alpha(T_{max} - T_y) \tag{13}$$

$$\sigma_{RS} = \frac{A_S}{A_T + A_S}\alpha E(T_{max} - T_y) \tag{14}$$

Although the thermal strain is the mechanism behind the development of stresses in the material, it is the plastic strain that locks in the residual stresses because as the part cools down back to the initial temperature, there will be no thermal strain due to zero temperature gradient. The bar model is a simple one-dimensional explanation of the formation of RS; however, in reality, the material expands and contracts in all three directions, hence inducing plastic strain in all three directions,

which add up to form the final RS profile. Applying Eqn. 14 in the vertical direction would indicate that the higher the building height (A_S), the higher the tensile RS, which agrees with the findings in the literature [50, 52].

By examining the surface RS in section 3.4, it is found that all process parameters induced tensile residual stresses with varying magnitudes. Generally, the surface RS increased with increasing the scan speed from 600 mm/s to 800 mm/s and then decreased as the speed reached 1000 mm/s; however, in other instances, this trend was flipped. The formation of RS, as discussed earlier and shown in Eqn.14, is mainly controlled by three factors, the coefficient of thermal expansion, the modulus of elasticity, and the temperature difference. The effect of temperature difference is manifested in the size of the melt pool and the surrounding heat affected zone (HAZ). Bigger melt pools cause a higher shrinkage, and the bigger HAZ means a large volume of solidifying material resisting the shrinkage and inducing higher RS. It is worth noting that there is a fourth factor that could affect the generation of RS, which is the cooling rate, being highly important due to the typically rapid solidification nature of SLM resulting in cooling rates in the range of $10^5 - 10^6\ K/s$ [53, 54]. Although there is no literature on the effect of cooling rate on the magnitude of RS, it was reported that in casting and quenching, despite the huge difference in cooling rates, increasing the cooling lead to an increase in RS [55]. Using the Rosenthal point source model [56] to calculate the temperature distribution for three different speeds, analytically, can help visualize the opposing effects of scan speed, as shown in Figure 3-30. As the speed increases, the melt

pool becomes thinner and smaller in volume, which, therefore, could decrease the magnitude of RS. Conversely, it is opposed by the increase in the cooling rate, which increases the magnitude of RS [45]. Although the Rosenthal model is widely used in the literature, it does not take into consideration the change of thermo-physical properties of materials with temperature, and it assumes a point heat source instead of an actual Gaussian distribution of laser intensity. Moreover, there is the effect of hatch spacing, which will affect the temperature, profiles and cooling rate due to the cyclic heating and cooling in multi-track exposure. The prediction of thermal history and cooling rates in the multi-track multi-layer problem is quite difficult to predict. Hence, it will require numerical modeling to provide an insight into the temperature profile and includes the thermo-fluid effects that occur within the meltpool, thus affecting the final temperature profile.

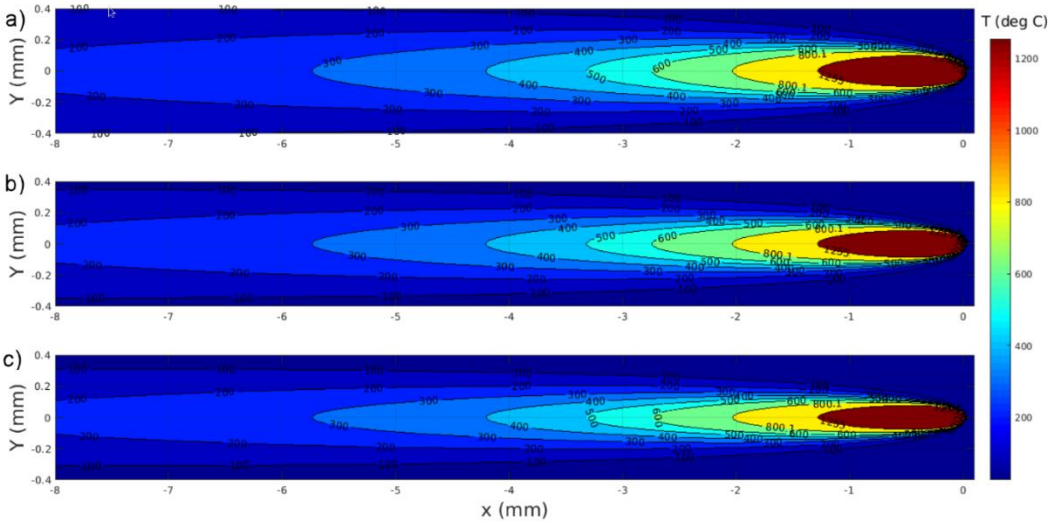

Figure 3-30 Temperature contours predicted using Rosenthal model for a) 600 mm/s b) 800 mm/s c)1000 mm/s

The modulus of elasticity and CTE can also affect RS. The modulus of elasticity could vary due to the anisotropic behavior due to the different grain structures. Additionally, the CTE changes with the change in chemical composition [57, 58] due to the possible vaporization or the concentration increase of some alloying elements, as shown in Table 3-6. Increasing the percentage of Fe, Mn, and Cr leads to an increase in CTE while increasing Al, Ti, and Mo percentage causes a decrease in CTE [57]. Based on the results in Table 3-6, it is shown that at a power of 220 W and hatch of 0.12 mm, increasing the scan speed from 600 mm/s to 800 mm/s resulted in a reduction in Fe and Cr percentages, possible leading to a decrease in CTE. Moreover, increasing the speed even further resulted in a drop in Fe and Cr concentrations and an increase in Al and Mn concentrations, which will decrease the CTE. The combination of lower CTE and smaller melt pool/ HAZ was more dominant than the increase in cooling rate, causing a decrease in RS with increasing scan speed. Consequently, further investigations are required to measure the CTE and modulus of elasticity for different process parameters to determine the effect of their variation on RS; however, this is out of the scope of the current study.

3.4.5. Melt pool Microstructure Formation

A comparison of the melt pool morphology between single tracks and multi-tracks/multi-layers showed a significant increase in melt pool width and depth. The increase is due to the cyclic temperature history of the solidified tracks due to the laser multi-pass. The added heat causes the melt pool to increase in volume, which is in agreement with the literature [59, 60]. The added heat reduces the possibility

of balling formation by increasing the melt volume and wettability, and the possibility of remelting any formed balls during the previous solidified tracks [6, 61].

The grain structure, shown in Figure 3-16, and Figure 3-17 is mainly a mixed structure except for a scan speed of 800 mm/s, which resulted in columnar grains. The grain structure is controlled by two factors the solidification front velocity (R) and the thermal gradient (G). Coupled with a solidification map shown in Figure 3-31, the solidified structure can be predicted. For example, at a scan speed of 1000 mm/s and at the centerline of the melt pool, which corresponds to the maximum solidification rate equaling the scan speed [6], the grain structure is mixed. By using the solidification map at R=1 m/s, the temperature gradient is found to be between 10^5 and $3x10^5$. At a scan speed of 800 mm/s, the input energy was higher, and consequently, the temperature gradient was steeper compared to 1000 mm/s, which resulted in a columnar grain structure. However, at the lower speed of 600 mm/s, the grain structure formed is mixed with columnar and equiaxed structure despite the possibly higher temperature gradient. This structure could be attributed to the formation of a higher percentage of γ'', as reported in the literature [27], which inhibits the epitaxial grain growth to form columnar structures. Moreover, the higher input energy at the lower scan speed could be sufficient to overcome the activation energy barrier required for nucleation of a new phase, thus prompting the equiaxed grain structure. The formation of a mixed grain structure reduces the anisotropy associated with the columnar grains, thus possibly improving the

mechanical properties of the as-built parts.Finally, a numerical model is required to better predict the temperature gradients, solidification rate and melt pool morphology which affects the direction of solid-liquid solidification front compared to the scan speed.

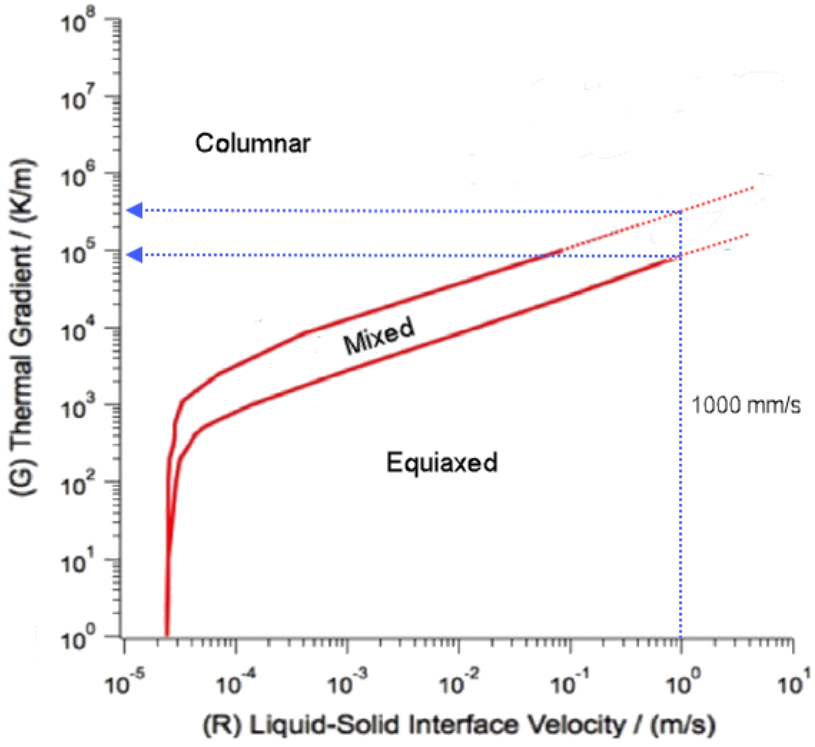

Figure 3-31 Solidification map for grain structure in IN718 [6]

The microstructure within the melt pool exhibited a fine columnar dendritic microstructure for different process parameters, as shown in Figure 3-18. During solidification, a competitive growth occurs between dendrites with different crystallographic orientations. The dendrites that are aligned with the highest temperature gradient direction (favorable heat flow) will outgrow the other directions. In SLM, it was found that dendrites growth favors crystallographic

orientation <001>, which corresponds to the build direction, as shown in Figure 3-20. However, the favorable heat flow direction changed from being parallel to the build direction to an inclined direction (perpendicular to melt pool boundary) as the hatch spacing increased due to the reduction in the input heat, as shown in Figure 3-18. The formation of columnar dendrites in IN718 is also governed by the temperature gradient (G) and the solidification rate (R). The G/R determines the type of in-grain microstructure, either equiaxed, columnar dendritic, or cellular. On the other hand, G*R, which is termed the cooling rate, determines the size of the microstructure, either coarse or fine [62]. Since SLM is a rapid solidification process with high cooling rates of 10^6 K/s [45, 53], the resulting microstructure is fine.

3.5. Conclusion

This study adds to the understanding of the process-structure-property in selective laser melting of Inconel 718. First, the effect of the two main process parameters, laser power and scan speed, was examined to produce stable continuous single tracks. Second, the study further showed the shortcomings of the use of single tracks as the sole predictor of the quality of parts.

The study further examined the gap on the effect of a wide range of process parameters on relative density, surface roughness and surface residual stresses simultaneously. The measured properties were used to plot process maps that are crucial to select the best process parameters combinations to achieve the optimum

part properties. It was found that there is no single process parameter combination that will result in optimized values for all three properties together. However, since surface residual stresses values were all found to be tensile, and since density and surface roughness are the main stress concentrators/crack initiators in fatigue failure, they outweighed surface residual stresses in priority. For this scenario, a laser power of 320 W, a scan speed of 600 mm/s, and a hatch spacing of 0.12 mm resulted in a relative density of 99.2%, a relatively low surface roughness of 3.5 μm. On the other hand, if the selection is made based on one property, density, as it is the cause for nucleation and growth in tensile testing, then a 270 W, 700 mm/s and 0.1 mm hatch spacing are the most suitable parameters. Finally, it was shown that the formation of columnar grains, which is widely reported in the literature, was only attained at a scan speed of 800 mm/s. For all other scan speeds, a mixed grain structure is formed, which can help lower the expected anisotropy in mechanical properties.

References

[1] F. Caiazzo, V. Alfieri, G. Corrado, and P. Argenio, "Laser powder-bed fusion of Inconel 718 to manufacture turbine blades," *The International Journal of Advanced Manufacturing Technology,* vol. 93, pp. 4023-4031, 2017.

[2] Z. Lu, J. Cao, H. Jing, T. Liu, F. Lu, D. Wang, *et al.*, "Review of main manufacturing processes of complex hollow turbine blades: This paper critically reviews conventional and advanced technologies used for manufacturing hollow turbine blades," *Virtual and Physical Prototyping,* vol. 8, pp. 87-95, 2013.

[3] D. F. Paulonis and J. J. Schirra, "Alloy 718 at Pratt & Whitney-Historical perspective and future challenges," *Superalloys,* vol. 718, pp. 13-23, 2001.

[4] D. Dudzinski, A. Devillez, A. Moufki, D. Larrouquere, V. Zerrouki, and J. Vigneau, "A review of developments towards dry and high speed machining of Inconel 718

alloy," *International Journal of Machine Tools and Manufacture,* vol. 44, pp. 439-456, 2004.

[5] E. Ezugwu, Z. Wang, and A. Machado, "The machinability of nickel-based alloys: a review," *Journal of Materials Processing Technology,* vol. 86, pp. 1-16, 1999.

[6] T. DebRoy, H. Wei, J. Zuback, T. Mukherjee, J. Elmer, J. Milewski, *et al.*, "Additive manufacturing of metallic components–process, structure and properties," *Progress in Materials Science,* vol. 92, pp. 112-224, 2018.

[7] X. Wang, X. Gong, and K. Chou, "Review on powder-bed laser additive manufacturing of Inconel 718 parts," *Proceedings of the Institution of Mechanical Engineers, Part B: Journal of Engineering Manufacture,* vol. 231, pp. 1890-1903, 2017.

[8] A. AB, "Case study: additive manufacturing of aerospace brackets," *Advanced Materials & Processes,* vol. 19, 2013.

[9] P. Kumar, J. Farah, J. Akram, C. Teng, J. Ginn, and M. Misra, "Influence of laser processing parameters on porosity in Inconel 718 during additive manufacturing," *The International Journal of Advanced Manufacturing Technology,* vol. 103, pp. 1497-1507, 2019.

[10] J.-P. Choi, G.-H. Shin, S. Yang, D.-Y. Yang, J.-S. Lee, M. Brochu, *et al.*, "Densification and microstructural investigation of Inconel 718 parts fabricated by selective laser melting," *Powder Technology,* vol. 310, pp. 60-66, 2017.

[11] K. Moussaoui, W. Rubio, M. Mousseigne, T. Sultan, and F. Rezai, "Effects of Selective Laser Melting additive manufacturing parameters of Inconel 718 on porosity, microstructure and mechanical properties," *Materials Science and Engineering: A,* vol. 735, pp. 182-190, 2018.

[12] Y. Lu, S. Wu, Y. Gan, T. Huang, C. Yang, L. Junjie, *et al.*, "Study on the microstructure, mechanical property and residual stress of SLM Inconel-718 alloy manufactured by differing island scanning strategy," *Optics & Laser Technology,* vol. 75, pp. 197-206, 2015.

[13] D. S. Watring, K. C. Carter, D. Crouse, B. Raeymaekers, and A. D. Spear, "Mechanisms driving high-cycle fatigue life of as-built Inconel 718 processed by laser powder bed fusion," *Materials Science and Engineering: A,* vol. 761, p. 137993, 2019.

[14] C. Pei, D. Shi, H. Yuan, and H. Li, "Assessment of mechanical properties and fatigue performance of a selective laser melted nickel-base superalloy Inconel 718," *Materials Science and Engineering: A,* vol. 759, pp. 278-287, 2019.

[15] J. Schneider, B. Lund, and M. Fullen, "Effect of heat treatment variations on the mechanical properties of Inconel 718 selective laser melted specimens," *Additive Manufacturing,* vol. 21, pp. 248-254, 2018.

[16] R. Konečná, L. Kunz, G. Nicoletto, and A. Bača, "Long fatigue crack growth in Inconel 718 produced by selective laser melting," *International Journal of Fatigue,* vol. 92, pp. 499-506, 2016.

[17] L. Scime and J. Beuth, "Melt pool geometry and morphology variability for the Inconel 718 alloy in a laser powder bed fusion additive manufacturing process," *Additive Manufacturing,* vol. 29, p. 100830, 2019.

[18] M. Sadowski, L. Ladani, W. Brindley, and J. Romano, "Optimizing quality of additively manufactured Inconel 718 using powder bed laser melting process," *Additive Manufacturing,* vol. 11, pp. 60-70, 2016.

[19] Z. Wang, K. Guan, M. Gao, X. Li, X. Chen, and X. Zeng, "The microstructure and mechanical properties of deposited-IN718 by selective laser melting," *Journal of Alloys and Compounds,* vol. 513, pp. 518-523, 2012.

[20] E. Chlebus, K. Gruber, B. Kuźnicka, J. Kurzac, and T. Kurzynowski, "Effect of heat treatment on the microstructure and mechanical properties of Inconel 718 processed by selective laser melting," *Materials Science and Engineering: A,* vol. 639, pp. 647-655, 2015.

[21] "ASTM E8 / E8M-21, Standard Test Methods for Tension Testing of Metallic Materials," ed. West Conshohocken, PA: ASTM International, 2021.

[22] Z. Zhao, L. Li, L. Tan, P. Bai, J. Li, L. Wu, *et al.*, "Simulation of Stress Field during the Selective Laser Melting Process of the Nickel-Based Superalloy, GH4169," *Materials,* vol. 11, p. 1525, 2018.

[23] A. Spierings and G. Levy, "Comparison of density of stainless steel 316L parts produced with selective laser melting using different powder grades," in *Proceedings of the Annual International Solid Freeform Fabrication Symposium*, 2009, pp. 342-353.

[24] A. B. Spierings, M. Schneider, and R. Eggenberger, "Comparison of density measurement techniques for additive manufactured metallic parts," *Rapid Prototyping Journal,* 2011.

[25] N. A. Kistler, "Characterization of inconel 718 fabricated through powder bed fusion additive manufacturing," Bachelor's Thesis, The Pennsylvania State University, University Park, PA, USA, 2015.

[26] L. K. Gillespie, *Design for Advanced Manufacturing: Technologies and Processes*: McGraw-Hill Education, 2017.

[27] K. Amato, S. Gaytan, L. Murr, E. Martinez, P. Shindo, J. Hernandez, *et al.*, "Microstructures and mechanical behavior of Inconel 718 fabricated by selective laser melting," *Acta Materialia,* vol. 60, pp. 2229-2239, 2012.

[28] J. Strößner, M. Terock, and U. Glatzel, "Mechanical and microstructural investigation of nickel-based superalloy IN718 manufactured by selective laser melting (SLM)," *Advanced Engineering Materials,* vol. 17, pp. 1099-1105, 2015.

[29] T. Heeling, M. Cloots, and K. Wegener, "Melt pool simulation for the evaluation of process parameters in selective laser melting," *Additive Manufacturing,* vol. 14, pp. 116-125, 2017.

[30] S. Katayama, *Handbook of laser welding technologies*: Elsevier, 2013.

[31] "ASTM E466-21, Standard Practice for Conducting Force Controlled Constant Amplitude Axial Fatigue Tests of Metallic Materials," ed. West Conshohocken, PA: ASTM International, 2021.

[32] C. Körner, A. Bauereiß, and E. Attar, "Fundamental consolidation mechanisms during selective beam melting of powders," *Modelling and Simulation in Materials Science and Engineering,* vol. 21, p. 085011, 2013.

[33] Z. Xiao, C. Chen, H. Zhu, Z. Hu, B. Nagarajan, L. Guo, *et al.*, "Study of residual stress in selective laser melting of Ti6Al4V," *Materials & Design,* vol. 193, p. 108846, 2020.

[34] D. Bovand, M. Allazadeh, M. Yousefpour, and S. Rasouli, "Suggesting a full two level experimental factorial model with three factors to optimize Ti-HA biocomposite properties," *Journal of Multidisciplinary Engineering Science and Technology,* vol. 5, pp. 9252-9258, 2018.

[35] C. Han, Y. Li, Q. Wang, D. Cai, Q. Wei, L. Yang, *et al.*, "Titanium/hydroxyapatite (Ti/HA) gradient materials with quasi-continuous ratios fabricated by SLM: material interface and fracture toughness," *Materials & Design,* vol. 141, pp. 256-266, 2018.

[36] H. Attar, K. G. Prashanth, L.-C. Zhang, M. Calin, I. V. Okulov, S. Scudino, *et al.*, "Effect of powder particle shape on the properties of in situ Ti–TiB composite materials produced by selective laser melting," *Journal of Materials Science & Technology,* vol. 31, pp. 1001-1005, 2015.

[37] J. R. Lawrence, *Advances in laser materials processing: technology, research and applications*: Woodhead Publishing, 2017.

[38] J. Dilip, S. Zhang, C. Teng, K. Zeng, C. Robinson, D. Pal, *et al.*, "Influence of processing parameters on the evolution of melt pool, porosity, and microstructures in Ti-6Al-4V alloy parts fabricated by selective laser melting," *Progress in Additive Manufacturing,* vol. 2, pp. 157-167, 2017.

[39] V. Authors, "ASM Handbook Volume 5: Surface Engineering," ed: ASM International, Materials Park, Ohio, USA, 1994.

[40] E. Maleki, O. Unal, M. Guagliano, and S. Bagherifard, "The effects of shot peening, laser shock peening and ultrasonic nanocrystal surface modification on the fatigue

strength of Inconel 718," *Materials Science and Engineering: A,* vol. 810, p. 141029, 2021.

[41] D. Lesyk, V. Dzhemelinskyi, S. Martinez, B. Mordyuk, and A. Lamikiz, "Surface Shot Peening Post-processing of Inconel 718 Alloy Parts Printed by Laser Powder Bed Fusion Additive Manufacturing," *Journal of Materials Engineering and Performance,* vol. 30, pp. 6982-6995, 2021.

[42] Z. Chen, Z. Wei, P. Wei, S. Chen, B. Lu, J. Du, *et al.*, "Experimental research on selective laser melting AlSi10Mg alloys: Process, densification and performance," *Journal of Materials Engineering and Performance,* vol. 26, pp. 5897-5905, 2017.

[43] M. Yakout, M. Elbestawi, and S. C. Veldhuis, "Density and mechanical properties in selective laser melting of Invar 36 and stainless steel 316L," *Journal of Materials Processing Technology,* vol. 266, pp. 397-420, 2019.

[44] V. P. Sabelkin, G. R. Cobb, T. E. Shelton, M. N. Hartsfield, D. J. Newell, R. P. O'Hara, *et al.*, "Mitigation of anisotropic fatigue in nickel alloy 718 manufactured via selective laser melting," *Materials & Design,* vol. 182, p. 108095, 2019.

[45] S. Ghosh, L. Ma, L. E. Levine, R. E. Ricker, M. R. Stoudt, J. C. Heigel, *et al.*, "Single-track melt-pool measurements and microstructures in inconel 625," *Jom,* vol. 70, pp. 1011-1016, 2018.

[46] P. J. Withers and H. Bhadeshia, "Residual stress. Part 1–measurement techniques," *Materials science and Technology,* vol. 17, pp. 355-365, 2001.

[47] P. J. Withers and H. Bhadeshia, "Residual stress. Part 2–Nature and origins," *Materials science and technology,* vol. 17, pp. 366-375, 2001.

[48] D. T. Ardi, L. Guowei, N. Maharjan, B. Mutiargo, S. H. Leng, and R. Srinivasan, "Effects of post-processing route on fatigue performance of laser powder bed fusion Inconel 718," *Additive Manufacturing,* vol. 36, p. 101442, 2020.

[49] J.-P. Kruth, J. Deckers, E. Yasa, and R. Wauthlé, "Assessing and comparing influencing factors of residual stresses in selective laser melting using a novel analysis method," *Proceedings of the institution of mechanical engineers, Part B: Journal of Engineering Manufacture,* vol. 226, pp. 980-991, 2012.

[50] P. Mercelis and J.-P. Kruth, "Residual stresses in selective laser sintering and selective laser melting," *Rapid Prototyping Journal,* vol. 12, pp. 254-265, 2006.

[51] Y. Ueda, H. Murakawa, and N. Ma, *Welding deformation and residual stress prevention*: Elsevier, 2012.

[52] Y. Liu, Y. Yang, and D. Wang, "A study on the residual stress during selective laser melting (SLM) of metallic powder," *The International Journal of Advanced Manufacturing Technology,* vol. 87, pp. 647-656, 2016.

[53] Z. Gan, Y. Lian, S. E. Lin, K. K. Jones, W. K. Liu, and G. J. Wagner, "Benchmark study of thermal behavior, surface topography, and dendritic microstructure in selective laser melting of Inconel 625," *Integrating Materials and Manufacturing Innovation*, vol. 8, pp. 178-193, 2019.

[54] J. C. Heigel and B. M. Lane, "The effect of powder on cooling rate and melt pool length measurements using in situ thermographic techniques," in *Solid freeform fabrication symposium*, 2017.

[55] G. E. Totten, *Handbook of residual stress and deformation of steel*: ASM international, 2002.

[56] S. Bontha, "The effect of process variables on microstructure in laser-deposited materials," 2006.

[57] F. Hull, S. Hwang, J. Wells, and R. Jaffee, "Effect of composition on thermal expansion of alloys used in power generation," *Journal of materials engineering*, vol. 9, pp. 81-92, 1987.

[58] M. Yakout, M. Elbestawi, and S. C. Veldhuis, "A study of thermal expansion coefficients and microstructure during selective laser melting of Invar 36 and stainless steel 316L," *Additive Manufacturing*, vol. 24, pp. 405-418, 2018.

[59] M. Xia, D. Gu, G. Yu, D. Dai, H. Chen, and Q. Shi, "Influence of hatch spacing on heat and mass transfer, thermodynamics and laser processability during additive manufacturing of Inconel 718 alloy," *International Journal of Machine Tools and Manufacture*, vol. 109, pp. 147-157, 2016.

[60] A. Hussein, L. Hao, C. Yan, and R. Everson, "Finite element simulation of the temperature and stress fields in single layers built without-support in selective laser melting," *Materials & Design*, vol. 52, pp. 638-647, 2013.

[61] R. Li, J. Liu, Y. Shi, L. Wang, and W. Jiang, "Balling behavior of stainless steel and nickel powder during selective laser melting process," *The International Journal of Advanced Manufacturing Technology*, vol. 59, pp. 1025-1035, 2012.

[62] S. Kou, "Welding metallurgy," *New Jersey, USA*, pp. 431-446, 2003.

Chapter 4

Multi-Scale Modeling of Residual Stresses Evolution in Laser Powder Bed Fusion of Inconel 625

Complete Citation:

Balbaa, Mohamed, and Mohamed Elbestawi. "Multi-Scale Modeling of Residual Stresses Evolution in Laser Powder Bed Fusion of Inconel 625." *Journal of Manufacturing and Materials Processing* 6.1 (2022): 2

Copyright:

Relative Contributions:

M. A. Balbaa: Created the numerical models, performed validation experiments, analysis, and data interpretation; wrote the first draft

M. A. Elbestawi: Revised and edited the manuscript

Acknowledgment:

The authors would like to thank Mr. H. Rezaeifar for his help with the temperature measurements.

Abstract:

Laser powder bed fusion exhibits many advantages for manufacturing complex geometries from hard to machine alloys such as IN625. However, a major drawback is the formation of high tensile residual stresses, and the complex relationship between the process parameters and the residual stresses is not fully investigated. The current study presents multi-scale models to examine the variation of process parameters on melt pool dimensions, cyclic temperature evolutions, cooling rate, and cyclic stress generation and how they affect the stress end state. In addition, the effect of the same energy density, which is often overlooked, on the generated residual stresses is investigated. Multi-level validation is performed based on melt pool dimensions, temperature measurements with a 2-color pyrometer, and, finally, in-depth residual stress measurement. The results show that scan speed has the strongest effect on residual stresses, followed by laser power and hatch spacing. The results are explained in light of the non-linear temperature evolution, temperature gradient, and cooling rate during the laser exposure, the cooling time, and the rate during the recoating time.

Keywords:

Inconel 625, Laser powder bed fusion, Multi-scale modeling, Temperature measurement, Residual stresses

4.1. Introduction

Laser powder bed fusion (LPBF) [1] is an additive manufacturing technology that has gained momentum in recent years due to design freedom to manufacture highly complex and customizable geometries along with its capability of processing metals and ceramics [2]. These advantages make LPBF desirable for many industries where it can be used, for example, to manufacture a conformally cooled mold for the tooling industry [3] or light-weighting or to reduce the number of assembled parts which makes it desirable for the automotive and aerospace industries [4-6]. Despite the many advantages of LPBF, it still has a few drawbacks that need to be overcome, such as porosity, dimensional accuracy, high surface roughness, and tensile residual stresses (RS) [7, 8]. The first three drawbacks have been extensively studied experimentally and controlled by optimizing the process parameters [9-12]. In addition, dimensional accuracy and surface roughness were also rectified by post-machining [2, 13, 14]. However, the surface and near-surface RS was mostly tensile regardless of the process parameters employed [15-18], which require post-processing such as stress relieving or peening to negate these undesirable stresses. Tensile RS is formed in LPBF due to the high-temperature gradient generated due to the large heat input under the laser beam, between the solidifying material and surrounding cool powder and substrate [19]. Therefore, to reduce the undesirable tensile RS, the effects of process parameters on the thermal history and temperature gradients on its formation mechanism need to be understood.

Modeling offers insight into the thermal cycles, temperature gradients, and cooling rates (CR) during LPBF, affecting stress formation and microstructure. In addition, predicting melt pool dimensions can determine if sufficient overlap between laser tracks will happen as it affects the resulting density. A vast array of work is done on the modeling of LPBF targeting different scales or modeling approaches, ranging from melt pool scale to part scale models. The first approach is modeling single tracks in LPBF, which can be modeled using Finite Element (FE) or computational fluid dynamics (CFD). For FE models, the studies aimed at predicting melt pool dimensions and temperature gradients along the melt pool width and length [20-24]. CFD models also simulate single tracks but with the added benefit of including the fluid dynamics effects such as the Marangoni effect, which drives the convection inside the melt pool, affecting the melt pool shape and CR that controls the final microstructure [25-28]. Both models were extended to simulate the effect of adjacent tracks on melt pool dimensions and temperature gradients; however, beyond that, there is little focus on the impact of process parameters [29-31].

Moreover, these models overlooked the effect of the temperature gradients, CR, and process parameters on stress formation during solidification. The only studies that have addressed this particular area were focused more on the effect of scan strategies on RS [32, 33]. The second approach used was part scale simulation of part deformation and showed an agreement between the predicted and the experimentally measured deformations or RS [34-36].

Despite the varying degrees of success of each of the previously mentioned modeling approaches, there are a few shortcomings or challenges regarding FE modeling of the LPBF process [37, 38] that need to be addressed. The first issue is the proper representation of the powder layer and its apparent thermal conductivity. Several studies assume the powder thermal conductivity as a fraction of the bulk material properties using the porosity ratio of the powder layer [20, 24, 39, 40]. However, by examining a unit volume of the powder layer, it is found that it comprises solid powder particles and the voids between particles filled with inert gas. Hence the heat transfer coefficient consists of the solid thermal conductivity, the inert stagnant gas thermal conductivity, and the radiation between the powder particles. The second issue is applying a Gaussian surface heat flux to represent the laser beam heat input, adopted from welding modeling [32, 41-43]. The problem with the surface heat flux is that it neglects the optical penetration of the incident laser through the voids between the powder particles and its consequent decay.

Conversely, a volume heat source that considers the powder layer's laser penetration relative to the powder size is essential to represent the heat input accurately. The third issue is the incapability of the FE models to include the Marangoni effects [43], which is important as convection is the dominant heat transfer mode inside the meltpool and will, in return, affect the melt pool dimensions and temperature. The fourth issue is the lack of experimentally measured laser absorptivity, which is important as the powder bed absorbs a portion of the incident laser beam energy. Several studies either assume the value for the

laser absorptivity or use some analytical models to calculate a more accurate value [44, 45]. In addition, there is a lack of experimental temperature measurements for validation of the numerically predicted temperature [43, 45].

The current work addresses the gaps in the literature regarding the modeling of LPBF of Inconel 625 using the following:

- Multi-scale modeling, including single track, multi-track layer, and part scale models
- Comparing different volumetric heat sources with optical penetration
- A proper powder material model is used to calculate the temperature-dependent thermal conductivity incorporating the solid conductivity, the nitrogen gas conductivity, and the inter-particle radiation
- The Marangoni effects inside the melt pool by calculating the Marangoni number and its equivalent thermal conductivity
- Validation of the melt pool dimensions for single tracks with the literature
- Experimental temperature measurement using a 2-color pyrometer to validate the temperature from the multi-track layer model.
- In-depth RS profile measurement using XRD to validate the part scale model RS predictions
- Study the effect of process parameters on thermal history, temperature gradients, CR, and their subsequent impact on the formation of RS.

4.2. Model setup

4.2.1. Transient thermal model

Heat transfer in powder bed fusion is governed by heat conduction defined by the transient heat transfer energy balance equation, Equation (1)

$$k\left(\frac{\partial^2 T}{\partial x^2}\right) + k\left(\frac{\partial^2 T}{\partial y^2}\right) + k\left(\frac{\partial^2 T}{\partial z^2}\right) + \dot{q} = \rho C \frac{\partial T}{\partial t} \quad (1)$$

Where:

k : Thermal conductivity of the powder bed (W/m.K)

T: Temperature (K)

$\dot{q}$: Energy generated per unit volume (W/m^3)

ρ: Density of the powder bed (kg/m^3)

C: Specific heat capacity (J/kg.K)

t: time (s)

The initial condition for Equation (1) is set as the powder bed preheat temperature of 80 ˚C and represented by Equation (2)

$$T(x, y, z, t_0) = T_{preheat} \quad (2)$$

4.2.2. Boundary conditions

Heat flux boundary condition

As the laser beam irradiates the surface of the powder bed, heat is added into the powder, which can be represented as a specified heat flux boundary condition (BC) and defined using the Fourier heat flux equation given in Equation (3)

$$Q_{laser} = Q_{in} = k\nabla T(x, y, z) \tag{3}$$

Convection boundary condition

A constant nitrogen gas flow is pumped into the build chamber to reduce the oxygen percentage and carry away any spatter and ejected particles from the melt pool. The gas flow over the powder bed surface draws away heat due to forced convection, which is calculated using Equation (4)

$$Q_{convection} = h_o\left(T_{pb} - T_\infty\right) \tag{4}$$

Where:

h_o: overall heat transfer coefficient due to forced convection (W/m^{2}K)

T_{pb}: Powder bed surface temperature

T_∞: Ambient temperature (assumed 300 K)

The heat transfer coefficient due to forced convection is calculated similarly to the flow over a flat plate. Therefore, h will depend on the speed of the inert gas, Equation (6) & Equation (7), and all fluid flow properties are to be calculated at film temperature [32, 46]. The film temperature is the average temperature between

the powder bed surface temperature and the gas flow temperature, Equation (5). The EOS M280 machine used to perform the experiments has an inert gas velocity of 3 m/s.

$$T_f = \frac{T_{pb}+T_\infty}{2} \tag{5}$$

$$h = \frac{k_g}{W}\frac{0.6776\ Re^{1/2}Pr^{1/3}}{[1+\frac{Pr}{0.0207}]} \tag{6}$$

$$Re = \frac{U_\infty W}{\gamma_g} \tag{7}$$

Where:

T_f: The film temperature (K)

k_g: Gas thermal conductivity (W/m.K)

W: Width of the powder bed (250 mm for EOS M280)

Re: Reynolds number calculated at the film temperature

Pr: Prandtl number

U_∞: Inert gas velocity (m/s)

γ_g: Kinematic viscosity (m^2/s)

Radiation boundary condition

Another source of heat loss is radiation heat transfer to the surroundings, which is defined using Equation (8)

$$Q_{radiation} = e\sigma_s({T_{pb}}^4 - {T_\infty}^4) \tag{8}$$

Where:

σ_s: Stefan-Boltzmann constant (W/m^2.K^4)

e: Emissivity of the powder bed

Since the powder bed is porous, the bulk material properties cannot be used. Therefore an analytical model is used to calculate the emissivity of the powder bed [47, 48], represented by Equations (9-11).

$$e = A_H\varepsilon_H + (1 - A_H)e_s \tag{9}$$

$$A_H = \frac{0.908\varphi^2}{1.908\varphi^2 - 2\varphi + 1} \tag{10}$$

$$e_H = \frac{\varepsilon_s[2 + 3.082\left(\frac{1-\varphi}{\varphi}\right)^2]}{\varepsilon_s\left[1 + 3.082\left(\frac{1-\varphi}{\varphi}\right)^2\right] - 1} \tag{11}$$

Where:

A_H: Porous area fraction of powder surface

φ: Powder bed porosity ratio

e_s: Emissivity of bulk material

The powder bed porosity depends on the recoating system and powder flowability [9]. However, it difficult to precisely measure the powder bed porosity and is usually assumed between 40% to 60%.

4.2.3. Material model

In PBF, the powder is heated consistently up to melting. Therefore, the material model is governed mainly by the temperature-dependent thermophysical properties of the powder. An analytical model developed by Sih and Barlow [47] is used to calculate the thermal conductivity of the powder bed based on the bulk material thermal conductivity and powder bed porosity ratio. The model, Equation (12), considers the radiation between particles, Equation (13), and the presence of stagnant inert gas in the voids between the powder particles.

$$k_{pb} = k_g[(1-\sqrt{1-\varphi})\left(1+\varphi\frac{k_r}{k_g}\right)+\sqrt{1-\varphi}\,(\frac{2}{1-{k_g}/{k_s}}(\frac{1}{1-{k_g}/{k_s}}ln\frac{k_s}{k_g}-1)+\frac{k_r}{k_g})] \quad (12)$$

Where:

k_{pb}: Powder bed thermal conductivity (W/m.K)

k_g: Inert gas thermal conductivity (temperature-dependent) (W/m.K)

φ : Powder bed porosity ratio

k_s: Thermal conductivity of the bulk material (temperature dependent)

k_r: Equivalent conductivity due to thermal radiation between powder particles

$$k_r = \frac{4\varepsilon\sigma T^3 D_p}{1-0.132\varepsilon} \quad (13)$$

e: Emissivity of the powder (calculated previously)

T: Temperature (K)

D_p: Average diameter of the powder particles (m)

The next two properties to model powder bed thermal behavior are the specific heat capacity and density. A simplistic linear is used based on the porosity of the powder bed

$$C_p = (1-\varphi)C_s \quad (14)$$

$$\rho_p = (1-\varphi)\rho_s \quad (15)$$

The temperature-dependent thermos-physical properties of bulk IN625 were obtained from [49] and the full material properties used are shown in **Error! R eference source not found.**

Table 4-1Thermo-physical properties of IN625

Property		Units	Ref.
Thermal conductivity (k_s)	10.1 - 31.6	W/m.K	[49]
Density (ρ_s)	8453 - 7925	Kg/m3	[49]
Specific heat capacity (C_{ps})	419 - 657	J/kg.K	[49]
Quescient liquid thermal conductivity (k_l)	30.078	W/m.K	[42]
Liquid specific heat capacity (C_{pl})	709.25	J/kg.K	[42]

Solidus temperature (T_s)	1563	K	[42]
Liquidus temperature (T_L)	1623	K	[42]
Boiling temperature (T_b)	3000	K	[42]
Latent heat of fusion (L_f)	290	kJ/kg.K	[42]
Latent heat of vaporization (L_V)	640	kJ/kg.K	[28]
Dynamics viscosity (μ)	7×10^{-3}	Pa.s	[42]
Temperature gradient of surface tension ($d\sigma/dT$)	-1.1×10^{-4}	N.m/K	[28]
Average powder size diameter (D_p)	27	μm	[50]
Powder bed porosity (φ)	0.4	-	-
Emissivity (e)	0.4	-	[42]
Nitrogen thermal conductivity (k_g)	0.02604 - 0.0947	W/m.K	[51]
Ambient temperature (T_∞)	313	K	-

The selection of a suitable material mode is essential to predict temperature history better. Since the primary mode of heat transfer in L-PBF is conduction, as mentioned above, a low thermal conductivity will lead to a high concentration of heat at the center of the melt pool and raise the predicted peak temperature. Employing the powder model shows that the solid thermal conductivity is 20 folds the powder thermal conductivity, as shown in Figure 4-1

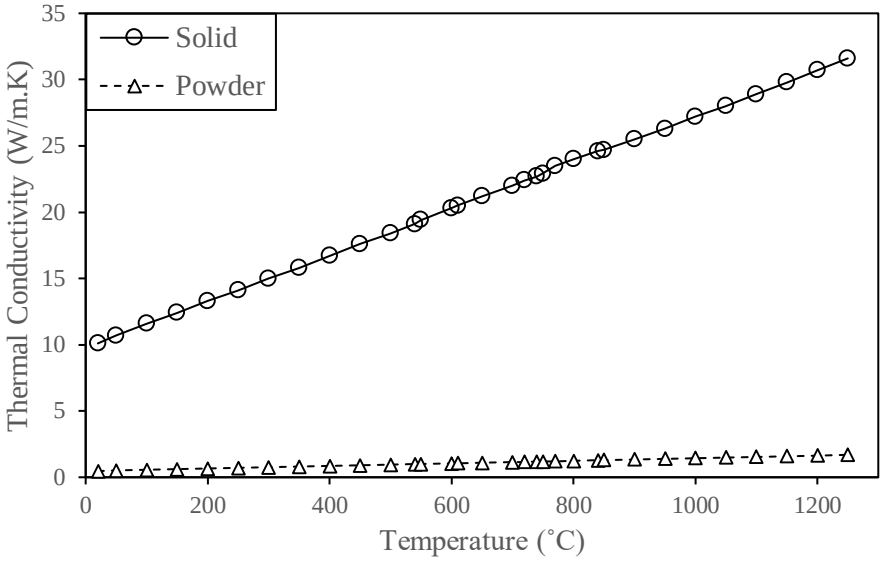

Figure 4-1**.** Thermal conductivity of solid vs. powder IN625

4.2.4. Heat source modeling

A volumetric heat source model is employed to consider the laser beam penetration into the porous powder bed. Three models are chosen for comparison, the Goldak double ellipsoidal model, shown in Equation (16), which was developed for welding [52].

$$Q_v = \frac{6\sqrt{3}A_c P}{abc\pi\sqrt{\pi}} e^{-\left[\frac{3(x-vt)^2}{a^2}+\frac{3(y-h)^2}{b^2}+\frac{3z^2}{c^2}\right]} \quad (16)$$

Where P is the laser power (W), A_c is the absorption coefficient, *x*, *y*, and *z* are the local, *a*, *b*, and *c* are the longitudinal, transverse, and depth dimensions of the heat source, *v* is the laser scan speed (mm/s), *t* is the time (s), and *h* is the hatch spacing (mm). The dimensions *a* and *b* were assumed as the radius of the laser spot, while the depth dimension *c* is set as the melt pool depth determined experimentally.

The second and third heat source models examined are categorized as attenuated volumetric heat sources, based on the assumption that as the laser penetrates the inter-particles voids, it gets scattered and loses its energy at a certain depth. This attenuation depth is called the optical penetration depth (OPD), and its value was measured for pure nickel [53] at different powder particle size distributions (PSD), as shown in **Table** 4-2. However, there are no measured values for OPD in IN625 powders, but since IN625 comprises 58% Ni, the values for pure nickel were used to calculate the OPD using interpolation. The experiments were done using an IN625 powder with a PSD of $-45\ \mu m$ [50], which gives an OPD of $100\ \mu m$.

Table 4-2 Optical penetration depth of pure Ni [53]

Particle size distribution	OPD
$-20\ \mu m$	$20\ \mu m$
$-75\ \mu m$	$200\ \mu m$

The difference between the two attenuated volumetric heat sources is the attenuation profile being either a linear decay model, represented by Equation (17), or an exponential decay model, calculated using Equation (18).

$$Q_v = \frac{2A_c P}{\pi r^2} e^{\left[\frac{-2((x-vt)^2+(y-h)^2)}{r^2}\right]} \times \frac{2}{d}\left(1-\frac{z}{d}\right) \tag{17}$$

$$Q_v = \frac{2A_c P}{\pi r^2 d} e^{\left[\frac{-2((x-vt)^2+(y-h)^2)}{r^2}\right]} \times e^{\left(-\frac{|z|}{d}\right)} \tag{18}$$

Where P is the laser power (W), A_c is the absorption coefficient, *x*, *y*, and *z* are the local, *d* is the OPD (mm), *r* is the laser spot radius (mm), *v* is the laser scan speed (mm/s), *t* is the time (s), and *h* is the hatch spacing (mm).

4.2.5. Melt pool modeling

The formation of a melt pool occurs in two steps; the first step occurs between the solidus and liquidus temperatures; hence it is governed by the latent heat of fusion, given in Table 4-1. The second step is the fully melted phase, where fluid mechanics such as the Marangoni effect and natural convection dominate heat transfer in the melt pool. Marangoni effects are important as they drive fluid flow inside the meltpool, hence altering its dimensions [54]. Additionally, Marangoni effect will influence the solidification process and the resulting grain formation [55, 56]. Simulation of the Marangoni effect requires the use of CFD; however, the current study employs an FE model to predict the RS. In order to overcome the absence of fluid flow modeling in FE, an effective thermal conductivity model [57] is used to account for heat transfer due to the Marangoni effect artificially, as shown in Equation (19).

$$k_{eff} = k_l + hL \tag{19}$$

Where k_{eff} is the effective thermal conductivity (W/m.K), k_l is the quiescent liquid thermal conductivity (W/m.K), h is the convective heat transfer coefficient (W/m^2.K), and L is the characteristic length (m) which is assumed as half the melt pool width [57, 58]. The value of the convective heat transfer coefficient inside the

melt pool can be calculated from the Nusselt number using Equation (20), which is the ratio of convective to conduction heat transfer. Since convection in the melt pool is driven by the Marangoni effect, then the Nusselt number can be calculated as a function of the Marangoni number shown in Equation (21) and Equation (22).

$$Nu = \frac{hL}{k_l} \tag{20}$$

$$Nu = 1.6129\, ln(Ma) - 10.183 \tag{21}$$

$$Ma = -\frac{d\sigma}{dT}\frac{L\Delta T \rho C_{pl}}{\mu k_l} \tag{22}$$

Where *Nu* is the Nusselt number, *Ma* is the dimensionless Marangoni number, $\frac{d\sigma}{dT}$ is the temperature gradient of surface tension (N.m/K), *L* is the characteristic length, ρ is the liquid density (kg/m^3), C_{pl} is the liquid specific heat capacity, k_l is the quiescent liquid thermal conductivity (W/m.K). μ is the dynamic viscosity (kg/m.s), and ΔT is the maximum temperature gradient in the melt pool, which is taken as the temperature difference between the center of the melt pool (peak temperature) to the boundary of the melt pool (solidus temperature) and is calculated using Equation (23)

$$\Delta T = \frac{-C_{pl} + \sqrt{{C_{pl}}^2 + 2(\frac{d\sigma 1}{dT\mu})^2 dt\frac{Q_v}{\rho}}}{(\frac{d\sigma 1}{dT\mu})^2} \tag{23}$$

$$dt = \frac{L}{v} \tag{24}$$

4.2.6. Modeling approach

The modeling approach is based on three models, each focusing on predicting a certain set of results to characterize the thermo-mechanical response occurring in L-PBF under different process parameters. The first model is a single-track model, with a very fine mesh, to test the validity of the proposed material, melt pool, and heat source models by predicting melt pool dimensions, temperature gradients, CR and comparing them to experimental results. The second model is a layer scale model with a coarser mesh to simulate the effects of multi-tracks on the temperature history, CR, melt pool dimensions, and the subsequent RS evolution in a single layer. The third model is a low fidelity part scale model, which examines the far-field temperature histories and how it drives the final in-depth RS and part distortion.

Single-track model

A 3D Lagrangian Finite Element (FE) model is built using ABAQUS to model single-track exposure of IN625. The model dimensions are 1 mm x 240 μm x 300 μm with the top 40 μm assigned as the powder layer, as shown in Figure 4-2. The model is meshed with heat transfer DC3D8 elements with a minimum size of 10 μm employed in the powder layer. The volumetric heat flux is applied as a body on the powder layer using the user subroutine DFLUX to simulate the spatial movement of the laser beam with time. Symmetry BC is assigned to reduce the model's size with the XZ plane taken as the plane of symmetry.

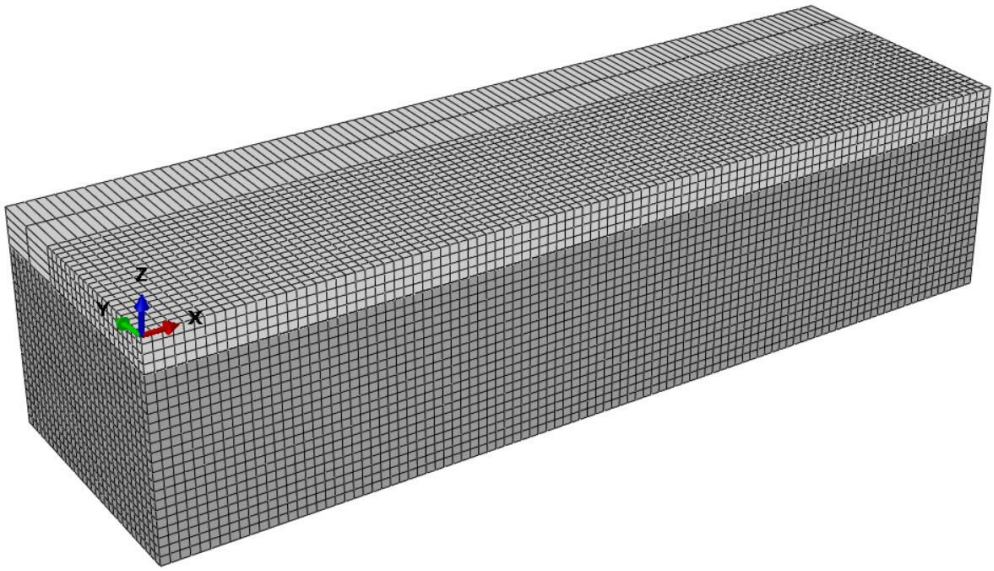

Figure 4-2 Single-track model setup

The user subroutine USDFLD changes the material model from powder to liquid and then to solid as the material solidifies. The criteria for changing the material state depends on the condition of reaching the melting temperature as shown below:

$$Material\ state\ variable\ (SV) = \begin{cases} 0 \rightarrow Powder & T < T_{melt} \\ 1 \rightarrow liquid & T > T_{melt} \\ 2 \rightarrow Solid & T < T_{melt}\ , T_{max} > T_{melt} \end{cases}$$

The melt pool dimensions, temperature gradient, and CR are extracted from the model when the melt pool reaches a steady-state, determined when the peak temperature reaches a constant value. The process parameters studied include two laser powers, 140 W and 220 W, and two scan speeds, 500 mm/s, and 650 mm/s.

Multi-track model

The multi-track model aims to observe the effect of hatch spacing, laser power, and scan speed on the temperature profile, temperature gradient, CR, and consequent effect on RS evolution during the solidification layer. In order to do so, a

sequentially coupled thermal-stress model is used since, in LPBF, the temperature change will drive a change in the stress, but the generation of stress will not cause an increase in temperature. Therefore, two separate models, 3D FE models, were built, firstly a pure heat transfer model to calculate the temperature fields generated due to laser exposure. Secondly, the temperature fields from the heat transfer model were imported into a static stress model to calculate the thermal stresses developed due to the cooling down of the material during solidification.

The heat transfer model has a powder layer with dimensions of 4 mm x 4 mm x 0.04 mm and is tie-constrained to the substrate having a thickness ten times the powder layer. The model was meshed with DC3D8 hexahedral elements having a uniform size of 40 μm. In contrast, the substrate had a coarser mesh with the element size biased towards the top surface, where the element size starts at 40 μm and increases to 140 μm, as shown in Figure 4-3. The user subroutine USDFLD changed the powder layer's material properties from powder to liquid and solid material due to material heating, melting, and cooling.

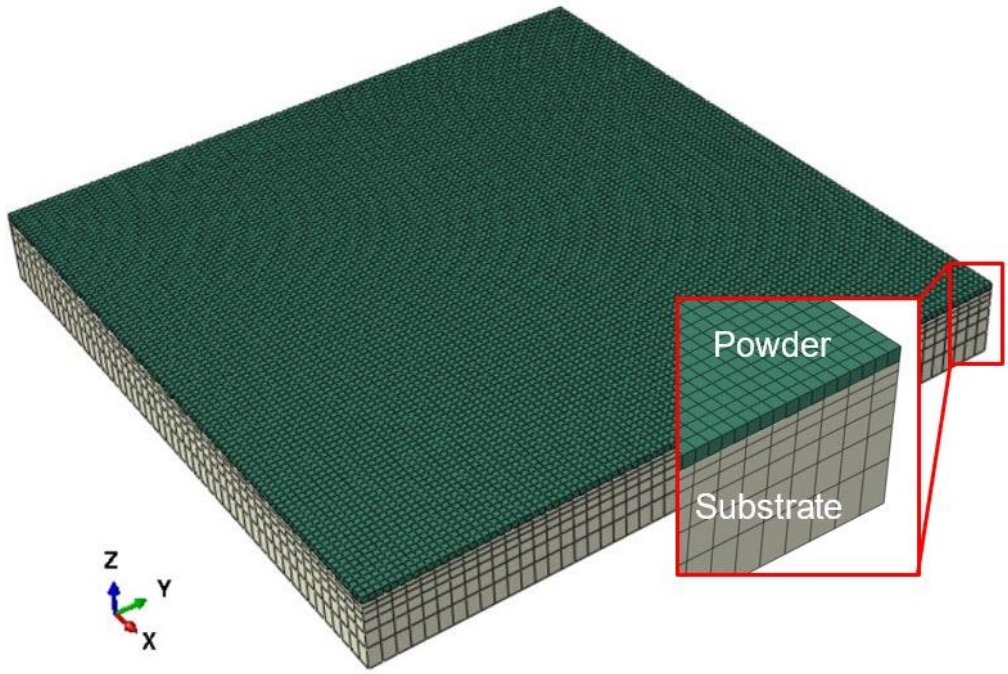

Figure 4-3 Multi-track model

The scan strategy employed was a stripe scan with serpentine laser motion [50]. The laser heat load was defined as a body flux acting on the powder layer, and the spatial motion of the laser beam was implemented using the DFLUX subroutine. The step time was set as the total time required to expose a layer with a cross-section of 10 mm x 10 mm, the same size as the experiments [50]. The laser process parameters are stated in Table 4-3. A preheat temperature of 80 ˚C was assigned to the whole model and set as a BC for the bottom surface of the substrate. Convection and radiation are defined for the top surface of the powder layer with an ambient temperature of 40 ˚C. The temperature profiles, temperature gradients, and CRs are extracted at the center point of the powder layer to examine the effect of multi-track laser exposures and hatch spacing on temperature evolution.

Table 4-3 Process parameters for LPBF of IN625

Parameter	Levels
Power (W)	140, 220, 270
Scan speed (mm/s)	500, 650, 800
Hatch spacing (mm)	0.08, 0.1, 0.12

The static stress model had the same dimensions and mesh size as the heat transfer model. Thermal stresses are the main driver of RS and deformation in LPBF; hence, the temperature field from the heat transfer model was assigned as an initial condition in the stress model. Since LPBF is characterized by rapid cooling, the molten material solidifies once the laser beam passes. This means that solidification and stress formation progressively follow the laser beam during the multi-track exposure. Therefore to model this behavior, "quiet" or "inactive" elements represented the powder material that did not develop any stresses yet. Once the laser beam passes over these elements, they are activated to calculate stress evolution during cooling. The user subroutine UEPACTIVATIONVOL was used for progressive activation of the powder layer elements in tangent with the laser scan strategy. The coordinates of the laser position are calculated at every increment, and the elements within a circle, with a diameter equal to the melt pool width calculated from the heat transfer model, are activated [59]. Due to a limitation in Abaqus, a set of elements with an area equal to the laser spot diameter needed to be activated priory to avoid convergence issues with UEPACTIVATIONVOL. In order to reduce computational time and improve the convergence of the non-linear

model, the unsymmetric stiffness matrix storage option is selected to use Newton's method to solve the non-linear problem. In addition, the strain state extrapolation feature is turned off to improve convergence[60, 61].

Multi-layer model

A large-scale FE model is required to predict stresses and deformations on a part scale. However, utilizing a fine mesh from the high fidelity model would be computationally infeasible. Therefore, a low fidelity model that predicts the far-field temperatures without focusing on the melt pool area during printing and recoating was proven to provide good predictions of part scale stresses and deformations [17, 61]. The ABAQUS AM module [62] was used to build the sequentially coupled temperature-stress part scale model, consisting of a heat transfer step followed by a stress analysis step and finally removing the part from the build plate.

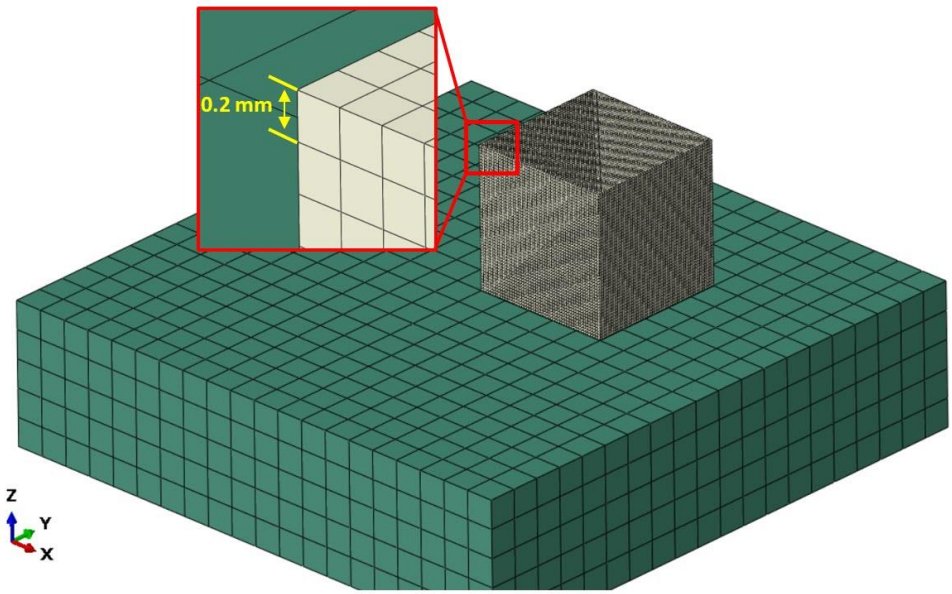

Figure 4-4 Multi-layer model

The heat transfer model consists of a 10 mm x 10 mm x 10 mm cube coupon meshed with DC3D8 200 μm elements, while the substrate has a coarser mesh of 2 mm in size, as shown in Figure 4-4. The 200 μm element used is a lump sum of 5 layers of 40 μm thickness to save on computational cost since the interest is the far-field temperature history [17, 61]. The part and the substrate are connected using a "tie-constraint." Simulation of the PBF process requires successive addition of material using UEPACTIVATIONVOL subroutine based on an event series that specifies the time instances where the recoating starts and ends. A Matlab code was written to generate the recoater event series file with the recoating time set at 5 seconds. The laser heat source is modeled as a point source, which is acceptable when the laser spot size is relatively smaller than the element size. A stripe scan with serpentine laser motion was used for in-layer exposure, while a 0˚-90˚, alternating scan was employed for subsequent layers exposures, as illustrated in Figure 4-5. An event series data set is created using Matlab to determine the time, spatial coordinates, laser power, and laser spot diameter corresponding to the employed scan strategy. The tool path – mesh intersection built-in module determines the intersection of the laser event series with the elements integration points, then calls the user subroutine UMDFLUX to apply heat flux at the corresponding time [61, 62]. The newly formed external surfaces are automatically determined, and the radiation and convection heat transfer is applied. Finally, after the whole part is exposed, it is left to cool down for 600 seconds.

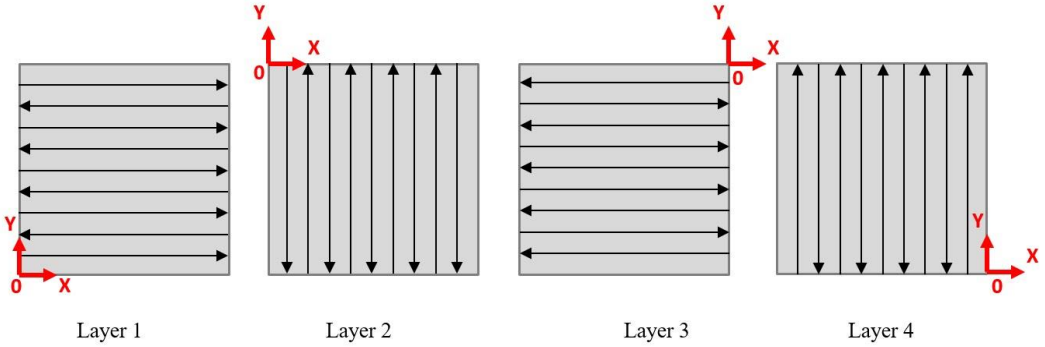

Figure 4-5 Alternating 0˚- 90˚ scan strategy

The same geometry and mesh size were used for the stress analysis model, where the temperature fields from the heat transfer model are imported into the stress model. The thermal strains and stresses were calculated by imposing an initial temperature of 1000 ˚C, above which thermal stress is negligible. The difference between this temperature and the imported part temperature will determine the thermal stress field [17, 61]. Temperature-dependent material properties were used [49, 63], while the Johnson-Cook (J-C) plasticity [64] was used to model the temperature-dependent plasticity according to Equation (25)

$$\sigma = (A + B\varepsilon^{n})(1 + C\, ln(\frac{\dot{\varepsilon}}{\dot{\varepsilon_o}}))(1 - \left(\frac{T - T_r}{T_m - T_r}\right)^{m}) \quad (25)$$

Where σ is the von mises flow stress, ε is the equivalent plastic strain, $\dot{\varepsilon}$ is the equivalent plastic strain rate, and $\dot{\varepsilon_o}$ is the reference plastic strain rate. T is the current temperature, T_m is the melting temperature, and T_r is the reference temperature at which the J-C parameters were determined. A is the initial yield strength, B is the strain hardening coefficient, n is the strain hardening exponent, C

is the strain rate coefficient, and *m* is the thermal softening exponent. The values for the J-C parameters used in the current study are listed in Table 4-4

Table 4-4 Johnson-Cook plasticity parameters [65]

Parameter	Value
A (MPa)	558
B (MPa)	2201.3
n	0.8
C	0.000209
m	1.146
T_m (˚C)	1290
T_r (˚C)	20
$\dot{\varepsilon_o}$ (s^{-1})	1670

The J-C parameters listed above were determined for a conventionally manufactured IN625; in an attempt to partially modify these parameters to match that of the additively manufactured IN625, a tensile test was performed at room temperature. A sub-size flat specimen was printed with dimensions according to the ASTM E8 standard [66] with a gauge length of 25 mm, a width of 6 mm, and a thickness of 5 mm. The true stress-strain curve was plotted, and the Ramberg-Osgood model [67] was used to fit the data according to Equation (26) and calculate the yield strength, the strength coefficient (K), and the strain hardening exponent (n), which are analogous to the A, B and n parameters in the J-C equation.

$$\varepsilon^{total} = \frac{\sigma_y}{E} + (\frac{\sigma}{K})^{1/n} \quad (26)$$

A total fixation BC is applied to the bottom surface of the substrate. After the part was built and cooled down, the substrate was removed using the model change feature to simulate the part's separation from the substrate. The substrate removal will release some stresses, and the RS inside the part will remain. For validation, the stresses are extracted and averaged across an area 2 mm in diameter to resemble the spot size of the experimentally measured RS using XRD measurement.

4.3. Experimental validation

4.3.1. Laser absorptivity measurement

Diffuse reflectance spectroscopy (DRS) was used to measure the optical absorptivity of the IN625 in a wavelength range of 400-1400 nm. The test measures the powder's reflectance, which is used to calculate the Kubelka-Munk absorption coefficient, as shown in [9]. For example, for an EOSM280, the Yb-fiber laser used has a wavelength of 1070 nm that corresponds to an absorptivity coefficient of 0.62.

4.3.2. Single track validation

The melt pool width and depth predicted by the single-track model are validated by comparing them to the experimental melt pool dimensions measured in literature [68, 69]. The single exposed by NIST[68] and Dilip et al. [69] were built with a layer thickness of 20 μm, and the model geometry was modified to accommodate the smaller layer thickness. The meltpool dimensions were measured by extracting the distance from the center of the melt pool to the outer temperature contour having a temperature corresponding the solidus temperature of 1290 ˚C.

4.3.3. Multi-track temperature measurement

A Fluke Endurance-series 2-color pyrometer was used to measure melt pool measurements during exposure of a single layer. The 2-colour pyrometer operation is based on the ratio of two separate infrared bands with a slight difference in wavelength to determine the object's temperature. Hence, temperature measurement would be independent of the emissivity, thus reducing measurement uncertainty. The pyrometer used has a Si/Si detector with a nominal wavelength of 1 μm, and the ratio between the two wavelengths, also called the slope, was calibrated as 0.96 [70]. The pyrometer has a temperature range of 1000 ˚C- 3000 ˚C, and it was installed inside the build chamber of an Omnitek L-PBF machine, as shown in Figure 4-6 (a), at a distance of 85 mm, which results in a measurement spot size of 2 mm in diameter.

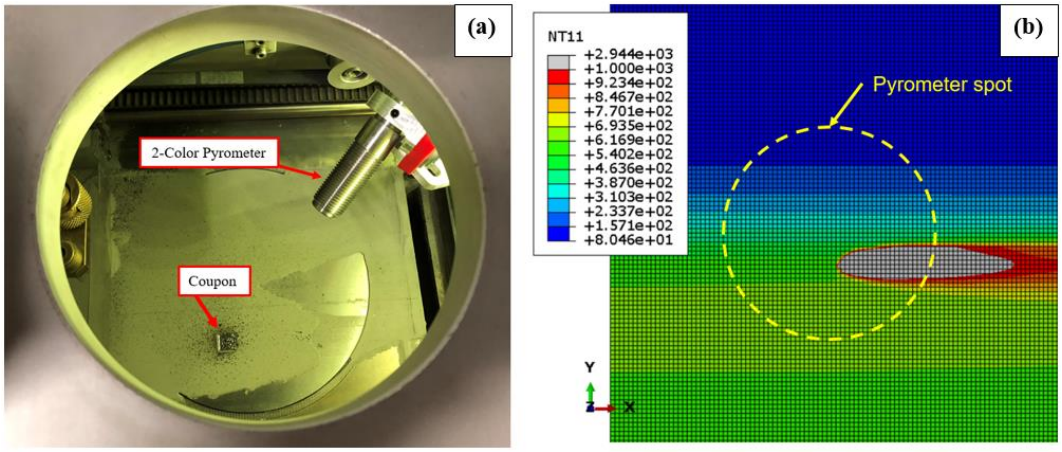

Figure 4-6 Pyrometer setup a) Experimental b) Numerical

For validation, the elements temperatures above 1000˚C,i.e., the lower limit of the pyrometer, within a 2 mm diameter circle were averaged and compared to the pyrometer measurements [71], as shown in Figure 4-6 (b). The tested parameters

were 220 W, 650 mm/s, 0.12 mm hatch spacing, and a layer thickness of 0.04 mm. Since the pyrometer had a response time of 10 ms, the temperatures calculated from the model are extracted and averaged at an increment of 10 ms.

4.3.4. Residual stresses measurements

In-depth RS were measured in IN625 cube coupons [50] using X-ray diffraction (XRD). Since X-ray penetration depth is about 5 μm in Inconel, electro-polishing was used to minimally affect the existing stress field [72]. The material was removed in 0.1 mm increments down to a depth of 1 mm from the top surface. RS were measured in two directions; parallel to the laser motion (scan direction) and perpendicular to it (hatch direction). The in-depth RS measurements were done on two samples corresponding to two laser powers, 140 W and 220 W, at a hatch spacing of 0.12 mm, and a constant scan speed of 650 mm/s. In addition, predicted RS is compared to surface RS measured by the current authors in a previous study [50] at different process parameters.

4.4. Results

4.4.1. Single tracks

The temperature contours of the predicted melt pool are shown in Figure 4-7 for the 20 μm layer thickness validation model with an exponential heat source. The grey-colored area represents temperatures above the solidus temperature of 1290 ˚C. The temperature profiles are plotted in the width direction, Figure 4-8, and in-depth, to calculate the melt pool dimensions, as shown in Figure 4-9. The

intersection point of the temperature profiles with the solidus temperature locus determines the width and depth of the melt pool.

Comparison of the experimentally measured melt pool width [68, 69] with the predicted melt pool width for the three heat source models is shown in Figure 4-8. The exponential heat source model predicted a melt pool width of 131 μm, which best agrees with the experimental measurements. However, the melt pool depth was underestimated for all three heat source models, as shown in Figure 4-9. The melt pool depth measured by NIST [68] was much deeper than the predicted value due to printing on the bare substrate without a powder layer. Therefore, the exponential heat source was chosen for subsequent simulations. The length of the melt pool was measured in the study by NIST [68] using a high-speed infrared camera. By comparing the result with the numerical prediction, Figure 4-10 shows that the model greatly underestimates the melt pool length. The underestimation could be attributed to approximating the Marangoni effect inside the melt pool and calculating its value based only on the outward flow in the melt pool width direction.

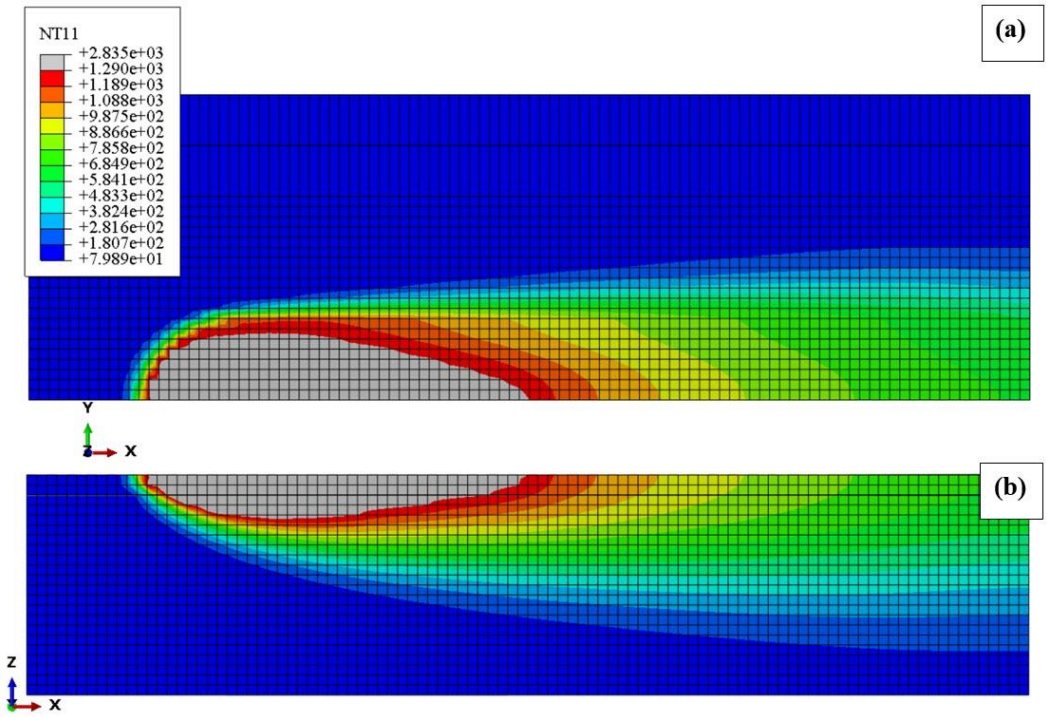

Figure 4-7 Predicted temperature contours a) top view b) front view

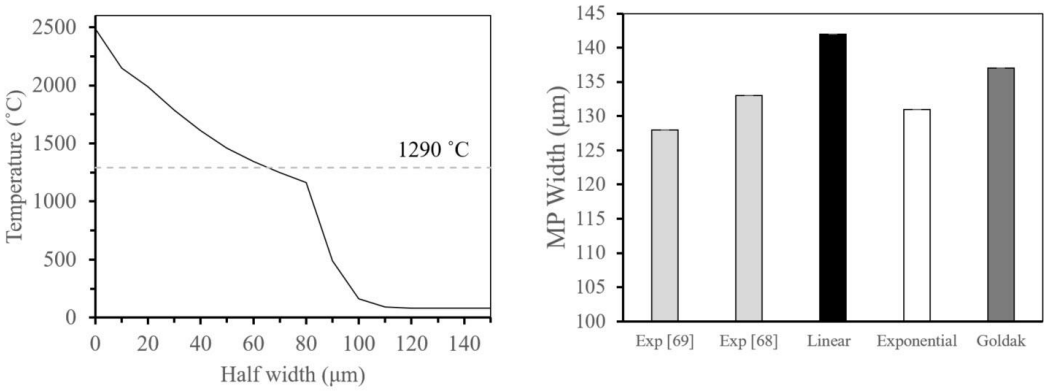

Figure 4-8 Validation of predicted melt pool width

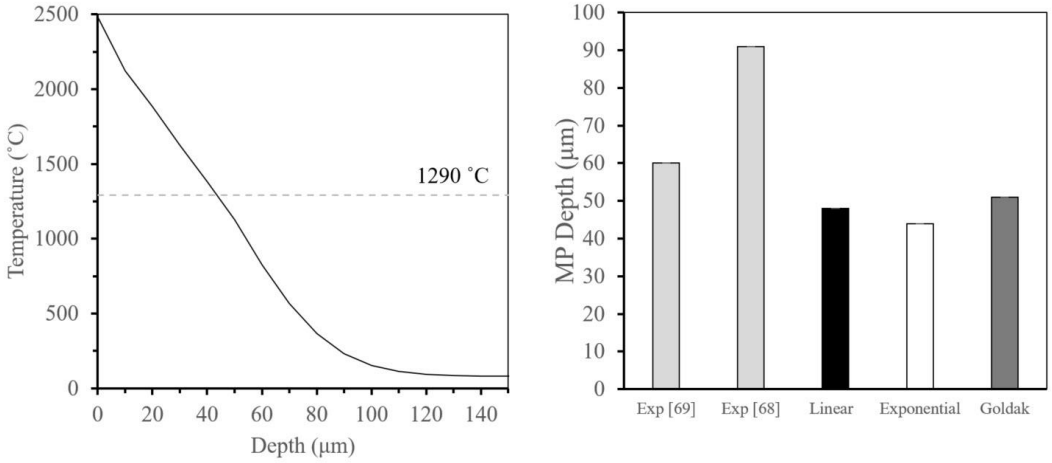

Figure 4-9 Validation of predicted melt pool depth

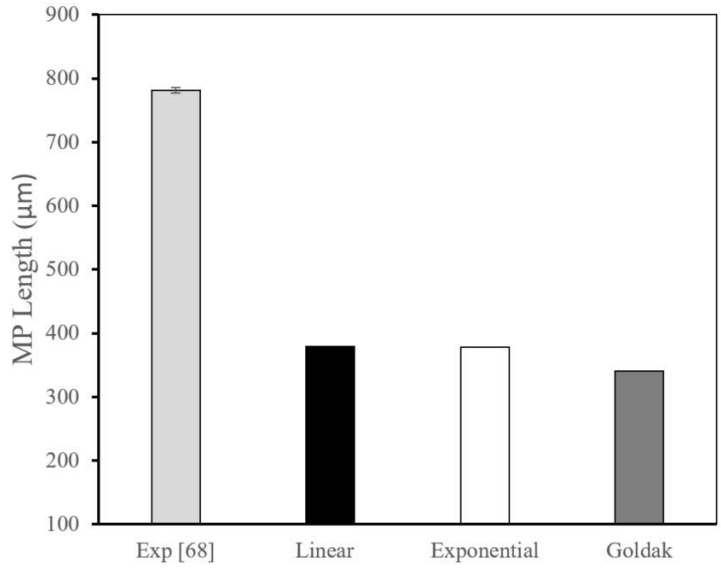

Figure 4-10 Melt pool length prediction for different heat source models

Calculating the melt pool width and depth for the parameters examined in the current study, Figure 4-11, shows that the melt pool dimensions decrease with increased scan speed, which agrees with the literature [68, 69, 73]. Furthermore, it is observed that the melt pool width is inversely proportional to the square of the scan speed, while the melt pool depth is inversely proportional to the scan speed.

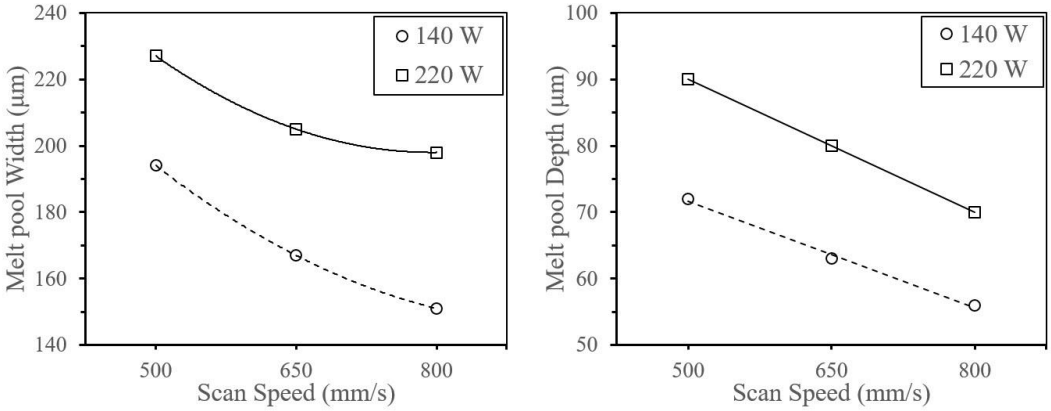

Figure 4-11 Single tracks melt pool dimensions at different process parameters

The temperature history is extracted at the midpoint along the laser scan path and plotted, as an example, for the case of 220 W and 650 mm/s, as shown in Figure 4-12. A rapid temperature rise is seen as the laser approaches the midpoint, followed by rapid cooling down to 1290 ˚C. Finally, the CR is calculated as the slope of the temperature history profile once the temperature drops below the solidification temperature, which will drive RS.

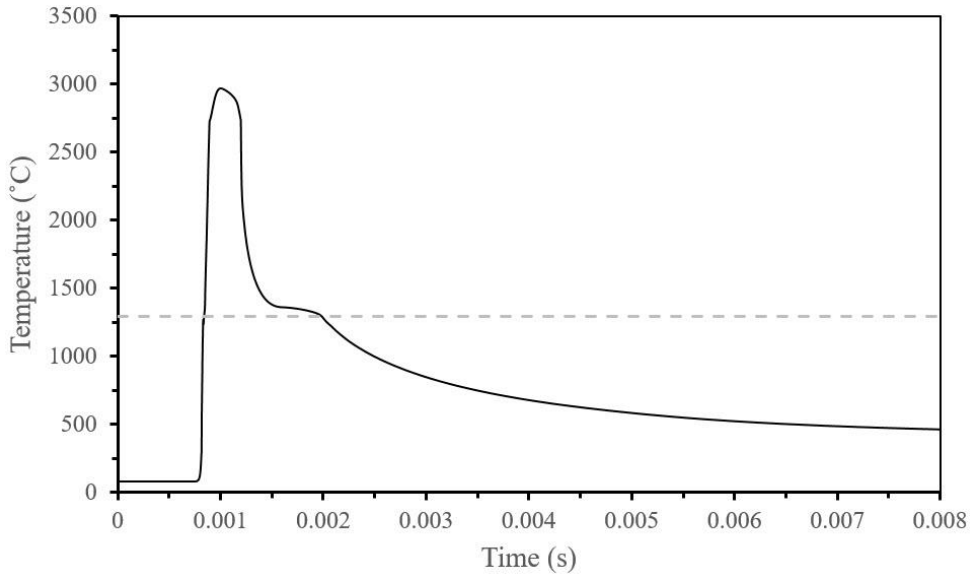

Figure 4-12 Temperature history evolution for a single track

The CR for all three scan speeds is plotted in Figure 4-13 and is on the order of 10^5 characteristic of rapid cooling. The cooling increases linearly with increasing scan speed regardless of the laser power. The temperature gradient is also plotted in Figure 4-13 as it affects the magnitude of thermal stresses formed during cooling according to Equation (27), where E is the modulus of elasticity (MPa), α is the thermal expansion coefficient, and ΔT is the temperature gradient (˚C).

$$\sigma = E\alpha\Delta T \tag{27}$$

The temperature gradient exhibits a downward trend with increased scan speed, resulting in RS with the same trend. However, previous experimental RS measurements show non-monotonic trends for RS values [50]. These trends could mean that RS is governed by a temperature gradient, and the opposite effect of CR could play a role in determining the final stress state [42].

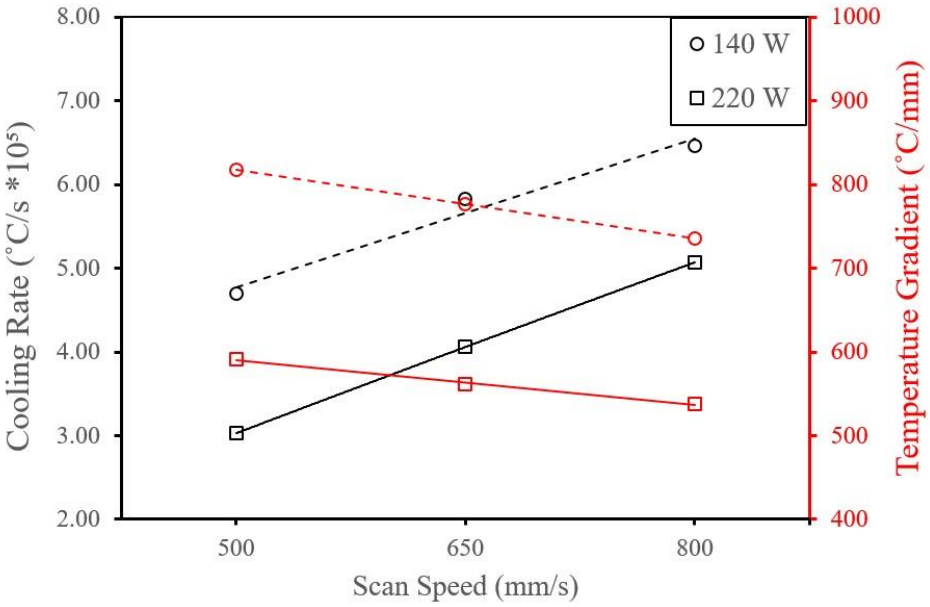

Figure 4-13 Single tracks CR and temperature gradients

4.4.2. Multi-track Model

Temperature validation and evolution

Temperature predictions from the multi-track model are compared to pyrometer measurements, as shown in Figure 4-14. The numerical temperature predictions are in good agreement with the experimental data. However, the discrepancy at the highest temperature predictions could be due to underestimating the melt pool length; since the calculated temperature is averaged over the melt pool, a difference in the melt pool area will affect temperature prediction.

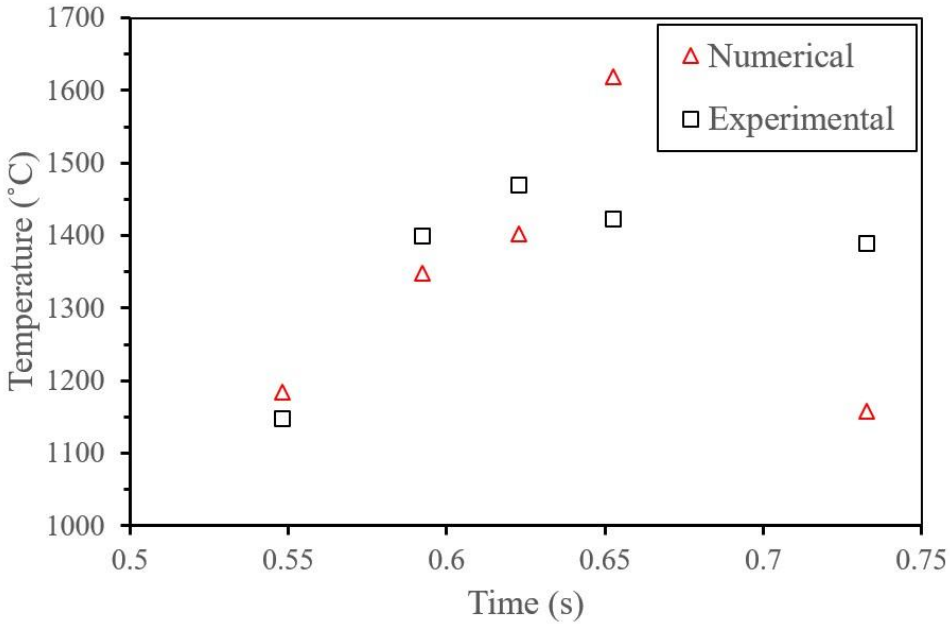

Figure 4-14 Experimental vs. numerical temperature measurement

The temperature history is plotted at three points, 1 mm apart, at 220 W laser power, 650 mm/s scan speed, and 0.12 mm hatch spacing, as shown in Figure 4-15. The three points exhibit the same thermal cycles where the temperature rises to a point shy of the melting temperature as the laser scans the precedent track. Afterward,

the temperature at the point of interest cools down to about 500 ˚C as the laser beam passes directly over it, resulting in a peak temperature higher than the boiling temperature. Due to rapid cooling, the temperature drops from 2900 ˚C down to 570 ˚C, where the heat from the subsequent track scan causes the temperature to rise again to 950 ˚C. Beyond that point, the temperature drops to a plateau of about 650 ˚C until the whole layer is scanned. The CR and temperature gradients are plotted in Figure 4-16 for the points mentioned above. The presented CR is calculated as the temperature cools down below 1000˚C. Although a larger surrounding solid area could indicate that the cooling will increase because the solid material has higher thermal conductivity and specific heat capacity compared to the powder state, it is shown that the CR decreases as the area of the solidified layer increases. The reason is that the larger solidified volume retains more heat; therefore, the area surrounding the melt pool has a relatively high temperature resulting in a lower temperature gradient, as shown in Figure 4-16, and lower heat transfer due to conduction.

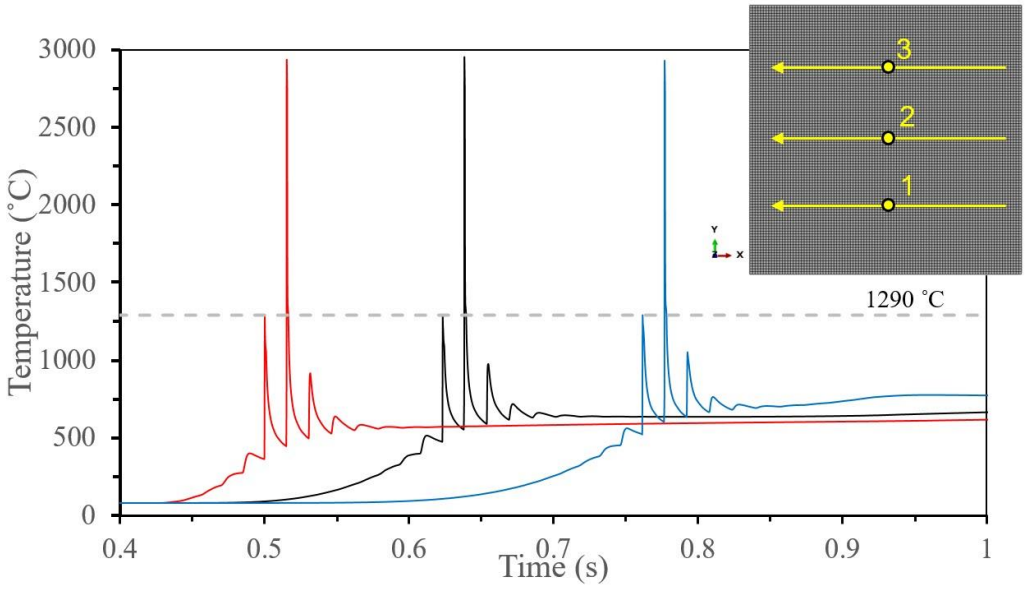

Figure 4-15 Temperature history at 220 W, 650 mm/s, and 0.12 mm

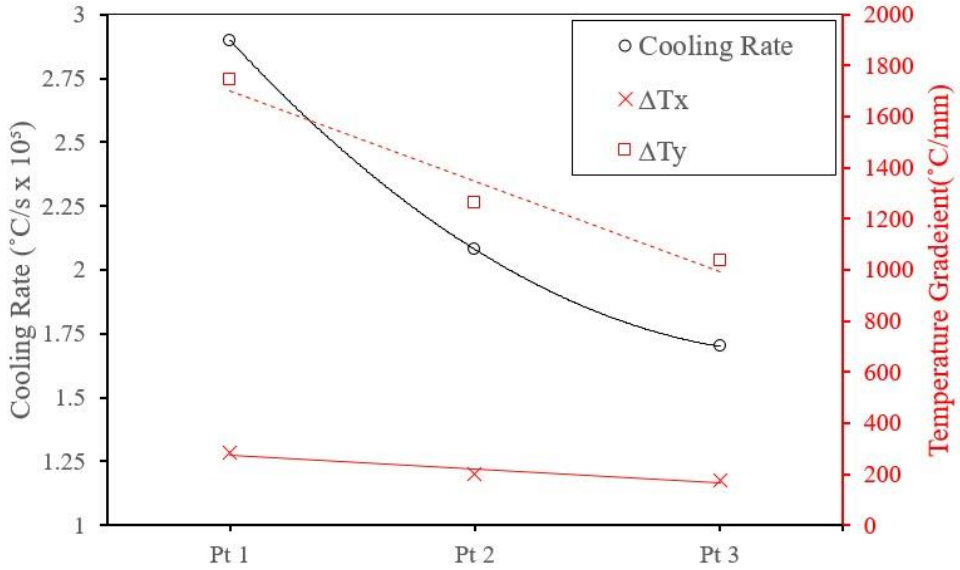

Figure 4-16 CR and temperature gradients at 220 W, 650 mm/s, and 0.12 mm

In addition, Figure 4-17 compares the temperature and Von Mises stress evolutions during the layer exposure at different time instances until the end of exposure at 1.25 s. The peak temperatures are mainly focused inside and around the boundary

of the melt pool and drastically decay beyond that. Conversely, the Mises stresses are minimum around the melt pool boundaries and increase farther away from the melt pool due to the rapid cooling and stress generation until it reaches its maximum value at the part edges, as seen in Figure 4-17 (f).

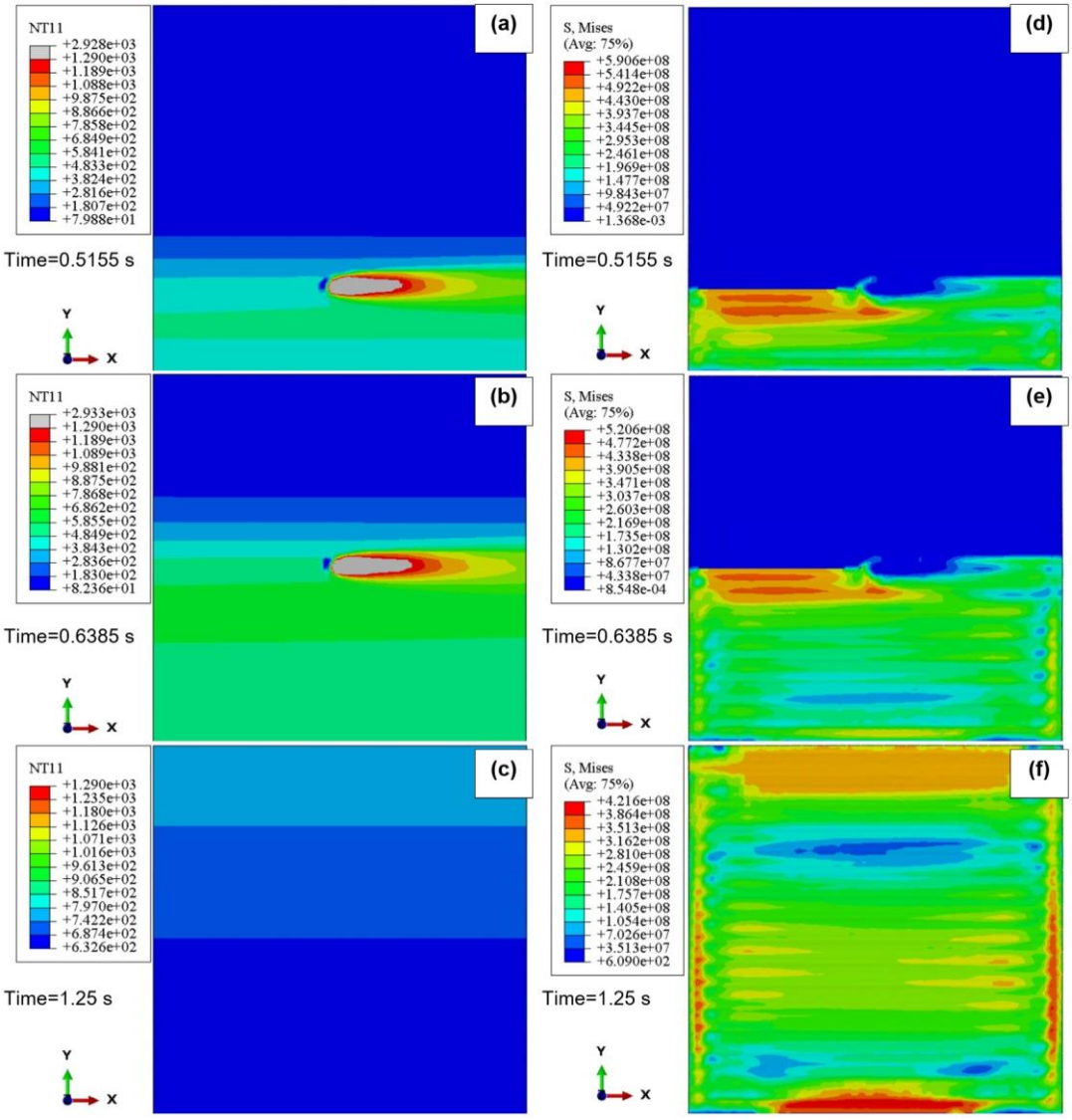

Figure 4-17 Temperature contours evolution (a-c) and Mises stress evolution (d-f) at different time stamps

The temperature evolution at the midpoint of the modeled area is plotted in Figure 4-18 for the total layer time of 6.25 seconds, corresponding to 1.25 seconds of laser exposure plus 5 seconds for powder recoating. The temperature profile can be divided into a rapid non-linear phase, which occurs during the first 1.25 seconds, followed by the linear phase. The thermal stresses are also plotted for the principal directions, the laser scan direction (S11), and the perpendicular direction, hatch direction (S22), where S11 is observed to be always greater than S22. To understand why S11 is greater than S22, the RS formation mechanism needs to be explained.

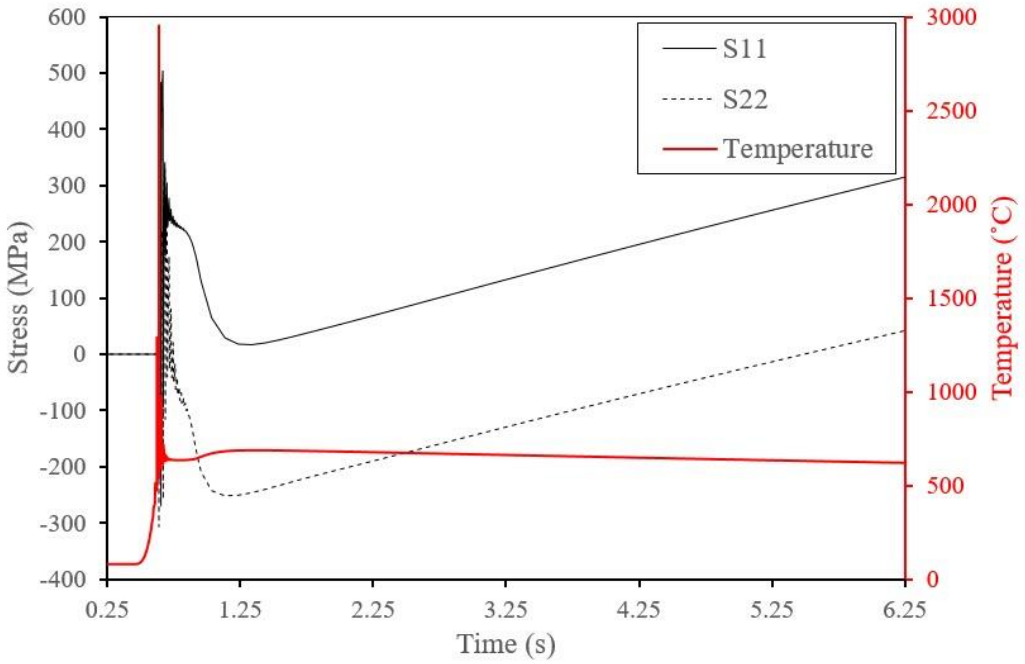

Figure 4-18 Layer stress and temperature evolution at 220 W, 650 mm/s, and 0.12 mm

RS in LPBF is formed due to the difference in thermal strains during subsequent heating and cooling during subsequent scans called the temperature gradient mechanism (TGM) [15, 73, 74], governed by Equation (26). To better understand the formation mechanism of RS, Figure 4-19 shows a layer during laser exposure where the yellow area,A_T, represents a track along the laser path surrounded by the previously solidified area, A_S, and the subsequent powder area. This layer can be represented by the bar model analogy for simplification, whereas bar T and S are constrained at one end and free to move on the other end. As bar T is heated, it expands and pulls on bar S, resisting the motion by inducing compressive stress. The stress cycle undergone by the material is represented by the stress-temperature plot in Figure 4-19, where the compressive stress increases with temperature till reaching the yield temperature (T_y) at point A, upon which plastic deformation occurs. As bar *T* cools down during solidification, the compressive strains and stresses decrease to zero at point C. As the temperature drops further, bar *T* shrinks and pulls on bar *S*, which resists this motion; therefore, bar *T* experiences tensile strains while bar *S* exhibits compressive strains. Finally, the tensile stress in bar *T* increases up to the yield point, where the material undergoes another plastic deformation until reaching equilibrium temperature. These plastic strains lock in the thermal stresses and prevent them from returning to zero, thus creating RS. The RS can be represented by Equation (28) or Equation (29), depending on the maximum temperature experienced by the material.

If $T_y \leq T_{max} < 2T_y$ then

$$\sigma_{RS} = \left|E\Delta\varepsilon_{p1}\right| = \alpha E(T_{max} - T_y) \tag{28}$$

If $2T_y \leq T_{max}$ then

$$\sigma_{RS} = \left|E\Delta\varepsilon_{p1} + E\Delta\varepsilon_{p2}\right| = \alpha E T_y \tag{29}$$

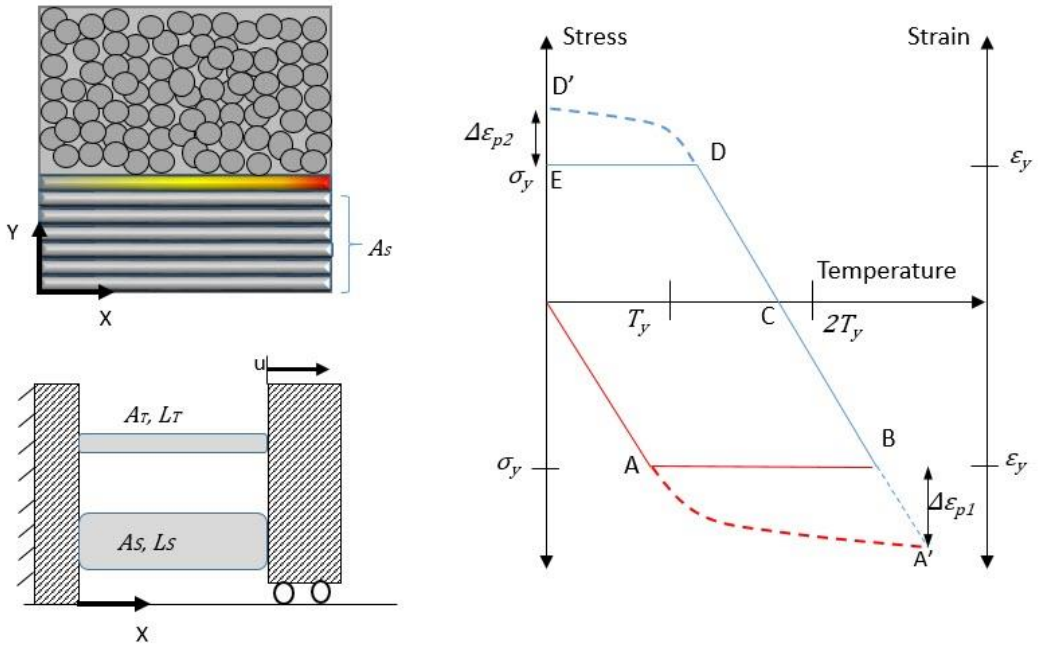

Figure 4-19 RS formation mechanism with the bar model analogy

The same bar model analogy can be used to explain why S11 is greater than S22 by examining Figure 4-20, where the bar model is superimposed on an arbitrary melt pool temperature contours [75]. The thermal stress in the X direction (S11) is generated due to the temperature difference with the adjacent area in the Y direction(ΔT_Y), while the thermal stress in Y direction (S22) arises due to the

temperature difference in the X direction (ΔT_X). As shown in Figure 4-16, (ΔT_Y) is always greater than(ΔT_X), hence S11 is always greater than S22.

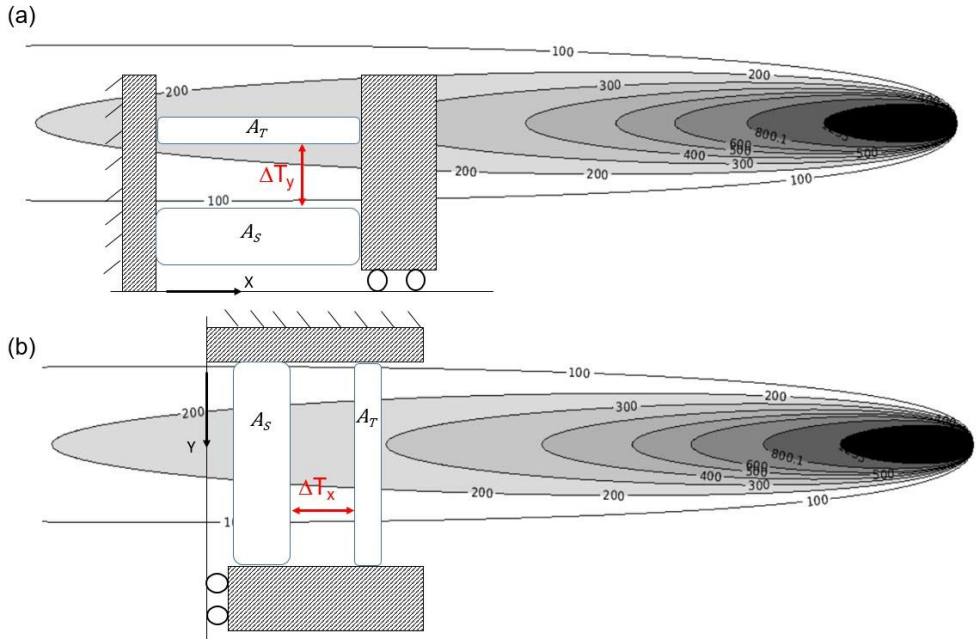

Figure 4-20 RS formation a) scan direction b) hatch direction

Figure 4-21 provides a closer examination of the non-linear stress formation phase, where the material undergoes a few heating and cooling cycles. Commonly stresses are generated due to a moving heat source were considered to be affected by the temperature gradient only and its thermal softening effect on the material. However, in LPBF, the material deforms at high strain rates due to the high CR, which causes strain rate hardening, thus opposing the thermal softening effect. Following the temperature and stress evolution in Figure 4-21, it is seen that the stress is zero as long as the temperature has not reached the melting temperature; hence, it remains in its powder state. As the laser passes over the point of interest during track n, the material melts, and as it solidifies, stresses are generated. By examining Figure 4-21

and Figure 4-22 simultaneously, to observe the stress and plastic strain formation during cooling, it is seen that as the temperature decreases, the compressive plastic strain decreases, analogous to line BD in Figure 4-19, while tensile stresses increase. As the laser beam exposes track n+1, the conducted heat causes a temperature rise of track n, as mentioned previously, thus causing an increase in compressive stress and a corresponding decrease in tensile stresses. Finally, the temperature due to the conducted heat reaches a maximum of 940 ˚C, the material cools down again, generating more tensile stresses. As the distance between track n and laser spot increases, the quantity of heat reaching track n decreases. Therefore, the material undergoes low peak heating and cooling cycles, which generates comparatively lower tensile stresses.

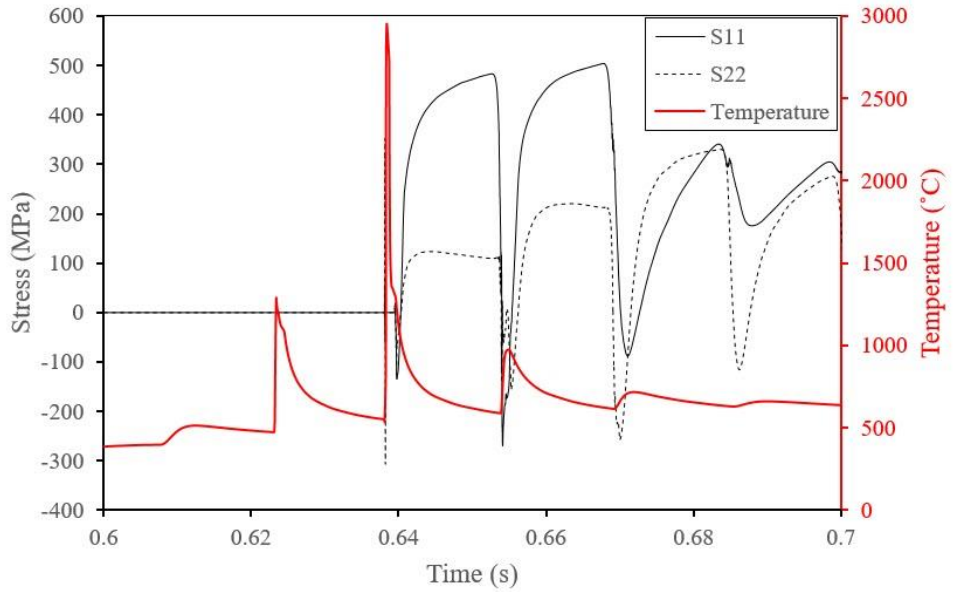

Figure 4-21 Non-linear temperature and stress evolution at 220 W, 650 mm/s, and 0.12 mm

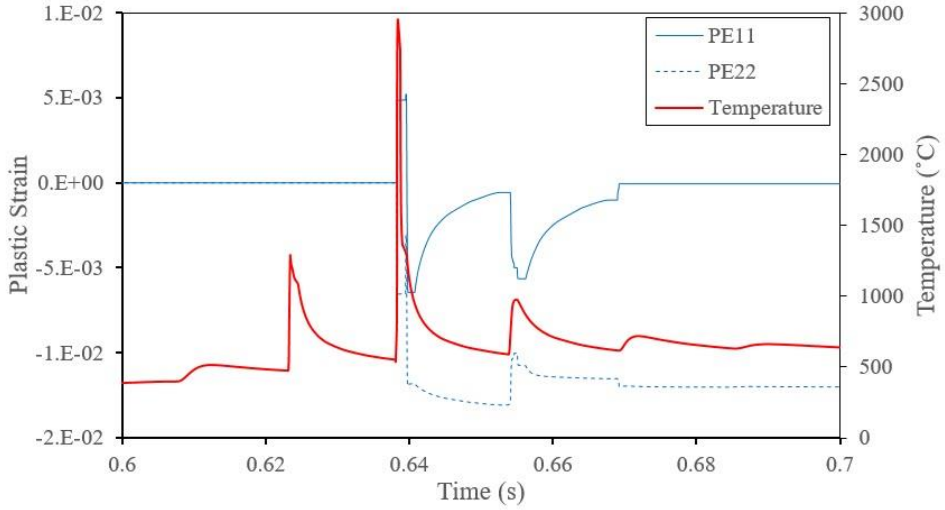

Figure 4-22 Plastic strain and temperature evolution at 220 W, 650 mm/s, and 0.12 mm

Effect of scan speed on RS

Examining the effect of the scan speed on the temperature history at the center point of the layer can be seen in Figure 4-23, where three scan speed levels of 500 mm/s, 650 mm/s, and 800 mm/s are shown. As expected, the temperature peaks decreased with increasing the scan speed. Yet, the temperature at the layer midpoint did not reach the melting temperature during the exposure of track n-1, as the hatch spacing was greater than the half-width of the melt pool. However, at a scan speed of 500 mm/s, the melt pool half-width was 120 μm, equal to the hatch spacing, but the peak temperature from track n-1 was just shy of the melting temperature.

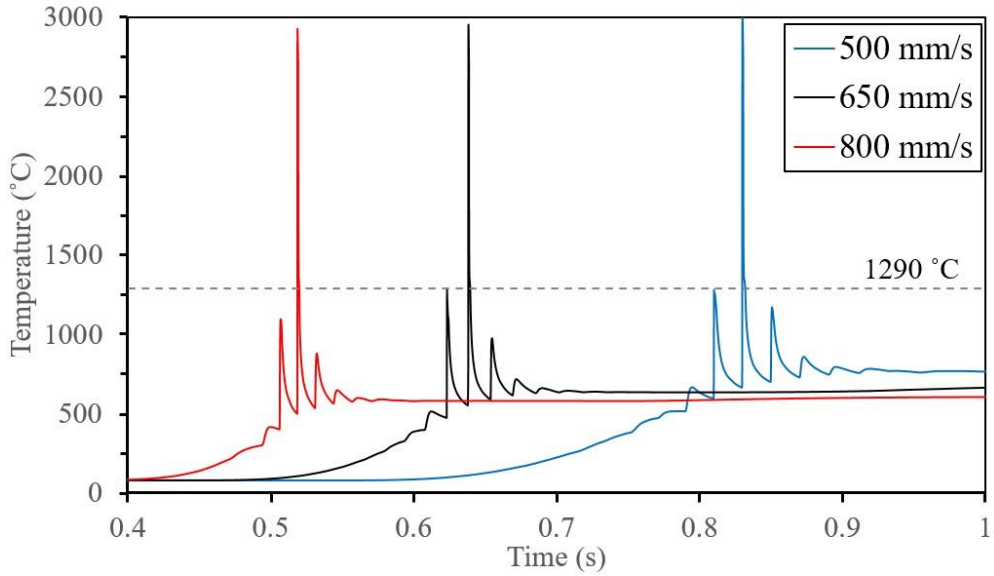

Figure 4-23 Temperature history for different scan speeds at 220 W and 0.12 mm

Surface RS are measured after laser exposure plus a relaxation time equal to the recoating time of 5 seconds. It is shown in Figure 4-24 that tensile RS is formed, and its magnitude increases linearly with the increase in scan speed. The RS increase is due to the corresponding increase in the temperature gradient and CR, Figure 4-25, which would induce higher thermal stresses. The increase in the temperature gradient occurs even though increasing the scan speed will cause a reduction in the energy density added to the powder layer. The increasing trend can be attributed to the increase in CR, which causes the surrounding material to cool faster, thus creating a more significant temperature difference. In addition, as the speed increases, the melt pool width decreases, resulting in less heating of the adjacent tracks and lower temperature peak, as seen in Figure 4-23, where the amplitude of the third peak is lower at the higher scan speeds. Therefore, the lower temperatures of the adjacent tracks will lead to a larger temperature gradient.

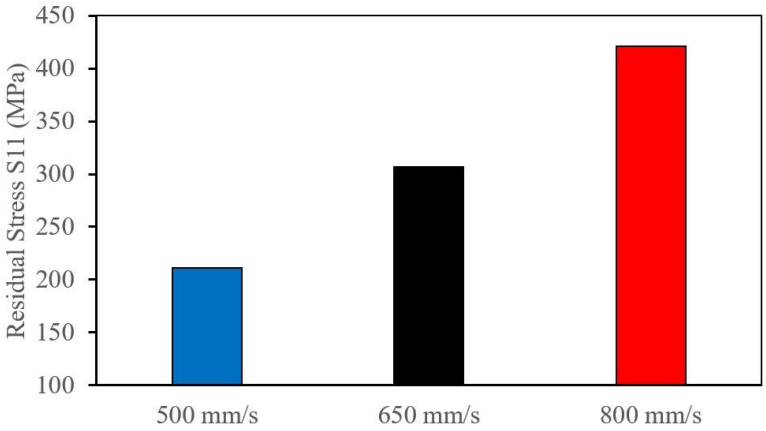

Figure 4-24 Effect of scan speed on the surface RS

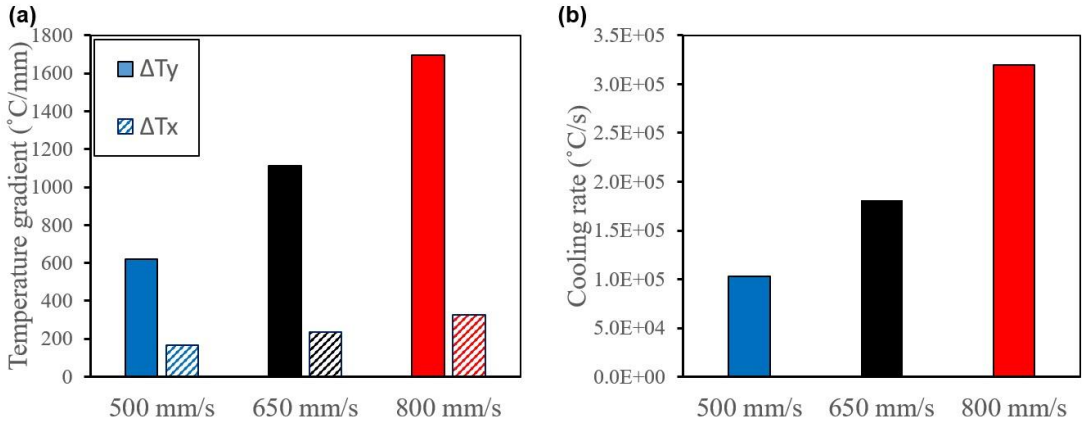

Figure 4-25 Effect of scan speed on a) Temperature gradient b) CR at 220 W and 0.12 mm

Effect of laser power on RS

Three different laser power levels were modeled at a constant scan speed of 650 mm/s and 0.12 mm hatch spacing to examine the effect of laser power on the temperature profiles and RS. The temperature history in Figure 4-26 shows similar temperature evolutions for all three laser powers at the midpoint of track n. At any time, the minimum temperature is recorded with the 140 W power and increases with increasing the laser power. At 270 W, the meltpool width was 300 μm, which

means that the half-width is larger than the hatch spacing. The larger inter-track overlap is reflected in the temperature history profile where the point on track n reached the melting point while the laser was still scanning track n-1, seen as the first peak on the red curve in Figure 4-26.

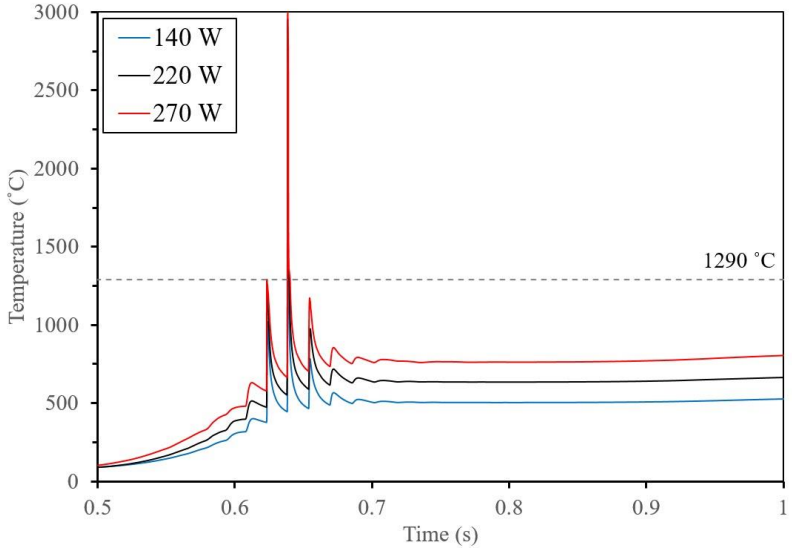

Figure 4-26 Temperature history for different laser powers at 650 mm/s and 0.12 mm

Prediction of RS at the midpoint of track n shows that a laser power of 140 W resulted in the highest surface RS, as shown in Figure 4-27, and RS decreases with the increase of laser power, which agrees with the literature [50]. The declining trend in RS is analogous to the temperature gradient and CR trend, shown in Figure 4-28, where the highest temperature gradient is recorded at 140 W. The decreasing trend can be traced back to the melt pool size, where the widths are measured to be 138 µm, 176 µm, and 298 µm, corresponding to 140 W, 220 W, and 270 W, respectively. Therefore, the wider melt pool will have a larger heat-affected zone

(HAZ), as shown in Figure 4-29, and the surrounding material will have a higher temperature. The higher temperature of the HAZ is evident by the amplitude of the third peak in Figure 4-26, which increases with the increase in laser power. The higher the amplitude, the lower the temperature difference between the second, below solidus temperature, and third peak, corresponding to a lower temperature gradient.

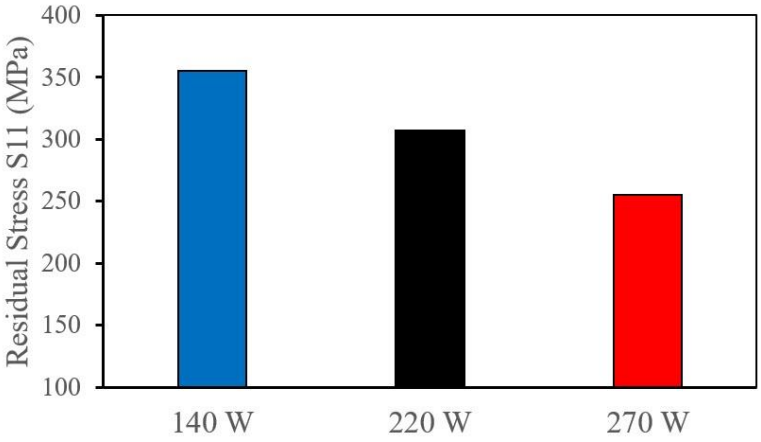

Figure 4-27 Effect of laser power on surface RS

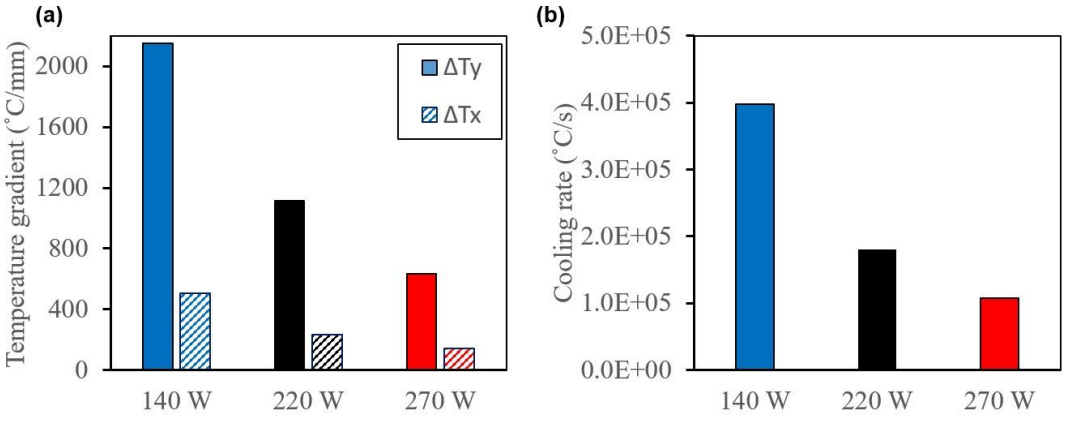

Figure 4-28 Effect of laser power on a) Temperature gradient b) CR at 650 mm/s and 0.12 mm

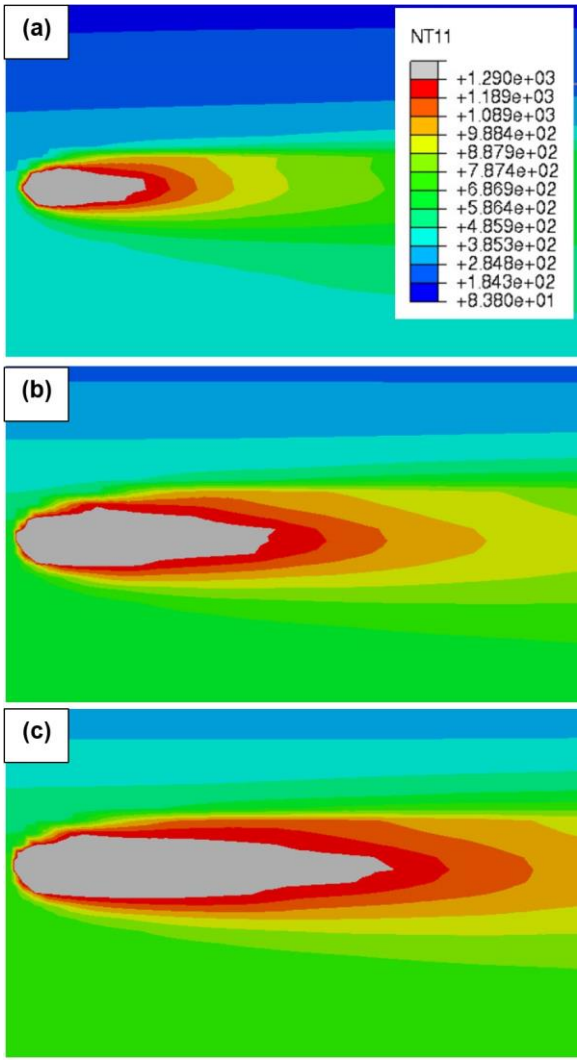

Figure 4-29 Melt pool size at a) 140 W b) 220 W c) 270 W

Effect of hatch spacing on RS

The increase of hatch spacing from 0.08 mm to 0.12 mm resulted in a temperature history profile, Figure 4-30, different from that under varying scan speed or laser power. At 0.08 mm, the distance between subsequent tracks is small so that the temperature of track n has peaked above the melting temperature three times

distinct by the first three peaks on the blue curve in Figure 4-30. As the hatch spacing increases to 0.1, there are only two peaks above the melting point. At the largest hatch spacing, there is not enough heat conducted between tracks to raise the temperature of track n, thus leading to only one peak above the melting point.

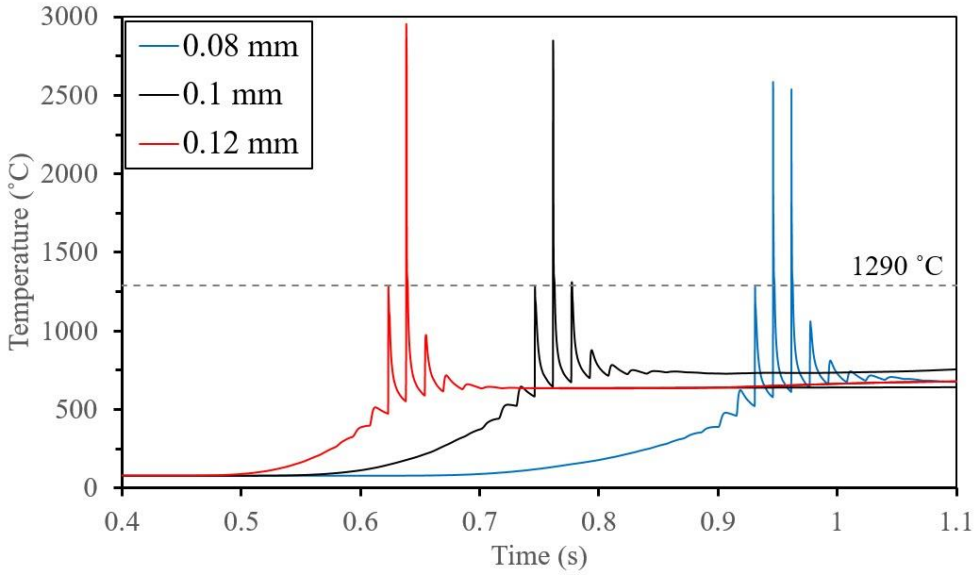

Figure 4-30 Temperature history for different hatch spacing at 220 W and 650 mm/s

The increase in hatch spacing, i.e., the decrease in energy density, caused the surface RS to drop from 389 MPa to 307 MPa, as shown in Figure 4-31. Conversely, the decrease in energy density by increasing the scan speed or decreasing the laser power led to an increase in surface RS, as shown in Figure 4-24 and Figure 4-27.

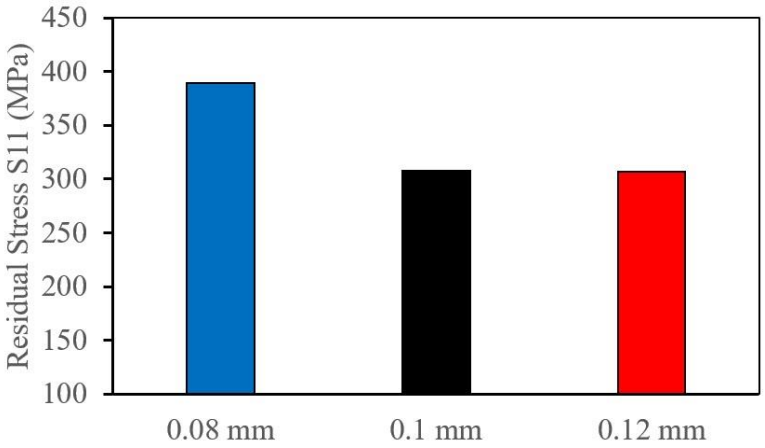

Figure 4-31 Effect of hatch spacing on surface RS

It is found that the surface RS trend is governed by the temperature gradient, which had a more dominant effect on the surface RS than the CR, as shown in Figure 4-32. As the hatch spacing increases from 0.08 mm to 0.1 mm, the temperature gradient decreases, hence the surface RS decrease. However, increasing the hatch spacing from 0.1 mm to 0.12 caused a reduction in the temperature gradient and an opposite increase in the CR, leading to a slightly lower surface RS.

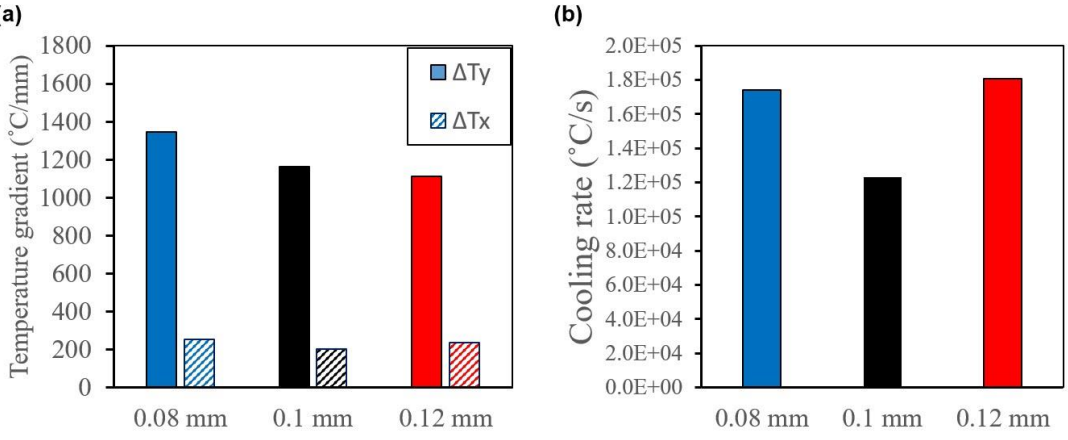

Figure 4-32 Effect of hatch spacing on a) Temperature gradient b) CR at 650 mm/s and 0.12 mm

Effect of same energy density

Studying the effects of laser power, scan speed, and hatch spacing on surface RS shows opposing effects, and consequently, non-monotonic trends for the effect of the energy density on the surface RS. Therefore, the effect of the individual process parameters needs to be investigated at constant energy density. The first set of simulations are performed at an energy density of $3.67 J/mm^2$ with a constant laser power of 220 W. Three levels for the scan speed, 500 mm/s, 600 mm/s, and 750 mm/s, are selected and three hatch spacing; 0.12 mm, 0.1 mm, and 0.08 mm, respectively.

The temperature history, presented in Figure 4-33, shows that all three parameter combinations resulted in multiple temperatures peaks above the melting point. However, it is noticed that the maximum peak temperature was achieved at the lowest scan speed of 500 mm/s and largest hatch spacing, which means that the scan speed has a more dominant effect on the maximum temperature versus the hatch spacing. Conversely, the hatch spacing has a more dominant effect when it comes to raising the temperature of the adjacent tracks, where the least hatch spacing resulted in two subsequent peaks with peak temperature highly above the melting point, as seen by the red curve in Figure 4-33.

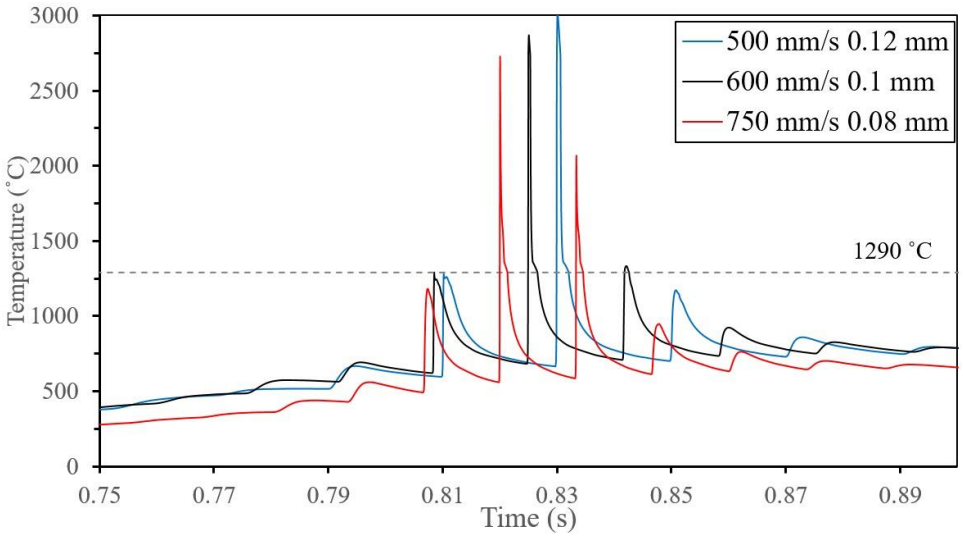

Figure 4-33 Temperature history at constant energy density 3.67 J/mm^2 with different scan speeds and hatch spacing

Examining the effect of the distinct temperature histories on the surface RS, presented in Figure 4-34, shows that the surface RS are lowest at 500 mm/s and 0.12 mm with a magnitude of 211 MPa and increases non-linearly to reach a maximum value of 454 MPa at 750 mm/s and 0.08 mm.

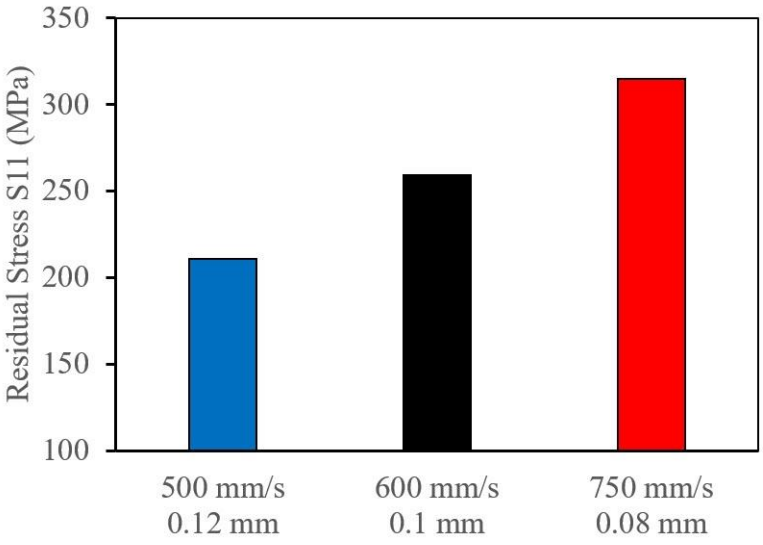

Figure 4-34 Surface RS at a constant energy density of 3.67 J/mm^2

The non-linear trend in the temperature gradient, shown in Figure 4-35, is the driver of the surface RS as the temperature gradient increases with the increase of scan speed and decrease of the hatch spacing. However, the CR decreases when the scan speed increases from 500 mm/s to 600 mm/s then increases beyond that point, which means that the temperature gradient mainly affects the surface RS. It can also be deducted that the scan speed has a more dominant effect than the hatch spacing on the surface RS since increasing the hatch spacing from 0.1 mm to 0.12 resulted in a negligible change in the surface RS, as shown in Figure 4-31. However, the variation of the scan speed caused the surface RS to increase prominently.

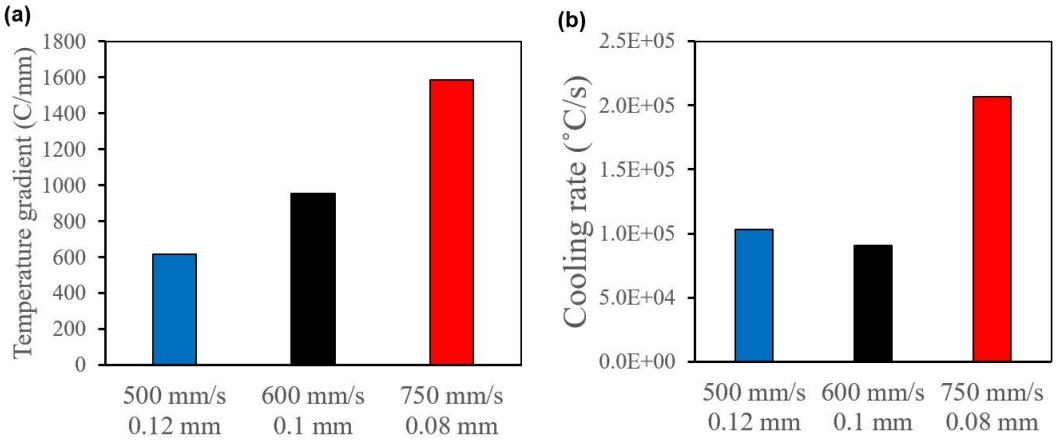

Figure 4-35 Effect of the same energy density of 3.67 J/mm^2 on a) Temperature gradient b) CR

To further investigate the effect of process parameters on surface RS with the same energy density, the laser power, and scan speed are varied while the hatch spacing is kept constant at 0.12 mm. Three power levels, 170 W, 220 W, and 270 W, and three scan speeds, 500 mm/s, 650 mm/s, and 800 mm/s to give an energy density of 2.82 67J/mm^2. All three parameter combinations resulted in almost identical

temperature profiles with a slight difference in the magnitude of the peaks, as shown in Figure 4-36.

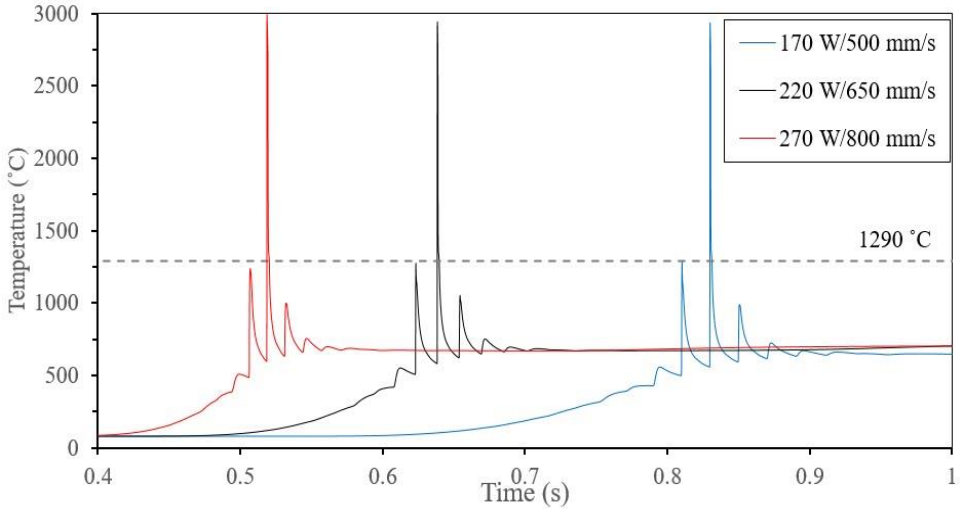

Figure 4-36 Temperature history at a constant energy density of 2.82 J/mm^2 with different laser powers and scan speeds

The results presented in sections 4.2.2 and 4.2.3 show that the increase in scan speed caused an increase in surface RS; conversely, the increase in laser power caused a decrease in surface RS. However, the combined effect of increasing the laser power and scan speed increased surface RS, as shown in Figure 4-37. Therefore, the scan speed has a more dominant effect on the surface RS than the laser power. To investigate the underlying causes that drive this trend in the surface RS, the temperature gradients and CRs are plotted in Figure 4-38.

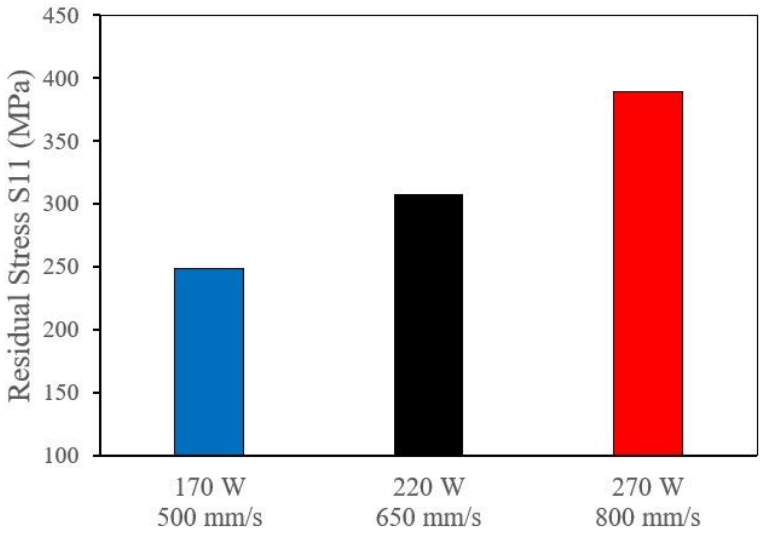

Figure 4-37 Surface RS at a constant energy density of 2.82 J/mm^2

The highest temperature gradient and CR were recorded at the lowest laser power and scan speed. Increasing the laser power and scan speed causes the temperature gradient and CR to decrease slightly and increase as the laser power and scan speed increase. Based on the previous observations, the surface RS followed the same trend as the temperature gradient. Therefore, if applied here, the surface RS should have been the highest at the 170 W/ 500 mm/s combination, decreasing at the 220 W/650 mm/s and then increasing again at 270 W/800 mm/s. However, this is not the case, as shown in Figure 4-37. Therefore, an in-depth investigation of the temperature and stress history is required.

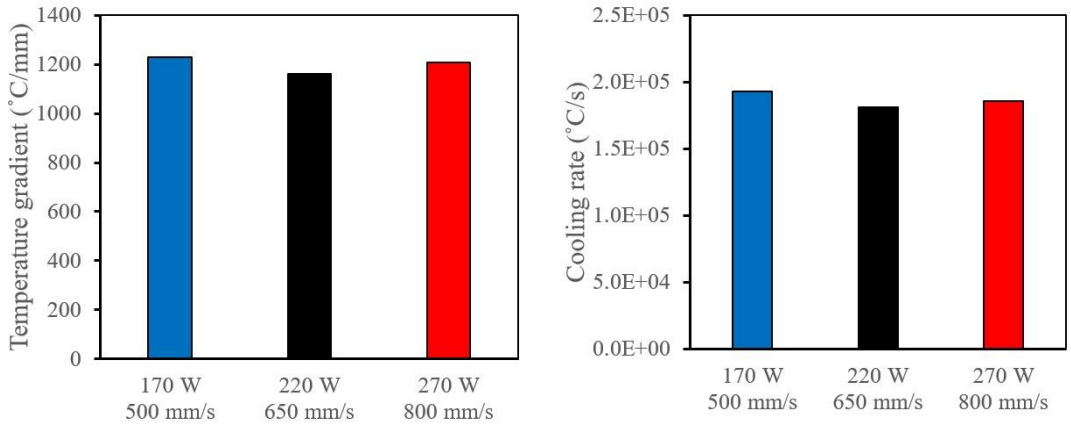

Figure 4-38 Effect of the same energy density of 2.82 J/mm^2 on a) Temperature gradient b) CR

The temperature and stress evolutions, plotted in Figure 4-39, show that after the laser melts track n, the material starts to solidify and generates high thermal stresses. The stress reaches a magnitude of 460 MPa, 440 MPa, and 445 MPa, corresponding to 170 W/500 mm/s, 220 W/650 mm/s, and 270 W/800 mm/s, respectively. The trend of these stresses is similar to the temperature gradients shown in Figure 4-38. However, the final stress state is not reached yet, and further stress changes occur with the subsequent laser passes. As heat is conducted from the subsequent tracks, the temperature of track n rises, thus relieving the previously generated stresses causing the cyclic change in stresses shown in the left column in Figure 4-39. As the laser travels far enough from track n, the magnitude of the cyclic stress decreases. The conducted heat will keep reaching track n until the laser has finished scanning the whole layer; hence the more time it takes for the laser to scan the layer, the more heat is conducted and consequently more reduction in the stress magnitude. The laser scanning time from track n to the end of the layer is

calculated at 0.84 s, 0.6 s, and 0.52 s, corresponding the 500 mm/s, 650 mm/s, and 800 mm/s, respectively as shown in the right column of Figure 4-39. The difference in time durations allows the conducted heat to reduce the stresses to -80 MPa, -21 MPa, and 70 MPa, respectively. Once the laser finishes scanning temperature of the whole layer cools down for the same period, thus raising the stresses to their final state, where the lowest stress is recorded at 170 W and 500 mm/s.

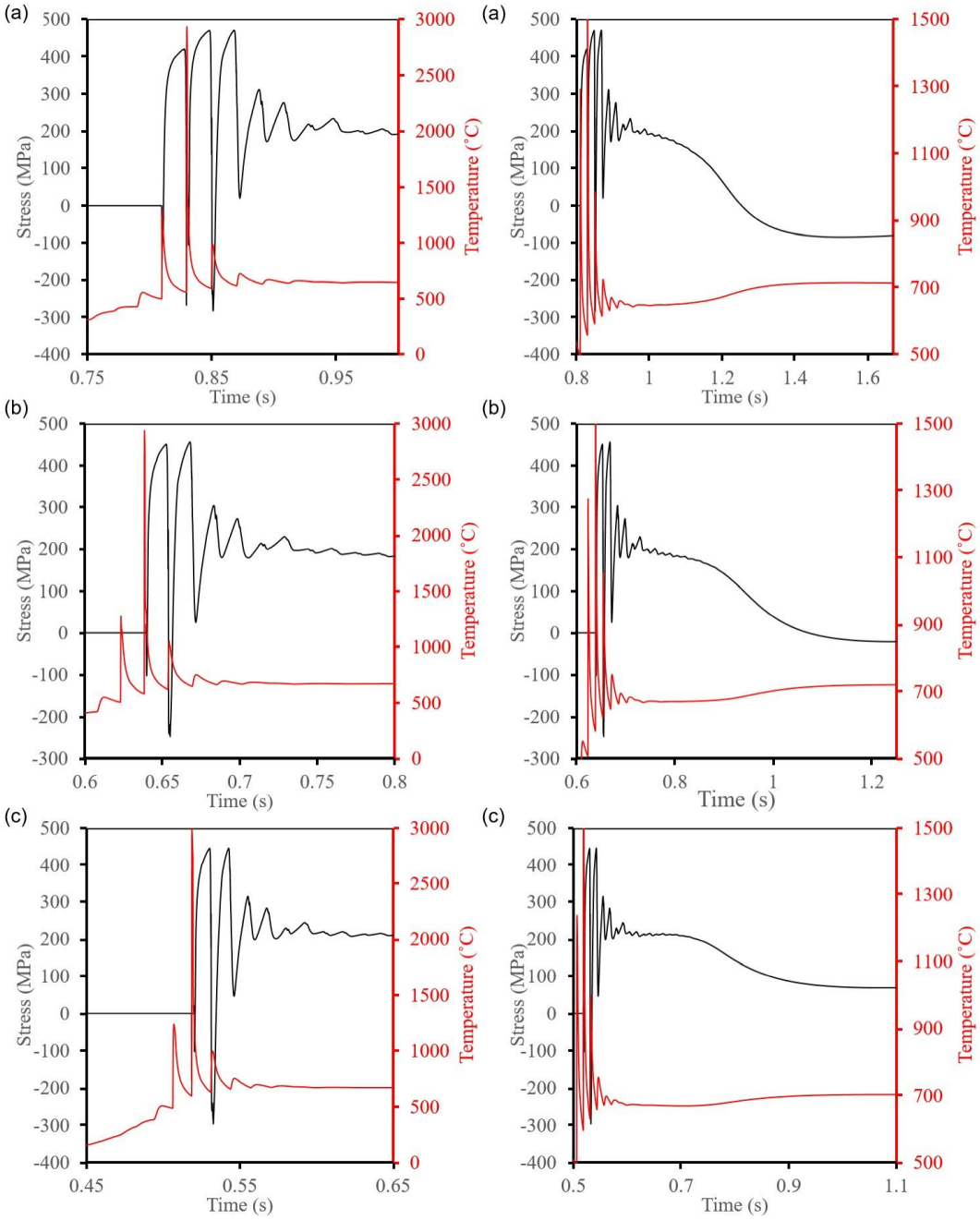

Figure 4-39 Temperature and stress evolution at energy density 2.82 J/mm^2

a) 170 W, 500 mm/s b) 220 W, 650 mm/s c) 270 W, 800 mm/s

4.4.3. Part Scale Model

Tensile test

Tensile testing of as-built condition showcased the sample undergoing ductile failure as presented by the true stress-strain curve shown in Figure 4-40. The yield strength at 0.2% elongation was 650 MPa, Young's modulus of 171 GPa, and the ultimate strength was 1191 MPa. By fitting the data to the Ramberg-Osgood equation, the strength coefficient was found to be 1618 MPa, and the strain hardening exponent was 0.243.

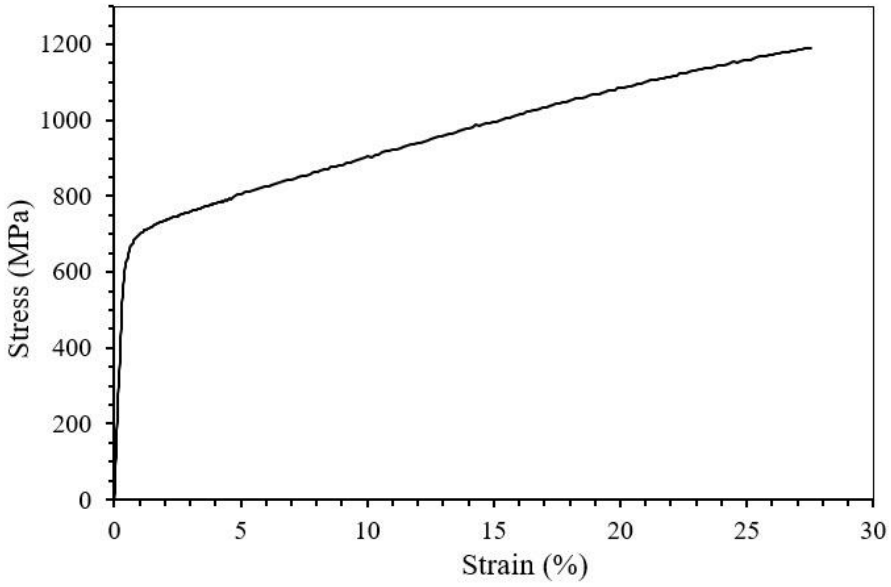

Figure 4-40 True stress-strain curve

The J-C model's A, B, and n parameters were changed to the new value to compare the predicted RS in-depth profile with the experimental data. Due to the absence of tensile testing data for different process parameters, the same values of A, B, and n were used for all simulated process parameters. Additionally, since the measured

Young's modulus is lower than its values reported in the literature, the newly measured value was used in the current study. Finally, Young's modulus was measured at room temperature. Still, Young's modulus data from the literature were offset by the difference between measured to get its values at high temperature. Their reported values at room temperature, as shown in Figure 4-41.

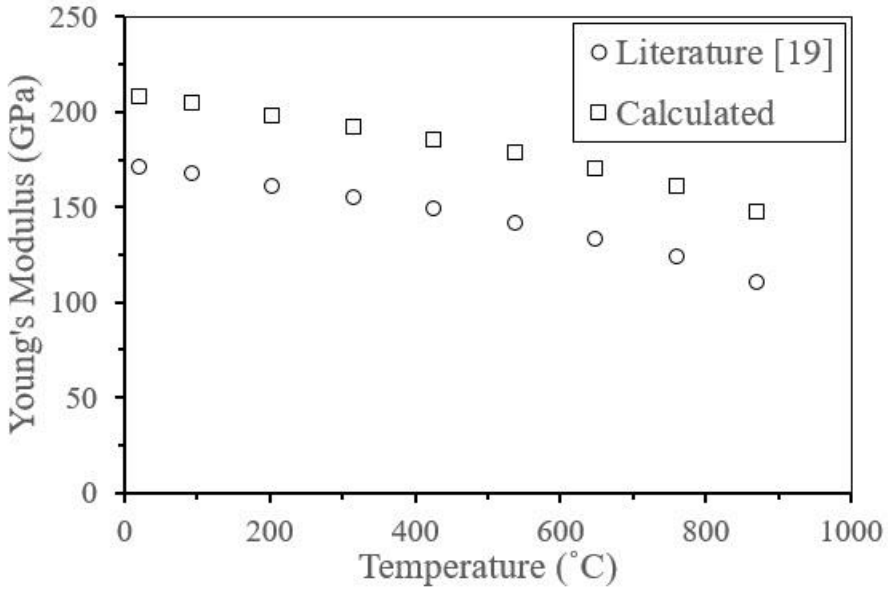

Figure 4-41 Elastic modulus variation with temperature

Numerical results

The part scale model is used to predict the RS distribution across the whole part and the deflection of the part, which will affect its dimensional accuracy. The evolution of the Mises stress can be seen in Figure 4-42 at different time instances. At a time of 667 s, i.e., after a 4 mm height, Figure 4-42 (a), the maximum stresses are predicted at the bottom of the part, at the interface between the part and the substrate. As the number of layers increases to reach 10 mm, more heat is added to

the top surface of the part and conducts downwards, causing the stress magnitude to decrease, as shown in Figure 4-42 (b). Once the laser exposure is done, the part begins to cool down for 600 s, at which point the stresses in the part increase again, Figure 4-42 (c), to reach its maximum value. Once the part is separated from the substrate, the stresses magnitudes decrease to reach their final value, as shown in Figure 4-42 (d)

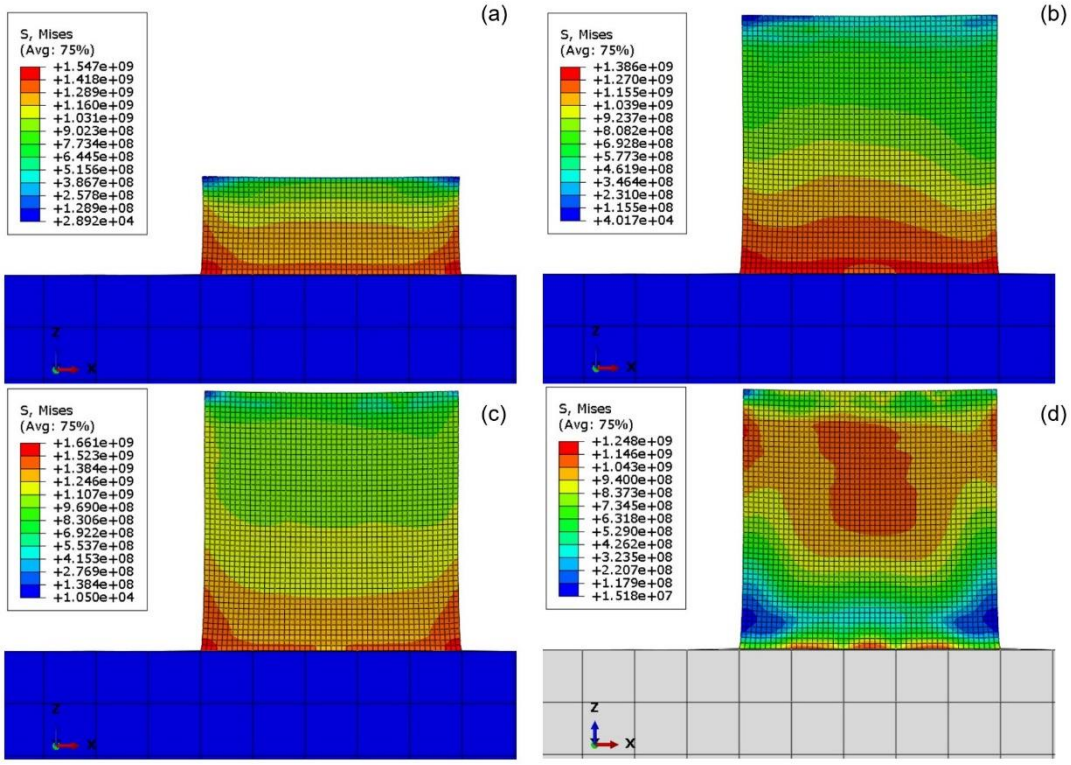

Figure 4-42 Evolution of the part scale Mises stress at a) 667 s b) 1714 s c) 2310 s d) after separation from the build plate at 220 W, 650 mm/s, and 0.12 mm

The RS were calculated at the end of the building process after a cooling time of 600 s, and separation from the build plate. The RS were calculated by averaging

the stresses across an area with a diameter of 2 mm. The predicted in-depth RS profile is validated by comparing to experimentally measured RS profile at two laser powers, 220 W and 140 W, scan speed of 650 mm/s and hatch spacing of 0.12 mm, as shown in Figure 4-43 and Figure 4-44, respectively.

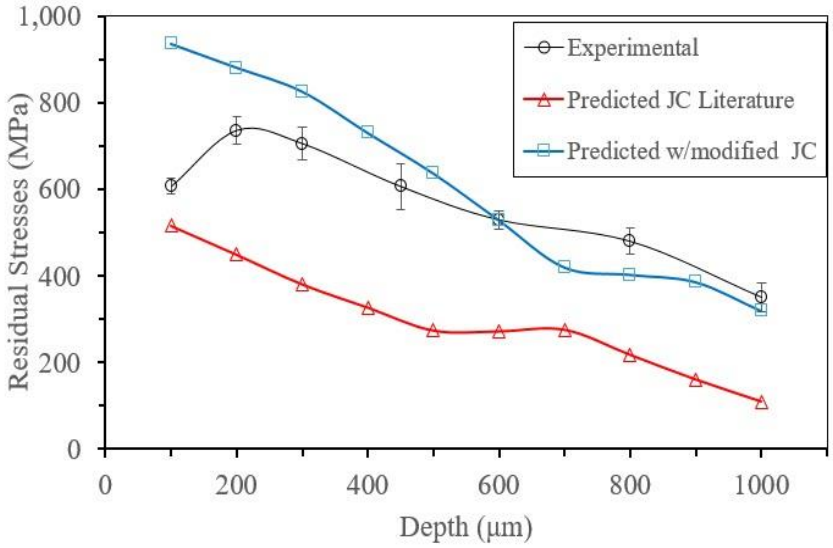

Figure 4-43 In-depth RS prediction at 220 W, 650 mm/s and 0.12 mm

Two RS profiles are compared to the experimental results; the first RS profile is calculated using the J-C parameters found in the literature [65]. The second RS profile is predicted with J-C parameters partially adjusted using data from tensile testing of IN625 manufactured using LPBF. It is found that the first profile under predicts the in-depth RS, while the second profile over predicts the RS profile. However, both profiles follow the same trend as the experimental results. These results highlight the need for J-C plasticity parameters for LPBF manufactured IN625 to predict the generated stresses better.

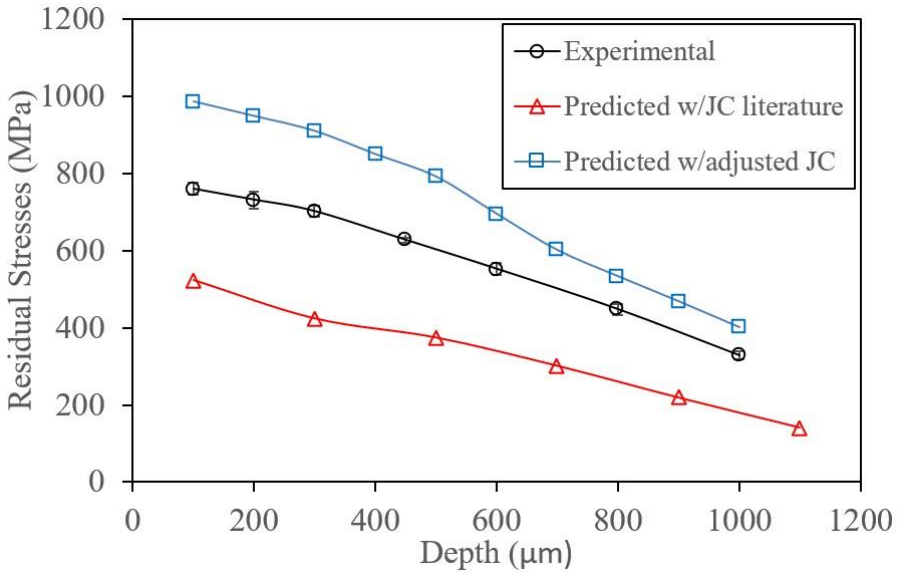

Figure 4-44 In-depth RS at 140 W, 650 mm/s and 0.12 mm

Prediction of the in-depth RS with increasing the hatch spacing shows that the hatch spacing does not affect the RS profile, as shown in Figure 4-45, regardless of the laser power used. The hatch effect absence could be attributed to using a point source heat model, which does not generate the teardrop shape of a melt pool, so the effect of melt pool overlap is negated and would not affect the predicted RS.

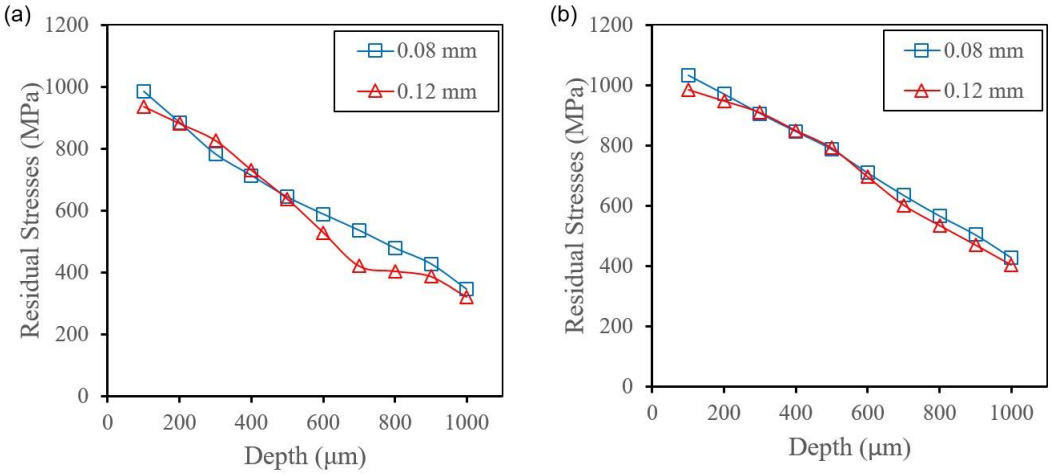

Figure 4-45 Effect of hatch spacing on in-depth RS at 650 mm/s and a) 220 W b) 140 W

Examining the effect of laser power on the in-depth RS and deflection show that increasing the laser power from 140 W to 270 W decreases the in-depth RS, as seen in Figure 4-46. However, the generated RS for all three laser powers are highly tensile down to a depth of 1 mm from the surface. This trend is similar to that predicted from the layer model for the surface RS, as presented in section 4.2.3. Increasing the scan speed also showed a similar trend to the results reported in section 4.2.2. The in-depth RS increased with increasing the scan speed, as shown in Figure 4-47 (a).

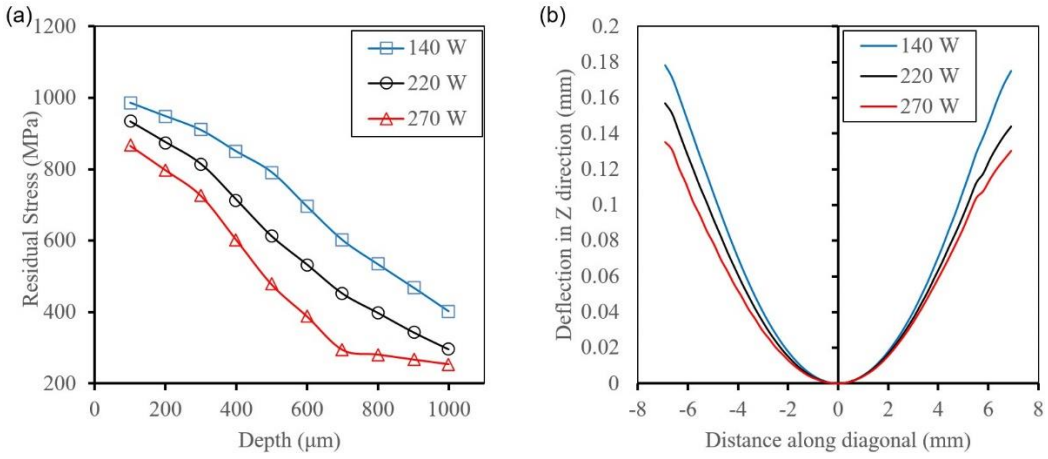

Figure 4-46 Effect of laser power on a) In-depth RS b) Deflection in the Z direction

The deflection of the top surface in the Z direction is of particular interest as it increases the chances of the recoater impacting the part and damaging or breaking the part off. Therefore, the deflection was extracted along the diagonal of the part, as shown in Figure 4-48 (a). It is observed that after cutting the part from the build plate, the edges of the part deflect upwards. At the same time, the center sinks in, resulting in a parabola-shaped surface.

Examining the effect of process parameters on the deflection shows that the laser power has the same effect on the deflection as on RS, as seen in Figure 4-46 (b), where the lowest power resulted in the largest deflection. Conversely, the scan speed increased top surface deflection, as shown in Figure 4-47 (b). This is because the deflection of the part edges means that part of the generated stresses is released; hence, the magnitude of the stresses is always lower at the outer edges.

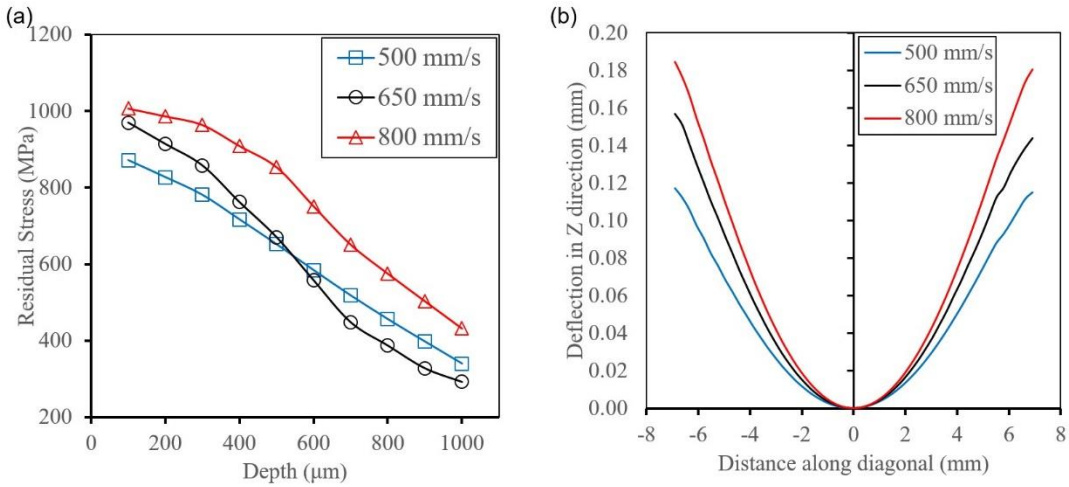

Figure 4-47 Effect of scan speed on a) In-depth RS b) Deflection in the Z direction

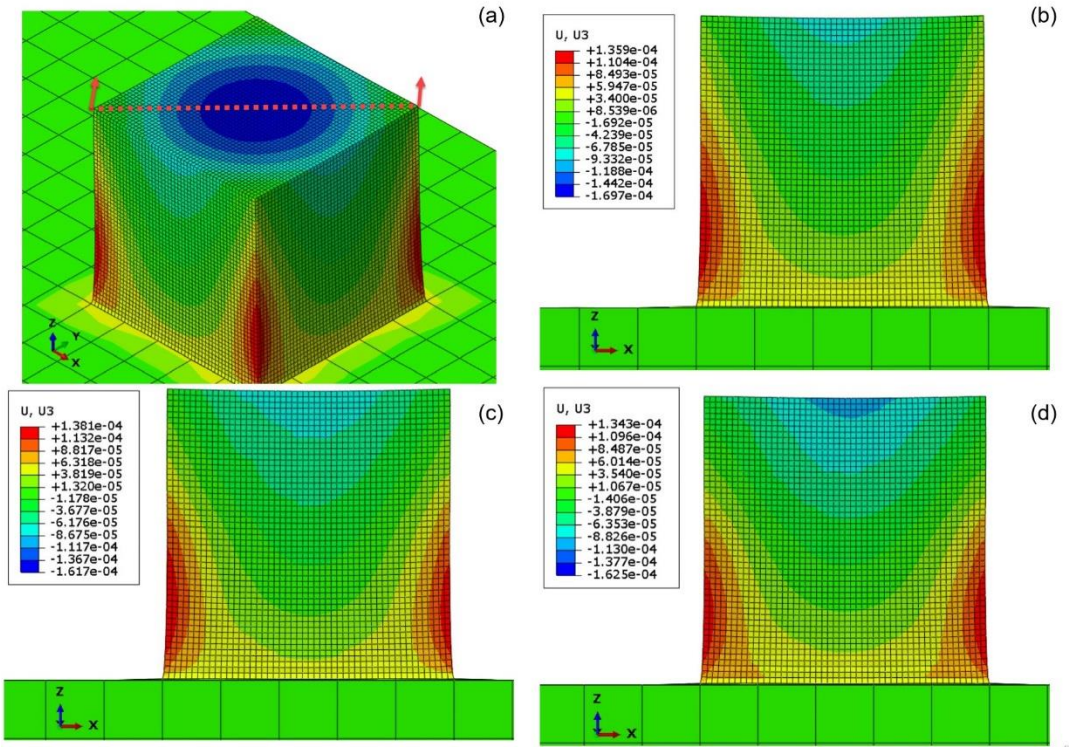

Figure 4-48 Deflection in Z direction at 650 mm/s and 0.12 mm a) Diagonal direction b) 140 W c) 220 W d) 270 W

4.5. Conclusion

The current work presented a systematic approach to different modeling scales of laser powder bed fusion of IN625, including single tracks, multi-tracks, and multi-layer models. The shortcomings found in the literature were addressed by employing a Gaussian volumetric heat source model, a material model to accurately represent the thermos-physical properties of the powder layer, artificial inclusion of the Marangoni effect, and the use of the Johnson-Cook plasticity model to include the strain hardening, strain rate effect, and thermal softening of the material. The results from all models were validated with multiple experimental results,

including melt pool dimensions, temperature measurements using a 2-color pyrometer, and in-depth residual stress profiles. The main findings can be summarized as follows:

- The exponential decay volumetric heat source, with an artificial increase in thermal conductivity to account for the Marangoni effects, resulted in the best prediction of melt pool dimensions.
- The maximum residual stress is generated along the laser scan direction, governed by the temperature gradient and cooling rate in the hatch direction.
- Increasing the scan speed resulted in an increase in the surface tensile residual stress due to the increase in the temperature gradient
- The surface tensile residual stress decreases with the increase in hatch spacing.
- At the same energy density, the thermal stresses are mostly affected by the scan speed, laser power, and hatch spacing.
- Although the high cooling rate will increase the strain rate experienced by the material, the evolution of the stresses is mainly dominated by the temperature gradient
- The cyclic temperature governs the final state of the stress during the non-linear phase and the cooling rate during the linear phase.
- In-depth residual stresses on a part scale and the top surface deflection exhibit the same trend, where increasing the laser power lowers the residual stresses.

- Increasing the scan speed increases the in-depth residual stresses as well as the top surface deflection.

References

[1] ISO/ASTM52900-15, "Standard Terminology for Additive Manufacturing – General Principles – Terminology," ed. ASTM International, West Conshohocken, PA, 2015, www.astm.org.

[2] T. DebRoy, H. Wei, J. Zuback, T. Mukherjee, J. Elmer, J. Milewski, *et al.*, "Additive manufacturing of metallic components–process, structure and properties," *Progress in Materials Science,* vol. 92, pp. 112-224, 2018.

[3] A. Armillotta, R. Baraggi, and S. Fasoli, "SLM tooling for die casting with conformal cooling channels," *The International Journal of Advanced Manufacturing Technology,* vol. 71, pp. 573-583, 2014.

[4] A. AB, "Case study: additive manufacturing of aerospace brackets," *Advanced Materials & Processes,* vol. 19, 2013.

[5] R. Huang, M. Riddle, D. Graziano, J. Warren, S. Das, S. Nimbalkar, *et al.*, "Energy and emissions saving potential of additive manufacturing: the case of lightweight aircraft components," *Journal of Cleaner Production,* vol. 135, pp. 1559-1570, 2016.

[6] R. Leal, F. Barreiros, L. Alves, F. Romeiro, J. Vasco, M. Santos, *et al.*, "Additive manufacturing tooling for the automotive industry," *The International Journal of Advanced Manufacturing Technology,* vol. 92, pp. 1671-1676, 2017.

[7] B. Zhang and Y. Li, "Q. Bai, Defect Formation Mechanisms in Selective Laser Melting," *A Review, Chinese J. Mech. Eng,* vol. 30, pp. 515-527, 2017.

[8] G. Piscopo, A. Salmi, and E. Atzeni, "On the quality of unsupported overhangs produced by laser powder bed fusion," *International Journal of Manufacturing Research,* vol. 14, pp. 198-216, 2019.

[9] M. Balbaa, A. Ghasemi, E. Fereiduni, M. Elbestawi, S. Jadhav, and J.-P. Kruth, "Role of Powder Particle Size on Laser Powder Bed Fusion Processability of AlSi10Mg Alloy," *Additive Manufacturing,* p. 101630, 2020.

[10] L. E. Criales, Y. M. Arısoy, B. Lane, S. Moylan, A. Donmez, and T. Özel, "Laser powder bed fusion of nickel alloy 625: Experimental investigations of effects of process parameters on melt pool size and shape with spatter analysis," *International Journal of Machine Tools and Manufacture,* 2017.

[11] A. H. Maamoun, Y. F. Xue, M. A. Elbestawi, and S. C. Veldhuis, "Effect of selective laser melting process parameters on the quality of al alloy parts: Powder

characterization, density, surface roughness, and dimensional accuracy," *Materials,* vol. 11, p. 2343, 2018.

[12] M. Narvan, K. S. Al-Rubaie, and M. Elbestawi, "Process-structure-property relationships of AISI H13 tool steel processed with selective laser melting," *Materials,* vol. 12, p. 2284, 2019.

[13] M. P. Sealy, G. Madireddy, R. E. Williams, P. Rao, and M. Toursangsaraki, "Hybrid processes in additive manufacturing," *Journal of manufacturing Science and Engineering,* vol. 140, 2018.

[14] S. Han, F. Salvatore, J. Rech, and J. Bajolet, "Abrasive flow machining (AFM) finishing of conformal cooling channels created by selective laser melting (SLM)," *Precision Engineering,* vol. 64, pp. 20-33, 2020.

[15] J.-P. Kruth, J. Deckers, E. Yasa, and R. Wauthlé, "Assessing and comparing influencing factors of residual stresses in selective laser melting using a novel analysis method," *Proceedings of the institution of mechanical engineers, Part B: Journal of Engineering Manufacture,* vol. 226, pp. 980-991, 2012.

[16] M. Narvan, A. Ghasemi, E. Fereiduni, S. Kendrish, and M. Elbestawi, "Part deflection and residual stresses in laser powder bed fusion of H13 tool steel," *Materials & Design,* vol. 204, p. 109659, 2021.

[17] Y. Yang, M. Allen, T. London, and V. Oancea, "Residual strain predictions for a powder bed fusion Inconel 625 single cantilever part," *Integrating Materials and Manufacturing Innovation,* vol. 8, pp. 294-304, 2019.

[18] T. Simson, A. Emmel, A. Dwars, and J. Böhm, "Residual stress measurements on AISI 316L samples manufactured by selective laser melting," *Additive Manufacturing,* vol. 17, pp. 183-189, 2017.

[19] J.-P. Kruth, P. Mercelis, J. Van Vaerenbergh, L. Froyen, and M. Rombouts, "Binding mechanisms in selective laser sintering and selective laser melting," *Rapid prototyping journal,* vol. 11, pp. 26-36, 2005.

[20] A. Hussein, L. Hao, C. Yan, and R. Everson, "Finite element simulation of the temperature and stress fields in single layers built without-support in selective laser melting," *Materials & Design,* vol. 52, pp. 638-647, 2013.

[21] C. Fu and Y. Guo, "3-Dimensional Finite Element Modeling of Selective Laser Melting Ti-6Al-4V Alloy," in *25th Annual International Solid Freeform Fabrication Symposium*, 2014.

[22] I. Roberts, C. Wang, R. Esterlein, M. Stanford, and D. Mynors, "A three-dimensional finite element analysis of the temperature field during laser melting of metal powders in additive layer manufacturing," *International Journal of Machine Tools and Manufacture,* vol. 49, pp. 916-923, 2009.

[23] L. Dong, A. Makradi, S. Ahzi, and Y. Remond, "Three-dimensional transient finite element analysis of the selective laser sintering process," *Journal of materials processing technology,* vol. 209, pp. 700-706, 2009.

[24] L. Dong, J. Correia, N. Barth, and S. Ahzi, "Finite element simulations of temperature distribution and of densification of a titanium powder during metal laser sintering," *Additive Manufacturing,* vol. 13, pp. 37-48, 2017.

[25] R. Andreotta, L. Ladani, and W. Brindley, "Finite element simulation of laser additive melting and solidification of Inconel 718 with experimentally tested thermal properties," *Finite Elements in Analysis and Design,* vol. 135, pp. 36-43, 2017.

[26] S. A. Khairallah and A. Anderson, "Mesoscopic simulation model of selective laser melting of stainless steel powder," *Journal of Materials Processing Technology,* vol. 214, pp. 2627-2636, 2014.

[27] T. Mukherjee, H. Wei, A. De, and T. DebRoy, "Heat and fluid flow in additive manufacturing—Part I: Modeling of powder bed fusion," *Computational Materials Science,* vol. 150, pp. 304-313, 2018.

[28] J. Robichaud, T. Vincent, B. Schultheis, and A. Chaudhary, "Integrated Computational Materials Engineering to Predict Melt-Pool Dimensions and 3D Grain Structures for Selective Laser Melting of Inconel 625," *Integrating Materials and Manufacturing Innovation,* vol. 8, pp. 305-317, 2019.

[29] M. Xia, D. Gu, G. Yu, D. Dai, H. Chen, and Q. Shi, "Influence of hatch spacing on heat and mass transfer, thermodynamics and laser processability during additive manufacturing of Inconel 718 alloy," *International Journal of Machine Tools and Manufacture,* vol. 109, pp. 147-157, 2016.

[30] E. R. Denlinger, V. Jagdale, G. Srinivasan, T. El-Wardany, and P. Michaleris, "Thermal modeling of Inconel 718 processed with powder bed fusion and experimental validation using in situ measurements," *Additive Manufacturing,* vol. 11, pp. 7-15, 2016.

[31] L. E. Criales, Y. M. Arısoy, B. Lane, S. Moylan, A. Donmez, and T. Özel, "Predictive modeling and optimization of multi-track processing for laser powder bed fusion of nickel alloy 625," *Additive Manufacturing,* vol. 13, pp. 14-36, 2017.

[32] M. Masoomi, S. M. Thompson, and N. Shamsaei, "Laser powder bed fusion of Ti-6Al-4V parts: Thermal modeling and mechanical implications," *International Journal of Machine Tools and Manufacture,* vol. 118, pp. 73-90, 2017.

[33] C. Chen, J. Yin, H. Zhu, Z. Xiao, L. Zhang, and X. Zeng, "Effect of overlap rate and pattern on residual stress in selective laser melting," *International Journal of Machine Tools and Manufacture,* vol. 145, p. 103433, 2019.

[34] A. Olleak and Z. Xi, "Efficient lpbf process simulation using finite element modeling with adaptive remeshing for distortions and residual stresses prediction," *Manufacturing Letters,* vol. 24, pp. 140-144, 2020.

[35] Q. Chen, X. Liang, D. Hayduke, J. Liu, L. Cheng, J. Oskin, *et al.*, "An inherent strain based multiscale modeling framework for simulating part-scale residual deformation for direct metal laser sintering," *Additive Manufacturing,* vol. 28, pp. 406-418, 2019.

[36] M. Gouge, E. Denlinger, J. Irwin, C. Li, and P. Michaleris, "Experimental validation of thermo-mechanical part-scale modeling for laser powder bed fusion processes," *Additive Manufacturing,* vol. 29, p. 100771, 2019.

[37] J. A. Turner, S. S. Babu, and C. Blue, "Advanced Simulation for Additive Manufacturing: Meeting Challenges Through Collaboration," 2015.

[38] N. P. Lavery, S. G. Brown, J. Sienz, J. Cherry, and F. Belblidia, "A review of Computational Modelling of Additive Layer Manufacturing–multi-scale and multi-physics," *Sustainable Design and Manufacturing,* vol. 651, p. 673, 2014.

[39] E. Mirkoohi, J. Ning, P. Bocchini, O. Fergani, K.-N. Chiang, and S. Y. Liang, "Thermal modeling of temperature distribution in metal additive manufacturing considering effects of build layers, latent heat, and temperature-sensitivity of material properties," *Journal of Manufacturing and Materials Processing,* vol. 2, p. 63, 2018.

[40] E. Neiva, M. Chiumenti, M. Cervera, E. Salsi, G. Piscopo, S. Badia, *et al.*, "Numerical modelling of heat transfer and experimental validation in powder-bed fusion with the virtual domain approximation," *Finite Elements in Analysis and Design,* vol. 168, p. 103343, 2020.

[41] L. E. Criales, Y. M. Arısoy, and T. Özel, "Sensitivity analysis of material and process parameters in finite element modeling of selective laser melting of Inconel 625," *The International Journal of Advanced Manufacturing Technology,* vol. 86, pp. 2653-2666, 2016.

[42] Z. Gan, Y. Lian, S. E. Lin, K. K. Jones, W. K. Liu, and G. J. Wagner, "Benchmark study of thermal behavior, surface topography, and dendritic microstructure in selective laser melting of Inconel 625," *Integrating Materials and Manufacturing Innovation,* vol. 8, pp. 178-193, 2019.

[43] Z. Zhao, L. Li, L. Tan, P. Bai, J. Li, L. Wu, *et al.*, "Simulation of Stress Field during the Selective Laser Melting Process of the Nickel-Based Superalloy, GH4169," *Materials,* vol. 11, p. 1525, 2018.

[44] T. Heeling, M. Cloots, and K. Wegener, "Melt pool simulation for the evaluation of process parameters in selective laser melting," *Additive Manufacturing,* vol. 14, pp. 116-125, 2017.

[45] Z. Xiao, C. Chen, H. Zhu, Z. Hu, B. Nagarajan, L. Guo, *et al.*, "Study of residual stress in selective laser melting of Ti6Al4V," *Materials & Design,* vol. 193, p. 108846, 2020.

[46] S. W. Churchill, "A comprehensive correlating equation for forced convection from flat plates," *AIChE Journal*, vol. 22, pp. 264-268, 1976.

[47] S. S. Sih and J. W. Barlow, "Emissivity of powder beds," in *1995 International Solid Freeform Fabrication Symposium*, 1995.

[48] S. S. Sih and J. W. Barlow, "The prediction of the emissivity and thermal conductivity of powder beds," *Particulate science and technology*, vol. 22, pp. 427-440, 2004.

[49] S. Heugenhauser and E. Kaschnitz, "Density and thermal expansion of the nickel-based superalloy INCONEL 625 in the solid and liquid states," *High Temperatures--High Pressures*, vol. 48, 2019.

[50] M. Balbaa, M. Elbestawi, and J. McIsaac, "An experimental investigation of surface integrity in selective laser melting of Inconel 625," *The International Journal of Advanced Manufacturing Technology*, vol. 104, pp. 3511-3529, 2019.

[51] N. ZIMINA and I. FOMICHEVA, "THERMAL ACCOMMODATION IN THE GAS-METAL SYSTEM. 3. NITROGEN," *ZHURNAL FIZICHESKOI KHIMII*, vol. 66, pp. 3184-3190, 1992.

[52] J. Goldak, A. Chakravarti, and M. Bibby, "A new finite element model for welding heat sources," *Metallurgical transactions B*, vol. 15, pp. 299-305, 1984.

[53] P. Fischer, V. Romano, H.-P. Weber, N. Karapatis, E. Boillat, and R. Glardon, "Sintering of commercially pure titanium powder with a Nd: YAG laser source," *Acta Materialia*, vol. 51, pp. 1651-1662, 2003.

[54] M. Markl and C. Körner, "Multiscale Modeling of Powder Bed–Based Additive Manufacturing," *Annual Review of Materials Research*, vol. 46, pp. 93-123, 2016.

[55] Y. Zhao, Y. Koizumi, K. Aoyagi, D. Wei, K. Yamanaka, and A. Chiba, "Molten pool behavior and effect of fluid flow on solidification conditions in selective electron beam melting (SEBM) of a biomedical Co-Cr-Mo alloy," *Additive Manufacturing*, vol. 26, pp. 202-214, 2019.

[56] Y. Miyata, M. Okugawa, Y. Koizumi, and T. Nakano, "Inverse Columnar-Equiaxed Transition (CET) in 304 and 316L Stainless Steels Melt by Electron Beam for Additive Manufacturing (AM)," *Crystals*, vol. 11, p. 856, 2021.

[57] L. Ladani, J. Romano, W. Brindley, and S. Burlatsky, "Effective liquid conductivity for improved simulation of thermal transport in laser beam melting powder bed technology," *Additive Manufacturing*, vol. 14, pp. 13-23, 2017.

[58] M. Van Elsen, F. Al-Bender, and J. P. Kruth, "Application of dimensional analysis to selective laser melting," *Rapid Prototyping Journal*, 2008.

[59] G. Piscopo, E. Atzeni, and A. Salmi, "A hybrid modeling of the physics-driven evolution of material addition and track generation in laser powder directed energy deposition," *Materials*, vol. 12, p. 2819, 2019.

[60] *Abaqus User's Manual*. Available: https://www.3ds.com/products-services/simulia/support/documentation

[61] X. Song, S. Feih, W. Zhai, C.-N. Sun, F. Li, R. Maiti, *et al.*, "Advances in additive manufacturing process simulation: Residual stresses and distortion predictions in complex metallic components," *Materials & Design*, vol. 193, p. 108779, 2020.

[62] A. Simulia, "6.19," *User's Manual,* 2019.

[63] *Special Metals, Inconel Alloy 625*. Available: https://www.specialmetals.com/assets/smc/documents/alloys/inconel/inconel-alloy-625.pdf

[64] G. R. Johnson, "A constitutive model and data for materials subjected to large strains, high strain rates, and high temperatures," *Proc. 7th Inf. Sympo. Ballistics*, pp. 541-547, 1983.

[65] M. Lotfi, M. Jahanbakhsh, and A. A. Farid, "Wear estimation of ceramic and coated carbide tools in turning of Inconel 625: 3D FE analysis," *Tribology International*, vol. 99, pp. 107-116, 2016.

[66] "ASTM E8 / E8M-21, Standard Test Methods for Tension Testing of Metallic Materials," ed. West Conshohocken, PA: ASTM International, 2021.

[67] W. Ramberg and W. R. Osgood, "Description of stress-strain curves by three parameters," 1943.

[68] B. Lane, J. Heigel, R. Ricker, I. Zhirnov, V. Khromschenko, J. Weaver, *et al.*, "Measurements of melt pool geometry and cooling rates of individual laser traces on IN625 bare plates," *Integrating Materials and Manufacturing Innovation*, pp. 1-15, 2020.

[69] J. Dilip, M. A. Anam, D. Pal, and B. Stucker, "A short study on the fabrication of single track deposits in SLM and characterization."

[70] H. Rezaeifar and M. Elbestawi, "On-line melt pool temperature control in L-PBF additive manufacturing," *The International Journal of Advanced Manufacturing Technology*, vol. 112, pp. 2789-2804, 2021.

[71] S. Li, H. Xiao, K. Liu, W. Xiao, Y. Li, X. Han, *et al.*, "Melt-pool motion, temperature variation and dendritic morphology of Inconel 718 during pulsed-and continuous-wave laser additive manufacturing: A comparative study," *Materials & design*, vol. 119, pp. 351-360, 2017.

[72] G. S. Schajer, *Practical residual stress measurement methods*: John Wiley & Sons, 2013.

[73] M. Balbaa, S. Mekhiel, M. Elbestawi, and J. McIsaac, "On selective laser melting of Inconel 718: Densification, surface roughness, and residual stresses," *Materials & Design*, p. 108818, 2020.

[74] P. Mercelis and J.-P. Kruth, "Residual stresses in selective laser sintering and selective laser melting," *Rapid Prototyping Journal*, vol. 12, pp. 254-265, 2006.

[75] S. Katayama, *Handbook of laser welding technologies*: Elsevier, 2013.

Chapter 5

Influence of Shot Peening on the Fatigue Performance of Laser Powder Bed Fusion Fabricated IN625 and IN718 Superalloys

Complete Citation:

Balbaa, M., Ghasemi, A., Fereiduni, E., Al-Rubaie, K., Elbestawi, M. Influence of Shot Peening on the Fatigue Performance of Laaser Powder Bed Fusion Fabricated IN625 and IN718 Superalloys. *Submitted to the special issue: Additive Manufacturing Process Qualification (AMPQ) of the Journal of Materials Processing Technology*, 2022.

Relative Contributions:

M. Balbaa: Performed experiments, data collection and analysis. Wrote the first draft of the manuscript.

A. Ghasemi: Performed experimental investigations, data collection and analysis, co-wrote the manuscript.

E. Fereiduni: Performed experimental investigations, data collection and analysis, co-wrote the manuscript.

K. Al-Rubaie: Methodology, and co-wrote the manuscript.

M. Elbestawi: Supervision, and revised the manuscript

Abstract:

This study aims at investigating the possibility of fabricating IN625 and IN718 Ni-based superalloys with acceptable room temperature fatigue lives using the laser powder bed fusion (LPBF) process. For this purpose, several test coupons were printed and compared in terms of (i) density, (ii) tensile strength, (iii) surface roughness, and (iv) residual stress to find the optimum sets of process parameters for both IN625 and IN718 superalloys. The optimum process parameters were utilized to print the fatigue test specimens, tested in as-built, and shot-peened conditions at multiple stress levels. The S-N curves were generated for both IN625 and IN718 in as-built and shot-peened states and compared to their wrought counterparts. The fatigue results obtained for each case were scrutinized by discussing the factors contributing to the fatigue performance, such as (i) surface roughness, (ii) residual stress state and magnitude, (iii) grain and sub-grain structure, and (iv) non-equilibrium phases in the microstructure. The fatigue life of both superalloys in as-built condition was inferior to their unnotched wrought counterparts, though exceeding the notched ones with a stress concentration factor of three. After shot peening, it was found out that the maximum stress level at infinite fatigue life for IN625 is the same as its unnotched annealed wrought counterpart. However, for shot-peened IN718, the fatigue life was still lower than that of the solution-annealed and aged wrought specimen in unnotched condition due to the absence of γ' and γ'' strengthening agents. The findings of this study suggest that the LPBF fabricated IN625 in the shot-peened state can be reliably

used as a substitute for annealed and wrought IN625 counterparts without the need for surface smoothening or performing heat treatments. Regarding the shot-peened IN718, its lower fatigue life than the solution-annealed and aged wrought counterpart has to be taken into account in the design stage upon skipping the heat treatment.

Keywords:

Fatigue performance; IN625 and IN718 superalloys; Shot peening; Residual stress, surface roughness; Laser powder bed fusion process.

Acknowledgment:

The authors would like to thank the Center for Advanced Nuclear Systems (CANS) at McMaster University for providing us with the EBSD analysis.

5.1. Introduction

Nickel-based superalloys are an exceptional class of engineering materials with extraordinary properties, including but not limited to high strength at elevated temperatures, good corrosion resistance, high fatigue endurance, and creep durability, as reported by [1, 2]. According to a report by Pulidindi [3] on market size of Ni-based superalloys, IN718 and IN625 are the most versatile products that have dominated the market in 2019 with a share of over 55% and 20%, respectively. In a review study by Patel et al [4], it has been noted that the very first application of these superalloys was in the steam lines of supercritical steam power plants, but they soon found their way in a wide variety of applications from high to low temperatures owing to the unrivaled opportunities offered by these materials to the surging demands from emerging applications in aviation, turbine, nuclear, aerospace, and oil & gas industries. The initial goal behind the invention and development of both superalloys by Eiselstein [5] was obtaining solid-solution strengthened superalloys with high creep resistance by adding different amounts of heavy elements such as Nb and Mo to a Ni-Cr matrix. However, Eiselstein and Tillack [6], later showed that higher content of Nb in IN718 (4-6 wt.%) could lead to the formation of metastable ordered body-centered tetragonal (BCT) γ''-Ni_3Nb phase in addition to the ordered face-centered cubic (FCC) γ'-Ni_3(Al, Ti) precipitates (due to the presence of Ti+Al in this superalloy) in the γ-Ni matrix through a controlled aging process at a narrow temperature range. As stated by Chang [7], solid solution is also a part of the strengthening mechanism in IN718

alloy, but precipitation hardening is the dominant strengthening mechanism. On this account, although conventionally manufactured IN625 end products (i.e., pipes, tubes, and plates) are in the annealed state, IN718 counterparts are preferred to be in annealed+aged condition, especially for high-temperature applications.

Debroy, and Fereiduni [8, 9] pointed out in their review studies that over the past two decades, additive manufacturing (AM) processes such as laser powder bed fusion (LPBF) have revolutionized almost all industries by making it possible to produce complex geometries, intricate features, and custom-designed components with very few constraints. Consequently, as reported by Kim et al [10], many of the existing components were redesigned and manufactured for AM with the aim of reducing the weight and enhancing efficiency. Such manufacturing transformation has also been happening to Ni-based superalloys, especially the widely used IN718 and IN625, as Sanchez et al [11] demonstrated that the LPBF processing of these two superalloys has been the target of most research studies found in the literature. Marchese et al [12] showed in their research study that the microstructure of the LPBF fabricated IN625 mainly consists of supersaturation solid solution γ-Ni with very low volume fraction of nanosize carbides (NbC and/or (Mo,Nb)-rich carbide). This is while for IN718, Zhao et al [13], found that the Laves phase was perceptible in the interdendritic regions instead of carbides. They also reported that the high cooling rates associated with the LPBF process hinder the formation of γ′ and γ″ phases in the AB condition in the LPBF fabricated IN718 superalloy. These are similar to the microstructures of IN625 and IN718 after solution treatment followed

by subsequent quenching. Therefore, while IN625 can be regarded as the end product without further heat treatments, aging is still required for IN718 to generate the desired precipitates.

Fatigue resistance of the additively manufactured IN625 and IN718 parts, which is the of this research study, is one of the most critical factors that must be considered prior to certification of AM processes in the abovementioned industries. This is especially important for applications in which these superalloys are in contact with a highly dynamic aqueous media or experience cyclic thermal and mechanical loadings. Highlights of the fatigue studies in the literature on the LPBF fabricated IN718 and IN625 superalloys are summarized in Table 5-1. As it is evident, they all share the same concept of applying solution annealing (for IN718 and IN625) and/or dual-temperature precipitation aging treatments (for IN718 as per AMS 5663, SAE AMS2774E, AMS 5597A, AMS 5596C, and AMS 5662N) prior to the fatigue test, the only distinguishing point being the time and temperature of the selected thermal cycles. The solution annealing heat treatment was conducted with the purpose of stress-relieving of the residual stresses (RS) generated during the LPBF process [14], alleviating the micro-segregation of Nb to make the final microstructure more uniform [12] and eliminating the carbide/laves phase from the as-printed IN718 and IN625 superalloys [15, 16]. According to the a research study by Zhou et al [14], the foremost aim for the double aging treatment was facilitating the formation of γ' and γ'' precipitates in IN718. Patel et al [4] implied that although IN718 segments require double aging cycles to operate at high temperatures, such

heat treatments might not be mandatory for room temperature (i.e., in aqueous environments) as well as cryogenic temperature (i.e., in liquid fuel rocket engines) applications. Therefore, IN718 can also be used in such applications without time-consuming post-process heat treatments. Both IN625 and IN718 superalloys have no ductile-to-brittle transition temperature and have acceptable corrosion resistance and phase stability in many aqueous and chemical media, making them suitable candidates for such applications, as stated by Lippold et al [1]. From this perspective, it is interesting to investigate the fatigue performance of IN718 in the AB condition where the strengthening precipitates are absent to understand whether the supersaturated solid solution matrix from the high content of Nb and minor amounts of Ti and Al can lead to a fatigue resistance comparable to that of the IN625 solid-solution strengthened superalloy with higher Mo and Cr contents.

Table 5-1 A literature review on the condition of LPBF fabricated IN718 and IN625 specimens prior to the fatigue test.

Material	Post-printing heat treatment	Ref.
IN718	HIP-treated for 3 h at 1163 °C/100 MPa + solution annealing at 954 °C/1 h + dual-temperature precipitation aging at 718 °C/8 h followed by furnace cooling to 621 °C and holding for 18 h as per AMS 5663	[17]
	Solution annealing at 980 °C/1 h + dual aging cycle at 720 °C/8 h followed by furnace cooling to 620 °C and holding for 8 h	[18]
	Solution annealing at 954 °C/10 min + dual aging cycle at 718°C/8 h and 621 °C/10 h as per SAE AMS2774E	[19]

	Cycle 1: stress relief at 1065 °C/1 h + solution annealing at 980 °C/1 h + dual aging cycle at 720 °C/8 h followed by furnace cooling to 620 °C and holding for 8 h Cycle 2: stress relief at 1065 °C/1 h + HIP-treated for 3.5 h at 1160 °C/1500 bar + solution annealing at 980 °C/1 h + dual aging cycle at 720 °C/8 h followed by furnace cooling to 620 °C and holding for 8 h	[20]
	Cycle 1: Solution annealing at 1038 °C/2 + double aging at 760 °C/10 h followed by furnace cooling to 649 °C and holding for a total duplex aging time of 20 h as per AMS 5597A Cycle 2: Solution annealing at 940 °C/2 h + double aging at 718 °C/8 h followed by cooling to 621 °C and holding for a total duplex aging time of 18 h as per AMS 5596C	[21]
	Cycle 1: Solution annealing at 980 °C/1 h + double aging cycle at 720 °C/8 h followed by furnace cooling to 620 °C in 2 h and hold at 620 °C for 8 h Cycle 2: Cycle 1 + HIP-treated at 980 °C/4 h at 100 MPa followed by rapid cooling with the cooling rate of 42 °C/min	[22]
	Cycle 2: Solution annealing at 980 °C/1 h + double step aging at 720 °C/8 h followed by slow cooling with the rate of 50 °C/h to 620 °C and holding for 8 h as per AMS 5662 Cycle 2: HIP-treated for 4 h at 1160 °C/150 MPa + double aging treatment under pressure at 710 °C/100 MPa for 8 h followed by 610 °C/90 MPa for another 8 h Cycle 3: HIP-treated for 4 h at 1160 °C/150 MPa + the same double aging treatment as that of cycle 2 without applying external pressure	[23]

	Stress relief at 970 °C/1h + double aging at 710 °C/8 h followed by furnace cooling to 610 °C and holding for 8 h	[24]
	Solution treatment at 954 °C/10 min + double aging at 718°C/8 h followed by furnace cooling to 621 °C with the total double aging time of 18 h as per AMS 5562N	[25]
	Cycle 1: double aging at 718 °C/8 h followed by furnace cooling to 621 °C and holding for 8 h Cycle 2: HIP-treated for 4 h at 1160 °C/100 MPa + solution annealing at 1065 °C/1 h + cycle 1	[26]
	Solution annealing at 980 °C/1 h and double aging cycle at 720 °C/8 h and then at 620 °C/8 h as per AMS 5663	[27]
IN625	Solution annealing at 1100 °C/1 h	[28-30]
	Stress relief annealing at 870 °C/1 h	[31-33]
	Stress relieving heat treatment at 800 °C/1 h + HIP treatment for 3 h at 1170 °C/150 MPa	[34]
	Stress relieving heat treatment at 870 °C/1 h + HIP treatment for 4 h at 1120 °C/100 MPa	[35]
	Cycle 1: Stress relieving heat treatment at 1032 °C/1 h followed by rapid air cooling Cycle 2: Cycle 1 + solution treatment at 1178 °C/1 h followed by rapid air cooling	[36]

Referring to Table 5-1, in addition to the solution annealing and/or double aging treatments, the LPBF fabricated IN625 and IN718 superalloys have also been subjected to other thermal cycles, namely, (i) stress-relieving and (ii) hot isostatic pressing (HIP). The purpose of stress-relieving heat treatment, mostly applied to

the LPBF fabricated IN625 parts, is to mitigate the tensile RS that develops during this layerwise manufacturing process. Narvan et al [37] thoroughly explained that such thermally induced RS is generated in the LPBF fabricated parts as a result of the lower contraction propensity of the previous layers due to the existence of a temperature gradient that restrains the free contraction of hot regions in the newly consolidated tracks/layers. The time and temperature of the stress-relieving cycle for the LPBF fabricated parts are usually selected based on the ASM recommendations for their conventionally manufactured counterparts which might not necessarily lead to desirable results. For instance, according to a research study conducted by Lass et al [38] on the microstructural evolutions of the LPBF processed IN625 during the stress-relieving treatment, it has been shown that the industry-recommended stress relieving cycle of 870 °C/1 h for wrought IN625 results in the formation of significant amounts of orthorhombic Ni_3Nb-δ phase in the LPBF fabricated IN625 which is detrimental to its fracture toughness, fatigue resistance and creep durability. Lass et al [38] also discussed that the formation of the δ phase in the LPBF fabricated IN625 was due to the high content of Nb and Mo elements in supersaturation solid solution γ-Ni matrix in the inter-dendritic regions of the AB solidification microstructure. Although alternatives such as performing the stress-relieving at lower temperatures (i.e., 800 °C) or homogenization heat treatment prior to the stress-relieving have been proposed in the same study to address these concerns, none of them can be confidently applied to the LPBF fabricated components because they are not standard procedures.

Moreover, stress-relieving heat treatment might only alleviate the tensile RS but cannot generate compressive stresses, which are highly beneficial for enhancing the fatigue life of the LPBF fabricated parts, as reported by Bartlett and Li [39]. When it comes to the HIP treatment, elimination of the defects of the LPBF fabricated parts is the main reason that arouses interest toward its implementation, as mentioned by Yu et al [20]. Although the literature suggests that the HIP-treated specimens possess a better fatigue life, such a post-processing treatment suffers from three major drawbacks, (i) formation of detrimental Laves clusters and acicular δ phase, which cannot be seen in wrought IN625 and IN718 superalloys unless after thousands of hours of operation (such phases might cause premature failure of the end products) [22], (ii) inability to generate compressive RS since the applied compressive stress is not high enough even to offset the high magnitude of tensile RS developed during the LPBF process [22], and (iii) in cases where subsequent heat treatment cycles (i.e., for IN718 based on **Error! Reference s ource not found.**) are applied to the HIP-treated parts, the closed pores can find another chance to regrow [23], which defeats the purpose of utilizing such treatment in the first place. Therefore, alternative post-processing must be taken into account when enhancement in fatigue resistance of AB parts is required.

This study strives to shed some light on the influence of shot peening on the fatigue life of the LPBF fabricated IN625 and IN718 superalloys. Kalentics et al [40] demonstrated that shot peening is an effective technique in generating surface compressive RS and improving fatigue life of the LPBF fabricated parts. However,

it has received scant attention in the literature (Table 5-1). The following sequence of steps were taken in this study to find the optimum samples in terms of fatigue resistance and to understand the role that shot peening plays in improving the fatigue life: (i) highly dense cubic coupons were printed, (ii) the number of samples was narrowed down by excluding samples having relative densities less than 99%, (iii) the remaining samples were tested in terms of tensile strength, surface quality, and RS to end up with one sample having the best combination of high relative density, high strength, and low surface roughness and tensile RS, (iv) the optimum IN625 and IN718 samples were shot-peened and subjected to fatigue testing along with the AB specimens as the reference, and (v) microstructure of each material was investigated before and after shot peening and the microstructural features in addition to the surface roughness and RS were correlated to the obtained fatigue results. The findings of this study suggest that shot peening can be a promising time-and-cost effective post-process treatment to remarkably improve the fatigue life of the LPBF fabricated IN625 and IN718 components.

5.2. Experimental procedures

5.2.1. Materials and process parameters

The starting powders used in this research were gas atomized IN625 and IN718 powders with the nominal chemical compositions reported in [41] and [42], respectively. Both powders had a nominal particle size distribution ranging between 15 and 45 μm. An EOS M280 machine (EOS, Krailling, Germany) equipped with a Yb-fiber laser system delivering power levels of up to 400 W was

used in this study. Based on the previous work conducted by the authors on IN625 [41] and IN718 [42], different sets of process parameters yielding relative densities above 99% were employed. Nevertheless, the optimum parameters among these sets were selected based on the best possible combinations of a high relative density, low surface roughness, high tensile strength, and low tensile RS. The process parameters employed in this study are presented in Table 5-2Table 5-2. The printing process was performed under a Nitrogen atmosphere to reduce the oxygen percentage below 1%. Tensile and fatigue samples were printed for each alloy with a layer thickness of 40 μm and a serpentine scan strategy with 90˚ rotation between layers, and a build plate preheat temperature of 80 °C.

Table 5-2 Process parameters employed for printing IN625 and IN718.

IN625				IN718			
Sample	Laser power (W)	Scanning speed (mm/s)	Hatch spacing (mm)	Sample	Laser power (W)	Scanning speed (mm/s)	Hatch spacing (mm)
1	170	500	0.1	1	220	600	0.08
2	220	500		2	320	600	0.08
3	220	550		3	270	600	0.1
4	220	600		4	270	700	0.1
5	270	600		5	320	700	0.1
				6	270	600	0.12
				7	320	600	0.12

Density, surface roughness, and residual stress

The relative density of samples was measured for both AB and SP conditions to examine the possible effect of SP in closing surface and near-surface pores and consequently increasing the relative density. Density was measured using the Archimedes method, where the mass of the sample was measured in air and water using a scale with a resolution of ± 0.1 mg.

The surface roughness of all samples was characterized in terms of the arithmetic mean roughness (R_a) measured along five different directions on each of the four sides of the fatigue samples using a Mitutoyo SJ-410 stylus profilometer.

In-depth RS was measured on the top and bottom surfaces for both alloys in AB and SP conditions using X-ray diffraction. An Mn- Kα radiation source was used, and the samples were oscillated about the mean Psi angles of 10 and 50° by ±1.5° to integrate the diffracted intensity over more grains to minimize the influence of the grain size. The irradiated area was 5 mm ×5 mm at the middle of the gauge length. The RS was measured in the longitudinal direction along the uniaxial fatigue loading direction. Electrolytic material removal was employed to minimize altering the subsurface RS. The material was removed, and RS was measured at different increments down to a depth of 0.38 mm.

5.2.2. Microstructural Characterization

Printed cubic samples were sectioned through the front plane and then ground and polished according to the standard metallography procedure. The final stage of

sample polishing was performed using colloidal silica with an average particle diameter of 0.06 µm. A Keyence (Osaka, Japan) VHX digital microscope was used to observe the non-etched sections and compare the densification level of parts qualitatively. The polished sections were chemically etched for microstructural studies using Kalling's 2 reagent for IN718 and a reagent containing 10 ml HCl, 10 ml HNO_3, and 15 ml CH_3COOH for IN625. High magnification imaging was conducted using a Tescan Vega scanning electron microscope (SEM) at an accelerating voltage of 20 keV. The microscope was equipped with an energy-dispersive X-ray spectroscopy (EDS) detector to identify the elemental chemical composition of micro-constituents. The electron backscatter diffraction (EBSD) analysis was utilized to characterize the texture, grain size/morphology, and dislocation density of AB and SP specimens. This analysis was performed using an FEI, Versa 3D field-emission scanning electron microscope (FE-SEM), operating at an accelerating voltage of 20 keV, and a tilt angle of 70° with a step size in the range of 0.3-0.7 µm. The EBSD data were collected using the TSL OIM 7 software and were analyzed using the HKL Channel 5 software package.

5.2.3. Tensile testing

Flat dogbone samples were printed for uniaxial tensile testing in accordance with the ASTM E8/E8M standard using the process parameters listed in Table 5-2. The tensile test specimens were subsize with a width of 6 mm and a gauge length of 32 mm, as shown in Figure 5-1. Uniaxial tensile testing was performed on an 810 MTS servo-hydraulic test frame with a maximum loading capacity of 50 kN, coupled

with a digital image correlation (DIC). Testing was conducted at room temperature with a strain rate of 8×10^{-3} s^{-1}, as per ASTM E8/E8M standard.

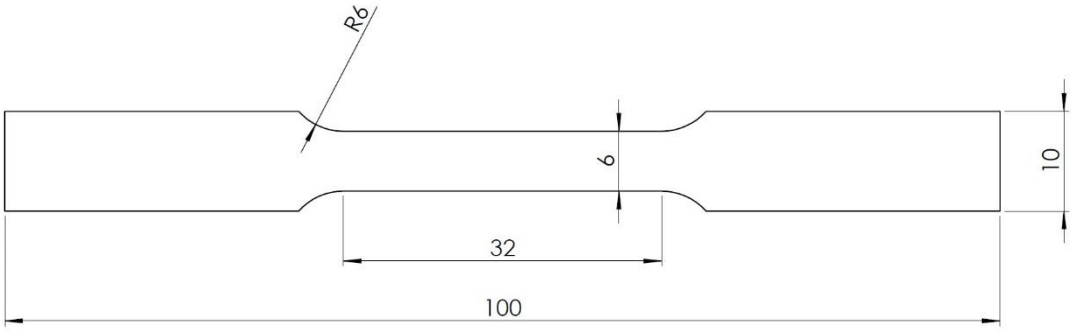

Figure 5-1. Schematic illustration of the tensile test specimen

5.2.4. Fatigue testing

Rectangular cross-section fatigue specimens were manufactured in accordance with the ASTM E466 standard. Fatigue specimens with tangentially blended fillets between the uniform test section and the ends were designed with a gauge width of 6.5 mm and thickness of 3.2 mm in line with the ASTM E466 standard, as shown in Figure 5-2. Twenty specimens were manufactured for each alloy using one set of process parameters leading to the best possible combination of a high relative density, low surface roughness, low surface tensile RS, and high tensile strength. The selection of these optimum sets of parameters will be discussed later in section 5.3. For both alloys, half of the fatigue specimens were shot-peened (SP) in a Trinco Dry-Blast 36x30/PC-BP cabinet with the ASR110 cast steel shot type. All specimens were peened at an Almen intensity of 8A to a coverage of 200%.

Uniaxial fatigue testing was performed at room temperature with a cyclic frequency of 30 Hz, a stress ratio of R= 0.1, and the runout was set at 5 million cycles. Ten

samples of each alloy were tested in the AB and SP conditions. The fracture surfaces were examined via SEM following the fatigue test to identify the crack initiation sites.

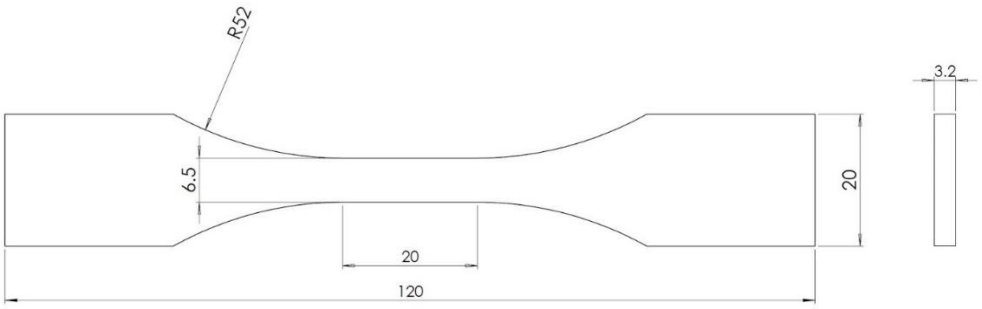

Figure 5-2. Schematic illustration of the fatigue test specimen.

5.3. Results and Discussion

5.3.1. Optimization of process parameters

As mentioned earlier, the selection of optimum process parameters for manufacturing the fatigue specimens was based on four criteria, namely, densification level, tensile strength, surface roughness, and RS. The densification level indicates the amount of pores in the specimen, which might serve as crack nucleation sites during the cyclic loading. High tensile strength is favored as Ni-based superalloys are most frequently utilized in applications demanding high strength. The surface roughness represents the possible micro-sized notches distributed along the outer surfaces of the sample that can act as stress concentrators and facilitate crack initiation. The tensile RS shortens the fatigue life of the part, as it serves to open up existing cracks and accelerate the crack propagation rate. Except for tensile strength, other factors were determined from previous studies by

the authors [41, 42], as provided in Table 5-3. In terms of the densification level, the relative density of 99% was considered the minimum value required for a reliable fatigue performance. Except for sample 2 of IN718, all other samples possessed relative densities above 99%, meeting the densification level requirement. To qualitatively investigate the size, morphology, and distribution of the porosities within samples, the cross-sections of the non-etched coupons were examined. According to the optical micrographs shown in Figure 5-3 for IN625 and Figure 5-4 for IN718, it is observed that the selected process parameters resulted in highly dense parts with only a few dispersed porosities (excluding sample 2 of IN718, where a large number of porosities is concentrated at the sides surfaces). These porosities are spherical with diameters less than 50 μm, uniformly distributed within the parts. All these features give evidence of the negligible adverse effect of such porosities on the fatigue life of the components fabricated by the selected process parameters. Since there is almost no difference between the size, morphology, and distribution of porosities in samples having relative densities higher than 99%, none of the sets of process parameters is preferred over the others from the densification level perspective.

Table 5-3. The relative density, surface roughness, and surface RS values for different samples of IN625 and IN718 superalloys [41, 42].

IN625				IN718			
Sample	Relative Density (%)	Surface Roughness R_a (μm)	Surface RS (MPa)	Sample	Relative Density (%)	Surface Roughness R_a (μm)	Surface RS (MPa)
1	99.4	3	-59	1	99.06	4.57	413
2	99.3	2.94	-163	2	98.72	2.73	302
3	99.2	2.53	86	3	99.13	3.48	508
4	99.7	3.13	19	4	99.56	4.37	594
5	99.3	3.12	-68	5	99.05	3.31	453
				6	99.01	3.53	429
				7	99.17	3.53	459

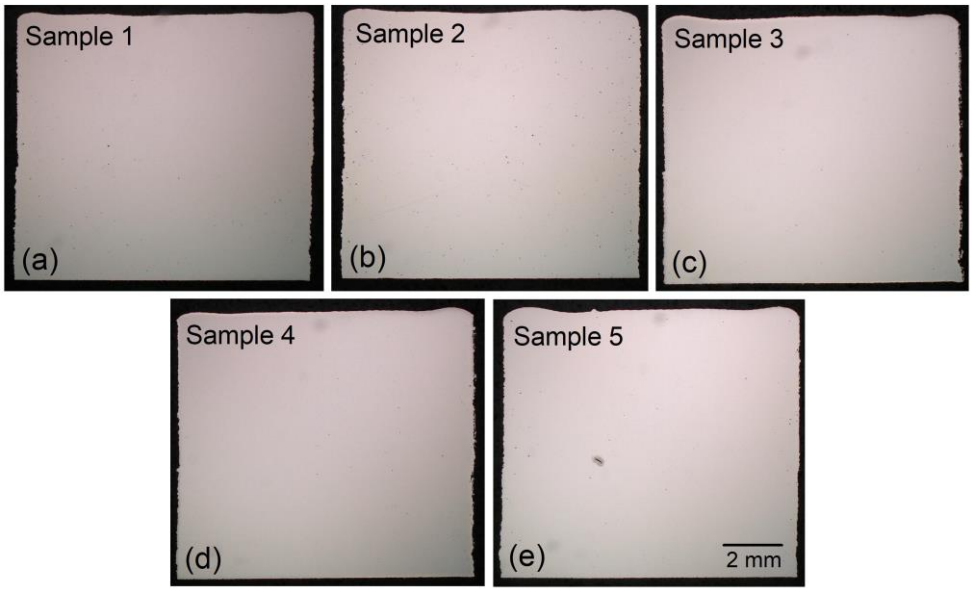

Figure 5-3. Non-etched optical micrographs of IN625 coupons.

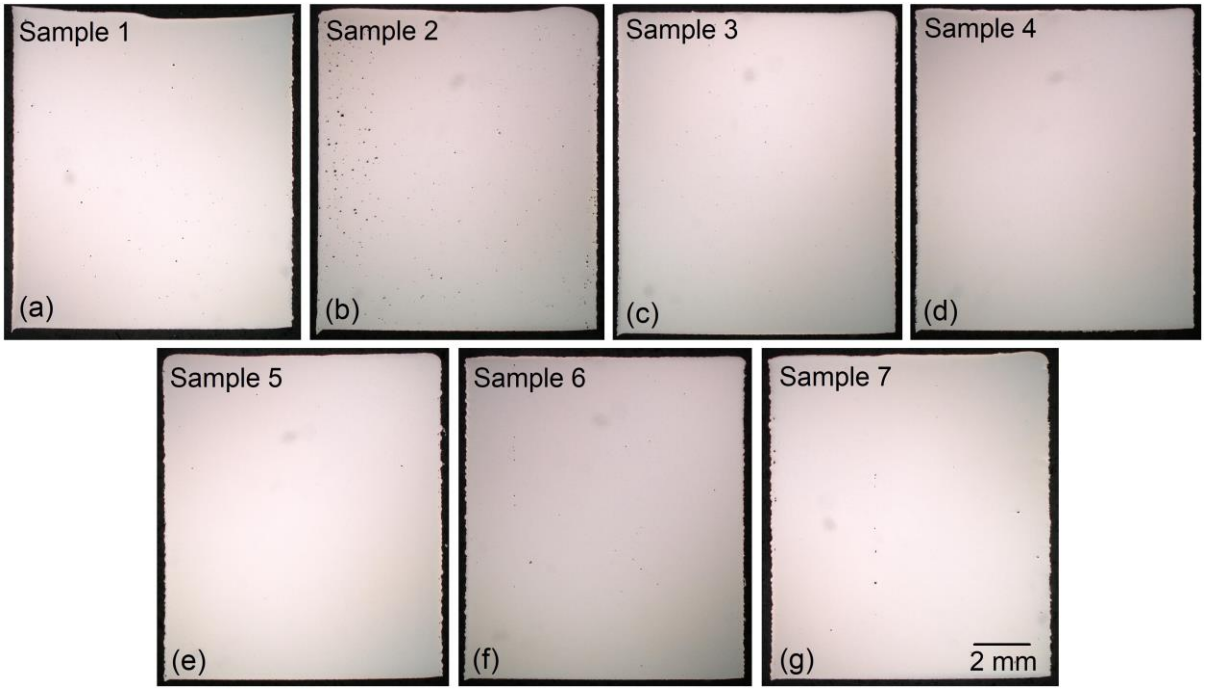

Figure 5-4. Non-etched optical micrographs of IN718 coupons.

Tensile specimens were fabricated using the sets of process parameters meeting the densification level requirement to investigate the effect of process parameters on the tensile strength criterion. Referring to the stress-strain curves provided in Figure 5-5, no significant difference was observed in the strength and elongation to fracture values of both IN718 and IN625 superalloys with varying process parameters. For IN625, yield strength of ~644 MPa and ultimate tensile strength of ~901 MPa were achieved. These strength values were643 and 935 MPa for IN718, respectively. Therefore, since tensile strength was almost the same for different specimens, all coupons that already passed the densification level requirement also meet the high tensile strength criterion, with none of the specimens being preferred over the others. Accordingly, samples were compared from the surface roughness

and the surface RS viewpoints to pinpoint the optimum set of process parameters for fabricating fatigue test specimens.

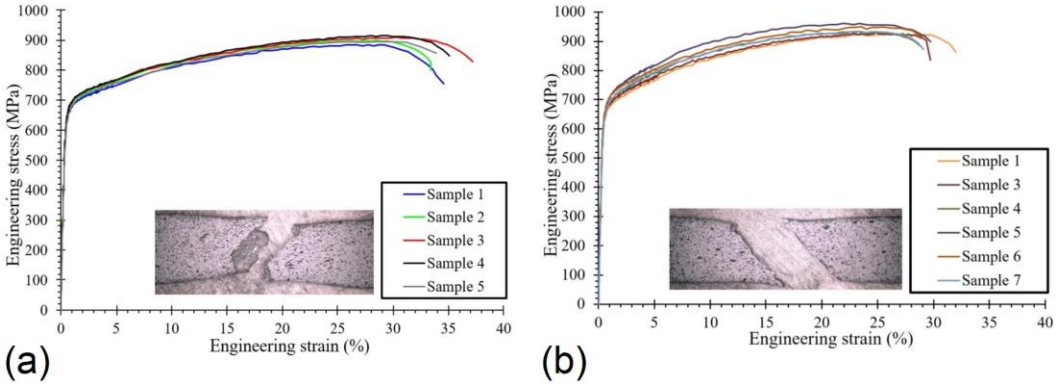

Figure 5-5. Engineering stress-strain curves (a) IN625 (b) IN718.

Surface roughness and RS results for IN625 and IN718 are listed in Table 5-3. For IN625, the R_a values were found to be in the range of 2.53-3.13 µm, revealing a minor change in surface roughness with varying process parameters. On the other hand, the top surface RS values were noticeably different in both magnitude and nature, ranging from -163 (compressive) to 86 (tensile) MPa. Although sample 3 featured the lowest R_a of 2.53 µm, it possessed the largest top surface tensile RS of 86 MPa. Sample 2 showed the second-lowest R_a value of 2.94 µm (16% higher than sample 3) and the highest top surface compressive RS (-163 MPa) among all samples. The rest of the samples (1, 4, and 5) were inferior to sample 2 in terms of surface roughness and RS. On this account, the process parameters of sample 2 were selected as the optimum parameters to fabricate the IN625 fatigue specimens. The same logic was used to find the optimum set of process parameters for IN718. Samples 1 and 4 were excluded since having relatively higher R_a values and/or

larger tensile RS than others. The remaining samples had almost the same surface roughness. Except for sample 3, they also showed almost equal RS. Therefore, samples 5, 6, and 7 could be considered optimum samples. Nevertheless, owing to the fact that the relative densities of samples 5 and 6 were marginally above 99%, the process parameters of sample 7 were selected as the optimum ones for IN718. It is worth noting that this sample also benefits from the highest building rate, making it suitable from the manufacturing cost and time perspectives.

5.3.2. Fatigue test results

After finding the optimum sets of process parameters based on the procedure explained in section 5.3.1, fatigue test specimens were fabricated and subsequently subjected to tensile cyclic loading at room temperature to investigate their fatigue life at different stress levels. For each superalloy, ten samples were tested in each AB and SP condition. The S-N results were fitted to the Basquin model given by Eq. (1), where N is the number of cycles to failure, S is the maximum stress applied, and A1 and A2 are the model parameters predicted from data.

Table 5-4 presents the A1 and A2 parameters, calculated using statistical analysis of the fatigue test data for IN625 and IN718 in AB and SP conditions.

$$\log N = A1 - A2 \log S \quad (1)$$

Table 5-4 Estimated parameters of fatigue life model used for IN625 and IN718 in the AB and after shot peening (SP), ordinary least squares (OLS).

Material	Parameter	Estimate	Std. error	t-value	p-value	95% LCL	95% UCL
IN 625	A1	17.3589	1.2139	14.2999	< 0.0001	14.5597	20.1583
	A2	4.5316	0.4618	9.8126	< 0.0001	3.4666	5.5952
IN 625 + SP	A1	42.4206	2.7592	15.3741	< 0.0001	35.8961	48.9451
	A2	13.1774	0.9927	13.2742	< 0.0001	10.8301	15.5248
IN 718	A1	17.6467	1.6528	10.6766	< 0.0001	13.7383	21.5550
	A2	4.7171	0.6279	7.5123	< 0.0001	3.2322	6.2019
IN 718 + SP	A1	34.9351	3.5726	9.7803	< 0.0001	25.0155	44.8524
	A2	10.6533	1.2921	8.2430	< 0.0001	7.0632	14.2403

Since the fatigue tests were carried out with a small number of specimens, the bootstrap simulation technique was used to estimate the probability distribution of each parameter [43]. In this approach, the ordinary least squares (OLS) fit was computed from the original S–N data. The residuals were then resampled and added to the predicted values of the original fit to obtain simulated log N data. These data were then fitted versus the actual maximum stress values (S) using the Basquin model, and the estimated parameters (A1 and A2) were recorded in an approach called residual resampling. This method was repeated hypothetically 10000 times to obtain the probability distribution of each parameter. The statistical parameters such as the mean, standard error, confidence interval, etc., can be found from the distribution. The simulation results after 10000 resamplings are shown in Table 5-5.

Table 5-5 Estimated parameters of fatigue life model used for IN 625 and IN 718 in the AB and after shot peening (SP), bootstrap simulation technique, 10000 resamplings

Material	Parameter	Estimate	Std. error	t-value	p-value	95% LCL	95% UCL
IN 625	A1	17.363	1.0583	17.44	< 0.0001	14.923	19.804
	A2	4.534	0.4026	11.97	< 0.0001	3.605	5.462
IN 625 + SP	A1	42.39	2.3693	19.48	< 0.0001	36.79	47.99
	A2	13.17	0.8524	16.81	< 0.0001	11.15	15.18
IN 718	A1	17.643	1.435	12.776	< 0.0001	14.251	21.035
	A2	4.716	0.545	8.989	< 0.0001	3.427	6.004
IN 718 + SP	A1	34.937	2.807	14.335	< 0.0001	27.144	42.729
	A2	10.652	1.0152	12.081	< 0.0001	7.834	13.471

From Table 5-5, it is evident that at the 0.05 level of significance, the estimated model parameters (A1 and A2) using the OLS fitting are statistically significant since the p-values are smaller than the level of significance. The same is valid for the mean values of A1 and A2 obtained by bootstrap simulation in Table 5-5. Besides, the A1 and A2 obtained by both OLS and bootstrap methods are very similar. However, the 95% confidence bands of A1 and A2 obtained by bootstrap simulation are narrower than those obtained by the OLS method. The histograms and density probability functions of the best-fit values of A1 and A2 for both IN 625 and IN 718 in AB and SP conditions are shown in Figure 5-6. It is seen that the best-fit values for both A1 and A2 are normally distributed, validating the parameters of the fatigue model used.

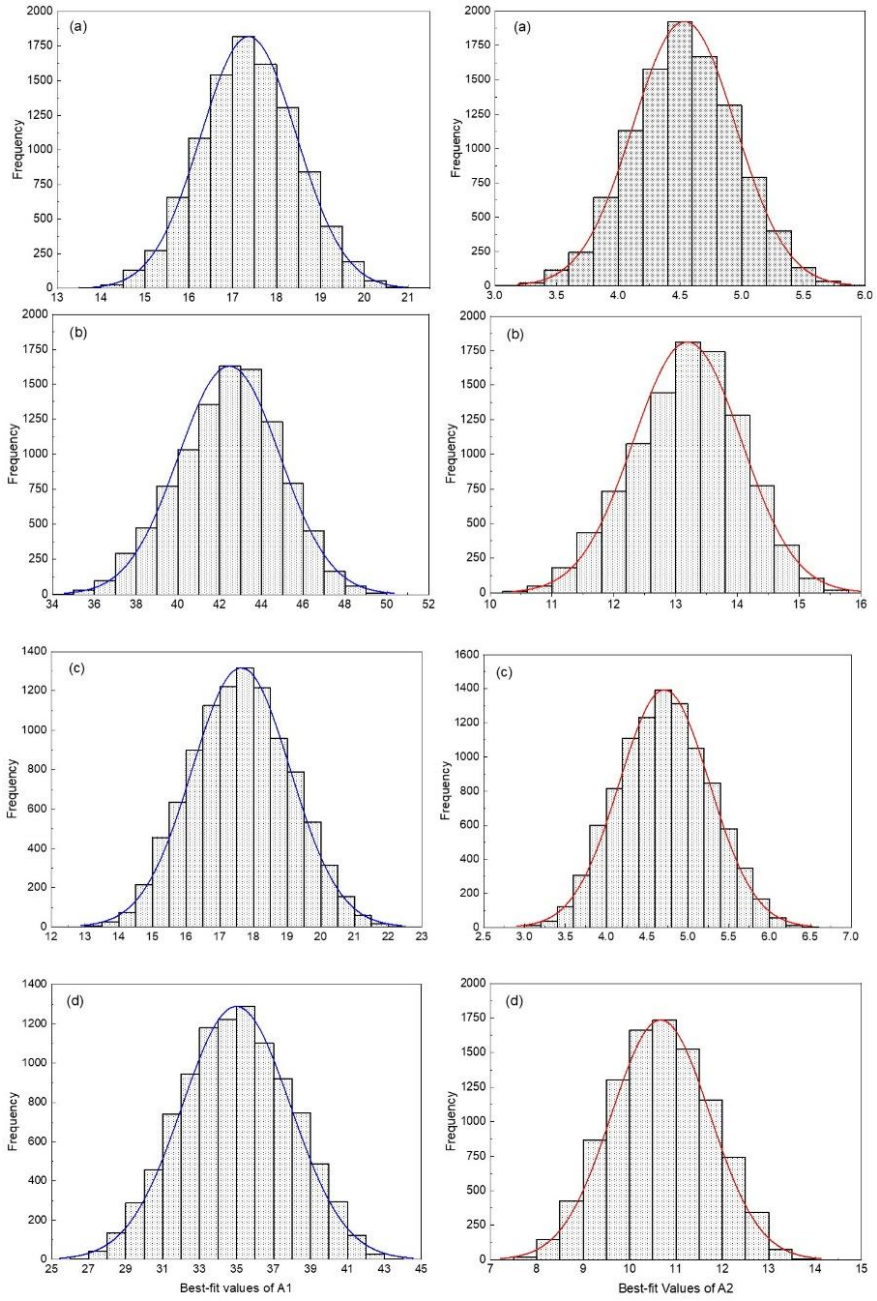

Figure 5-6. Density probability functions obtained by bootstrap simulation of the fatigue model parameters (A1 and A2). (a) AB IN625, (b) SP IN625, (c) AB IN718, and (d) SP IN718.

Fatigue test results are presented as S-N curves in Figure 5-7 for IN625 and IN718. The data points are plotted along with the best-fit curve for the AB and the SP conditions. In addition, the S-N curves for the wrought unnotched and notched (stress concentration factor-$K_t = 3$) samples obtained from MMPDS [44] are also plotted using the equations highlighted in Appendix A.

The AB IN625 reached an infinite life at a maximum stress level of 260 MPa, which was much lower than that of the unnotched annealed wrought specimen. However, the AB sample had a better fatigue life compared to the notched annealed wrought sample with $K_t = 3$. Conversely, shot peening significantly improved the fatigue life of IN625, resulting in a fatigue life slightly lower than that of the unnotched annealed wrought specimen and an infinite life at a maximum stress level of 550 MPa.

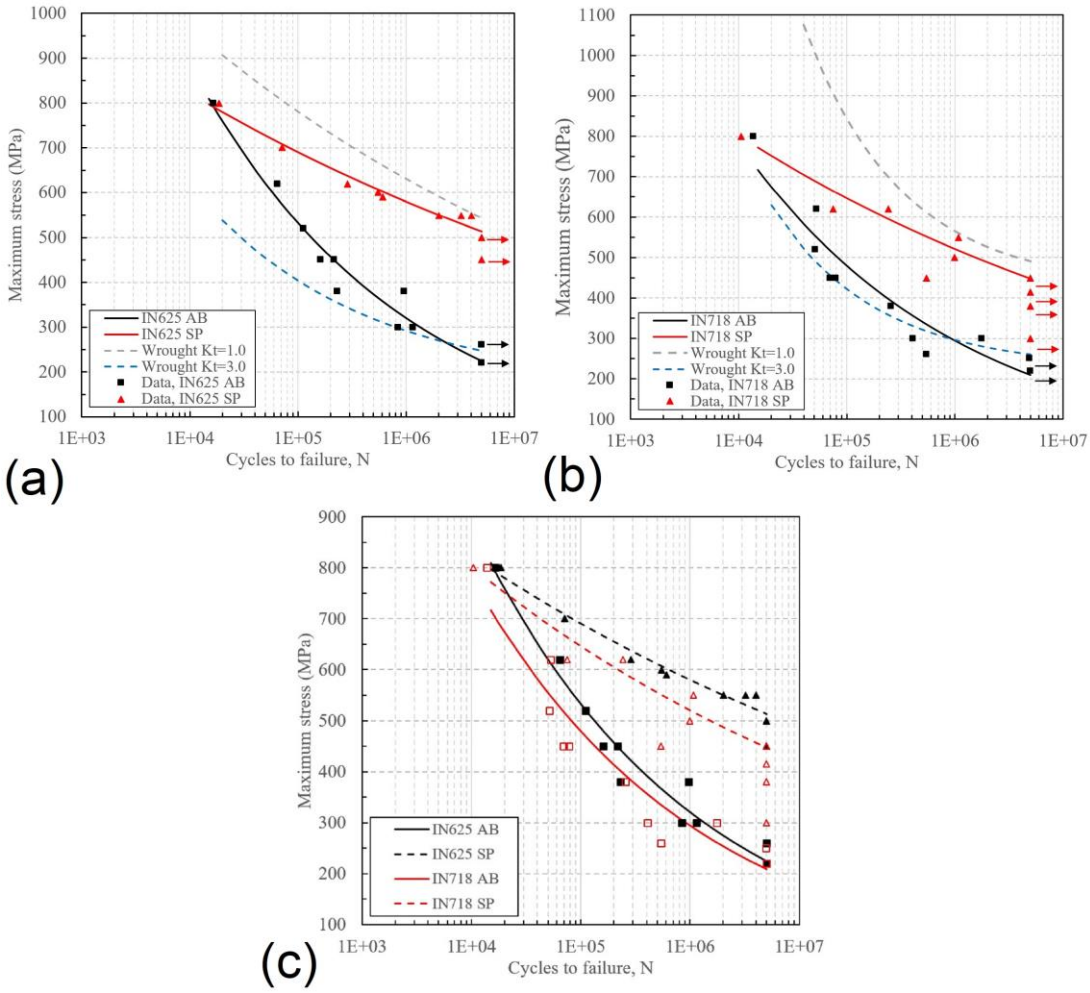

Figure 5-7. S-N plots for (a) AB and SP IN625 vs. wrought unnotched and notched IN625, (b) AB and SP IN718 vs. wrought unnotched and notched IN718, and (c) IN625 vs. IN718 in AB and SP conditions.

For IN718, the AB samples had a fatigue life far lower than the unnotched solution-annealed and aged wrought IN718. The AB IN718 featured an infinite fatigue life at maximum stress of 220 MPa, and the fatigue life was similar to that of notched solution-annealed and aged wrought IN718 with a $K_t = 3$. Shot peening improved the fatigue life of IN718, where an infinite life was reached at maximum stress of

450 MPa, doubling that of AB samples. However, the fatigue life of SP IN718 was still inferior to that of the unnotched solution-annealed and aged wrought IN718, especially in the high stress-low cycle zone of the S-N curve.

Finally, the fatigue lives of IN625 and IN718 were compared in AB and SP conditions. Figure 5-7(c) presents the S-N curves for both superalloys, where the fatigue life of AB IN625 was slightly better than that of IN718. For the SP condition, the difference between the fatigue lives of IN625 and IN718 became even higher.

5.3.3. Characterization of the fatigue specimens

As discussed in section 5.3.2, the SP IN625 and IN718 showed superior fatigue performance than the AB ones. Since the fatigue specimens differ in geometry and size from the coupons investigated in section 5.3.1, the relative density, surface roughness, and RS were also measured for the fatigue specimens in AB and SP conditions.

Relative density: The relative density was measured to investigate the possible effect of shot peening in closing the near-surface pores and increasing the overall density of the fatigue specimens. As it is evident in Figure 5-8, shot peening did not affect the relative density for both IN625 and IN718. Given that the density of the specimens was already above 99%, with the pores being dispersed throughout the sample and not concentrated near the surface (Figure 5-3 and Figure 5-4), such an observation is justifiable.

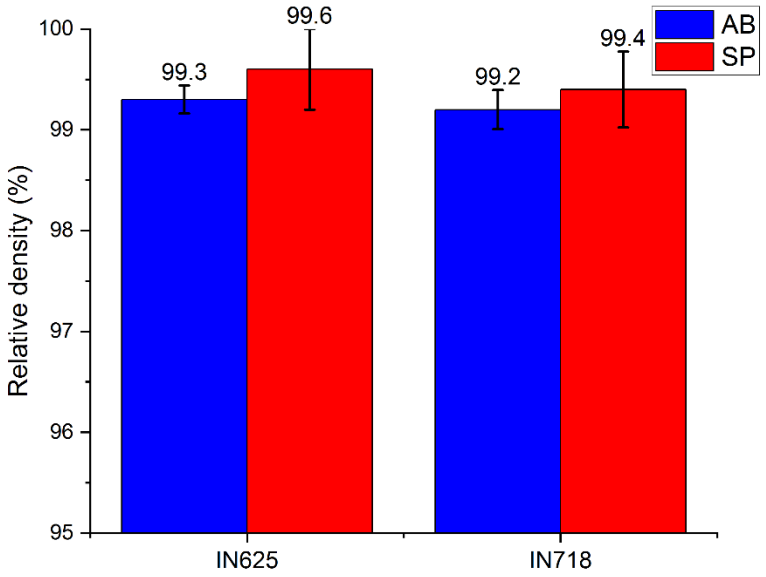

Figure 5-8. Relative density of samples in AB and SP conditions.

Surface roughness: the surface roughness was measured across all four sides for fatigue specimens of IN625 and IN718 in AB and SP conditions. According to the 3D surface topography maps shown in Figure 5-9 (IN625) and Figure 5-10 (IN718), the top surface roughness of the AB specimens was higher than that of the bottom surface subjected to the wire EDM due to the existence of the laser tracks on the former. The side surfaces exhibited higher surface roughness caused by the adherence of many powder particles to these surfaces during the LPBF process. Shot peening of the fatigue specimens led to a significant decrease in the surface roughness of all surfaces. To quantitatively assess the surface quality for the AB and SP specimens, R_a was measured for all four sides (Figure 5-11). For IN625, the R_a value for the top surface was higher than that of the bottom surface, which is in line with the surface topography maps shown in Figure 5-9. The quality of the side

surfaces was even lower than the top surface with 70% higher R_a, as shown in Figure 5-11. The side surface facing the inert gas flow showed an inferior surface quality to the other. This is attributable to the gas pushing powder particles towards the hot side surface and causing them to be sintered. Shot peening reduced the roughness of all surfaces with a maximum improvement of 40% for the side surfaces. Similarly, shot peening could decrease the surface roughness of IN718 (Figure 5-11) by 28% to 65%, with the maximum improvement recorded for the side surface facing the inert gas flow.

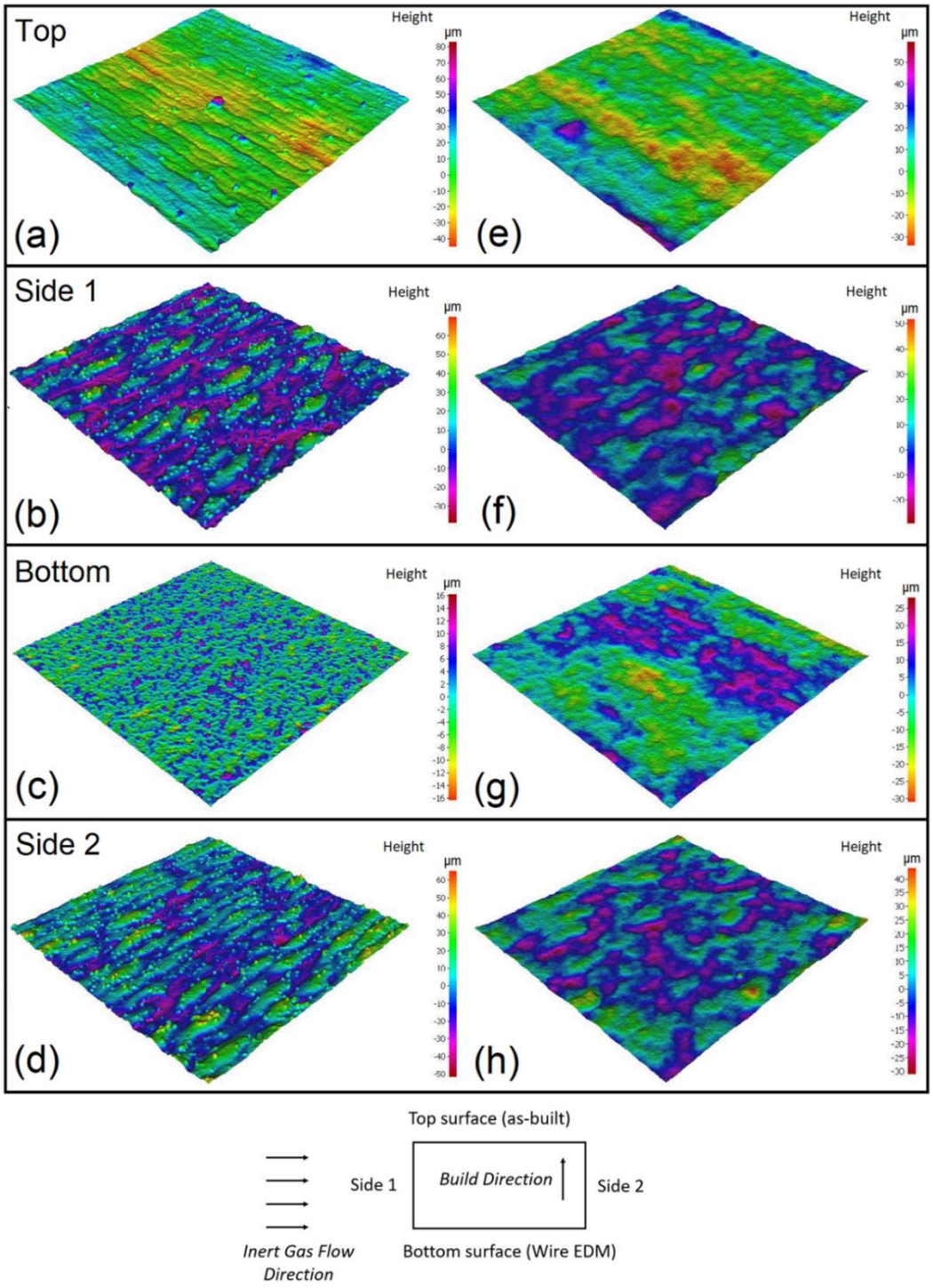

Figure 5-9. 3D surface topography of the lateral surface of IN625 fatigue samples for (a) AB, and (b) SP conditions.

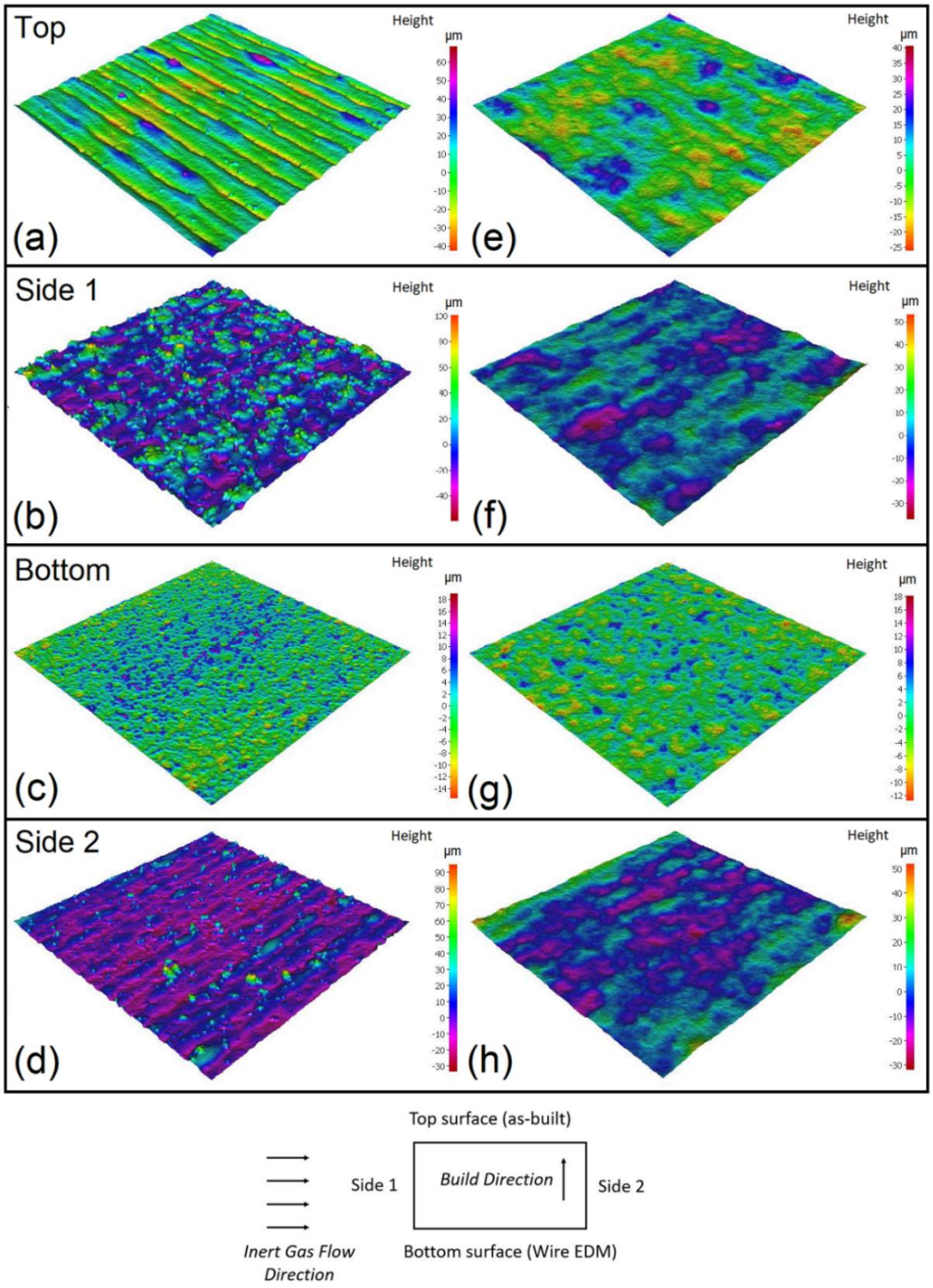

Figure 5-10. 3D surface topography of the lateral surface of IN718 fatigue samples for (a) AB, and (b) SP conditions.

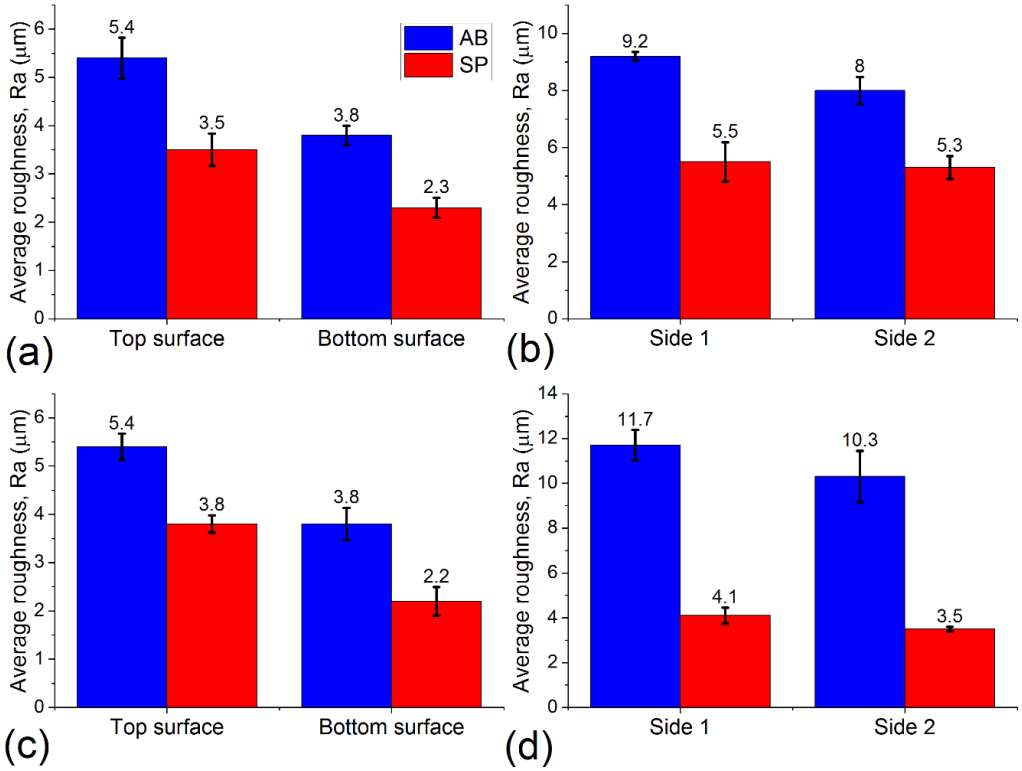

Figure 5-11. Average surface roughness of top, bottom, and side surfaces in AB and SP conditions for (a,b) IN625 and (c,d) IN718.

Residual stress: the in-depth RS profiles were measured from the top and bottom surfaces to compare their level of RS. Figure 5-12(a) shows the measured RS for IN625, where the wire EDMed surface (bottom) had a higher tensile RS than the top surface. In fact, the magnitude of surface RS on the wire EDM side was eight folds the RS on the top surface; however, the high tensile RS dropped to near zero after a depth of 75 µm. On the other hand, for the top surface, a relatively high RS existed down to a depth of 300 µm. Almost the same trend as IN625 was observed for IN718, as shown in Figure 5-12(b); however, the top surface featured a compressive RS down to a depth of 75 µm, while wire EDM induced a high tensile

RS profile along the measured depth. It is worth noting that a relatively moderate tensile RS existed below the top surface, starting from a depth of 100 µm. Shot peening induced a high compressive RS that penetrated deeply into each surface to a depth of 250 µm for both IN625 and IN718. The maximum compressive RS value corresponds to the depth of 50 µm for top and bottom surfaces.

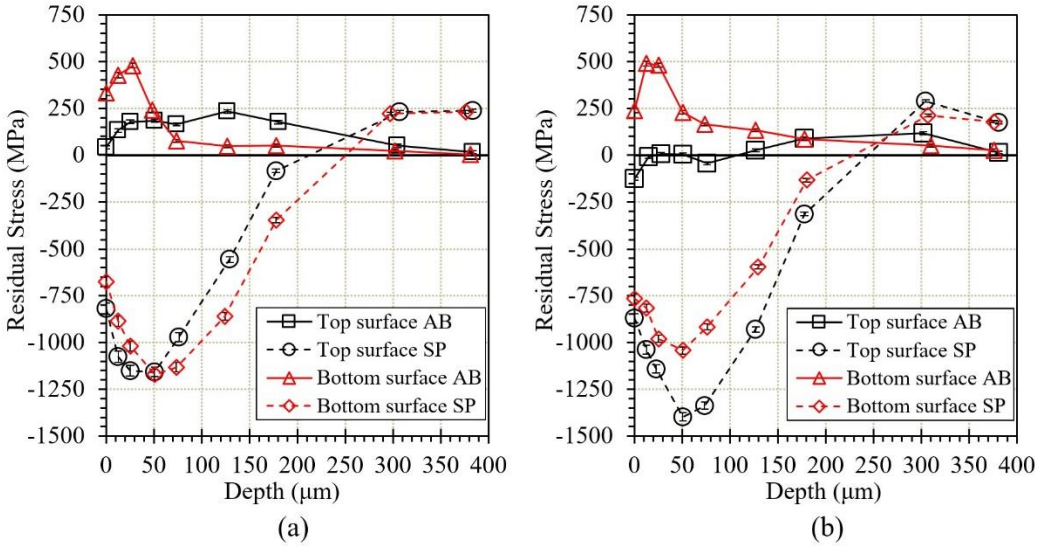

Figure 5-12. In-depth RS measured from top and bottom surfaces of fatigue specimens for (a) IN625 (b) IN718.

Microstructural evolutions: To understand the influence of shot peening on the microstructural features, EBSD analysis was performed on fatigue specimens after the failure. The inverse pole figure (IPF-Z) EBSD maps for IN625 and IN718 in both AB and SP conditions are provided in Figure 5-13. As can be seen in Figure 5-13(a) and (c), the microstructure of both AB IN625 and IN718 consists of large columnar grains that are elongated along the building direction, with some grains spanning across several hundred µm. However, the IPF-Z maps suggest that the

grains in AB IN718 are noticeably finer than those of the AB IN625 counterpart. Figure 5-13(b) and (d) show the IPF-Z maps of SP IN625 and IN718 at the immediate vicinity of the side surface. The reason behind performing EBSD analysis near the side surface is discussed in section 5.3.4. By comparing the IPF-Z maps of each material in AB and SP conditions, it can be inferred that some sub-grains have been formed within the large columnar grains as a result of the plastic deformation introduced by the shot peening. Such sub-grains were much more prevalent in the SP IN625 specimen than the SP IN718.

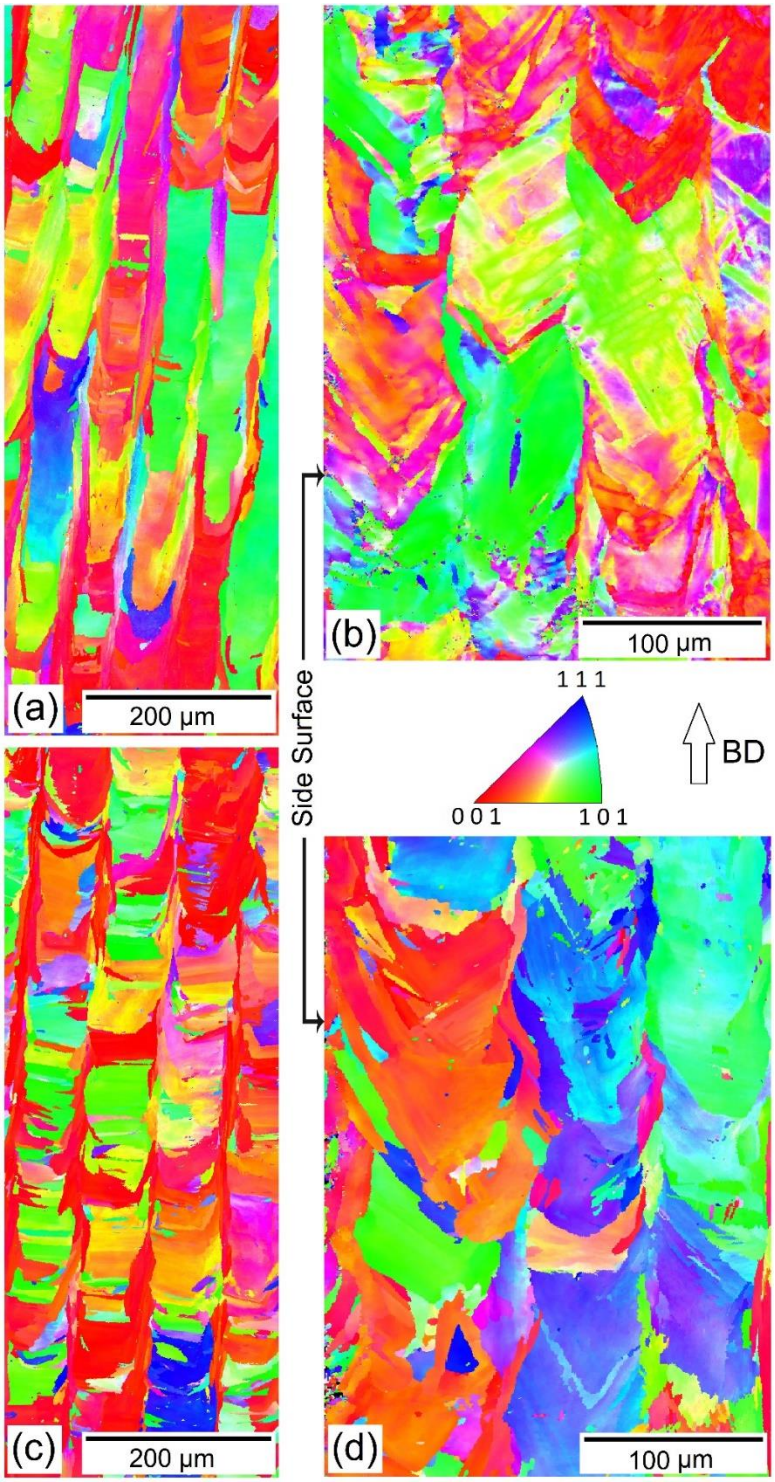

Figure 5-13. The IPF-Z EBSD maps of (a) AB IN625, (b) SP IN625, (c) AB IN718, and (d) SP IN718.

Band contrast micrographs and the Kernel averaged misorientation (KAM) maps of the fatigue specimens are shown in Figure 5-14. According to Figure 5-14(b), the bulk of AB IN625 specimen contains a significant amount of dislocations, confirming the presence of plastic strains generated from high thermal stresses originating from the layerwise nature of the LPBF process. Referring to Figure 5-14(a) and (b), dislocations are mainly concentrated between the wide columnar grains. By comparing Figure 5-14(b) and (d), it can be inferred that after shot peening, the dislocation density is increased within the prior columnar grains of IN625. These dislocations are mainly located at the sub-grain boundaries that are perceptible in Figure 5-13(b) and Figure 5-14(c). Compared to AB IN625, the AB IN718 showed a remarkably lower dislocation density (Figure 5-14(e) and (f)). In addition, the dislocations can be found not only between wide grains but also within them. This is attributable to a higher frequency of grain boundaries owing to the smaller grain size in this specimen, as shown in Figure 5-13(c) and Figure 5-14(e). As opposed to SP IN625, shot peening did not have a major influence on the dislocation density in SP IN718 (Figure 5-14(g) and (h)).

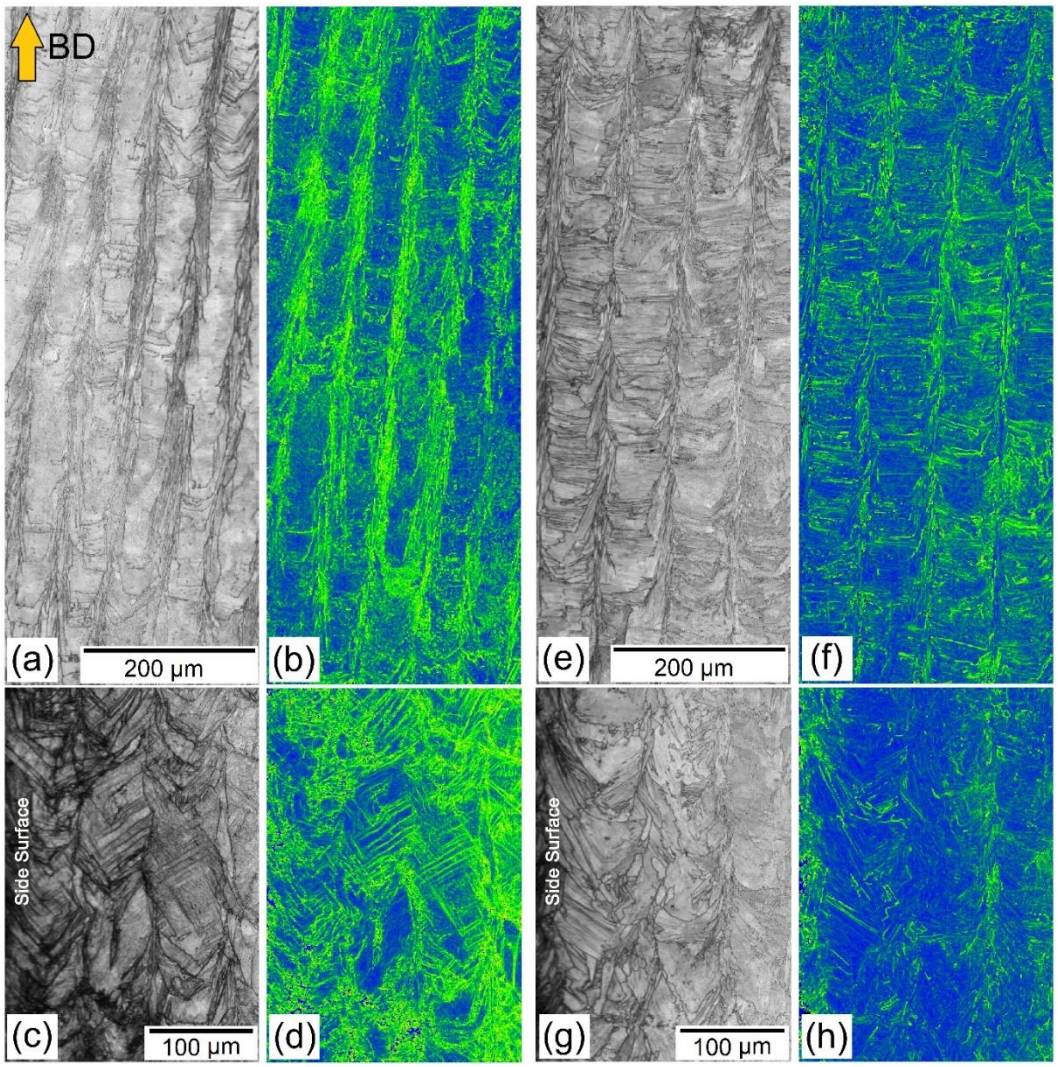

Figure 5-14. The band contrast and KAM maps for (a,b) AB IN625, (c,d) SP IN625, (e,f) AB IN718 and (g,h) SP IN718.

5.3.4. Fractography of fatigue specimens

The overview of the fractured surfaces of fatigue specimens for AB IN625 and AB IN718 tested at the stress level of 620 MPa are shown in Figure 5-15(a) and (d), respectively. The characteristic beach marks in both specimens indicate that the cracks have initiated from the left side surface and then propagated toward the right

side. Since the beach marks are not concentric in AB specimens, it can be concluded that there is not a single crack initiation site but rather a locus of sites located along the side surface. Further examination of the fracture surfaces at higher magnification showed that the initiation sites were located right at the surface (Figure 5-15(b) and (e)); hence, the fatigue crack initiation did not originate at the sub-surface. In addition, due to the absence of gas pores, lack of fusion porosities, or inclusions, the crack initiation could be attributed to the high side surface roughness, as presented earlier in Figure 5-9, Figure 5-10, and Figure 5-11 for IN625 and IN718 in the AB condition. Referring to Figure 5-15(c) and (f), adhered powder particles and the overlap curvature of the laser scan tracks are the main sources of the side surface roughness, acting as the stress concentrating sites during fatigue loading and favoring the crack initiation.

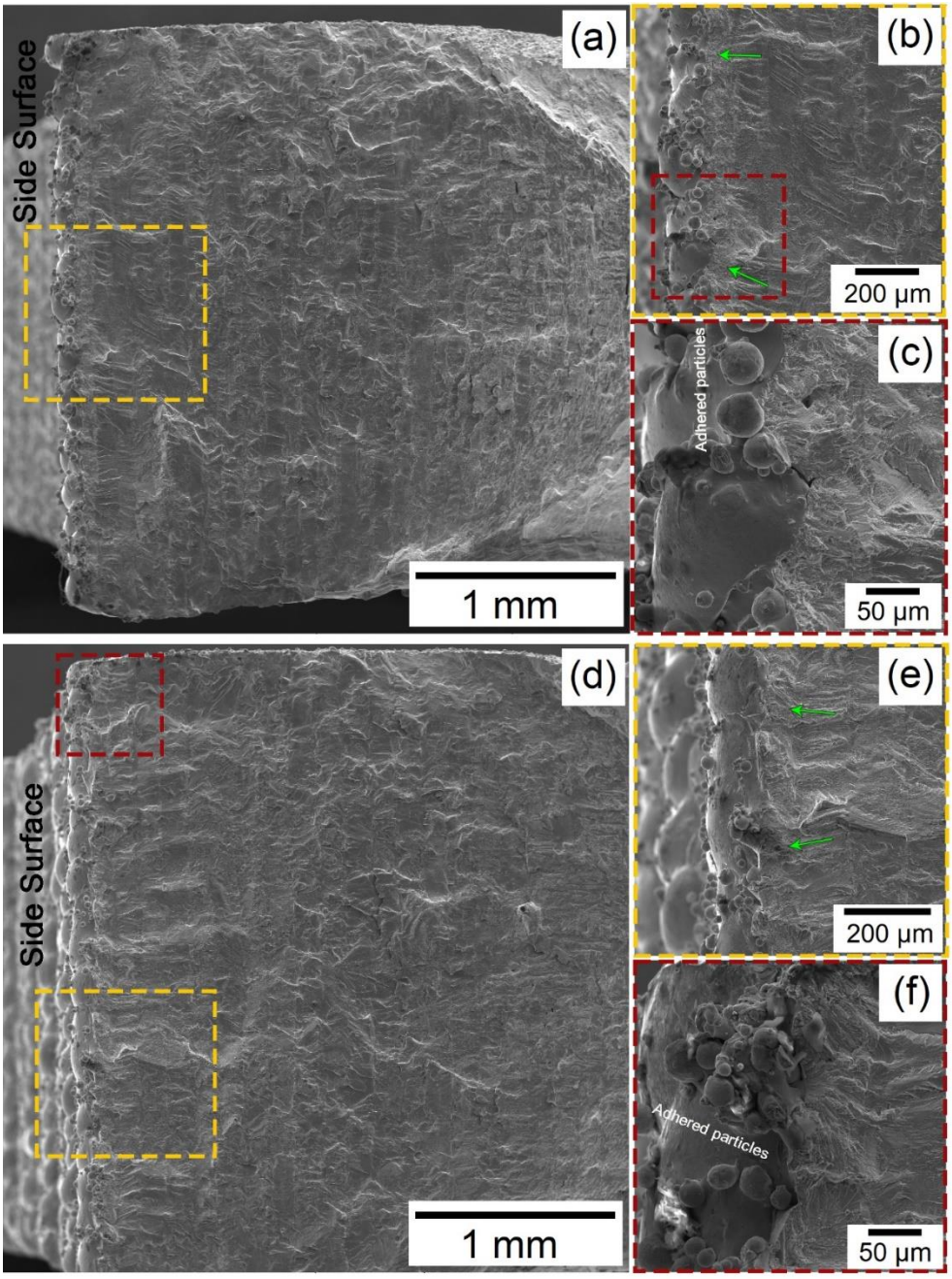

Figure 5-15. Fatigue failure surface for AB (a-c) IN625 and (d-f) IN718 at stress level 620 MPa.

The SEM micrographs of the fractured IN625 and IN718 in SP condition at the stress level of 620 MPa are provided in Figure 5-16. Shot peening did not change the location of the crack initiation sites but instead reduced the number of them (as shown in Figure 5-16(b), (c), and (f)). Moreover, these initiation sites were all located at the corner of the specimens, as shown in Figure 5-16(a) and (d). Therefore, shot peening has caused a deviation of the crack initiation locus towards the corner; however, no pore/inclusion that might have altered the cause of the crack initiation was observed. The detailed examinations revealed that the sub-surface initiation sites are absent, indicating that the surface roughness is still the leading cause behind the formation of these cracks.

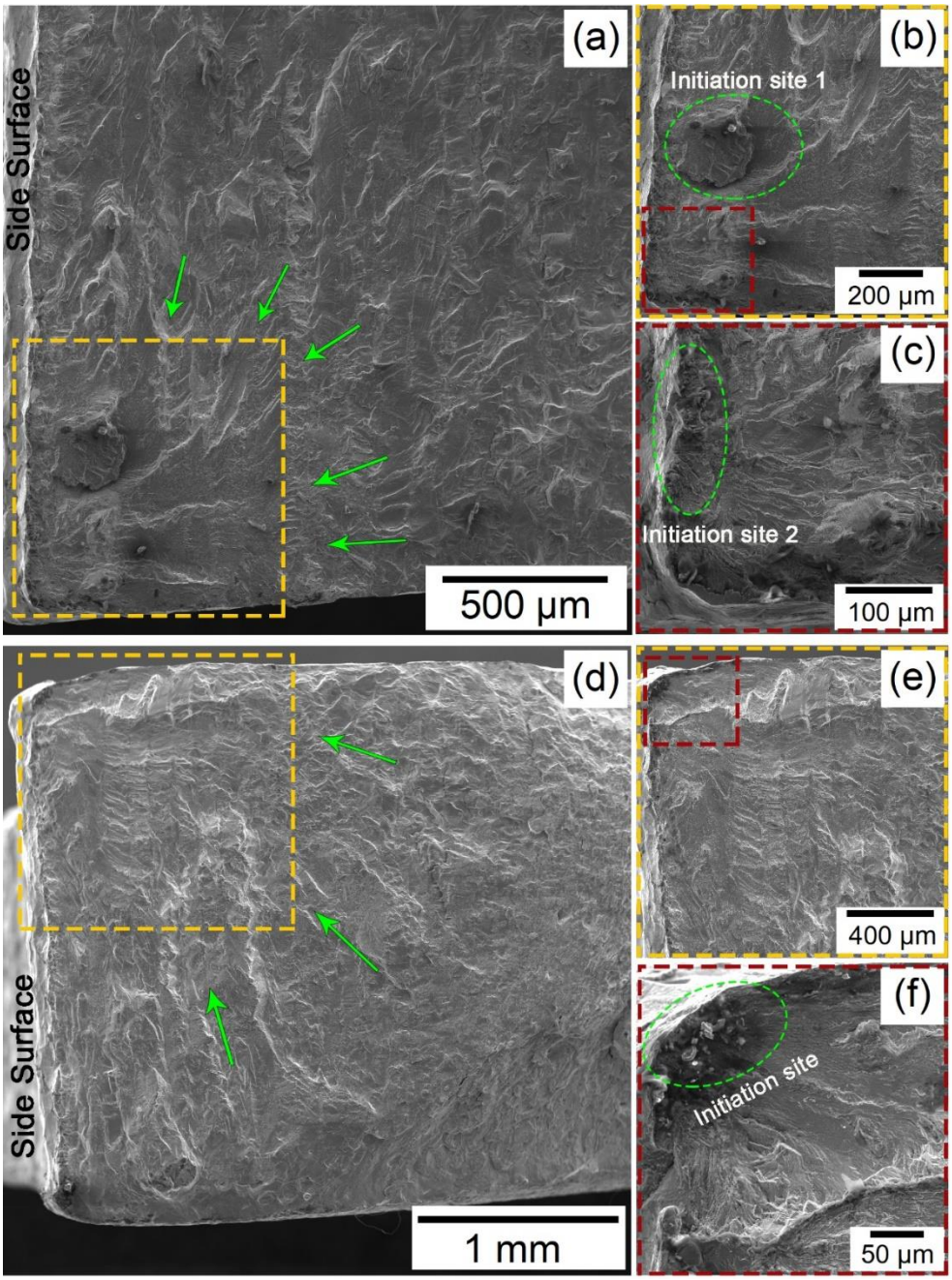

Figure 5-16. Fatigue failure surface for SP (a-c) IN625 and (d-f) IN718 at stress level 620 MPa.

5.3.5. Influence of shot peening on the fatigue life

According to the S-N curves provided in Figure 5-7 for IN625 and IN718, respectively, the shot peening significantly improved fatigue performance. In addition, the maximum stress level for having infinite fatigue life was found to increase by 110 and 105% for IN625 and IN718 specimens, respectively. To understand the reasons behind such an improvement, the fatigue test specimens were thoroughly investigated (section 5.3.3) in terms of (i) surface roughness, (ii) RS regime, and (iii) microstructure in both AB and SP conditions. The influence of each of these factors on enhancing the fatigue life of SP specimens can be discussed as follows:

I. Surface roughness reduction: Referring to surface topography maps shown in Figure 5-9 and Figure 5-10, the surface quality of the specimens was noticeably improved through shot peening. The R_a values shown in Figure 5-11 gave quantitative evidence of surface roughness reduction for all four SP surfaces. While the top and bottom surfaces also experienced a relatively high roughness reduction, the maximum R_a reduction of 40% and 65% corresponded to the side surfaces of IN625 and IN718, respectively. Such a roughness reduction finds its roots in the removal/crushing of adhered powder particles and/or the flattening of inter-track overlap curvatures (due to the plastic deformation) existing on the surface, as is evident in Figure 5-17. The surface roughness reduction caused by the shot peening leads to improved fatigue life by decreasing the frequency of potential crack initiation sites and lessening the stress concentration factor of a few sites still remaining on the surface. According to Figure 5-17(b) and (d), a few adhered powder particles and inter-track discontinuities are occasionally visible on the side surface, meaning that the employed shot

peening could not fully eliminate the preferential crack initiation sites. That is why the side surfaces were still the locations at which crack initiation occurred after shot peening, as can be seen in Figure 5-15 and Figure 5-16.

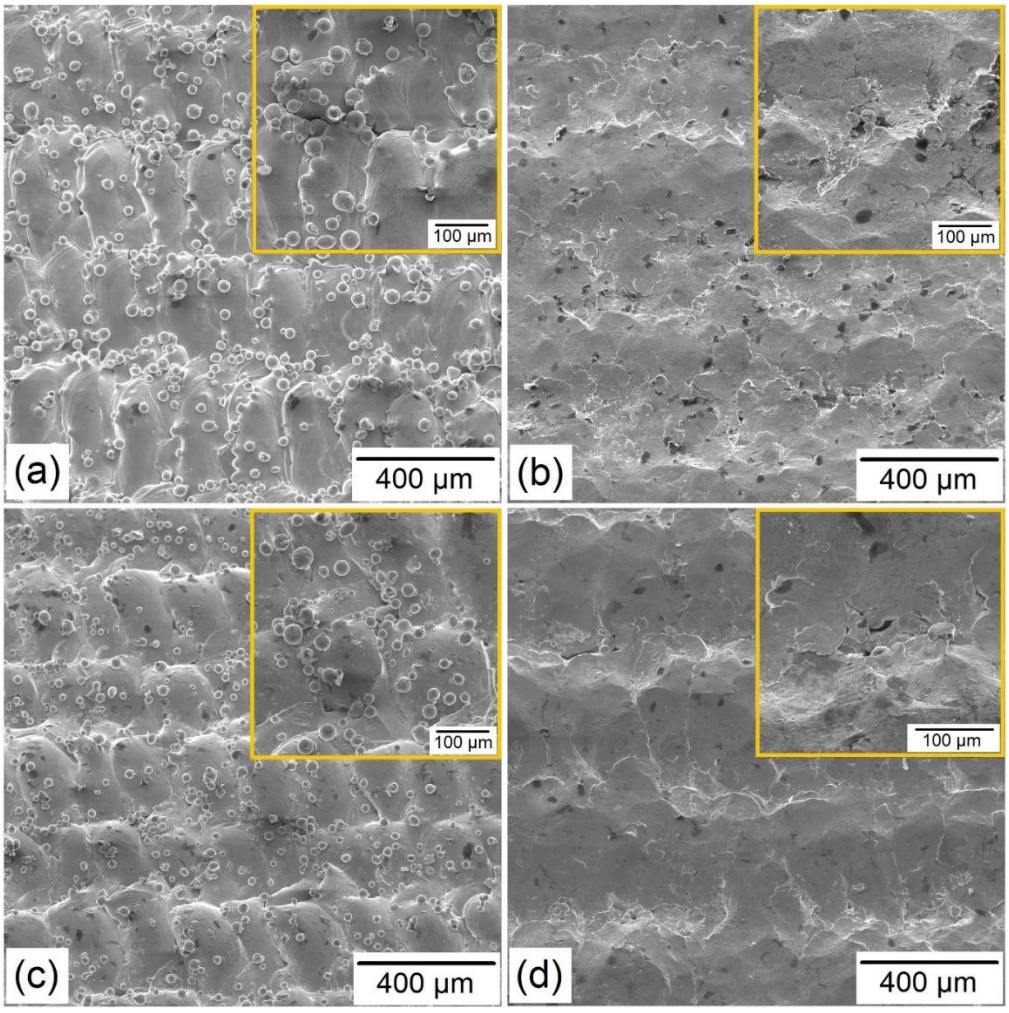

Figure 5-17. SEM micrographs from the side surface of (a) AB IN625, (b) SP IN625, (c) AB IN718, and (d) SP IN718 fatigue specimens.

II. Generation of compressive RS: Referring to the in-depth RS measurements shown in Figure 5-12, the top and bottom RS profiles in the AB IN625 were tensile, and in AB IN718 were slightly compressive or tensile along the measurement depth. However, the RS regime changed to compressive as a result of the shot peening. For the top surface profile, the maximum

compressive RS measured for the SP IN625 and SP IN718 was -1200 and -1400 MPa, respectively, both at a depth of 50 µm from the top surface. On the other hand, the bottom surface with higher tensile RS (500 MPa) than the top one in the AB condition featured a lower RS of ~-1000 MPa in SP IN625, while it was almost identical to that of the top surface in SP IN718. The RS was compressive to the depth of 250 µm from both sides in SP specimens. Although the RS measurements were conducted on the top and bottom surfaces, the same RS trend is expected for the side surfaces. Given that the fractography analysis results shown in Figure 5-15 and Figure 5-16 confirmed the crack initiation and propagation from the side and/or corner of the fatigue specimens, the EBSD analysis was performed adjacent to the side surfaces in the SP specimens. The KAM maps in Figure 5-14(b) and (d) for IN625 showed that the dislocation density increased (across the investigated depth) significantly after shot peening, which is in line with the in-depth RS measurements provided in Figure 5-12(a). Although the increase in dislocation density was also observed for the SP IN718 (compared to the AB condition), this was only limited to a shallow depth of 20 µm from the side surface. This observation for the side surface is not in agreement with the in-depth RS profiles of top and bottom surfaces shown in Figure 5-12(b). Considering either the in-depth RS profiles of top and bottom surfaces or the KAM maps of the side surfaces, it can be concluded that the shot peening has indeed generated compressive RS on all surfaces down to a specific depth. Compressive RS can improve the fatigue life by acting to resist the applied tensile stress during the fatigue loading. The maximum stress at infinite life also increases through the development of compressive RS, as suggested by [45]:

$$\Delta\sigma = -m\sigma_r \quad (2)$$

where $\Delta\sigma$ is the change of fatigue limit caused by shot peening, m is the mean stress sensitivity coefficient which depends on the material, and σ_r is

the RS. Finally, it should be mentioned that the plastic deformation induced by the shot peening can also close the existing sub-surface porosities, which improves fatigue life.

III. Changes in the grain/sub-grain structure: Figure 5-18 shows the grain size distribution for IN625 and IN718 in AB and SP conditions. In these measurements, boundaries with misorientation angles higher than 15° were considered as grain boundaries. As it is evident, the average weighted mean (AWM) grain size did not change noticeably after shot peening for both superalloys. However, based on the IPF-Z maps shown in Figure 5-13, the plastic deformation caused by the shot peening process led to the formation of sub-grains with misorientation angles below 15° (mostly below 5°) which were not considered as grains in the results provided in Figure 5-18. Nevertheless, such sub-grains can impede the movement of dislocations during the cyclic loading and, consequently, increase the fatigue life.

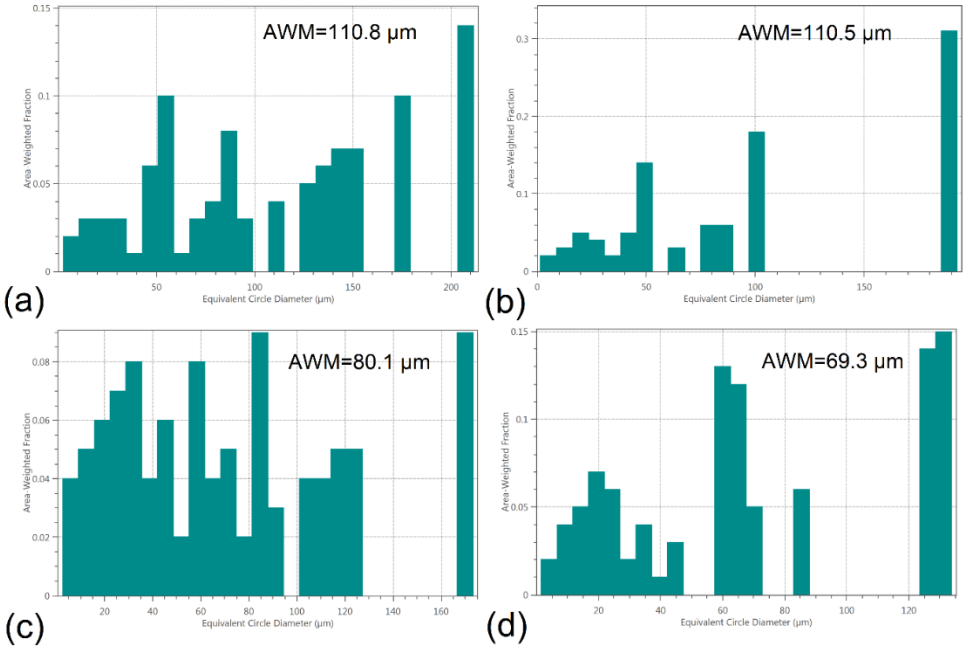

Figure 5-18. The grain size distribution of (a) AB IN625, (b) SP IN625, (c) AB IN718, and (d) SP IN718. The term "AWM" refers to average weighted mean grain size.

5.3.6. Mechanical properties-LPBF fabricated vs. wrought

When comparing the tensile strength of the LPBF fabricated IN625 (AB) with wrought IN625 [44], it was found that both yield (S_y) and ultimate tensile (S_u) strengths were ~25% higher for the LBPF fabricated ones. From the elongation to failure perspective, the LPBF fabricated IN625 showed an elongation of 35%, which is higher than that of the wrought IN625 (30%). Conversely, in the AB condition, LPBF resulted in lower S_y and S_u compared to the wrought+heat treated IN718, as per AMS5596 [44]; however, the elongation to failure of the LPBF fabricated part was 29%, which is remarkably higher than 12% for the wrought+heat treated counterpart [44].

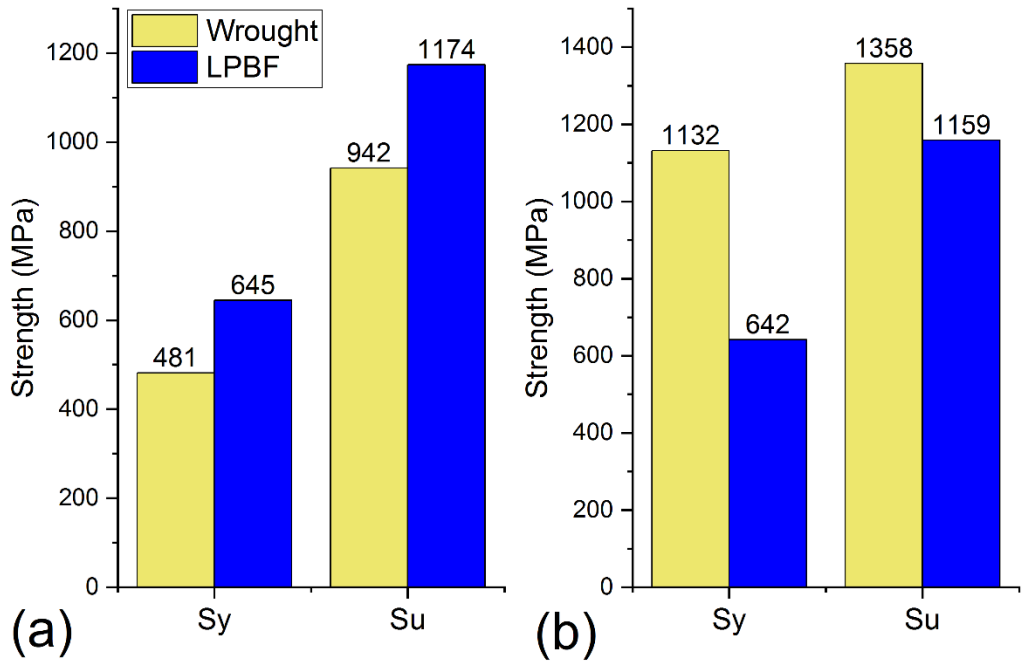

Figure 5-19. Comparison of mechanical strength for LPBF vs. wrought (a) IN625 and (b) IN718.

Referring to the S-N curves shown in Figure 5-7 for IN625, the infinite life at a maximum stress level of 260 MPa was obtained for AB condition, which is better than that of the notched (K_t=3) annealed wrought specimen but far below that of the unnotched one. In other words, the stress concentration caused by the micro-sized notches distributed along the outer surfaces (originating from high surface roughness) combined with the tensile RS in the AB IN625 seems to be equivalent to a notched wrought IN625 specimen with a K_t of 3. The maximum stress level of 550 MPa was achieved for the SP IN625, almost the same as that of the unnotched wrought specimen. This clearly reveals the significant role that the surface roughness reduction and generation of compressive RS have played in improving

the fatigue performance of LPBF fabricated IN625. Although the R_a of SP IN625 is yet higher than that of the wrought counterpart with a polished surface, the compressive RS could compensate for the adverse influence of this factor on the fatigue performance. Therefore, the LPBF fabricated IN625 can be considered as the end-use product in AB and SP conditions in applications demanding the same or even improved room temperature tensile strength and fatigue performance compared to the wrought state, respectively. It is worth noting that the microstructure of the LPBF fabricated IN625 consisted of a cellular structure with both cells and cell walls being Ni-based supersaturated solid solution, as shown in Figure 5-20(a) and (b). The line scan EDS analysis results in Figure 5-20(c) suggest a higher concentration of C, Nb, and Mo in the inter-cellular regions due to their high tendency to segregate during solidification , as reported by [1]. The microstructure of the wrought annealed IN625 is composed of a Ni-based solid solution, with the only difference being that the microstructure is fully homogeneous with some relatively large size carbides dispersed in the matrix. The noticeably higher tensile strength of the LPBF fabricated IN625 (Figure 5-19(a)) is attributed to the combination of three microstructural features, including (i) fine cellular structure, (ii) chemical composition heterogeneity in sub-micron scale, and (iii) formation of a supersaturated solid solution (with very low volume fraction of nano-sized carbides). All these features originate from the rapid cooling associated with the LPBF process and act to increase the strength by impeding the dislocation movement during loading.

For AB IN718, the fatigue life was significantly shorter than the unnotched solution-annealed and aged wrought case. Nevertheless, it showed an infinite fatigue life at a maximum stress level of 220 MPa, which is identical to that of the notched solution-annealed and aged wrought IN718 with a $K_t = 3$. Even after shot peening, an infinite life at a maximum stress level of 450 MPa was achieved, 10% below the unnotched solution-annealed and aged wrought IN718. The inferiority of the SP IN718 specimen was even more pronounced in the low cycle fatigue zone. Since the surface roughness and compressive RS of SP IN718 are in the same order as those of SP IN625, its shorter fatigue life should have been caused by the microstructural characteristics. Figure 5-20(d) shows the microstructure overview of the LPBF fabricated IN718. The higher magnification micrograph in Figure 5-20(e) as well as the line scan EDS analysis results in Figure 5-20(f) revealed the presence of phases other than Ni-based supersaturation solid solution in the microstructure, which have been reported to be Laves phase [13]. However, there was no evidence that the main strengthening agents of γ' and γ'' exist in the microstructure, as opposed to the solution-annealed and aged wrought IN718. This is consistent with the TEM investigations of the AB IN718 reported by [13]. The absence of γ' and γ'' is believed to be the primary reason behind the lower S_y, S_u and fatigue life of the LPBF fabricated IN718 than its solution-annealed and aged wrought counterpart.

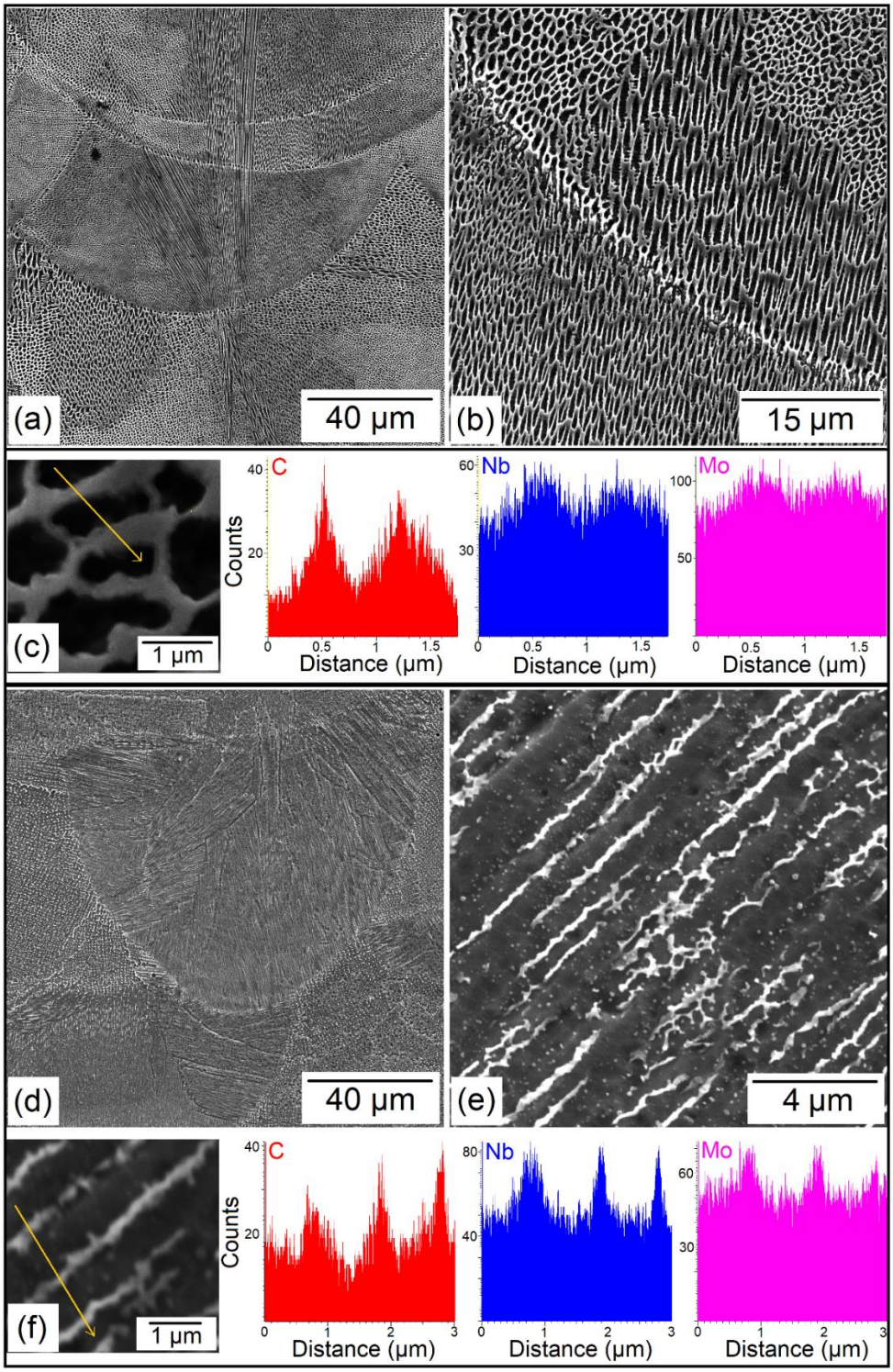

Figure 5-20. SEM micrographs and line scan EDS analysis results for (a-c) IN625 and (d-f) IN718.

5.3.7. Fatigue performance-IN625 vs. IN718

As shown in Figure 5-7(c), the fatigue performance of IN625 was superior to IN718 both in the AB and SP conditions. The maximum stress at the infinite life was 18 and 22% higher in IN625 compared to IN718 for AB and SP conditions, respectively. This is while the grain size of IN718 was 27-36% lower than IN625 in both AB and SP cases. Given that the crack initiated from the side surface of the AB specimens (Figure 5-15), the R_a values for the side surfaces (Figure 5-11(b) and (d)) should be used to justify the role of this factor. The R_a of side surfaces in the AB IN625 was lower than that of the AB IN718; however, R_a fails to explain the better fatigue performance of IN625 in SP condition since its higher surface roughness did not lead to shorter fatigue life. From the RS perspective, the AB IN718 featured lower RS, especially for the top surface (Figure 5-12). Nevertheless, its fatigue life was shorter. The shot peening process caused a compressive RS with a higher magnitude and farther depth on the side surface of the SP IN625 specimen, which can be one of the reasons behind its superior fatigue performance. Moreover, as confirmed by the IPF-Z map in Figure 5-13, a high amount of sub-grains in the SP IN625 specimen may also have acted to enhance the fatigue life by impeding the dislocation movement. However, none of the already mentioned factors can explain the large difference observed between the fatigue lives of IN625 and IN718. Given that both annealed IN625 and annealed+aged IN718 have almost the same fatigue performance in the wrought condition, the difference observed between their LPBF fabricated counterparts has to be attributed to their different

microstructural characteristics. The annealed+aged wrought IN718 contains γ′ and γ″ phases, as opposed to the AB IN718 in which such phases are absent (as confirmed by microstructural observations in Figure 5-20). Since precipitation hardening by these two phases is the main strengthening mechanism of the IN718 superalloy, the LPBF fabricated part cannot reach its maximum fatigue endurance capacity. On the other hand, the LPBF fabricated IN625 shares almost the same microstructural features as its wrought counterpart. That is why the LPBF fabricated IN718 showed inferior fatigue performance than IN625.

5.4. Conclusions

This research study aimed at investigating the effect of shot peening on the fatigue performance of the LPBF fabricated IN625 and IN718 superalloys. For this purpose, the optimum set of process parameters was found for each superalloy from the densification level, tensile strength, surface roughness, and residual stress perspectives. These optimum parameters were used to fabricate fatigue test samples. The LPBF fabricated fatigue test samples were tested in the as-built and shot-peened conditions. Results revealed the significant role of shot peening in improving the fatigue performance of both superalloys. The maximum stress level at infinite life increased by 110 and 105% for the shot-peened IN625 and IN718 compared to their as-built counterparts, respectively, mainly due to the surface roughness reduction and generation of compressive residual stresses on the surfaces. In the as-built condition, the IN625 and IN718 specimens performed better than their wrought counterparts with a stress concentration factor of 3. The

fatigue performance of the shot-peened IN625 was almost identical to that of the unnotched wrought specimen. However, compared to the unnotched solution-annealed and aged wrought IN718, the fatigue life of the shot-peened IN718 was still inferior mainly owing to the absence of γ' and γ'' phases in the microstructure of the LPBF fabricated IN718. As confirmed in this study, shot peening can be considered as a promising time-and-cost effective post-processing technique to improve the fatigue performance of L-PBF fabricated IN625 and IN718 parts used in room temperature applications.

References

[1] J. C. Lippold, S. D. Kiser, and J. N. DuPont, *Welding metallurgy and weldability of nickel-base alloys*: John Wiley & Sons, 2011.

[2] U. Heubner, *Nickel alloys*: CRC Press, 2000.

[3] A. P. Kiran Pulidindi. (2020). *Nickel Superalloy Market Size, By Type (Alloy 600/601/602, Alloy 625, Alloy 718, Alloy 825, Alloy 925, Hastelloy C276/C22/X, Waspaloy), By Shape (Bar, Wire, Sheet & Plate), By Application (Aerospace & Defense, Power Generation, Oil & Gas, Refinery, Chemical), Industry Analysis Report, Regional Outlook, Application Growth Potential, Price Trends, Competitive Market Share & Forecast, 2020 – 2026 (https://www.gminsights.com/industry-analysis/nickel-superalloy-market)*.

[4] S. Patel, J. deBarbadillo, and S. Coryell, "Superalloy 718: evolution of the alloy from high to low temperature application," in *Proceedings of the 9th International Symposium on Superalloy 718 & Derivatives: Energy, Aerospace, and Industrial Applications*, 2018, pp. 23-49.

[5] H. Eiselstein, "Metallurgy of a columbium-hardened nickel-chromium-iron alloy," in *Advances in the technology of stainless steels and related alloys*, ed: ASTM International, 1965.

[6] H. Eiselstein and D. Tillack, "Superalloys 718, 625 and various derivatives," *TMS, Warrendale, PA, EA Loria (Eds.)*, p. 1, 1991.

[7] S.-H. Chang, "In situ TEM observation of γ′, γ ″and δ precipitations on Inconel 718 superalloy through HIP treatment," *Journal of alloys and compounds,* vol. 486, pp. 716-721, 2009.

[8] E. Fereiduni, A. Ghasemi, and M. Elbestawi, "Selective Laser Melting of Aluminum and Titanium Matrix Composites: Recent Progress and Potential Applications in the Aerospace Industry," *Aerospace,* vol. 7, p. 77, 2020.

[9] T. DebRoy, H. Wei, J. Zuback, T. Mukherjee, J. Elmer, J. Milewski, *et al.*, "Additive manufacturing of metallic components–process, structure and properties," *Progress in Materials Science,* vol. 92, pp. 112-224, 2018.

[10] S. H. Kim, S.-M. Yeon, J. H. Lee, Y. W. Kim, H. Lee, J. Park, *et al.*, "Additive manufacturing of a shift block via laser powder bed fusion: the simultaneous utilisation of optimised topology and a lattice structure," *Virtual and Physical Prototyping,* vol. 15, pp. 460-480, 2020.

[11] S. Sanchez, P. Smith, Z. Xu, G. Gaspard, C. J. Hyde, W. W. Wits, *et al.*, "Powder bed fusion of nickel-based superalloys: A review," *International Journal of Machine Tools and Manufacture,* p. 103729, 2021.

[12] G. Marchese, M. Lorusso, S. Parizia, E. Bassini, J.-W. Lee, F. Calignano, *et al.*, "Influence of heat treatments on microstructure evolution and mechanical properties of Inconel 625 processed by laser powder bed fusion," *Materials Science and Engineering: A,* vol. 729, pp. 64-75, 2018.

[13] Y. Zhao, K. Li, M. Gargani, and W. Xiong, "A comparative analysis of Inconel 718 made by additive manufacturing and suction casting: Microstructure evolution in homogenization," *Additive Manufacturing,* vol. 36, p. 101404, 2020.

[14] L. Zhou, A. Mehta, B. McWilliams, K. Cho, and Y. Sohn, "Microstructure, precipitates and mechanical properties of powder bed fused inconel 718 before and after heat treatment," *Journal of Materials Science & Technology,* vol. 35, pp. 1153-1164, 2019.

[15] A. Kreitcberg, V. Brailovski, and S. Turenne, "Effect of heat treatment and hot isostatic pressing on the microstructure and mechanical properties of Inconel 625 alloy processed by laser powder bed fusion," *Materials Science and Engineering: A,* vol. 689, pp. 1-10, 2017.

[16] J. Schröder, T. Mishurova, T. Fritsch, I. Serrano-Munoz, A. Evans, M. Sprengel, *et al.*, "On the influence of heat treatment on microstructure and mechanical behavior of laser powder bed fused Inconel 718," *Materials Science and Engineering: A,* vol. 805, p. 140555, 2021.

[17] D. B. Witkin, D. Patel, T. V. Albright, G. E. Bean, and T. McLouth, "Influence of surface conditions and specimen orientation on high cycle fatigue properties of Inconel 718 prepared by laser powder bed fusion," *International Journal of Fatigue,* vol. 132, p. 105392, 2020.

[18] S. Kim, H. Choi, J. Lee, and S. Kim, "Room and elevated temperature fatigue crack propagation behavior of Inconel 718 alloy fabricated by laser powder bed fusion," *International Journal of Fatigue,* vol. 140, p. 105802, 2020.

[19] M. Muhammad, P. Frye, J. Simsiriwong, S. Shao, and N. Shamsaei, "An investigation into the effects of cyclic strain rate on the high cycle and very high cycle fatigue behaviors of wrought and additively manufactured Inconel 718," *International Journal of Fatigue,* vol. 144, p. 106038, 2021.

[20] C. Yu, Z. Huang, Z. Zhang, J. Shen, J. Wang, and Z. Xu, "Influence of post-processing on very high cycle fatigue resistance of Inconel 718 obtained with laser powder bed fusion," *International Journal of Fatigue,* vol. 153, p. 106510, 2021.

[21] C. Pei, D. Shi, H. Yuan, and H. Li, "Assessment of mechanical properties and fatigue performance of a selective laser melted nickel-base superalloy Inconel 718," *Materials Science and Engineering: A,* vol. 759, pp. 278-287, 2019.

[22] D. T. Ardi, L. Guowei, N. Maharjan, B. Mutiargo, S. H. Leng, and R. Srinivasan, "Effects of post-processing route on fatigue performance of laser powder bed fusion Inconel 718," *Additive Manufacturing,* vol. 36, p. 101442, 2020.

[23] A. Kaletsch, S. Qin, S. Herzog, and C. Broeckmann, "Influence of high initial porosity introduced by laser powder bed fusion on the fatigue strength of Inconel 718 after post-processing with hot isostatic pressing," *Additive Manufacturing,* vol. 47, p. 102331, 2021.

[24] R. Konečná, G. Nicoletto, L. Kunz, and A. Bača, "Microstructure and directional fatigue behavior of Inconel 718 produced by selective laser melting," *Procedia Structural Integrity,* vol. 2, pp. 2381-2388, 2016.

[25] P. Frye, M. Muhammad, J. Simsiriwong, and N. Shamsaei, "Very high cycle fatigue behavior of laser beam-powder bed fused Inconel 718," in *Conference proceedings of the 2019 Solid Freeform Fabrication Symposium*.

[26] A. R. Balachandramurthi, N. R. Jaladurgam, C. Kumara, T. Hansson, J. Moverare, J. Gårdstam, *et al.*, "On the Microstructure of Laser Beam Powder Bed Fusion Alloy 718 and Its Influence on the Low Cycle Fatigue Behaviour," *Materials,* vol. 13, p. 5198, 2020.

[27] Z. Song, W. Gao, D. Wang, Z. Wu, M. Yan, L. Huang, *et al.*, "Very-High-Cycle Fatigue Behavior of Inconel 718 Alloy Fabricated by Selective Laser Melting at Elevated Temperature," *Materials,* vol. 14, p. 1001, 2021.

[28] D. Ren, Z. Xue, Y. Jiang, X. Hu, and Y. Zhang, "Influence of single tensile overload on fatigue crack propagation behavior of the selective laser melting inconel 625 superalloy," *Engineering Fracture Mechanics,* vol. 239, p. 107305, 2020.

[29] X. Hu, Z. Xue, T. Ren, Y. Jiang, C. Dong, and F. Liu, "On the fatigue crack growth behaviour of selective laser melting fabricated Inconel 625: Effects of build

orientation and stress ratio," *Fatigue & Fracture of Engineering Materials & Structures,* vol. 43, pp. 771-787, 2020.

[30] D. Ren, Y. Jiang, Y. Zhang, and X. Hu, "A Comparative Study of Selective Laser Melting Processed Inconel 625 Superalloy: Fatigue Performances under Constant Amplitude Loading and Single Tensile Overload," in *Journal of Physics: Conference Series*, 2020, p. 012131.

[31] J.-R. Poulin, V. Brailovski, and P. Terriault, "Long fatigue crack propagation behavior of Inconel 625 processed by laser powder bed fusion: Influence of build orientation and post-processing conditions," *International Journal of Fatigue,* vol. 116, pp. 634-647, 2018.

[32] J.-R. Poulin, A. Kreitcberg, P. Terriault, and V. Brailovski, "Long fatigue crack propagation behavior of laser powder bed-fused inconel 625 with intentionally-seeded porosity," *International Journal of Fatigue,* vol. 127, pp. 144-156, 2019.

[33] J.-R. Poulin, A. Kreitcberg, P. Terriault, and V. Brailovski, "Fatigue strength prediction of laser powder bed fusion processed Inconel 625 specimens with intentionally-seeded porosity: Feasibility study," *International Journal of Fatigue,* vol. 132, p. 105394, 2020.

[34] K.-S. Kim, T.-H. Kang, M. E. Kassner, K.-T. Son, and K.-A. Lee, "High-temperature tensile and high cycle fatigue properties of inconel 625 alloy manufactured by laser powder bed fusion," *Additive Manufacturing,* vol. 35, p. 101377, 2020.

[35] J.-R. Poulin, A. Kreitcberg, and V. Brailovski, "Effect of hot isostatic pressing of laser powder bed fused Inconel 625 with purposely induced defects on the residual porosity and fatigue crack propagation behavior," *Additive Manufacturing,* vol. 47, p. 102324, 2021.

[36] M. Komarasamy, S. Shukla, S. Williams, K. Kandasamy, S. Kelly, and R. S. Mishra, "Exceptional fatigue resistance and impact toughness of additively manufactured nickel alloy 625 by laser powder bed fusion," *International Journal of Powder Metallurgy,* vol. 54, 2019.

[37] M. Narvan, K. S. Al-Rubaie, and M. Elbestawi, "Process-structure-property relationships of AISI H13 tool steel processed with selective laser melting," *Materials,* vol. 12, p. 2284, 2019.

[38] E. A. Lass, M. R. Stoudt, M. E. Williams, M. B. Katz, L. E. Levine, T. Q. Phan, *et al.*, "Formation of the Ni 3 Nb δ-phase in stress-relieved Inconel 625 produced via laser powder-bed fusion additive manufacturing," *Metallurgical and Materials Transactions A,* vol. 48, pp. 5547-5558, 2017.

[39] J. L. Bartlett and X. Li, "An overview of residual stresses in metal powder bed fusion," *Additive Manufacturing,* vol. 27, pp. 131-149, 2019.

[40] N. Kalentics, E. Boillat, P. Peyre, S. Ćirić-Kostić, N. Bogojević, and R. E. Logé, "Tailoring residual stress profile of selective laser melted parts by laser shock peening," *Additive Manufacturing,* vol. 16, pp. 90-97, 2017.

[41] M. Balbaa, M. Elbestawi, and J. McIsaac, "An experimental investigation of surface integrity in selective laser melting of Inconel 625," *The International Journal of Advanced Manufacturing Technology,* vol. 104, pp. 3511-3529, 2019.

[42] M. Balbaa, S. Mekhiel, M. Elbestawi, and J. McIsaac, "On selective laser melting of Inconel 718: Densification, surface roughness, and residual stresses," *Materials & Design,* vol. 193, p. 108818, 2020.

[43] K. S. Al-Rubaie, M. A. Del Grande, D. N. Travessa, and K. R. Cardoso, "Effect of pre-strain on the fatigue life of 7050-T7451 aluminium alloy," *Materials Science and Engineering: A,* vol. 464, pp. 141-150, 2007.

[44] B. M. Institute, *Metallic Materials Properties Development and Standardization (MMPDS-09)*: Federal Aviation Administration, 2014.

[45] X. Pan, X. Li, L. Zhou, X. Feng, S. Luo, and W. He, "Effect of Residual Stress on S–N Curves and Fracture Morphology of Ti6Al4V Titanium Alloy after Laser Shock Peening without Protective Coating," *Materials,* vol. 12, p. 3799, 2019.

[1] J. C. Lippold, S. D. Kiser, and J. N. DuPont, *Welding metallurgy and weldability of nickel-base alloys*: John Wiley & Sons, 2011.

[2] U. Heubner, *Nickel alloys*: CRC Press, 2000.

[3] A. P. Kiran Pulidindi. (2020). *Nickel Superalloy Market Size, By Type (Alloy 600/601/602, Alloy 625, Alloy 718, Alloy 825, Alloy 925, Hastelloy C276/C22/X, Waspaloy), By Shape (Bar, Wire, Sheet & Plate), By Application (Aerospace & Defense, Power Generation, Oil & Gas, Refinery, Chemical), Industry Analysis Report, Regional Outlook, Application Growth Potential, Price Trends, Competitive Market Share & Forecast, 2020 – 2026 (https://www.gminsights.com/industry-analysis/nickel-superalloy-market)*.

[4] S. Patel, J. deBarbadillo, and S. Coryell, "Superalloy 718: evolution of the alloy from high to low temperature application," in *Proceedings of the 9th International Symposium on Superalloy 718 & Derivatives: Energy, Aerospace, and Industrial Applications*, 2018, pp. 23-49.

[5] H. Eiselstein, "Metallurgy of a columbium-hardened nickel-chromium-iron alloy," in *Advances in the technology of stainless steels and related alloys*, ed: ASTM International, 1965.

[6] H. Eiselstein and D. Tillack, "Superalloys 718, 625 and various derivatives," *TMS, Warrendale, PA, EA Loria (Eds.),* p. 1, 1991.

[7] S.-H. Chang, "In situ TEM observation of γ′, γ ″and δ precipitations on Inconel 718 superalloy through HIP treatment," *Journal of alloys and compounds,* vol. 486, pp. 716-721, 2009.

[8] E. Fereiduni, A. Ghasemi, and M. Elbestawi, "Selective Laser Melting of Aluminum and Titanium Matrix Composites: Recent Progress and Potential Applications in the Aerospace Industry," *Aerospace,* vol. 7, p. 77, 2020.

[9] T. DebRoy, H. Wei, J. Zuback, T. Mukherjee, J. Elmer, J. Milewski, *et al.*, "Additive manufacturing of metallic components–process, structure and properties," *Progress in Materials Science,* vol. 92, pp. 112-224, 2018.

[10] S. H. Kim, S.-M. Yeon, J. H. Lee, Y. W. Kim, H. Lee, J. Park, *et al.*, "Additive manufacturing of a shift block via laser powder bed fusion: the simultaneous utilisation of optimised topology and a lattice structure," *Virtual and Physical Prototyping,* vol. 15, pp. 460-480, 2020.

[11] S. Sanchez, P. Smith, Z. Xu, G. Gaspard, C. J. Hyde, W. W. Wits, *et al.*, "Powder bed fusion of nickel-based superalloys: A review," *International Journal of Machine Tools and Manufacture,* p. 103729, 2021.

[12] G. Marchese, M. Lorusso, S. Parizia, E. Bassini, J.-W. Lee, F. Calignano, *et al.*, "Influence of heat treatments on microstructure evolution and mechanical properties of Inconel 625 processed by laser powder bed fusion," *Materials Science and Engineering: A,* vol. 729, pp. 64-75, 2018.

[13] Y. Zhao, K. Li, M. Gargani, and W. Xiong, "A comparative analysis of Inconel 718 made by additive manufacturing and suction casting: Microstructure evolution in homogenization," *Additive Manufacturing,* vol. 36, p. 101404, 2020.

[14] L. Zhou, A. Mehta, B. McWilliams, K. Cho, and Y. Sohn, "Microstructure, precipitates and mechanical properties of powder bed fused inconel 718 before and after heat treatment," *Journal of Materials Science & Technology,* vol. 35, pp. 1153-1164, 2019.

[15] A. Kreitcberg, V. Brailovski, and S. Turenne, "Effect of heat treatment and hot isostatic pressing on the microstructure and mechanical properties of Inconel 625 alloy processed by laser powder bed fusion," *Materials Science and Engineering: A,* vol. 689, pp. 1-10, 2017.

[16] J. Schröder, T. Mishurova, T. Fritsch, I. Serrano-Munoz, A. Evans, M. Sprengel, *et al.*, "On the influence of heat treatment on microstructure and mechanical behavior of laser powder bed fused Inconel 718," *Materials Science and Engineering: A,* vol. 805, p. 140555, 2021.

[17] D. B. Witkin, D. Patel, T. V. Albright, G. E. Bean, and T. McLouth, "Influence of surface conditions and specimen orientation on high cycle fatigue properties of Inconel 718 prepared by laser powder bed fusion," *International Journal of Fatigue,* vol. 132, p. 105392, 2020.

[18] S. Kim, H. Choi, J. Lee, and S. Kim, "Room and elevated temperature fatigue crack propagation behavior of Inconel 718 alloy fabricated by laser powder bed fusion," *International Journal of Fatigue,* vol. 140, p. 105802, 2020.

[19] M. Muhammad, P. Frye, J. Simsiriwong, S. Shao, and N. Shamsaei, "An investigation into the effects of cyclic strain rate on the high cycle and very high cycle fatigue behaviors of wrought and additively manufactured Inconel 718," *International Journal of Fatigue,* vol. 144, p. 106038, 2021.

[20] C. Yu, Z. Huang, Z. Zhang, J. Shen, J. Wang, and Z. Xu, "Influence of post-processing on very high cycle fatigue resistance of Inconel 718 obtained with laser powder bed fusion," *International Journal of Fatigue,* vol. 153, p. 106510, 2021.

[21] C. Pei, D. Shi, H. Yuan, and H. Li, "Assessment of mechanical properties and fatigue performance of a selective laser melted nickel-base superalloy Inconel 718," *Materials Science and Engineering: A,* vol. 759, pp. 278-287, 2019.

[22] D. T. Ardi, L. Guowei, N. Maharjan, B. Mutiargo, S. H. Leng, and R. Srinivasan, "Effects of post-processing route on fatigue performance of laser powder bed fusion Inconel 718," *Additive Manufacturing,* vol. 36, p. 101442, 2020.

[23] A. Kaletsch, S. Qin, S. Herzog, and C. Broeckmann, "Influence of high initial porosity introduced by laser powder bed fusion on the fatigue strength of Inconel 718 after post-processing with hot isostatic pressing," *Additive Manufacturing,* vol. 47, p. 102331, 2021.

[24] R. Konečná, G. Nicoletto, L. Kunz, and A. Bača, "Microstructure and directional fatigue behavior of Inconel 718 produced by selective laser melting," *Procedia Structural Integrity,* vol. 2, pp. 2381-2388, 2016.

[25] P. Frye, M. Muhammad, J. Simsiriwong, and N. Shamsaei, "Very high cycle fatigue behavior of laser beam-powder bed fused Inconel 718," in *Conference proceedings of the 2019 Solid Freeform Fabrication Symposium*.

[26] A. R. Balachandramurthi, N. R. Jaladurgam, C. Kumara, T. Hansson, J. Moverare, J. Gårdstam, *et al.*, "On the Microstructure of Laser Beam Powder Bed Fusion Alloy 718 and Its Influence on the Low Cycle Fatigue Behaviour," *Materials,* vol. 13, p. 5198, 2020.

[27] Z. Song, W. Gao, D. Wang, Z. Wu, M. Yan, L. Huang, *et al.*, "Very-High-Cycle Fatigue Behavior of Inconel 718 Alloy Fabricated by Selective Laser Melting at Elevated Temperature," *Materials,* vol. 14, p. 1001, 2021.

[28] D. Ren, Z. Xue, Y. Jiang, X. Hu, and Y. Zhang, "Influence of single tensile overload on fatigue crack propagation behavior of the selective laser melting inconel 625 superalloy," *Engineering Fracture Mechanics,* vol. 239, p. 107305, 2020.

[29] X. Hu, Z. Xue, T. Ren, Y. Jiang, C. Dong, and F. Liu, "On the fatigue crack growth behaviour of selective laser melting fabricated Inconel 625: Effects of build

orientation and stress ratio," *Fatigue & Fracture of Engineering Materials & Structures,* vol. 43, pp. 771-787, 2020.

[30] D. Ren, Y. Jiang, Y. Zhang, and X. Hu, "A Comparative Study of Selective Laser Melting Processed Inconel 625 Superalloy: Fatigue Performances under Constant Amplitude Loading and Single Tensile Overload," in *Journal of Physics: Conference Series*, 2020, p. 012131.

[31] J.-R. Poulin, V. Brailovski, and P. Terriault, "Long fatigue crack propagation behavior of Inconel 625 processed by laser powder bed fusion: Influence of build orientation and post-processing conditions," *International Journal of Fatigue,* vol. 116, pp. 634-647, 2018.

[32] J.-R. Poulin, A. Kreitcberg, P. Terriault, and V. Brailovski, "Long fatigue crack propagation behavior of laser powder bed-fused inconel 625 with intentionally-seeded porosity," *International Journal of Fatigue,* vol. 127, pp. 144-156, 2019.

[33] J.-R. Poulin, A. Kreitcberg, P. Terriault, and V. Brailovski, "Fatigue strength prediction of laser powder bed fusion processed Inconel 625 specimens with intentionally-seeded porosity: Feasibility study," *International Journal of Fatigue,* vol. 132, p. 105394, 2020.

[34] K.-S. Kim, T.-H. Kang, M. E. Kassner, K.-T. Son, and K.-A. Lee, "High-temperature tensile and high cycle fatigue properties of inconel 625 alloy manufactured by laser powder bed fusion," *Additive Manufacturing,* vol. 35, p. 101377, 2020.

[35] J.-R. Poulin, A. Kreitcberg, and V. Brailovski, "Effect of hot isostatic pressing of laser powder bed fused Inconel 625 with purposely induced defects on the residual porosity and fatigue crack propagation behavior," *Additive Manufacturing,* vol. 47, p. 102324, 2021.

[36] M. Komarasamy, S. Shukla, S. Williams, K. Kandasamy, S. Kelly, and R. S. Mishra, "Exceptional fatigue resistance and impact toughness of additively manufactured nickel alloy 625 by laser powder bed fusion," *International Journal of Powder Metallurgy,* vol. 54, 2019.

[37] M. Narvan, K. S. Al-Rubaie, and M. Elbestawi, "Process-structure-property relationships of AISI H13 tool steel processed with selective laser melting," *Materials,* vol. 12, p. 2284, 2019.

[38] E. A. Lass, M. R. Stoudt, M. E. Williams, M. B. Katz, L. E. Levine, T. Q. Phan, *et al.*, "Formation of the Ni 3 Nb δ-phase in stress-relieved Inconel 625 produced via laser powder-bed fusion additive manufacturing," *Metallurgical and Materials Transactions A,* vol. 48, pp. 5547-5558, 2017.

[39] J. L. Bartlett and X. Li, "An overview of residual stresses in metal powder bed fusion," *Additive Manufacturing,* vol. 27, pp. 131-149, 2019.

[40] N. Kalentics, E. Boillat, P. Peyre, S. Ćirić-Kostić, N. Bogojević, and R. E. Logé, "Tailoring residual stress profile of selective laser melted parts by laser shock peening," *Additive Manufacturing,* vol. 16, pp. 90-97, 2017.

[41] M. Balbaa, M. Elbestawi, and J. McIsaac, "An experimental investigation of surface integrity in selective laser melting of Inconel 625," *The International Journal of Advanced Manufacturing Technology,* vol. 104, pp. 3511-3529, 2019.

[42] M. Balbaa, S. Mekhiel, M. Elbestawi, and J. McIsaac, "On selective laser melting of Inconel 718: Densification, surface roughness, and residual stresses," *Materials & Design,* vol. 193, p. 108818, 2020.

[43] K. S. Al-Rubaie, M. A. Del Grande, D. N. Travessa, and K. R. Cardoso, "Effect of pre-strain on the fatigue life of 7050-T7451 aluminium alloy," *Materials Science and Engineering: A,* vol. 464, pp. 141-150, 2007.

[44] B. M. Institute, *Metallic Materials Properties Development and Standardization (MMPDS-09)*: Federal Aviation Administration, 2014.

[45] X. Pan, X. Li, L. Zhou, X. Feng, S. Luo, and W. He, "Effect of Residual Stress on S–N Curves and Fracture Morphology of Ti6Al4V Titanium Alloy after Laser Shock Peening without Protective Coating," *Materials,* vol. 12, p. 3799, 2019.

Chapter 6

A novel post-processing approach towards improving hole accuracy and surface integrity in laser powder bed fusion of IN625

Complete Citation:

Balbaa, Mohamed, et al. "A novel post-processing approach towards improving hole accuracy and surface integrity in laser powder bed fusion of IN625." The International Journal of Advanced Manufacturing Technology (2022): 1-10.

Copyright:

Relative Contributions:

M. A. Balbaa: Performed experiments, analysis, and data interpretation; wrote the first draft of the manuscript

R. Hussein: Performed experiments, data collection, and co-wrote the first draft

L. Hackel: Performed experiments, and revised the manuscript

M. A. Elbestawi: Revised and edited the manuscript

Abstract:

Laser powder bed fusion (LPBF) has been widely used to manufacture intricate geometries that would otherwise be costly to conventionally manufacture due to the complexity of design and the hard-to-machine nature of Ni-based superalloys such as IN625. However, the advantage of LPBF is opposed by the formation of high tensile residual stresses (RS), poor surface quality, and dimensional accuracy, which would require several post processes to correct these drawbacks. This work evaluates the possibility of reducing the number of post-processing steps by using drilling to improve both the RS and geometrical accuracy of printed holes compared to the widely used post-process Laser peening (LP). First, both conventional drilling and Low-frequency vibration-assisted drilling (LF-VAD) were carried out on a printed plate with differently sized pilot holes, using a range of cutting parameters to determine the optimum cutting parameters. Next, the geometrical accuracy, surface roughness, microhardness, and in-depth RS were measured compared to as-built and LP holes. Drilling had the combined advantage of improving the hole accuracy compared to the undersized as-built holes, increasing the microhardness and inducing in-depth compressive RS. However, although LP induced high compressive RS, it had no beneficial effect on the geometric accuracy or surface roughness except the deeper depth of the compressive RS layer compared to the drilling process.

Keywords:

Inconel 625, Laser powder bed fusion, Post-processing, Vibration-assisted drilling, Laser peening, Residual stress

Acronyms

AB	As-built
AM	Additive Manufacturing
LF-VAD	Low-Frequency Vibration-assisted Drilling
LPBF	Laser Powder Bed Fusion
LP	Laser peened
RS	Residual Stress
VAD	Vibration-assisted Drilling

Notations

A_m	Vibration amplitude (mm)
f	Feed rate (mm/rev)
h	Hatch spacing (mm)
N	Cutting speed (rpm)
P	Power (W)
t	Layer thickness (mm)
v	Scan speed (mm/s)
Φ_{pilot}	Pilot hole diameter (mm)

6.1. Introduction

The superior thermo-mechanical properties of the Ni-based alloy IN625, such as high-temperature strength, corrosion resistance, oxidation, and fatigue resistance, entices their broad application in the aerospace, marine, and nuclear industries [1, 2]. However, these properties classify IN 625 as a hard-to-cut material. Furthermore, the high-temperature strength combined with a high work-hardening tendency results in premature tool failure due to the high tool wear or material-tool adhesion [3, 4]. These adverse properties make IN625 suitable for additive manufacturing (AM), specifically Laser powder bed fusion (LPBF). LPBF's advantage is its ability to produce complex shapes with fine features and a high level of customization. Consequently, these advantages accelerated the employment of LPBF across a wide range of industrial sectors such as aerospace [5, 6], automotive [7, 8], rapid tooling [9], and biomedical [10, 11] sectors.

LPBF of Ni-based superalloys is commonly associated with sub-optimal geometrical accuracy and high tensile residual stresses (RS) [12, 13]. The poor geometrical accuracy can be linked to the sintering of satellite powder particles that alter the part dimensions [14]. The high tensile RS is attributed to the melt pool's localized high temperature [15, 16], the cyclic heating and cooling, and the thermal gradient between the melt pool and the previously consolidated layer [13, 17]. Therefore, these adverse part properties necessitate the post-processing steps to reduce the surface roughness, improve dimensional accuracy, and reverse the tensile RS to enhance fatigue life and part performance. Although LPBF

manufactured parts may require post-machining to remove the support structures [18], the focus currently is on the possible post-processes to improve the part properties.

Different post-processing routes have been investigated to enhance the properties of LPBF IN625 [13]. Heat treatments were the most widely investigated post-processing techniques. Studies employed various methodologies such as stress relief (SR) annealing, recrystallization annealing (RA), solution treatment (ST), and hot isostatic pressing (HIP), and can be summarized as follows:

- Stress relief annealing is a heat treatment process typically applied in the temperature range of 650°C to 870°C, before separating the parts from the build plate. This process targets residual stress reduction while maintaining geometrical dimensions [13, 19].
- Recrystallization annealing reduces the material anisotropy through recrystallization of the material grain structure, generally applied in the 930°C to 1040°C temperature range [13, 20].
- Solution treatment is used to dissolve the material carbides and δ-phase precipitates at 1040°C to 1200°C before age-hardening [13, 19].
- Hot Isostatic pressing (HIP) is a technique where the part is heat-treated at 1100°C to 1240°C under pressurized Argon atmosphere (100-165 MPa) for 1-3 h to enhance the mechanical properties and density (from 98.5% to 99.5%) by decreasing the anisotropy and the structure micro-porosity, respectively [21].

Despite the beneficial impact of heat treatment on grain structure enhancement, RS relief, and reducing the mechanical properties anisotropy, the heat-treatment post-process does not improve the surface topography and geometrical accuracy or even generate compressive RS at a specific location to increase the part fatigue life, which is critical for the aerospace sector.

Conversely, mechanical post-processing, such as shot peening (SP) or Laser peening (LP), for example, provides a solution to the drawbacks of heat treatment post-processing, as it can induce compressive RS in critical areas [22]. Both SP and LP aim at cold working the material to generate plastic strain and compressive RS. However, the application media differs from steel balls for the former and a laser beam for the latter [22, 23]. Although there are no investigations on SP or LP's effect on LPBF IN625, there are a few studies on LPBF IN718. It was shown that SP improved the surface roughness, generated compressive RS, and improved the fatigue life of IN718 [24, 25]. Furthermore, the effects of LP were compared to SP for LPBF IN718, and it was found that both methods induced equal compressive RS magnitudes near the surface and nearly the same fatigue life. However, LP had a higher penetration depth of compressive RS compared to SP [26].

On another note, mechanical fastening is commonly used for parts assemblies, which otherwise cannot be manufactured as a single part. Fastening ensures good reliability, convenient inspection, and easy detachability; hence, hole drilling is necessary during the manufacturing life cycle. The machined surface is subjected to high thermal and mechanical loads during the drilling process, which could

enhance the surface topography, geometrical accuracy, hardness, surface, and subsurface RS. Conventional drilling of IN718 fabricated by LPBF has been investigated using different cutting speeds and feed rates [12]. The results showed improvements in surface roughness and micro-hardness. The surface roughness decreased from 8 µm for the as-built to 1.5-3 µm, while the micro-hardness increased by 100 HV, and this effect was evident to a depth of 100 µm. Despite the advantages of conventional drilling in terms of surface roughness, geometrical accuracy, and micro-hardness, the drilling process suffers from catastrophic tool filer due to high tool wear or material-tool welding, which increases the production cost and lead time [3, 4], thus raising the need for unconventional drilling techniques.

Vibration-assisted drilling (VAD) is an advanced machining process, where an axial oscillation is superimposed to the tool's feed motion to enhance the chip removal mechanism, lower the thermal load, and alter the machining induced RS profile [27]. For a wide range of difficult-to-cut materials [27-29], VAD showed a significant enhancement in terms of geometrical accuracy and machining induced RS. VAD of Titanium alloy resulted in a lower hole tolerance grade (from IT10 grade for conventional drilling to IT9 grade for VAD according to the ISO 286), up to 25% reduction in the machined surface roughness (R_a), and generation of a 242 MPa surface compressive RS, as presented in [30]. VAD of aluminum alloy 7075 succeeded in overcoming the high burr formation issue (49.5% to 52.6% burr height reduction), as investigated in [31]. Regarding Ni-based superalloys, a limited

number of studies investigate the effect of VAD on part quality. Ultrasonic vibration-assisted drilling of wrought IN718 improved the generated surface roughness and enhanced tool life, as presented in [32, 33].

Based on the reviewed studies, it is evident that there is a lack of investigations of the effects of mechanical post-processing/ hybrid manufacturing of LPBF IN625. These gaps can be summarized as follows:

- Assessment of the dimensional accuracy and surface conditions of as-built LPBF IN625
- Investigating the feasibility of post-LPBF drilling of IN625 LPBF manufactured parts
- Examining the effects of conventional drilling and low-frequency VAD on the quality and surface integrity of LPBF IN625.
- Comparison between the effects of LP vs. drilling on inducing compressive in-depth RS in LPBF IN625
- Study the feasibility of using conventional drilling or VAD as a fast, cost-effective post-processing route compared to LP.

6.2. Experimental procedures

6.2.1. Feedstock and LPBF process parameters

An EOS M280 LPBF equipped with a 400 W Ytterbium fiber laser and a 100 µm laser spot size was used to manufacture parts using a feedstock of gas atomized IN625 powder. The powder had a powder size distribution of 15 – 45 µm and a

chemical composition listed in Table 6-1. Based on a previous investigation [4], the process parameters were selected, as shown in Table 6-2, to result in a high density while having a relatively high surface roughness and surface tensile RS.

Table 6-1: Chemical Composition of Inconel 625 powder (wt%).

Element	Wt%
Ni	Balance
Cr	20-23
Mo	8-10
Nb	3.15-4.15
Fe	<5
Si	<0.5
Mn	<0.5
Al	<0.4
C	<0.1
Co	<1
S	<0.015
Ti	<0.04
P	<0.015

Table 6-2: the Inconel 625 process parameters

Parameter	Value
Power (P)	140 W
Scan speed (v)	500 mm/s
Hatch spacing (h)	0.1 mm
Layer thickness (t)	40 μm

6.2.2. Part geometry

An IN625 plate was designed and manufactured with dimensions of 130 mm x 130 mm and 5 mm thickness. In order to save energy and cost during drilling, the plate was designed with an array of pilot holes with diameters less than the final intended 6 mm holes. Additionally, the built plate had 17 columns of 4 different pilot hole sizes (3, 3.5, 4, and 4.5 mm), as shown in Figure 6-1, to investigate the effect of different drilling techniques and pilot hole diameter. In addition, the plate had nine 6 mm holes used for the as-built comparison and the application of laser peening.

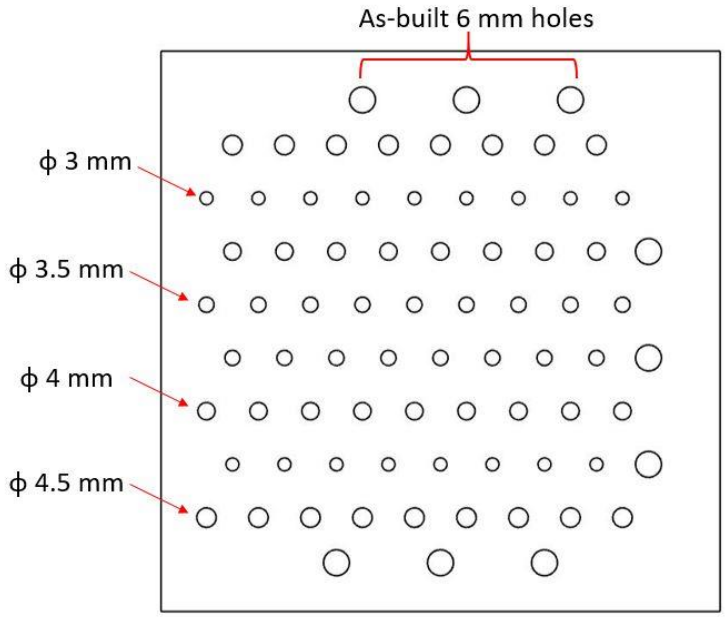

Figure 6-1Geometry of the proposed plate with pilot holes

6.2.3. Drilling parameters

The additively manufactured plate was mounted on a 5-axis Makino A88ε machine center to perform the drilling process, as shown in Figure 6-2. VAD was performed

using a 2.5 oscillation/rev commercially available MITIS tool holder PG8045B3_HSK-A100_ER40 [34]. This module can generate a vibrational amplitude of 0.01-0.48 mm with a 3500 rpm speed limitation. The drilling process was performed using a 6 mm uncoated tungsten carbide (WC) twist drill with118 [35], with a wide range of cutting parameters, shown in **Table 6-3**.

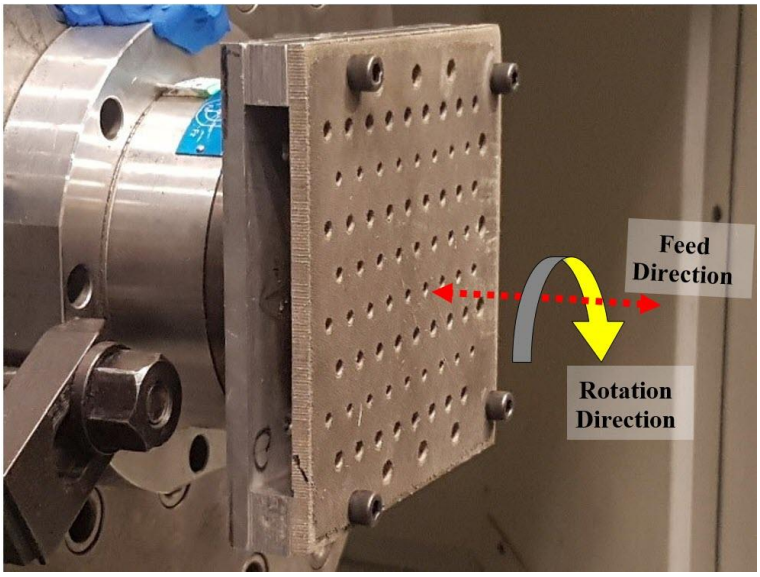

Figure 6-2 Experimental setup for the drilling process of IN 625 plate manufactured by LPBF technique

Table 6-3: experiment study process parameters

Parameter	Levels
Cutting speed (rpm)	500, 1000
Feed rate (mm/rev)	0.025, 0.075
Vibration amplitude (mm)	0, 0.1, 0.16, 0.25
Pilot hole diameter (mm)	3, 3.5, 4, 4.5

6.2.4. Laser peening

Laser peening was performed on the plate using a 1000 MW peak-power laser with a wavelength of 1053 μm. The 6 mm as-built holes were peened with an energy intensity of 10 GW/cm^2 and an 18 ns pulse duration. Three layers of peening were applied without using a separate ablative layer of aluminum tape. Each laser spot was a 3 mm square with the placement of one spot to the next by 3% spot-to-spot overlap. The first layer of peening was applied as a rectangular array of equally spaced square spots. The second layer array of peening was offset from the first layer by 1.5 mm in both planar directions. Finally, the third layer of peening was placed in the same array position as the first layer.

6.2.5. Holes quality characterization

A Mitutoyo Coordinate Measuring Machine (CMM) was used to calculate the holes' geometrical accuracy by measuring an average of ten points. The diameters of the pilot holes were measured in addition to the final 6 mm diameters under different post-processing conditions. Additionally, the surface roughness of the inner walls of the 6 mm holes was measured using an SJ-410 stylus profilometer with a 0.0001 μm resolution and represented in terms of the arithmetic average surface roughness (R_a). In-depth RS was measured from the top surface of the plate at a location 1 mm away from the hole edge in a direction parallel to the solidified laser tracks. XRD method was used with a Mn radiation source, a Bragg's angle of 152^o. The Beta angle had 11 tilts, and a 3^o oscillation was superimposed on the collimator with a 2 mm aperture and the modulus of elasticity was set to 200 GPa.

The plates were cut using waterjet abrasive cutting, mounted, and polished using the typical metallography steps. Microhardness was measured using a Vickers hardness test with a load of 100 gf applied for 10 s. Measurements were done in two directions; the first is in a radial direction away from the hole's inner surface, i.e., the machined surface. The second direction is the axial direction starting at the top surface of the plate adjacent to the hole edge.

6.3. Results and discussion

6.3.1. Hole size accuracy and surface roughness

The diameters of the pilot holes in the as-built state are presented in Figure 6-3, where the measured diameters are compared to the nominal diameters. All as-built pilot holes had an undersized diameter, which agrees with the literature [36, 37]. However, it is observed that the 4.5 mm diameter pilot hole had the least deviation from the nominal diameter with a mean diameter of 4.477 mm. The reason that the as-built hole diameters are undersized could be attributed to part shrinkage and distortion as it cools down, which is observed post-printing where the plate separated from the supports underneath at the corners, as shown in Figure 6-4. In addition, the sintering of satellite powders to the sidewalls, in this case, the inner surface of the holes, causes a deviation of the dimensional accuracy [14]. On the other hand, the least deviation at the 4.5 mm diameter could be attributed to the larger lateral area of the hole thus more heat is transferred, and reducing the heat accumulation that would increase the expansion and the amount of sintered satellite powder.

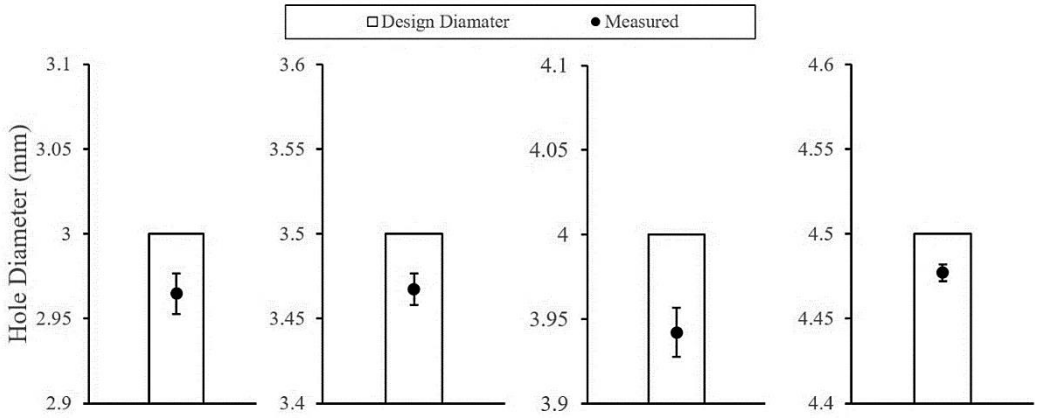

Figure 6-3 Hole accuracy measurement of pilot holes in as-built condition

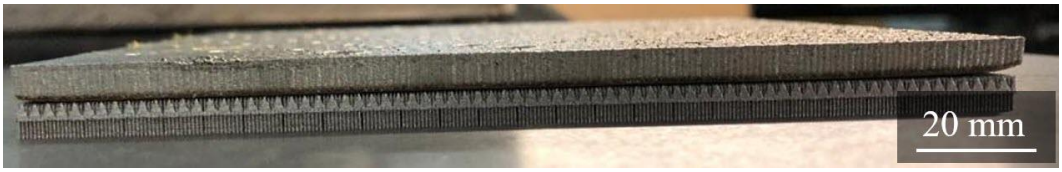

Figure 6-4 Distortion and separation of the printed plate from its supports

The pilot holes were drilled using conventional drilling and LF-VAD with different vibration amplitudes. The highest amplitude of 0.25 mm resulted in tool failure; hence, it was discarded from the current study. The measured hole diameters post-drilling and the as-built holes are presented in Figure 6-5 for a cutting speed of 1000 rpm and a feed rate of 0.025 mm/rev. Compared to the nominal diameter of 6 mm, the additively manufactured hole geometry resulted in an undersized diameter with an IT grade of 14 according to the ISO 286 standard. Conversely, the post-process machining resulted in an oversized hole diameter with conventional drilling resulting in the least deviation of the hole diameter. The geometrical deviation was found to be in the range of +31 µm to +50 µm relative to the mean value, which corresponds to an IT grade of 10 according to the ISO 286 standard.

Additionally, increasing the pilot hole diameter had a negligible impact on the geometrical accuracy. However, the vibration amplitude had a prominent effect on the hole dimensional accuracy post-LF-VAD. For A_m= 0.1 mm, increasing the pilot hole diameter enhanced the geometrical accuracy. The geometrical deviation was reduced from +131 µm at a 3 mm pilot hole diameter to +76 µm at a 4.5mm pilot hole diameter, corresponding to an IT grade of 11. The geometrical accuracy enhancement could be attributed to the lower machined material volume, which resulted in less heat generation and reduced thermal distortion of the tool and the workpiece [38, 39].

On the other hand, increasing the vibration amplitude to 0.16 mm resulted in poor geometrical accuracy, where the deviation increased to reach 283 µm at a 4.5 mm pilot hole diameter. This significant increase could be attributed to the higher repetitive tool-workpiece impacts that resulted in a relative hardening of workpiece material and a higher heat generation. Moreover, increasing the pilot hole diameter concentrated the cutting action near the tool margin. Hence, the cutting edge tends to wear and fracture, resulting in a non-homogenous cutting process and poor machining performance. The reduction in geometrical deviation with increasing the pilot hole was observed for other cutting parameters, as shown in Figure 6-6, for conventional drilling and LF-VAD. Additionally, the hole lateral surface roughness was measured and plotted in Figure 6-7. It was found that the as-built holes had the highest surface roughness, which contributes to the below nominal diameters.

However, drilling processes, both conventional and LF-VAD, improved the surface roughness equally.

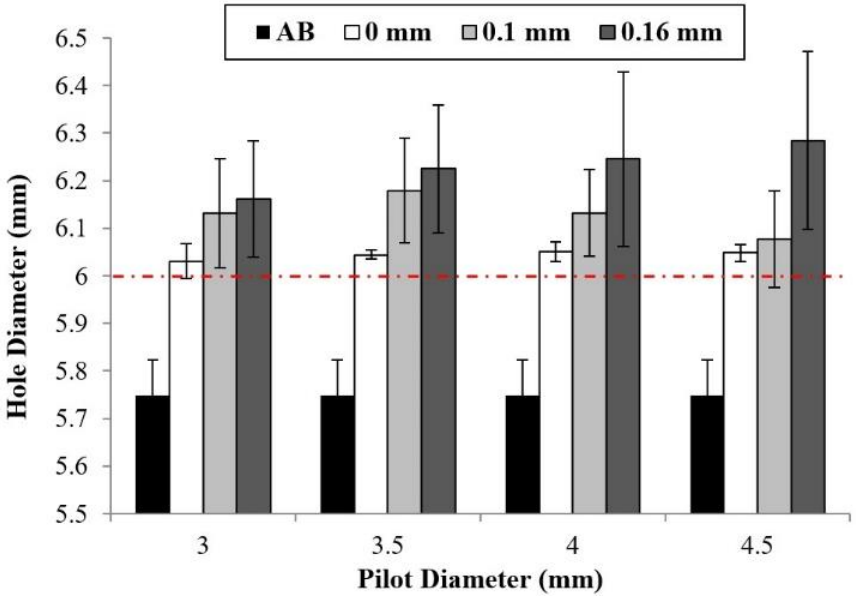

Figure 6-5: The effect of the drilling vibration amplitude on the hole accuracy at 1000 rpm and 0.025 mm/rev compared to the as-built hole diameter

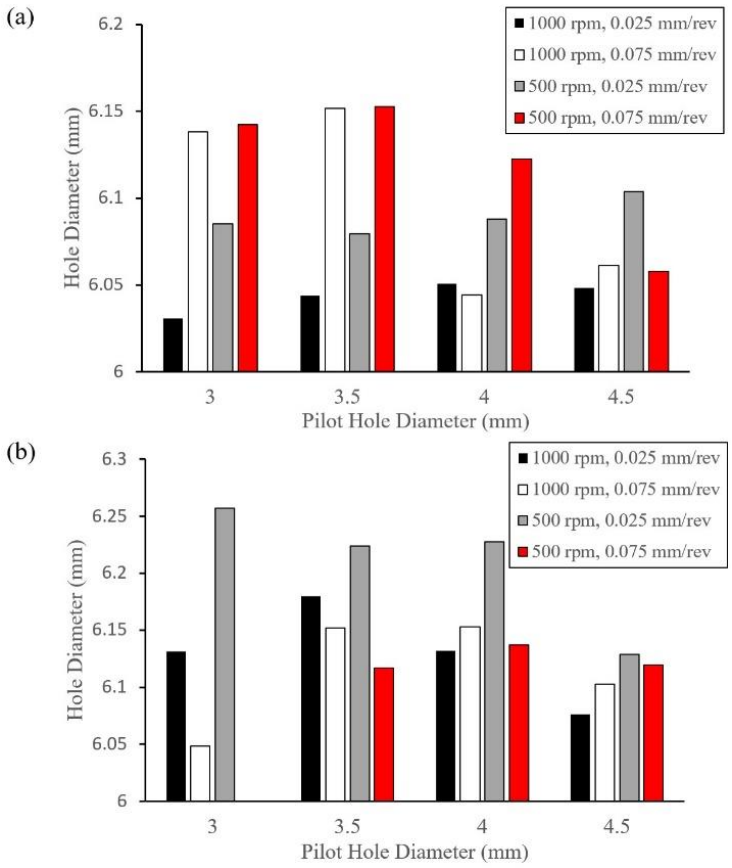

Figure 6-6 Hole accuracy post-drilling for different cutting parameters a) conventional drilling b) VAD A_m=0.1 mm

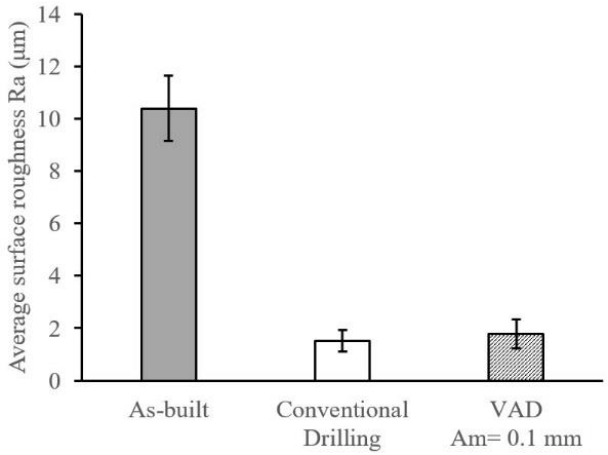

Figure 6-7 Arithmetic average roughness R_a (µm) for as-built, conventionally drilled, and VAD with amplitude of 0.1 mm

Therefore, based on the results mentioned above, the 4.5 mm pilot hole was chosen for further surface integrity investigation based on the abovementioned results. In addition, the larger pilot hole will also translate into less material removal, hence less energy cost. The cutting parameters of 1000 rpm and 0.025 mm/rev were selected along with the 4.5 mm pilot hole, resulting in the least diameter size deviation.

6.3.2. Micro-hardness

The effect of the selected post-process parameters, for conventional drilling and LF-VAD, on the surface integrity was investigated. Since LP is a commonly used post-process, it was applied to the as-built hole to compare and evaluate the possible benefits of drilling vs. LP for surface integrity. Figure 6-8 presents the surface and subsurface microhardness profile of the IN625 after different processes. The microhardness profile was measured in the radial direction at a distance of 25 μm from the hole lateral surface. It was observed that the surface microhardness exhibited a higher value for all investigated processing techniques compared to the bulk material, i.e., away from the hole's surface. This phenomenon could be attributed to: i) Thermal load and ii) Work hardening due to plastic deformation [12, 40], as follows:

- *Thermal load*: For both LPBF and drilling processes, the material was exposed to repetitive heating and cooling cycles, which have the maximum values at the hole sidewalls. This process resulted in a relatively higher

cooling rate at the surface compared to the bulk material; hence, resulting in higher hardness.

- *Work hardening due to plastic deformation*: The combined effect of the cutting mechanical load and the generated pressure under the cutting edge increased the material hardening due to the plastic strains induced in the uncut workpiece. Work hardening propagated the dislocations through the Inconel lattice structure, which added a critical limitation during the machining process of Inconel material [41, 42]. The same effects were exhibited under LP, which induced plastic strains due to the rapid expansion of the confined plasma layer, thus causing a plastic strain of the surrounding material [22, 43].

The machining process resulted in a slight increase in the surface and subsurface microhardness. The microhardness increased by 7 Hv for conventional drilling and 10 Hv for the LF-VAD process. On the other hand, the LP significantly increased the surface and subsurface values, where the microhardness increased by an average of 30 Hv compared to the as-built microhardness. The same trends were found for the in-depth microhardness profiles, i.e., parallel to the build direction, as shown in Figure 6-9, measured from the top surface and at 25 μm from the hole edge. The drilling process effect diminished at about 100 μm from the surface, while LP had a much deeper effect in radial and axial directions.

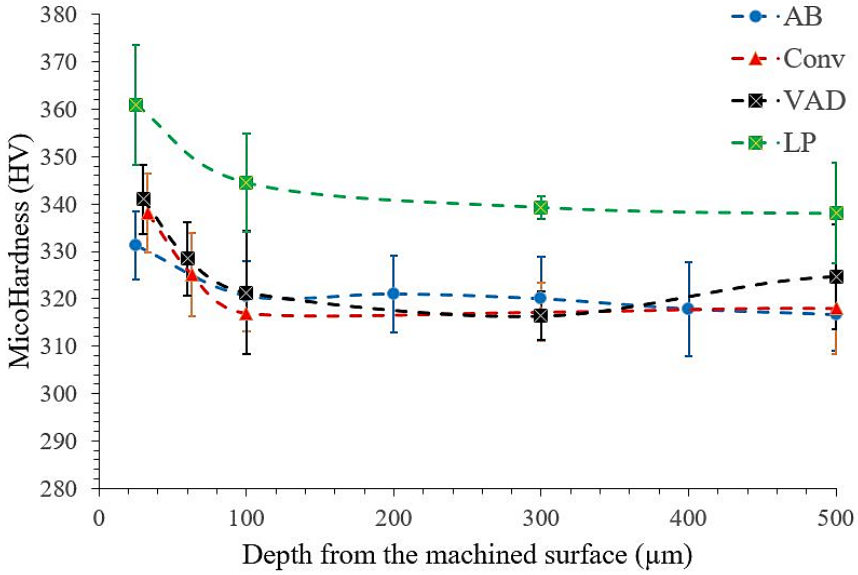

Figure 6-8: The microhardness profile in the radial direction for the as-built IN625 and post-processed with conventional drilling, vibration-assisted drilling, and laser peening

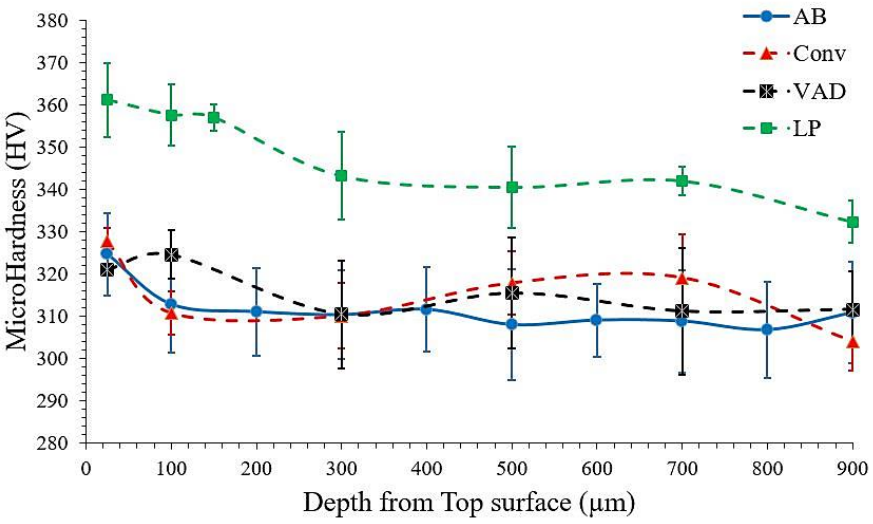

Figure 6-9: The microhardness profile in the axial direction for the as-built IN625 and post-processed with conventional drilling, vibration-assisted drilling, and laser peening

6.3.3. Residual stresses

Figure 6-10 presents the surface RS measured at the plate's top surface and 1 mm from the hole edge for the as-built, post-processed conventionally drilled LF-VAD and the LP conditions. The as-built measurement showed a surface tensile RS of 51 MPa, typical for LPBF due to the high thermal gradients and the cyclic heating and cooling between the melt pool and the previously consolidated layer [13, 17, 44]. However, post-printing conventional drilling increased the surface tensile RS to 93 MPa, as shown in Figure 6-10. This increase could be attributed to the generated heat during the drilling process. Since IN625 has a low thermal conductivity, the heat cannot be dissipated effectively, and the high temperature is localized near the cutting surface, which causes tensile RS[42].

On the other hand, the vibration-assisted drilling with A_m=0.1 mm resulted in surface compressive RS. This inversion in RS could be attributed to a better chip evacuation mechanism, which takes away heat from the cutting zone, and the intermittent cutting action. Therefore, less heat is generated and retained below the machined surface, reducing the chance of tensile RS generation. In addition, the presence of a repetitive tool-workpiece impact mechanism and lower temperature concentration would mean that the mechanical deformation is more dominant hence generating compressive RS, as reported in [30, 45]. LP significantly affected the material surface RS, inducing a 166 MPa surface compressive RS. The desired compressive RS was induced due to the high plastic deformation with minimal heat

generation; hence, the plastic strain is highly dominant and induced compressive RS [22, 46].

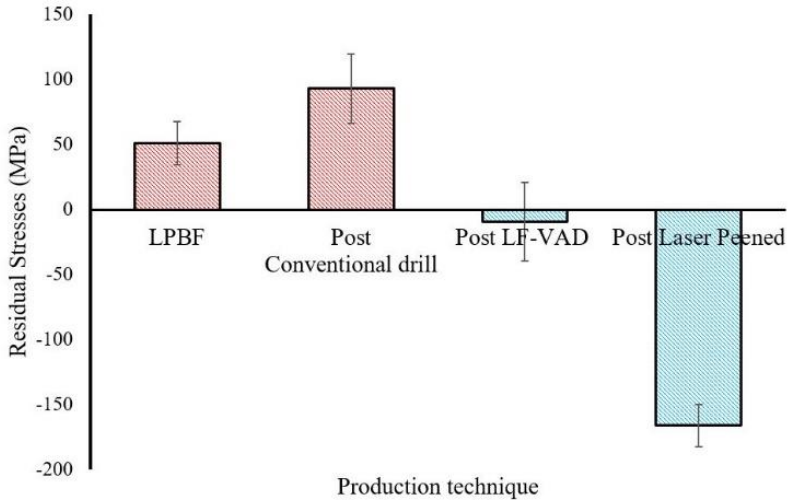

Figure 6-10: The effect of post-processing machining technique on the surface RS measured along the laser scan direction

The in-depth RS for all four conditions was measured and presented in Figure 6-11. For the as-built condition, the tensile RS increased from 51 MPa at the surface to reach 108 MPa at a depth of 76 µm measured from the top surface, followed by a gradual decline to 210 µm, where compressive stress has been observed. This increase could be attributed to the subsurface's poor cooling performance compared to the surface. These high tensile stresses will have a direct negative impact on the part fatigue life. Despite observing relatively higher tensile surface stresses, the subsurface investigation for the post-conventional drilling process did not show any subsurface tensile stress peaks but rather a rapid decline into compressive RS at a 40 µm depth. The RS trend improvement could be attributed to the added plastic

strain during the drilling process. LF-VAD showed a 10 MPa surface compressive RS which increased along the depth to reach a maximum of 270 MPa at 178 µm depth, with the whole stress profile being compressive until a depth of 450 µm, which agrees with the results reported in [39]. The favored compressive RS will have a positive impact on the part fatigue life. LP induced a high surface compressive stress of 166 MPa, which increased to a maximum of 670 MPa at a depth of 178 µm, beyond which the RS trend continued to be compressive down to 450 µm, thus indicating a deep penetration depth of compressive RS.

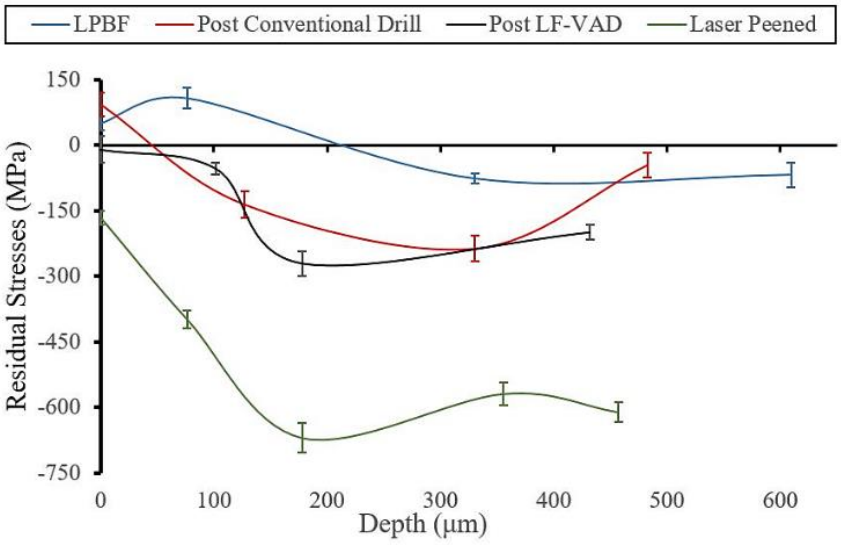

Figure 6-11: The effect of post-processing machining technique on the subsurface RS measured along the laser scan direction

6.4. Conclusions

LPBF suffers from drawbacks such as high tensile residual stresses, inferior surface quality, and geometrical dimensions inaccuracy despite LPBF's unique advantages, such as manufacturing intricate, custom, and complex designs at a low cost. Correction of these drawbacks requires several post-processing steps, which pose an additional cost to the manufacturing process. This study aims first to assess the manufacturing quality of Laser powder bed fusion of IN625 parts in terms of hole accuracy and surface integrity. Secondly, investigate the feasibility of reducing the number of post-processes by employing either conventional drilling or low-frequency vibration-assisted drilling to obtain the desired hole accuracy and surface integrity compared to the typically used post-process of Laser peening. It was found that LPBF produced undersized holes with high internal surface roughness. Conventional drilling and vibration-assisted drilling of LPBF parts reduced the hole diameter deviation by 80% and 40%, respectively, when starting with a printed pilot hole diameter of 4.5 mm. In addition, both drilling techniques induced in-depth compressive residual stress, thus correcting the as-printed in-depth tensile residual stresses. However, conventional drilling-induced increased the surface tensile residual stress by two folds compared to as-built conditions. Despite surface tensile residual stress, the benefit of conventional drilling was its ability to invert the tensile residual stress to compressive at a depth of 40 μm compared to 500 μm for the as-built state. In comparison, Laser peening was superior to drilling in its ability to generate a deeper penetration of the compressive residual stresses with a

magnitude three folds that generated under drilling. However, laser peening will require an additional process such as reaming to improve the dimensional accuracy, thus making the proposed drilling approach a more cost-effective route.

References

[1] G. Marchese, X. Garmendia Colera, F. Calignano, M. Lorusso, S. Biamino, P. Minetola, *et al.*, "Characterization and comparison of Inconel 625 processed by selective laser melting and laser metal deposition," *Advanced Engineering Materials*, vol. 19, p. 1600635, 2017.

[2] G. Dinda, A. Dasgupta, and J. Mazumder, "Laser aided direct metal deposition of Inconel 625 superalloy: Microstructural evolution and thermal stability," *Materials Science and Engineering: A*, vol. 509, pp. 98-104, 2009.

[3] E. Ezugwu, Z. Wang, and A. Machado, "The machinability of nickel-based alloys: a review," *Journal of Materials Processing Technology*, vol. 86, pp. 1-16, 1999.

[4] M. Balbaa, M. Elbestawi, and J. McIsaac, "An experimental investigation of surface integrity in selective laser melting of Inconel 625," *The International Journal of Advanced Manufacturing Technology*, vol. 104, pp. 3511-3529, 2019.

[5] M. Yakout, A. Cadamuro, M. Elbestawi, and S. C. Veldhuis, "The selection of process parameters in additive manufacturing for aerospace alloys," *The International Journal of Advanced Manufacturing Technology*, vol. 92, pp. 2081-2098, 2017.

[6] M. Yakout, M. Elbestawi, and S. C. Veldhuis, "Process-structure-property relationship for selective laser melting of aerospace alloys," in *The 7th International Conference on Virtual Machining Process Technology (VMPT)*, 2018.

[7] D. Mueller and H. Mueller, "Experiences using rapid prototyping techniques to manufacture sheet metal forming tools," in *Proc. ISATA Conference, Dublin*, 2000, pp. 25-27.

[8] M. Yakout, M. Elbestawi, L. Wang, and R. Muizelaar, "Selective laser melting of soft magnetic alloys for automotive applications," in *Joint Special Interest Group meeting between euspen and ASPE*, 2019.

[9] J. Choi and J. Mazumder, "Rapid manufacturing by laser aided direct metal deposition process: issues and examples," in *International Design Engineering Technical Conferences and Computers and Information in Engineering Conference*, 2001, pp. 333-338.

[10] D. Mahmoud and M. A. Elbestawi, "Lattice structures and functionally graded materials applications in additive manufacturing of orthopedic implants: a review," *Journal of Manufacturing and Materials Processing,* vol. 1, p. 13, 2017.

[11] D. Mahmoud and M. Elbestawi, "Selective laser melting of porosity graded lattice structures for bone implants," *The International Journal of Advanced Manufacturing Technology,* vol. 100, pp. 2915-2927, 2019.

[12] Y. Karabulut and Y. Kaynak, "Drilling process and resulting surface properties of Inconel 718 alloy fabricated by Selective Laser Melting Additive Manufacturing," *Procedia CIRP,* vol. 87, pp. 355-359, 2020.

[13] A. Kreitcberg, V. Brailovski, and S. Turenne, "Effect of heat treatment and hot isostatic pressing on the microstructure and mechanical properties of Inconel 625 alloy processed by laser powder bed fusion," *Materials Science and Engineering: A,* vol. 689, pp. 1-10, 2017.

[14] M. Balbaa, A. Ghasemi, E. Fereiduni, M. Elbestawi, S. Jadhav, and J.-P. Kruth, "Role of Powder Particle Size on Laser Powder Bed Fusion Processability of AlSi10Mg Alloy," *Additive Manufacturing,* p. 101630, 2020.

[15] D. D. Gu, W. Meiners, K. Wissenbach, and R. Poprawe, "Laser additive manufacturing of metallic components: materials, processes and mechanisms," *International materials reviews,* vol. 57, pp. 133-164, 2012.

[16] S. Wen and Y. C. Shin, "Modeling of transport phenomena in direct laser deposition of metal matrix composite," *International journal of heat and mass transfer,* vol. 54, pp. 5319-5326, 2011.

[17] Z. Tian, C. Zhang, D. Wang, W. Liu, X. Fang, D. Wellmann, *et al.*, "A review on laser powder bed fusion of inconel 625 nickel-based alloy," *Applied Sciences,* vol. 10, p. 81, 2020.

[18] J. Jiang, X. Xu, and J. Stringer, "Support structures for additive manufacturing: a review," *Journal of Manufacturing and Materials Processing,* vol. 2, p. 64, 2018.

[19] M. J. Donachie and S. J. Donachie, *Superalloys: a technical guide*: ASM international, 2002.

[20] L. M. Suave, D. Bertheau, J. Cormier, P. Villechaise, A. Soula, Z. Hervier, *et al.*, "Impact of thermomechanical aging on alloy 625 high temperature mechanical properties," in *8th International Symposium on Superalloy 718 and Derivatives*, 2014, pp. 317-331.

[21] S. Das, M. Wohlert, J. J. Beaman, and D. L. Bourell, "Direct selective laser sintering and containerless hot isostatic pressing for high performance metal components," in *1997 International Solid Freeform Fabrication Symposium*, 1997.

[22] L. K. Gillespie, *Design for Advanced Manufacturing: Technologies and Processes*: McGraw-Hill Education, 2017.

[23] V. Authors, "ASM Handbook Volume 5: Surface Engineering," ed: ASM International, Materials Park, Ohio, USA, 1994.

[24] D. T. Ardi, L. Guowei, N. Maharjan, B. Mutiargo, S. H. Leng, and R. Srinivasan, "Effects of post-processing route on fatigue performance of laser powder bed fusion Inconel 718," *Additive Manufacturing*, vol. 36, p. 101442, 2020.

[25] D. Lesyk, V. Dzhemelinskyi, S. Martinez, B. Mordyuk, and A. Lamikiz, "Surface Shot Peening Post-processing of Inconel 718 Alloy Parts Printed by Laser Powder Bed Fusion Additive Manufacturing," *Journal of Materials Engineering and Performance*, vol. 30, pp. 6982-6995, 2021.

[26] E. Maleki, O. Unal, M. Guagliano, and S. Bagherifard, "The effects of shot peening, laser shock peening and ultrasonic nanocrystal surface modification on the fatigue strength of Inconel 718," *Materials Science and Engineering: A*, vol. 810, p. 141029, 2021.

[27] R. Hussein, "Vibration Assisted Drilling of Carbon Fiber Reinforced Polymer and Titanium Alloy for Aerospace Application," 2019.

[28] C. Kuo, Z. Li, and C. Wang, "Multi-objective optimisation in vibration-assisted drilling of CFRP/Al stacks," *Composite Structures*, vol. 173, pp. 196-209, 2017/08/01/ 2017.

[29] J. Xu, C. Li, M. Chen, and F. Ren, "A comparison between vibration assisted and conventional drilling of CFRP/Ti6Al4V stacks," *Materials and Manufacturing Processes*, vol. 34, pp. 1182-1193, 2019.

[30] R. Hussein, A. Sadek, M. A. Elbestawi, and M. H. Attia, "Surface and microstructure characterization of low-frequency vibration-assisted drilling of Ti6Al4V," *The International Journal of Advanced Manufacturing Technology*, vol. 103, pp. 1443-1457, April 05 2019.

[31] S. Li, D. Zhang, C. Liu, and H. Tang, "Exit burr height mechanistic modeling and experimental validation for low-frequency vibration-assisted drilling of aluminum 7075-T6 alloy," *Journal of Manufacturing Processes*, vol. 56, pp. 350-361, 2020/08/01/ 2020.

[32] Y. S. Liao, Y. C. Chen, and H. M. Lin, "Feasibility study of the ultrasonic vibration assisted drilling of Inconel superalloy," *International Journal of Machine Tools and Manufacture*, vol. 47, pp. 1988-1996, 2007/10/01/ 2007.

[33] S. Chen, P. Zou, Y. Tian, J. Duan, and W. Wang, "Study on modal analysis and chip breaking mechanism of Inconel 718 by ultrasonic vibration-assisted drilling," *The International Journal of Advanced Manufacturing Technology*, vol. 105, pp. 177-191, 2019.

[34] MITIS Engineer. *MITIS Tool Holder*. Available: https://www.mitis.fr/

[35] Y.-C. group. *YG-1 CANADA GROUP*. Available: http://www.yg1.ca/

[36] P. R. Gradl, D. C. Tinker, J. Ivester, S. W. Skinner, T. Teasley, and J. L. Bili, "Geometric feature reproducibility for laser powder bed fusion (L-PBF) additive manufacturing with Inconel 718," *Additive Manufacturing,* vol. 47, p. 102305, 2021.

[37] S. Gruber, C. Grunert, M. Riede, E. López, A. Marquardt, F. Brueckner, *et al.*, "Comparison of dimensional accuracy and tolerances of powder bed based and nozzle based additive manufacturing processes," *Journal of Laser Applications,* vol. 32, p. 032016, 2020.

[38] M. Bono and J. Ni, "The effects of thermal distortions on the diameter and cylindricity of dry drilled holes," *International Journal of Machine Tools and Manufacture,* vol. 41, pp. 2261-2270, 2001.

[39] R. Hussein, A. Sadek, M. A. Elbestawi, and M. Attia, "Low-frequency vibration-assisted drilling of hybrid CFRP/Ti6Al4V stacked material," *International Journal of Advanced Manufacturing Technology,* vol. 98, pp. 2801-2817, Oct 2018.

[40] E. Ezugwu and S. Tang, "Surface abuse when machining cast iron (G-17) and nickel-base superalloy (Inconel 718) with ceramic tools," *Journal of Materials Processing Technology,* vol. 55, pp. 63-69, 1995.

[41] D. G. Thakur, B. Ramamoorthy, and L. Vijayaraghavan, "Effect of cutting parameters on the degree of work hardening and tool life during high-speed machining of Inconel 718," *The International Journal of Advanced Manufacturing Technology,* vol. 59, pp. 483-489, 2012.

[42] R. Pawade, S. S. Joshi, and P. Brahmankar, "Effect of machining parameters and cutting edge geometry on surface integrity of high-speed turned Inconel 718," *International Journal of Machine Tools and Manufacture,* vol. 48, pp. 15-28, 2008.

[43] M. Rozmus-Górnikowska, J. Kusiński, and Ł. Cieniek, "Effect of laser shock peening on the microstructure and properties of the inconel 625 surface layer," *Journal of Materials Engineering and Performance,* vol. 29, pp. 1544-1549, 2020.

[44] M. Balbaa, S. Mekhiel, M. Elbestawi, and J. McIsaac, "On selective laser melting of Inconel 718: Densification, surface roughness, and residual stresses," *Materials & Design,* p. 108818, 2020.

[45] N. K. Maroju and V. K. Pasam, "FE modeling and experimental analysis of residual stresses in vibration assisted turning of Ti6Al4V," *International Journal of Precision Engineering and Manufacturing,* vol. 20, pp. 417-425, 2019.

[46] A. Jinoop, S. K. Subbu, C. Paul, and I. Palani, "Post-processing of laser additive manufactured Inconel 718 using laser shock peening," *International Journal of Precision Engineering and Manufacturing,* vol. 20, pp. 1621-1628, 2019.

Chapter 7

Summary and Conclusions

7.1. Summary and conclusive remarks

Laser powder bed fusion (LPBF) of nickel-based superalloys has been studied over the past decade. Most studies focus on the effect of LPBF on the microstructure or the impact of different heat treatments on the microstructure. There is limited research on the process-structure-property (PSP) of LPBF of nickel-based superalloys. Most studies employ either the default or a limited range of process parameters. This thesis concentrates on the whole production cycle of reliable end-use parts by investigating the surface integrity, fatigue life, and post-processing of nickel-based superalloys IN625 and IN718.

A wide range of process parameters, namely, Laser power, scan speed, and hatch spacing, was investigated to assess the PSP in LPBF of both alloys. The part properties investigated were the relative density, the surface roughness, and the surface residual stress (RS), as these three properties will affect the part mechanical properties. Process maps were developed to serve as a guide to select the proper process parameters to predict the part properties.

A multi-scale finite element (FE) model was developed to predict the RS and understand the effect of process parameters on the temperature gradients and cooling rates and their subsequent effect on inducing RS. The numerical results were validated experimentally with temperature measurements carried out using a two-color pyrometer and in-depth RS profiles.

The process maps developed earlier were used to select a subset of parameters that would result in a high relative density (>99%), low surface roughness, and the least tensile surface RS. Moreover, tensile testing was done to determine the optimum process parameters that would possess good surface integrity and high mechanical properties. In addition, fatigue testing was performed for both alloys in as-built and shot-peened conditions to investigate the effect of post-processing. It was found that shot peening can lead to fatigue life similar to that of wrought alloy, requiring post-printing heat treatment.

Additionally, other post-process were investigated to determine the feasibility of reducing the number of post processes and cost to enhance the part properties. Conventional drilling, vibration-assisted drilling (VAD), and laser peening were investigated, and their effect on dimensional accuracy, surface roughness, and RS was explored. It was found that VAD could improve the dimensional accuracy of as-built parts and the surface roughness and induce compressive RS, which are beneficial for improving fatigue life.

In summary, IN625 and IN718 can be successfully processed using LPBF by employing the following process parameters: 220 W, 500 mm/s at a hatch spacing of 0.1 mm for IN625 and 320 W, 600 mm/s at a hatch spacing of 0.12 mm to produce parts with high density and low surface roughness. In order to overcome the adverse effect of the tensile residual stresses and improve fatigue life, post-processing is recommended by either applying shot peening or laser peening. Additionally, low-frequency vibration-assisted drilling is a low cost effective solution to improve the surface integrity.

7.2.Future work

The current study investigated the PSP of IN625 and IN718 during LPBF, modeling the LPBF process, tensile, and fatigue testing of IN625 and IN718 manufactured using an optimum set of process parameters, and the effect of subsequent post-process to improve part properties while reducing the cost and time. However, additional future steps are suggested to increase the manufacturing capabilities and quality of LPBF parts as follows:

Investigate the effect of different scan strategies, such as contouring, pre-exposure, and re-melting, on the parts density, surface roughness, residual stresses, and dimensional accuracy. This will help determine the feasibility of obtaining higher quality as-built parts, which would require fewer post-processing steps.

The FE model captured the melt dynamics artificially by changing the thermal properties of the material model. However, a hybrid computational fluid dynamics

(CFD) and FE would be a better fit for a multi-scale model where CFD can be applied to a high fidelity model to get a better prediction of the temperature gradient and cooling rate, as well as predict the surface topography, and keyhole formation. In addition, using an adaptive meshing for the FE model of the part scale will reduce the computational time while converting the part scale model into a high fidelity model to gain an insight into the temperature gradient and cooling across the added layers.

Finally, the mechanical properties of both alloys can be tested at high temperatures to assess the efficacy of post-processing to impose favorable surface integrity and maintain good mechanical properties, which will extend the alloys used for high-temperature applications such as the aerospace industry.

7.3.Contribution

This thesis gives a deep understanding of the manufacturability, PSP, and the entire production cycle of IN625 and IN718 LPBF parts. Furthermore, the findings of this study provide a better process parameters selection map to obtain end-use parts with good mechanical properties suitable for highly demanding applications.

Appendix A: Fatigue S-N Curves Equations for Wrought IN625 and IN718

The equations for the best-fit curves for S-N plots of wrought alloys tested at room temperature are as follows:

- Wrought IN625 unnotched sheet

$$\log N_f = 26.91 - 10.77 \log S_{eq}$$

$$S_{eq} = S_{max}(1 - R)^{0.43}$$

- Wrought IN625 notched sheet ($K_t = 3$)

$$\log N_f = 10.35 - 3.56 \log(S_{eq} - 22.89)$$

$$S_{eq} = S_{max}(1 - R)^{0.64}$$

- Wrought IN718 unnotched sheet

$$\log N_f = 8.63 - 2.07 \log(S_{eq} - 58.48)$$

$$S_{eq} = S_{max}(1 - R)^{0.58}$$

- Wrought IN718 notched sheet ($K_t = 3$)

$$\log N_f = 8.17 - 2.23 \log(S_{eq} - 30.58)$$

$$S_{eq} = S_{max}(1 - R)^{0.68}$$